A Treatise on Open Problems in Robotics : from Cable-Driven Platforms to Persistent Manifolds

Vincenzo Di Paola

COLLEGE DOCTORAL PAYS DE LA LOIRE
SCIENCES DE L'INGENIERIE ET DES SYSTEMES

CENTRALE NANTES

Università di Genova

MEMOIRE DE DOCTORAT DE

L'ECOLE CENTRALE DE NANTES
ET UNIVERSITA' DI GENOVA

ECOLE DOCTORALE N° 602
Sciences de l'Ingénierie et des Systèmes
Spécialité : *Robotique*

Par
Vincenzo DI PAOLA

A Treatise on Open Problems in Robotics:
from Cable-Driven Platforms to Persistent Manifolds

Projet de recherche doctoral présenté et soutenu à Bologne, le 15 Décembre 2023
Unité de recherche : UMR 6004, Laboratoire des Sciences du Numérique de Nantes (LS2N)

Rapporteurs avant soutenance :

Andreas MÜLLER	Full Professor, Johannes Kepler University, Autriche
Xianwen KONG	Associate Professor, Heriot-Watt University, Royaume-Uni

Composition du Jury :

Président :	Andreas MÜLLER	Full Professor, Johannes Kepler University, Autriche
Examinateurs	Xianwen KONG	Associate Professor, Heriot-Watt University, Royaume-Uni
	Christine CHEVALLEREAU	Directrice de recherche CNRS, École Centrale de Nantes
	Matteo VEROTTI	Associate Professor, University of Genova, Italie

Directeur de recherches doctorales:	Stéphane CARO, Directeur de recherche CNRS, École Centrale de Nantes
Directeur de recherches doctorales:	Matteo ZOPPI, Full Professor, University of Genova, Italie
Co-enc. de recherches doctorales:	Marco CARRICATO, Full Professor, University of Bologna, Italie
Co-enc. de recherches doctorales:	Alexandre GOLDSZTEJN, Chargé de recherche, École Centrale de Nantes

Titre : Un Traité sur les Problémes Ouverts en Robotique : Depuis les Plateformes Câblées aux Variétés Persitantes

Mots clés : Plateformes à câbles, contrôle adaptatif, cinématique théorique, systemes persistants

Résumé : Malgré les nombreux efforts en cours pour développer des questions dans le domaine de la robotique, il existe tout autant de problèmes ouverts et non résolus. Cette thèse se propose donc de s'attaquer à certains défis, dans le but d'effleurer la surface et de faire émerger de nouvelles idées ou de nouvelles voies. Les thèmes abordés seront divisés en deux parties. La première concerne le développement et l'amélioration des techniques de contrôle des systèmes robotiques à câbles. La seconde se concentre sur l'étude des variétés persistantes constituant des aspects de la cinématique théorique. En détail,

- la partie I concerne les robots parallèles à câbles. Elle développe à la fois une technique de calcul des tensions à appliquer aux câbles et la conception d'un contrôleur robuste. L'objectif est donc d'améliorer les deux éléments de base constituant le schéma de commande général d'un robot afin d'accroître les performances lors de l'exécution d'une task;
- La deuxième partie est dédiée à la cinématique théorique. La découverte et la classification des systèmes \textit{invariants} de torseurs ont permis d'éclairer de nombreux aspects de la mobilité et de la synthèse des chaînes cinématiques. De plus, cette dernière a généré l'émergence de nouvelles idées et de questions encore non résolues. Parmi celles-ci, l'une des plus connues concerne l'identification et la classification des variétés persistantes à 5 dimensions.

Title : A Treatise on Open Problems in Robotics: from Cable-Driven Platforms to Persistent Manifolds

Keywords : Cable-Driven Platforms, Adaptive Control, Theoretical Kinematics, Persistent Screw Systems

Abstract : Although many efforts are continuously devoted to the advancement of robotics, there are still many open and unresolved problems to be faced. This thesis, therefore, sets out to tackle some of them with the aim of scratching the surface and look a little further for new ideas or solutions. The topics covered are mainly two. The first part deals with the development and improvement of control techniques for cable-driven robot. The second focuses on the study of persistent manifolds seen as constituting aspects of theoretical kinematics. In detail,

- part I deals with cable-driven platforms. In it, both techniques for selecting cable tensions and the design of a robust controller are developed. The aim is, therefore, to enhance the two building blocks of the overall control scheme in order to improve the performance of these robots during the execution of tracking tasks.
- Part II delves into theoretical kinematics. The discovery and classification of invariant screw systems shed light on numerous aspects of robot mobility and synthesis. Nevertheless, this generated the emergence of new ideas and questions that are still unresolved. Among them, one of the more notable concerns the identification and classification of 5-dimensional.

Acknowledgment

This thesis was developed within the framework of an international joint PhD program between the University of Genoa (Italy) and École Centrale de Nantes (France). Collaboration extended to other prestigious institutions such as the University of Bologna and London South Bank University, which significantly contributed to the project. Across these universities, comprehensive support from various labs and faculties was consistently provided, facilitating the seamless progression of the research.

Abstract

Although many efforts are continuously devoted to the advancement of robotics, there are still many open and unresolved problems to be faced. This thesis, therefore, sets out to tackle some of them with the aim of scratching the surface and look a little further for new ideas or solutions.

The topics covered in the manuscript are mainly two. The first part deals with the development and improvement of control techniques for cable-driven robots. The second focuses on the study of persistent manifolds considered as constituting aspects of theoretical kinematics.

In detail:

- Part I deals with cable-driven platforms. Within this part, both techniques for selecting cable tensions and the design of a robust controller are developed. The aim is, therefore, to enhance the two building blocks of the overall control scheme in order to improve the performance of these robots during the execution of tracking tasks.

  - The first chapter introduces to open problems and recalls the main concepts necessary to understand the following chapters;
  - the contribution of the second chapter consists of the introduction of the *Analytic Centre*. It allows the generation of continuous and differentiable tension profiles while taking into account non-linear phenomena such as friction in the computation of tensions to be applied;
  - the third chapter, although still at a preliminary stage, introduces sensitivity for tension calculation methods, offering perspectives of considerable interest for tension control in the current scientific context;
  - the fourth chapter proposes the design of an adaptive controller. It allows external disturbances and/or uncertainties in the model to be faced such that the task can be performed with as little error as possible. The controller architecture is the innovative peculiarity conferring autonomy to cable systems. Initially applied to counteract wind in aerial systems it is now also used for cable breakage scenarios;
  - the conclusions, at first, draw together the results obtained. In addition, they emphasise the lack of the techniques introduced in order to outline possible future paths and topics that need further investigation.

- Part II delves into theoretical kinematics. The discovery and classification of invariant screw systems shed light on numerous aspects of robot mobility and synthesis. Nevertheless, this generated the emergence of new ideas and questions that are still unresolved. Among them, one of the more notable concerns the identification and classification of 5-dimensional persistent manifolds.

- Similarly to the first part, the first chapter provides an overview of the problems addressed and the theoretical notions necessary to understand the subsequent contributions;
- the second chapter contributes by directly tackling the above-mentioned question by exploiting the properties of dual quaternions, the Study quadric and differential geometry. A library of 5-persistent varieties, so far missing in the literature, is presented along with theorems that extend and generalise previous ones in the literature;
- an original work, concerning line motions and synthesis of mechanisms that generate them, is reported in the third chapter as a spin-off of the studies on persistent manifolds;
- the conclusions wrap up the obtained results trying to highlight gaps and deficiencies to be dealt with in the future. Here, two small sections are dedicated to ongoing works regarding the persistence definition and the screw systems' invariants and subvariants.

Résumé

Malgré les nombreux efforts en cours pour développer des questions dans le domaine de la robotique, ils existent tout autant des problèmes ouverts et non résolus. Cette thèse se propose donc de s'attaquer à certains défis, dans le but d'effleurer la surface et de faire émerger des nouvelles idées ou des nouvelles voies.

Les thèmes abordés seront divisés en deux parties. La première concerne le développement et l'amélioration des techniques de contrôle des systèmes robotiques à câbles. La seconde se concentre sur l'étude des variétés persistantes constituant des aspects de la cinématique théorique.

En détail:

- la partie I concerne les robots parallèles à câbles. Elle développe à la fois une technique de calcul des tensions à appliquer aux câbles et la conception d'un contrôleur robuste. L'objectif est donc d'améliorer les deux éléments de base constituant le schéma de commande général d'un robot afin d'accroître les performances lors de l'exécution d'une *tracking task*.

  - le premier chapitre présente la problématique abordée et rappelle les principales notions nécessaires à la compréhension des chapitres suivants;
  - la contribution du deuxième chapitre consiste en l'introduction du *Centre Analytique* pour le calcul des tensions dans les câbles. Cette technique permet de générer des profils de tension continus et différentiables tout en tenant compte de phénomènes non linéaires tels que le frottement dans le calcul des tensions à appliquer;
  - le troisième chapitre, bien qu'encore préliminaire, introduit la sensibilité des méthodes de calcul des contraintes, offrant des perspectives de grand intérêt pour le contrôle de la tension dans le paysage scientifique actuel;
  - le quatrième chapitre propose la conception d'un contrôleur adaptatif. Il permet de faire face aux perturbations externes et/ou aux incertitudes du modèle de manière à ce que la tâche puisse être exécutée avec le moins d'erreur possible. L'architecture du contrôleur est la particularité innovante qui confère l'autonomie aux systèmes de câbles. Initialement appliquée pour contrer le vent dans les systèmes aériens, elle est maintenant également utilisée pour les scénarios de rupture de câble;
  - les conclusions, en premier lieu, rassemblent les résultats obtenus. En outre, elles visent à souligner les inconvénients et les lacunes des techniques introduites afin d'esquisser des pistes pour l'avenir et des questions qui doivent être approfondies.

- La deuxième partie est dédiée à la cinématique théorique. La découverte et la classification des systèmes *invariants* de torseurs ont permis d'éclairer de nombreux aspects de la mobilité et de la synthèse des chaînes cinématiques. De plus, cette

dernière a généré l'émergence de nouvelles idées et de questions encore non résolues. Parmi celles-ci, l'une des plus connues concerne l'identification et la classification des variétés persistantes à 5 dimensions.

- Comme la première partie, le premier chapitre donne une vue d'ensemble des problèmes abordés et est consacré au rappel des principaux concepts théoriques nécessaires à une meilleure compréhension des contributions suivantes;
- le deuxième chapitre contribue directement à la question ci-dessus en exploitant les propriétés des quaternions duals, de la quadrique de Study et de la géométrie différentielle. Une bibliothèque de variétés 5-persistantes, jusqu'à présent absente de la littérature, est donnée avec des théorèmes qui complètent et généralisent les précédents dans la littérature;
- un travail original, concernant les mouvements des lignes et la synthèse des mécanismes qui les génèrent, a été réalisé en tant que spin-off et rapporté dans le troisième chapitre;
- les conclusions résument les résultats obtenus en essayant de mettre en évidence les lacunes et les déficiences à traiter à l'avenir. Ici, deux petites sections sont consacrées aux travaux en cours concernant la définition de la persistance et les invariants et sous-invarints des systèmes de vis.

Riassunto

Nonostante siano numerosi e continui gli sforzi atti allo sviluppo delle tematiche nell'ambito della robotica, altrettanto numerosi risultano i problemi aperti e irrisolti. Questa tesi, quindi, si propone di affrontarne alcuni con l'obiettivo di scalfirne la superficie e dar vita a nuove idee o strade percorribili in futuro.

Gli argomenti trattati verranno suddivisi in due parti. La prima riguarda lo sviluppo e miglioramento delle tecniche di controllo per sistemi robotici a cavi. La seconda verte sullo studio delle varietà persistenti costituenti aspetti di cinematica teorica.

In dettaglio:

- la I parte riguarda robot paralleli a cavi. In essa si sviluppano sia una tecnica per la scelta delle tensioni da applicare ai cavi che il design di un controllore robusto. Lo scopo è, quindi, quello di migliorare i due elementi di base, costituenti lo schema di controllo generale di un robot in modo da incrementare le prestazioni durante l'esecuzione di un *tracking task*.

  - il primo capitolo introduce i problemi affrontati e richiama le principali nozioni necessarie per comprendere i capitoli successivi;
  - il contributo del secondo capitolo consiste nell'introduzione del *Centro Analitico* per il computo delle tensioni lungo i cavi. Questa tecnica consente di generare profili di tensione continui, differenziabili potendo tenere conto di fenomeni non lineari quali l'attrito nel computo delle tensioni stesse;
  - il terzo capitolo, sebbene ancora in fase preliminare, introduce la sensitività per i metodi di calcolo delle tensioni, offrendo prospettive di grande interesse per il controllo in tensione nell'attuale panorama scientifico.
  - il quarto capitolo propone il design di un controllore adattivo che permette di affrontare disturbi esterni e/o incertezze del modello facendo in modo che il task possa essere effettuato con il minor errore possibile. L' architettura del controllore conferisce, infatti, maggior autonomia ai sistemi a cavi. Inizialmente applicata per contrastare il vento nei sistemi aerei poi impiegata anche per scenari ove si verifica la rottura di un cavo;
  - le conclusioni, in prima battuta, raccolgono i risultati ottenuti. Inoltre, si propongono di enfatizzare gli svantaggi e le mancanze delle tecniche introdotte in modo da delineare le possibili strade future e tematiche che necessitano di ulteriore approfondimento.

- La II parte approfondisce tematiche di cinematica teorica. La scoperta e classificazione dei sistemi di torsori *invarianti* ha fatto luce su numerosi aspetti di mobilità e sintesi di catene cinematiche. Inoltre, quest'ultima, ha generato l'insorgere di nuove idee e questioni tutt'ora irrisolte. Fra esse, una delle più note riguarda l'identificazione e classificazione di varietà persistenti 5-dimensionali.

- Analogamente alla prima parte, il primo capitolo offre una panoramica dei problemi affrontati e delle nozioni teoriche necessarie a comprendere i contributi successivi;
- il secondo capitolo contribuisce direttamente alla domanda suddetta sfruttando le proprietà dei quaternioni duali, della quadrica di Study e della geometria differenziale. Una libreria di varietà 5-persistenti, fin'ora mancante in letteratura, viene riportata assieme ai teoremi che completano e generalizzano quelli precedenti in letteratur;
- un lavoro originale, riguardante i moti di linea e sintesi di meccanismi che li generano, è stato realizzato come spin-off e riportato come terzo capitolo;
- le conclusioni riassumono i risultati ottenuti cercando di evidenziare lacune e carenze da affrontare in futuro. Due piccole sezioni sono dedicate ai lavori in corso sulla definizione di persistenza e sugli invarianti e sottoinvarianti dei sistemi di torsori.

Contributions

Accepted Papers

- Selig J., Di Paola V. Mechanisms Generating Line Trajectories. In Mechanism Machine Theory (2024). https://doi.org/10.1016/j.mechmachtheory.2023.105494
- Di Paola V., Caro S., Zoppi M. Sensitivity Analysis of Tension Distribution Algorithms. In IDETC/CIE, ASME (2023).
- Di Paola V., Goldsztejn, A., Zoppi, M., Caro, S. Design of a Sliding Mode-Adaptive PID Control for Aerial Systems with a Suspended Load Exposed to Wind Gusts. In Journal of Computational Nonlinear Dynamics, ASME (2023). https://doi.org/10.1115/1.4062324
- Di Paola V. Ida E., Zoppi M., Caro S. A Preliminary Study of Factors Influencing the Stiffness of Aerial Cable Towed Systems. In ROMANSY 24 (2022) [Book chapter]. https://doi.org/10.1007/978-3-031-06409-8_29

Papers Under Review

- Di Paola V., Caro S., Zoppi M. Performance Investigation of a SM-APID Control for Cable-Breakage Scenario. In Mechanism Machine Theory.
- Di Paola V., Goldsztejn A., Zoppi M., Caro S. Analytic Centre Based Tension Distribution for Cable-Driven Platforms (CDPs). In Journal of Mechanisms and Robotics.
- Selig J., Di Paola V. Some Five Dimensional Persistent Submanifolds of the Study Quadric. In Mechanism Machine Theory.

In Preparation

- Di Paola V., Selig J. Invariants and Subinvariants for Screw Systems Identifications.

Contents

Nomenclature

Aerial System Variables

$\boldsymbol{\omega}_i \in \mathbb{R}^3$ angular velocity of the i^{th} link in F_O

$\mathbf{R}_i \in SO(3)$ orientation of the i^{th} robot with respect to F_O

$\mathbf{R}_o \in SO(3)$ orientation of the platform with respect to F_O

$\boldsymbol{\Omega}_i, \dot{\boldsymbol{\Omega}}_i \in \mathbb{R}^3$ angular velocity, acceleration of the robot in F_{Q_i}

$\mathbf{J}_i \in \mathbb{R}^{3\times3}$ inertia tensor of the i^{th} robot in F_{Q_i}

$\mathbf{J}_o \in \mathbb{R}^{3\times3}$ inertia tensor of the platform

$\mathbf{m}_i \in \mathbb{R}^3$ control moment of the i^{th} drone in F_{Q_i}

$\mathbf{x}_i$, $\dot{\mathbf{x}}_i$, $\ddot{\mathbf{x}}_i \in \mathbb{R}^3$ position, linear velocity, acceleration of the i^{th} drone in F_O

$f_i \in \mathbb{R}$ thrust force of the i^{th} robot

m_i mass of the i^{th} drone

$\mathbf{i}_i, \mathbf{j}_i, \mathbf{k}_i$ canonical base of drone frame (Q_i, x_i, y_i, z_i)

Control Variables

$\mathbf{e} \in \mathbb{R}^n$ error state

$\mathbf{u} \in \mathbb{R}^n$ control action

$\mathbf{x} \in \mathbb{R}^n$ actual state

$\mathbf{y} \in \mathbb{R}^n$ desired state

General Variables

$\mathfrak{se}(3)$ Lie algebra to the group $SE(3)$

$\mathfrak{so}(3)$ Lie algebra to the group $SO(3)$

$\mathbf{I}$ identity matrix

$\mathbf{W} \in \mathbb{R}^{n \times m}$ wrench matrix

$\tau_i \in \mathbb{R}$ tension magnitude along the i^{th} link

$\mathbf{q}_i \in \mathbb{R}^3$ unit vector identifying cable/link direction in F_O

$\mathbf{w}_e \in \mathbb{R}^n$ external wrench

g gravity acceleration magnitude

m_L mass of the load

$SE(3)$ Special Euclidean Group

$SO(3)$ Special Orthogonal Group

F_O inertial frame

$\mathbf{e}_1, \mathbf{e}_2, \mathbf{e}_3$ canonical base of inertial frame (O, X, Y, Z)

Theoretical Kinematics

$\mathbb{PR}^n$ n-dimensional real projective space

$\mathbf{h}$ dual quaternion

$\mathbf{w}_d$ dual wrench

G group

g group element

$GL(n)$ General Linear group

H_p screw motion subgroup

M manifold

Acronyms

CDP Cable-Driven Platform

CDPR Cable-Driven Parallel Robot

MCDPR Mobile Cable-Driven Parallel Robot

ACTS Aerial Cable Towed System

PM Point Mass

RB Rigid Body

MB Mobile Base

TDA Tension Distribution Algorithm

LP Linear Programming

QP Quadratic Programming

AC Analytic Centre

IGM Inverse Geometric Model

IKM Inverse Kinematic Model

PID Proportional Integrative Derivative

SM-APID Sliding Mode-Adaptive Proportional Integrative Derivative

SQ Study Quadric

TPM Translational Parallel Manipulator

ISS Invariant Screw System

PSS Persistent Screw System

Part I

Cable-Driven Platforms

Chapter I.1

Introduction

I.1.1 Open Problems and Contributions

This section attempts to shed some light on the topics undertaken in the first part. As mentioned, similarities between Cable-Driven Parallel Robots (CDPRs) and Aerial Cable Towed System (ACTSs) not only lead to a unique class of robots but can help solving common problems and technical issues by means of analogy.

As a matter of fact, for ACTSs, one critical aspect has always been the control part. In particular, many challenges are present in the context of aerial transportation. To mention some of them, the idea is to accomplish tracking tasks with an ACTS covering long distances while being able to avoid obstacles [1], communicate in cluttered environments [2], [3] and deal with external disturbances such as wind gusts, for example. It is then clear that the researchers' direction consists in making them as autonomous as possible.

Several techniques were developed so far to steer the load along a trajectory. The majority of techniques developed span from Flatness [4]–[9] to Geometric control [10]–[15]. However, none of them seriously addressed the problem of guiding the system in outdoor conditions.

Therefore, one work tackled and presented hereby, resembles in the design of a control allowing satisfying the tracking problem in presence of external disturbances and/or uncertainties. Thus, one could ask *where is the link with CDPRs?*

First, CDPRs literature raised the question on how to guide the load when a cable breaks Sec.I.4.4. Therefore, in this context, one can understand that using a proper control method might help to increase safety. Thus, instead of using an *emergency strategy* only to manage this scenario, proposed approach, developed for controlling highly non-linear systems (even chaotic), can be also extremely useful to face cable failure.

Secondly, ACTS can benefit from the multiple studies on tension distribution, typically deeply studied for CDPRs. Indeed, another topics of relevance and fundamental to properly control the load rely on the Tension Distribution Algorithm (TDA) used. Choosing which tension and then motor torques should be applied to the cables is an

hot topic among researchers; typically solved by formulating an optimization problem. Several methods were introduced to deal with this problem and a deep review and comparison of them is made in the following chapter. The fundamental contribution here shows that, the Analytic Centre, provide a way to consider non-linear constraints inside the solution of the optimization problem. Hence, many non-linear phenomena, such as friction, can now be correctly considered while finding cable tensions. The Analytic Centre and all the other methods hereby considered, are also implemented in a real hardware and compared to validate what found theoretically. This latter work showed promising results but it is still in its preliminary phase.

The last topic, merely touched in this dissertation, is the sensitivity analysis of TDAs. As mentioned, there are many methods to solve the tension problem and the idea was to provide a quantitative way to compare them. Moreover, this study provides interesting information regarding tension variation when the external wrench variates. In practice, tension measures are affected by noise and then using them for cable tension control becomes an hard task [16]. Hence, another motivation behind the study of sensitivity, consists in defining an upper limit to the possible tension variation. Eventually, this will allow sensor noise to be further filtered and possibly use this signal for control.

To conclude, it appears evident that both robot architectures share similarities and can benefit from the studies and research accomplished as different systems so far. Further, though only particular examples were mentioned here, the motivation behind the introduction of CDPs should be now clear and rooted. Consequently, one can pass to the other sections being able to see that every work is valid and then applicable to both CDPRs and ACTSs, regardless the system considered.

I.1.2 Why Cable-Driven Platforms?

Nowadays the motivation behind the introduction of Cable-Driven Parallel Robots (CDPRs) is well settled and known among researchers. Indeed, there are several survey and reviews available in the literature that states and explain their technical features and peculiarities in deepth [17], [18]. However, here, some historical traces characterizing the growth of cable-robots are reported to create a solid layer allowing to motivate the introduction of Cable-Drive Platform (CDP).

A first intent is, clearly, to broaden the CDPR class to include newcomers recently presented in the literature. Further, one should observe that this naming is also functional in terms of modelling and control; it is not only a mere renaming and this will be motivated in what follows.

So far, the majority of employed robots are obtained as a sequence of linked rigid bodies called *open kinematic chain* shown in Fig.I.1.1. Technically, they are well-known as serial robots and, currently, many studies were done to asses their performances. In particular, the main drawback resembles into a small payload to robot ratio [18], [19] because of their open architecture. These drawbacks, and a few others, were partially solved by the introduction of the *closed kinematic chain* (or parallel manipulator) shown in Fig.I.1.2. Therefore, splitting the joint weights among the parallel legs provided the

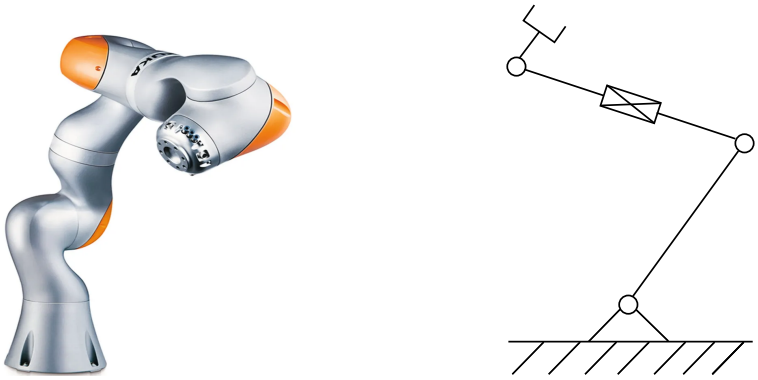

(a) (b)

Figure I.1.1: Serial Chain: (a) represents a real KUKA manipulator with 7-*DoF* whereas (b) a schematic view of an open chain.

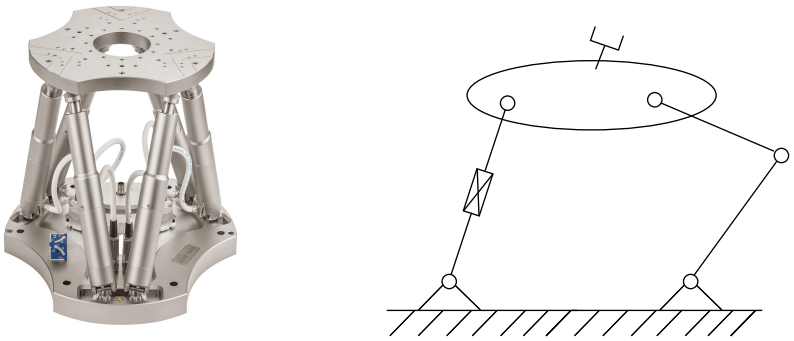

(a) (b)

Figure I.1.2: Serial Chain: (a) a Hexapod parallel manipulator whereas (b) a schematic view of a closed chain.

solution to increase the payload of the manipulator. However, this new architecture leads to a sensible workspace reduction posing new technical challenges to be addressed.

In this context, the idea was to substitute rigid legs with cables and then control the platform pose by varying the cable lengths. These structural changes made these robots highly deployable and then very attractive for many applications. Hence, this flexibility together with reduced mass allowed us to build big cable robot with large workspace.

Now, with this in mind, in [17] the following definition of CDPR was given

Definition 1. *A cable-driven parallel robot or simply cable-robot is a parallel manipulator having the mobile platform connected to the fixed base only by cables and its pose being controlled only by changing the lengths of the cables.*

This definition allows to discriminate other types of existing cable-driven robots as robotic hands [20] or tensegrity [21].

However, with the recent developments of the technology, it is typical that definitions can evolve and be subject to variations or updates in order to stay at the pace of the fast technological growth.

From the 1980s and 1990s onwards, continuous investments in the field of computer science have seen not only a reduction in the size of processors (hardware in general) but also an increase in their computational capabilities. Consequently, among the many categories of robots that have benefited from these developments, aerial robotics is certainly one of them. This explains the recent spread of low-cost drones on the market [22]–[25].

When discussing drones, one generally refers to a precise category of vehicles recognised under the name Unmanned Aerial Vehicle (UAV). A big variety of aerial vehicles is available today. Each one of them has several distinguishing features making them useful for different applications. Briefly, there exists

- Fixed Wings UAVs (FWUAVs) Fig.I.1.3-(a) are known for their long-range flight capabilities. They require large spaces for manoeuvring: landing and take-off cannot be realized vertically;
- Rotary Wings UAVs (RWUAVs) can be subdivided in two main categories: helicopters Fig.I.1.3-(b) and multi-rotors drones Fig.I.1.3-(c). They both allow vertical landing and take-off. Helicopters have a higher payload than multi-rotor drones: the presence of several motors is a drawback in terms of payload. Anyway, this latter peculiarity allows multi-rotor drones higher manoeuvrability as well as more safety with respect to helicopters.
- Flapping Wings UAVs (FlWUAVs) Fig.I.1.3-(d) are inspired by the flight of birds, insects and bats. Their dimension is usually smaller than hand size. This class of UAVs generates lifting and forward force by flapping its wings.

Here, only the most common actuated UAVs were reported. Hence, recently, because of their advantageous characteristics w.r.t. other drones, quadrotors and cables have been combined to displace a load and cover long distances. Thus, flying robots, also known as Aerial Cable Towed System (ACTS) Figs.I.1.4b, were born and intensively studied. Consequently, at this point, it should be clear that CDPRs and both their Reconfigurable (RCDPR) [26] or Mobile (MCDPR) [27] versions can be seen as particular cases of ACTSs. With this in mind, a new definition can now be formulated as follows

Definition 2. *A Cable-Driven Platform is a parallel manipulator whose platform (load) is guided by pulling cables.*

Unlike CDPRs, in this definition, the type of actuation is not mentioned as well as the presence of a frame fixed. Consequently, the definition results more general such that, for example, also hybric cable-robots [28] shown in Fig.I.1.4c are included.

(a)

(b)

(c)

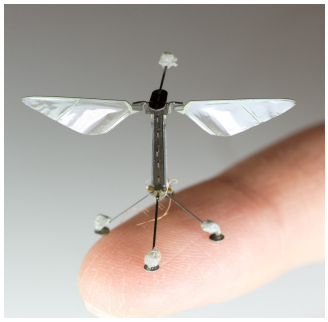

(d)

Figure I.1.3: Different types of UAVs: (a) is named Futura™ Fixed Wings Drone, `https://baam.tech/aircraft/futura-fixed-wing` (b) is a Rotary Wings Drone called CSIRO helicopter [22] (c) is a Mavic Air 2 quadcopter, `https://www.dji.com/it/mavic-air-2?site=brandsite&from=eol_mavic` and (d) is a Flapping Wings Drone named RoboBees, `https://wyss.harvard.edu/technology/robobees-autonomous-flying-microrobots/`

I.1.3 Cable-Driven Platform Model

In this section, the main equations and symbols necessary to describe the CDPs are reported. The static or dynamic equilibrium of a platform in the space, guided by m cables, is governed by the following equation

$$\mathbf{W}\boldsymbol{\tau} + \mathbf{w}_e = \mathbf{0}, \tag{I.1.1}$$

where, in general, $\mathbf{w}_e \in \mathbb{R}^6$ is the external wrench which also takes into account dynamical actions applied to the platform, $\boldsymbol{\tau} \in \mathbb{R}^m$ is the cable tensions vector, $\mathbf{W} \in \mathbb{R}^{6\times m}$ is the wrench matrix which is defined as

$$\mathbf{W} = \begin{pmatrix} \mathbf{q}_1 & \dots & \mathbf{q}_m \\ \mathbf{b}_1 \times \mathbf{q}_1 & \dots & \mathbf{b}_m \times \mathbf{q}_m \end{pmatrix}, \tag{I.1.2}$$

$\mathbf{q}_i \in \mathbb{R}^3$ represents the ith cable direction (unitary vector) and $\mathbf{b}_i \in \mathbb{R}^3$ represents the ith attachment point on the platform. Thus, if DoR[1]≥ 1, there exist infinite solutions

[1]The Degree of Redundancy is defined as $DoR = m - n$ where m is the cable number and n stands for the *Degree of Freedom* (DoF) of the platform.

(a) (b) (c)

Figure I.1.4: Cable-Driven Platform: different types of cable-driven robots are reported (a) depicts a CDPR [29] figure (b) shows an ACTS [9] and (c) an Hybrid version of the two [28]

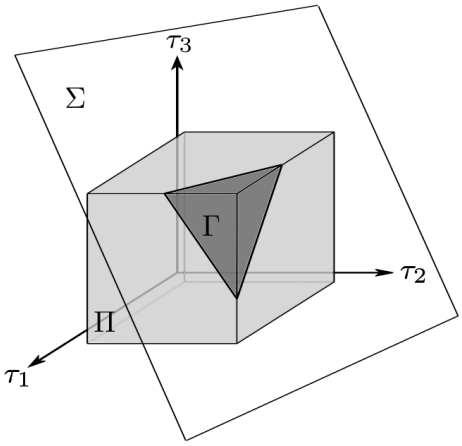

Figure I.1.5: Feasible Solution: graphical representation of Π, Σ and Γ for the case of $m = 3$.

of Eq.(I.1.1) grouped in the following set

$$\Sigma = \{\boldsymbol{\tau} \,|\, \mathbf{W}\boldsymbol{\tau} + \mathbf{w}_e = \mathbf{0}\}. \tag{I.1.3}$$

However, to maintain the equilibrium of the platform the cable tension limits have to be taken into account. Hence, the m-dimensional convex hypercube Π, that defines the domain of the *feasible* tensions, is

$$\Pi = \{\boldsymbol{\tau} \,|\, \mathbf{0} < \underline{\boldsymbol{\tau}} \leq \boldsymbol{\tau} \leq \overline{\boldsymbol{\tau}}\}, \tag{I.1.4}$$

where $\underline{\boldsymbol{\tau}}, \overline{\boldsymbol{\tau}} \in \mathbb{R}^{m,+}$ are positive tension vectors limits containing the ith lower and upper cable tension limits as components, which, without loss of generality, will be considered equal to each other, respectively. Consequently, the set of feasible solutions Γ satisfying

both Eq.(I.1.3) and Eq.(I.1.4), is

$$\Gamma = \Sigma \cap \Pi. \tag{I.1.5}$$

Practically, the cable tensions can be computed as [30]

$$\begin{aligned} \boldsymbol{\tau} &= -\mathbf{W}^{\dagger}\mathbf{w}_e + \mathbf{N}\boldsymbol{\lambda} \\ &= \boldsymbol{\tau}_p + \boldsymbol{\tau}_g, \end{aligned} \tag{I.1.6}$$

where $\mathbf{W}^{\dagger} = \mathbf{W}^T(\mathbf{W}\mathbf{W}^T)^{-1}$ is the Moore-Penrose pseudo-inverse matrix of $\mathbf{W}$, $\mathbf{N} \in \mathbb{R}^{m\times(m-n)}$ contains the vectors that span the kernel of $\mathbf{W}$, $\boldsymbol{\lambda} \in \mathbb{R}^{(m-n)}$ belongs to the polytope Λ in Eq.(I.1.7) and $\boldsymbol{\tau}_p$, $\boldsymbol{\tau}_g$ are the particular and general solution of Eq.(I.1.1), respectively. For sake of clarity, the definition of the convex polytope Λ is reported in

$$\Lambda := \{\boldsymbol{\lambda} \in \mathbb{R}^{(m-n)} \,|\, \underline{\boldsymbol{\tau}} \leq -\mathbf{W}^{\dagger}\mathbf{w}_e + \mathbf{N}\boldsymbol{\lambda} \leq \overline{\boldsymbol{\tau}}\}. \tag{I.1.7}$$

It turns out that, to cope with the cable intrinsic property, guaranteeing the controllability of the platform during the tasks, a natural way to deal with Eq.(I.1.6) consists in solving an optimization problem. So far, several approaches were presented in the literature; see ChapterI.2 for further discussion.

Chapter I.2

Analytic Centre-Based Tension Distribution Algorithm

Abstract: *For redundant Cable-Driven Platform, the choice of the cable tensions belong to a set with infinite solutions. This chapter proposes the use of the Analytic Centre to solve the tension distribution problem and select a particular solution in mentioned set. Indeed, adopting this technique allows finding tensions far from the tension limits (namely robust) as well as tension profiles continuous and differentiable in time. The continuity, differentiability and uniqueness of the solution is also proven. Moreover, the possibility of including non-linear constraints acting on the tensions (e.g. friction) is a further contribution. The computational time with the proposed approach is compared to the existing techniques to assess its real-time applicability. Finally, several simulations are reported as well as an experimental test to demonstrate the method's capabilities.*

I.2.1 Introduction and Motivation

Guaranteeing cable tautness and smooth variations of the tension values during the execution of a task poses several problems. The management of cable tensions is still a topic of ongoing research. When the Degree of Redundancy $DoR \geq 1$ namely *redundant* CDPs are considered, infinitely many solutions to the tension distribution problem may exist. In this view, one chance of solving this problem is to formulate an optimisation problem and solve it iteratively. The 1-norm of the tension vector $\boldsymbol{\tau}$ is the protagonist of several previous works [31]–[33]. Linear Program (LP) are notable for their fast convergence, which makes them suitable for real-time applications. Though, the optimal point is always placed at the edge of the tension box and, between two iterations, it can jump from one edge of the polyhedron to the other, resulting in discontinuities between two successive solutions. The same can happen also with the ∞-norm [34], thus, to overcome this issue and guarantee continuity between solutions, the p-norm $1 < p < \infty$ can be used [35]. In fact, practically, a natural extension consists in using the 2-norm of the

tension vector [36], [37] and in solving a Quadratic Program (QP) whose accessibility makes it popular. Even so, other solutions were explored for example, in [38], [39] the Dykstra alternating-projection algorithm is used to solve the minimum 2-norm tension distribution. Another alternative to tackle the tension distribution problem, ensuring continuity, takes the barycenter of the polyhedron as the optimal solution [40]. Evidently, the criteria are different and their choice depends on the assigned task. Indeed, for example, the 2-norm methods can guarantee reducing power consumption whereas barycenter is said to be *safe* since the solution is far from cable tension limits. Besides, the Improved-Closed Form method [41], built on its predecessor [42], tries to reduce the method complexity by maintaining real-time efficiency, generality w.r.t. the DoR and continuity of the tension profiles. Even so, these methods do not guarantee the convergence in the entire Wrench Feasible Workspace (WFW) [43]. In addition, since the Improved-Closed Form approach set outbound cable tensions to their maximum or minimum value, the smoothness of tension profiles can be compromised. Analogously, with the intention of maximising the applicability of the method within the WFW without degrading continuity and algorithm speed, in [44] they take their inspiration from [41] and develop the Improved Puncture Method. A strategy for tension distribution dealing with CDPRs operating beyond their WFW is also explored in [45]. Actually, many works were proposed to establish a proper set of tensions to be used during the fulfilment of a given task. Anyway, only one [46] introduces a versatile tension distribution algorithm, which allows computing several types of mentioned techniques. Nevertheless, the introduced algorithm can be applied only for CDPRs with, at most, $DoR = 2$. In this context, this chapter sheds light on the Analytic Centre (AC) method. Indeed, thought this technique has been introduced in a short paper [47], several important peculiarities have been omitted. Hence, the additional contributions here are the following

1. a detailed review of the existing TDAs is given in Section I.2.1.1. This allows both comparisons and understanding why the AC approach is indeed relevant. Moreover, additional information about sensitivity of the TDAs are also given to shed the light on how they work;

2. the extension of the method to include non-linear constraints (e.g. friction) in the optimisation problem. Notice that, incorporating time-varying non-linear constraints to compute cable tensions increases the range of applicability of this TDA to other types of CDP as, for example, for the Mobile Cable-Driven Parallel Robots (MCDPRs) [27], [48];

3. proof of the continuity and differentiability of cable tension profiles. This was presented also in [47]. However, here, it is given in a topological fashion which indeed results to be more general by taking into account, explicitly, the possibility of including non-linear constraints;

4. the main disadvantages and limitations are outlined as a comprehensive analysis of the AC method.

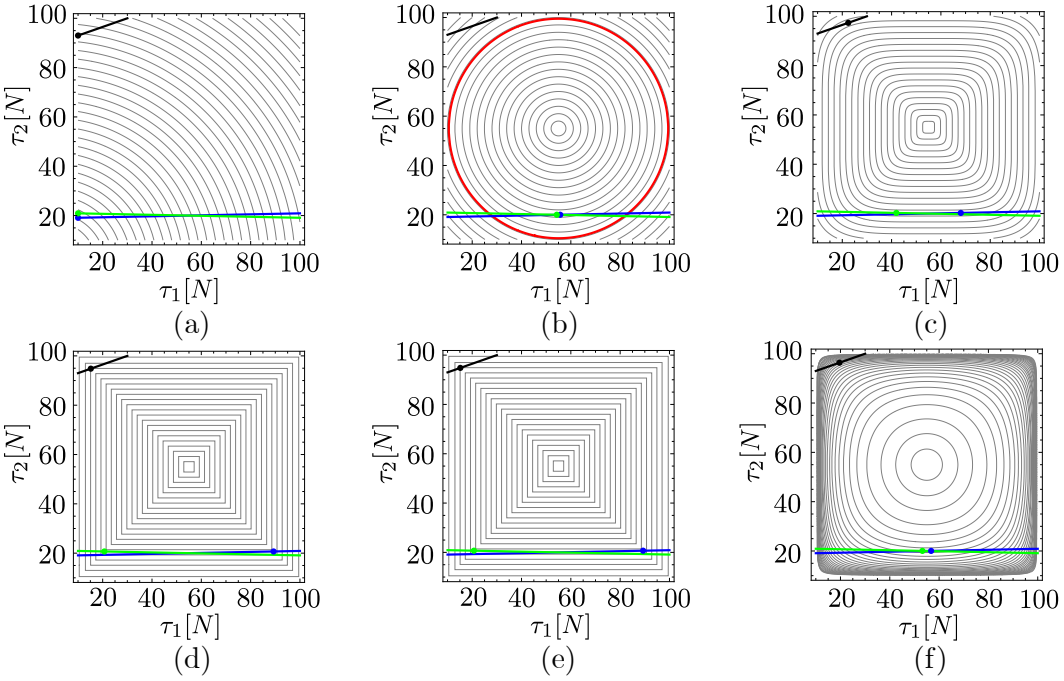

Figure I.2.1: Level-sets: (a) the 2-norm with respect to the origin $(0, 0)$, (b) the 2-norm with respect to the centre of Π, (c) the 5-norm within Π, (d) the ∞-norm within Π, (e) the distance to the closest boundary of Π and (f) the logarithmic barrier over Π. Three test cases are displayed in black, blue and green respectively. From the Lagrange optimality conditions, if a minimizer lies strictly inside the cable tension box, then the level-set of the cost function and the linear subspace $\mathbf{W}\boldsymbol{\tau} + \mathbf{w}_e = \mathbf{0}$ are tangent at this minimizer. Using generalized gradients, this tangency condition is satisfied at corners of non-smooth level-sets in the figures (d) and (e).

I.2.1.1 Motivating Example

This section considers an academic example that consists in distributing two tensions $\boldsymbol{\tau} = (\tau_1, \tau_2)$ belonging to a box $\Pi = \left\{\boldsymbol{\tau} \,|\, \mathbf{0} < \mathbf{10} \leq \boldsymbol{\tau} \leq \mathbf{100}\right\}$ with corners $\underline{\boldsymbol{\tau}} = (10, 10)$ and $\overline{\boldsymbol{\tau}} = (100, 100)$. The level-sets of different tension distribution optimization problems are displayed in Figure I.2.1. Tensions are required to satisfy the static equilibrium constraint $\mathbf{W}\boldsymbol{\tau} + \mathbf{w}_e = \mathbf{0}$ with $\mathbf{W} \in \mathbb{R}^{1\times 2}$ and $\mathbf{w}_e \in \mathbb{R}$. Three test cases are considered: the first takes $\mathbf{W} = (-7, 20)$ and $\mathbf{w}_e = (-1790)\, N$ and it is displayed in black in Figure I.2.1. The second takes $\mathbf{W} = (-1, 50)$ and $\mathbf{w}_e = (-945)\, N$ and it is displayed in blue in Figure I.2.1. The third takes $\mathbf{W} = (1, 50)$ and $\mathbf{w}_e = (-1055)\, N$ and it is displayed in green in Figure I.2.1. The last two sets of data are very similar to each other, being representative of close poses or of the effect of uncertainties on a pose, and are presented to illustrate the sensitivity of the solution given by the Tension Distribution Algorithms (TDAs).

In all the cases, the barycenter of the feasible polytope Λ coincides with the midpoint

of the two intersections between the line $\mathbf{W}\boldsymbol{\tau} + \mathbf{w}_e = \mathbf{0}$ and the borders of Π.

I.2.1.2 State-of-the-Art Optimization Based TDAs

TDAs based on minimizing the 2-norm have been widely investigated and used. They rely on solving the linearly constrained quadratic problems

$$\underset{\substack{\mathbf{W}\boldsymbol{\tau}+\mathbf{w}_e=\mathbf{0}\\ \boldsymbol{\tau}\in\Pi}}{\operatorname{argmin}} \|\boldsymbol{\tau}\|_2 \quad \text{and} \quad \underset{\mathbf{W}\boldsymbol{\tau}+\mathbf{w}_e=\mathbf{0}}{\operatorname{argmin}} \|\boldsymbol{\tau}-\hat{\boldsymbol{\tau}}\|_2 \tag{I.2.1}$$

with $\hat{\boldsymbol{\tau}} = \frac{1}{2}(\underline{\boldsymbol{\tau}} + \overline{\boldsymbol{\tau}})$ the midpoint of Π. The first allows minimizing the required energy to the actuators, hence it offers a limited stiffness. Furthermore, its minimizer often lies on the boundary of Π and is therefore not considered in the context of robust tension distribution. The level-sets of the cost function $\|\boldsymbol{\tau}\|_2$ and the corresponding minimizers are shown in Figure I.2.1-(a). It is possible to see that green and blue tension vectors are close to each other, indicating a low sensitivity of the investigated TDA. Minimizing $\|\boldsymbol{\tau}-\hat{\boldsymbol{\tau}}\|_2$ is meant to compute tension vectors as close as possible to the centre of Π. It is therefore attracting for pursuing robust tension distribution. Using the 2-norm allows for a Closed Form solution of Eq.(I.2.1), see [42]. This Closed Form solution is additionally attractive because its computation requires only to evaluate the pseudo-inverse of $\mathbf{W}$. The green and blue solutions displayed in Figure I.2.1-(b) are seen to be very close to each other, showing again a low sensitivity of this TDA.

Since the inequality constraints are not taken into account, the solution of the optimization problem can be outside Π while some feasible solution exists, and indeed the black solution is not visible in Figure I.2.1-(b) because it is outside Π (see also Figure 2 in [42] for a more detailed discussion). This results in a reduced WFW coverage. A corrected version of the Closed Form formula, aiming at setting to the lower or upper limit cable tensions that exceed the boundaries, was introduced in [41], but with no sound of theoretical foundation for the convergence and continuity. Furthermore, this adjusted Closed Form tension vector is meant to lie on the boundary of Π, hence not satisfactory with respect to robustness.

Remark 1. *Correcting the Closed Form formula (or directly) solving Eq.*(I.2.1) *with the inequality constraints* $\boldsymbol{\tau} \in \Pi$ *using a numerical solver seems to not have been considered in the literature yet. Its Eq.*(I.2.1) *numerical optimization is as complex as with* $\hat{\boldsymbol{\tau}} = \mathbf{0}$*, and is therefore also attractive. However, when the Closed Form solution is outside* Π*, the corrected constrained solution will lie on the* Π *boundary, hence not being satisfactory in terms of robustness.*

Remark 2. *Using p-norms, including* $p = \infty$*, was discussed in [49] while the case* $p = 4$ *was extensively discussed in [34] where a Closed Form solution is also given. The level-sets of the* ∞*-norm w.r.t. the centre of* Π *are shown in Figure I.2.1-(d). The tangency condition (i.e. optimality) is satisfied when the linear subspace meets a corner of the level-set, as illustrated by the three solutions represented. Because the level-sets are straight lines, cases where the linear subspace* $\mathbf{W}\boldsymbol{\tau} + \mathbf{w}_e = \mathbf{0}$ *is parallel to the level-sets have an entire segment of solutions, and an infinitesimal change in the data of the*

problem will cause an abrupt transition to one or the other segment endpoints. This occurrence is illustrated on Figure I.2.1-(d) by the high sensitivity of the blue and green neighbour problems, whose solutions are characterized by a large distance. Intermediate behaviors are obtained considering p-norms with $2 < p < \infty$: Figure I.2.1-(c) shows the level-sets of the 5-norm. The black solution computed is now inside Π. There is no straight level sets anymore, but the presence of almost straight level-sets show a strong sensitivity as well, as illustrated by the large distance between the blue and green solutions.

With the aim of maximizing the robustness of the TDA, in [31] it was proposed to maximize the distance to the closest face of Π. This leads to the following optimization problem:

$$\underset{\substack{\mathbf{W}\boldsymbol{\tau}+\mathbf{w}_e=\mathbf{0}\\ \boldsymbol{\tau}\in\Pi}}{\operatorname{argmax}} \; d(\boldsymbol{\tau}), \tag{I.2.2}$$

where $d(\boldsymbol{\tau}) = \min\{\overline{\tau}-\tau_1, \tau_1-\underline{\tau}, \overline{\tau}-\tau_2, \tau_2-\underline{\tau}\}$ is the distance to the closest face of Π or, equivalently, the *robustness index*. This optimization problem is classically reformulated to an easy-to-solve Linear Program (LP). Figure I.2.1-(e) shows the level-set of $d(\boldsymbol{\tau})$. In spite of its advantage in terms of robustness, this approach shows a very high sensitivity, illustrated by the large distance between the blue and green solutions. This happens when the linear subspace $\mathbf{W}\boldsymbol{\tau} + \mathbf{w}_e = \mathbf{0}$ is close to be parallel to an axis. Although, in practice, the exact time where the linear subspace is exactly parallel to an axis is in general not at a time-step where the optimization problem is solved, this leads to potentially discontinuous tension profiles, as detailed in [31].

Remark 3. *Figures I.2.1-(d) and (e) show a surprising coincidence between the level-sets of the ∞-norm with respect to the centre and the distance to the closest face. This coincidence leads to the same minimal and maximal tension vectors. Thus, looking at the literature, seem that this coincidence was not made explicit, and actually holds, in general, when tension limits are independent of cables[1], i.e., $\underline{\tau}_i = \underline{\tau}_j = \underline{\tau}$ and $\overline{\tau}_i = \overline{\tau}_j = \overline{\tau}$. The distance to the closest face of Π is then*

$$d(\boldsymbol{\tau}) = \min\{\overline{\tau}-\tau_1, \tau_1-\underline{\tau}, \ldots, \overline{\tau}-\tau_m, \tau_m-\underline{\tau}\}. \tag{I.2.3}$$

In the following, the constraints $\mathbf{W}\boldsymbol{\tau} + \mathbf{w}_e = \mathbf{0}$ and $\underline{\boldsymbol{\tau}} \leq \boldsymbol{\tau} \leq \overline{\boldsymbol{\tau}}$ are implicit in the optimization problems to lighten the notation. Recall that $\operatorname{argmax} f = \operatorname{argmin}(-f)$ *and that adding the radius $r = \frac{1}{2}(\overline{\tau}-\underline{\tau})$ to the cost function does not change its argument. Furthermore, the radius r and centre $\hat{\tau} = \frac{1}{2}(\overline{\tau}+\underline{\tau})$ are related by $\overline{\tau}-r = \hat{\tau}$ and $\underline{\tau}+r = \hat{\tau}$. Then, basic manipulations show that:*

$$\begin{aligned}
&\operatorname{argmax} d(\boldsymbol{\tau}) = \operatorname{argmin}\big(-d(\boldsymbol{\tau}) + r\big) && \text{(I.2.4a)}\\
&= \operatorname{argmin} \max\{\tau_1-\hat{\tau}, \hat{\tau}-\tau_1, \ldots, \tau_m-\hat{\tau}, \hat{\tau}-\tau_m\} && \text{(I.2.4b)}\\
&= \operatorname{argmin} \max\{|\tau_1-\hat{\tau}|, \ldots, |\tau_m-\hat{\tau}|\} && \text{(I.2.4c)}\\
&= \operatorname{argmin} \|\boldsymbol{\tau}-\hat{\boldsymbol{\tau}}\|_\infty. && \text{(I.2.4d)}
\end{aligned}$$

[1]Both TDAs are not well defined in case of cable dependent tensions limits since the aim is to maximize the distance $d(\boldsymbol{\tau})$ from the boundaries $\overline{\tau}$ and $\underline{\tau}$.

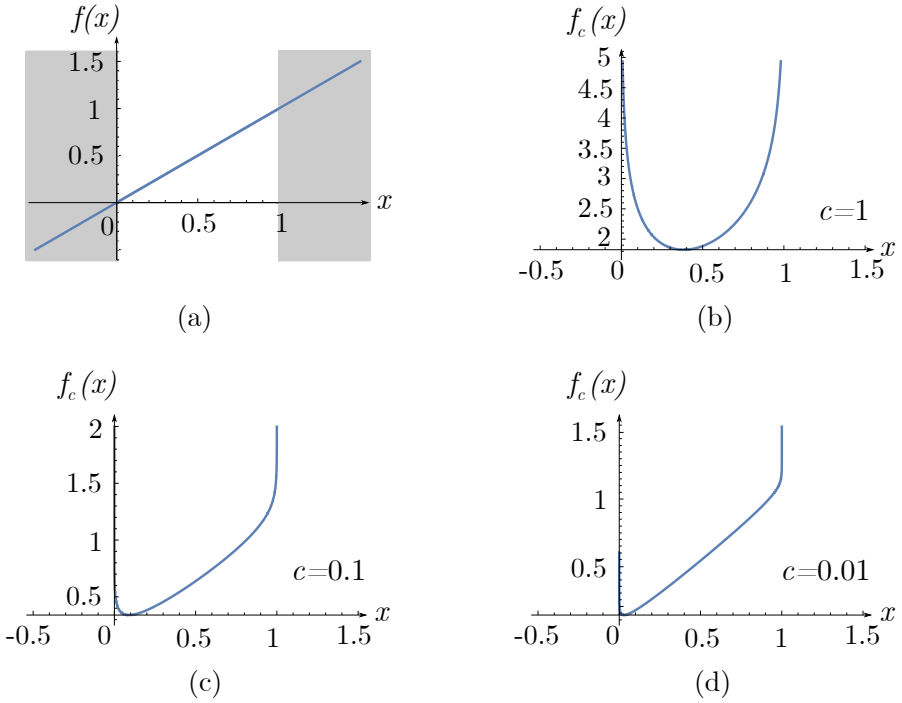

Figure I.2.2: Barrier function: (a) the cost function $f(x) = x$ subject to $g(x) = x(x-1) \leq 0$. Remaining graphics (b),(c) and (d): the unconstrained problem $f_c(x) = c\log(-x(x-1))$ with $c \in \{1, 0.1, 0.01\}$. One can observe that the unconstrained minimizer converges toward the constrained minimizer as c converges to 0.

I.2.2 The Analytic Centre

A great advantage of the TDA corresponding to the distance to centre with 2-norm and no inequality constraints is that the absence of inequality constraints allows an efficient resolution. In this special case, a Closed Form solution is available but, in general, numerical optimization is easier and more efficient when only linear equality constraints are enforced: basically, inequality constraints require determining which inequality is active at minimizer, entailing more complex algorithms. One escamotage in optimization foresees the usage of logarithmic barrier functions, which change inequality constrained minimization problems of $f(x)$, subject to inequality constraints $g_i(x) \leq 0$, to unconstrained minimization problems consisting in minimizing $f(x) - c\sum_i \log\big(-g_i(x)\big)$. In the context of inequality constrained optimization, the parameter c is meant to converge to zero during the resolution in order to reduce the impact of the barrier function on the objective, see Figure I.2.2.

Remark 4. *The logarithmic barrier is preferred to other barrier functions like* $\frac{1}{g(x)}$ *or* $\frac{1}{g(x)^2}$ *because it is self-concordant, following a theory introduced in the late 80's by Nesterov and Nemirovski [50] which allows bounding the number of Newton iterations required to reach a prescribed accuracy on the minimum. Such a good convergence char-*

acterization of the numerical optimization is of critical importance for real time usage of the TDA.

For a fixed value of the barrier coefficient c, the barrier actually attracts the solution inside the solution set. Hence, one aim of this section is to exploit this property to enforce the robustness on the tension solution. This can be achieved considering the so-called Analytic Centre associated with the constraints $\boldsymbol{\tau} \in \Pi$ and $\mathbf{W}\boldsymbol{\tau} + \mathbf{w}_e = \mathbf{0}$, which is defined as

$$\underset{\mathbf{W}\boldsymbol{\tau}+\mathbf{w}_e=\mathbf{0}}{\operatorname{argmin}} \ \phi(\boldsymbol{\tau}) \quad \text{with} \quad \phi(\boldsymbol{\tau}) = \sum_{i=1}^{2} -\log(\overline{\tau} - \tau_i) - \log(\tau_i - \underline{\tau}). \tag{I.2.5}$$

The Analytic Centre definition, as well as many properties and related methods of numerical optimization, can be found in [51]. As seen in Eq.(I.2.5), the logarithm barrier function enforces $\boldsymbol{\tau}$ to be strictly inside Π.

Remark 5. *In the framework of convex optimization, it is classical to consider the constraint* $\boldsymbol{\tau} \in \operatorname{int}(\Pi)$ *(i.e. interior of* Π*) implicit in Eq.*(I.2.5) *with* $\phi(\boldsymbol{\tau}) = +\infty$ *when logarithms are not defined. In particular, this emphasizes that optimization methods dedicated to problems with linear equality constraints and no inequality constraints are used to solve Eq.*(I.2.5)*.*

The level-sets of $\phi(\boldsymbol{\tau})$ are shown in Figure I.2.1-(f). One can observe that the Analytic Centre optimization problem offers a much better compromise between the 2-norm to the centre and the ∞-norm to the centre of Π than the 5-norm does[2]: first, contrarily to the 2-norm to the centre and similarly to the ∞-distance to the centre of Π, the Analytic Centre is inside Π under the weak assumption[3] that the linear subspace $\mathbf{W}\boldsymbol{\tau} + \mathbf{w}_e = \mathbf{0}$ intersects the interior of Π, see the black solution for a typical case where the minimal 2-norm is outside Π while the analytic centre is inside. Second, the level sets are similar to circles in a neighborhood of the centre of Π, hence showing a low sensitivity in this area, as illustrated by the blue and green solutions in Figure I.2.1-(f), which can be compared to the ones in Figure I.2.1-(c), where the blue and green solutions are far away in the case of the 5-norm to the centre of Π.

Remark 6. *Every TDA must show a high sensitivity near the boundary of* Π*. This is illustrated with the minimal* 2*-norm and the barycenter by the following limit case: with the same* Π *as before, let* $\mathbf{W}(t) = (1-t, -1)$ *and* $\mathbf{w}_e = 100 + 45|1-t| - 55(1-t)$*. The time varying linear subspace* $\mathbf{W}(t)\boldsymbol{\tau} + \mathbf{w}_e(t) = \mathbf{0}$ *is displayed in Figure I.2.3-(a). It intersects only the boundary of* Π*, hence not satisfying Slater's condition at any time. More precisely, one can observe that, for* $t < 1$*, the only feasible tension is* $\boldsymbol{\tau} = (10, 100)$*, therefore both TDAs in Figs. I.2.3-(b)(c) will output this tension while, for* $t > 1$*, the only feasible tension is* $\boldsymbol{\tau} = (100, 100)$*, and, then, both TDAs will output this tension.*

[2]Or equivalently, the distance to the closest face of Π.

[3]This condition is known as Slater's condition and it is typical in convex optimization. Data not satisfying this condition have no Analytic Centre. This correspond to the very boundary of the WFW, and has no practical impact.

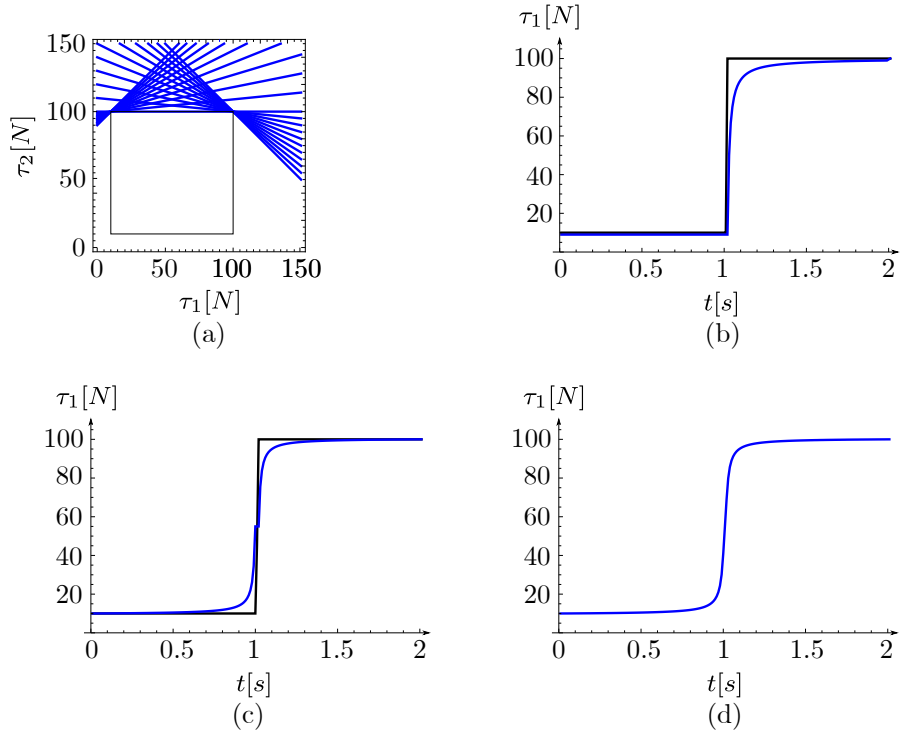

Figure I.2.3: Discontinuity example: (a) intersection of Π with the time dependent linear constraint which does not satisfy Slater's condition. Remaining graphics: in black, the tension profile $\tau_1(t)$, for (b) the minimal 2-norm to the origin, (c) the barycenter and (d) the Analytic Centre. In blue, the same profile for a slightly enlarged Π.

For $t = 1$, the whole upper face of Π is feasible, so the minimal 2-norm is attained for $\boldsymbol{\tau} = (10, 110)$, while the barycenter is $\boldsymbol{\tau} = (55, 110)$. The profiles $\tau_1(t)$ for both TDAs are depicted in black in Figures I.2.3-(b)(c), and are seen to be discontinuous[4]. Now, enlarging slightly Π as $\Pi = \{\boldsymbol{\tau} \,|\, \mathbf{0} < \mathbf{9} \leq \boldsymbol{\tau} \leq \mathbf{111}\}$, the Slater's condition is satisfied at all time and, as expected, the profiles become continuous as shown in blue in the same graphics. The Analytic Centre can now be computed and the tension profile of the first cable is depicted in Figure I.2.3-(d). One can see that, because of the proximity of the boundary where the tension profile was discontinuous, all TDAs give rise to an abrupt change of the tension.

[4]The statement and the proof of the continuity of the Barycenter presented in [40] do not involve Slater's condition, so the example provided here shows it must be not fully correct. The proof of continuity of the norm based TDA given in [52] is difficult, involving continuity of set-valued mappings and Berge maximum theorem. Condition (4.53) in Lemma 4.6 requires that the linear subspace has full dimension within Π, which seems closely related to Slater's condition.

I.2.2.1 General Definition and Main Properties

A cable tension set Ξ, defined as the intersection between Π and the set of convex inequality constraints $\mathcal{C} = \{\boldsymbol{\tau} \,|\, g_i(\boldsymbol{\tau}) \leq 0\}$, $\Xi = \Pi \cap \mathcal{C}$ is considered. Then, the (weighted) Analytic Centre is the optimal tension vector $\boldsymbol{\tau}$ that minimizes the function $\phi(\boldsymbol{\tau})$ defined by

$$\phi(\boldsymbol{\tau}) = -\sum_{i=1}^{m} \left(\underline{c}_i \log(\tau_i - \underline{\tau}_i) - \overline{c}_i \log(\overline{\tau}_i - \tau_i) \right) - \sum_{i=1}^{p} \tilde{c}_i \log(-g_i(\boldsymbol{\tau})), \tag{I.2.6}$$

subject to the equality constraints $\mathbf{W}\boldsymbol{\tau} + \mathbf{w}_e = \mathbf{0}$. As said previously, the constraints $\boldsymbol{\tau} \in \Pi$ are implicit in this problem formulation and are enforced by the objective logarithmic barriers. From now on, one can assume that the equality constraints are feasible with respect to these strict inequality constraints, which corresponds to the Slater's constraint qualification for convex optimization. In practice, this means that the pose is not on the boundary of the WFW.

Remark 7. *The requirement of Slater's condition to hold is not a drawback of the Analytic Centre. Most TDAs will fail in computing tensions if the Slater's condition is not satisfied. Moreover, such poses being exactly on the boundary of the WFW have no practical interest.*

The logarithmic barriers are strictly convex constraints in all directions, which, together with the convexity of the logarithmic barriers of the nonlinear constraints, make the function $\phi(\boldsymbol{\tau})$ strictly convex. Therefore, the Analytic Centre is uniquely defined.

The behavior of TDA for time varying poses is of critical importance. Discontinuities in tension profiles or in their derivatives can create unwanted vibrations on the end-effector. Consequently, one asks for tension profiles to be as smooth as possible. Formally, suppose that the pose $\mathbf{p}(t)$ and the external wrench $\mathbf{w}_e(t)$ are k times differentiable. The expression of the wrench matrix $\mathbf{W}(\mathbf{p}(t))$ shows it is as smooth as $\mathbf{p}(t)$. To lighten the notation, in the rest of the chapter $\mathbf{W}(t)$ is the same as $\mathbf{W}(\mathbf{p}(t))$. Then, the Analytic Centre $\boldsymbol{\tau}(t)$ is uniquely defined for each time instant by

$$\boldsymbol{\tau}(t) = \underset{\mathbf{W}(t)\boldsymbol{\tau}+\mathbf{w}_e(t)=\mathbf{0}}{\operatorname{argmin}} \phi(\boldsymbol{\tau}). \tag{I.2.7}$$

The following Theorem 1 shows the smoothness of $\boldsymbol{\tau}(t)$. A proof relying on the application of the implicit function theorem for k times differentiable functions is possible because the optimization problem in Eq.(I.2.7) is strictly convex with no inequality constraints[5].

Theorem 1. *Let's assume the cost function $\phi(\boldsymbol{\tau})$ strictly convex and, at each instant of time, the optimization problem feasible,[6] while $\mathbf{W}(t)$ is full rank. Provided that $\mathbf{W}(t)$*

[5]Non strict convexity or change in constraint activation entails non-regularities of the first order conditions Jacobian matrix that prevent applying the implicit function theorem as in the proof of Theorem 1.

[6]I.e., the cable tension set defined by $\underline{\boldsymbol{\tau}} < \boldsymbol{\tau} < \overline{\boldsymbol{\tau}}$ and $g_i(\boldsymbol{\tau}) < 0$ intersects the linear subspace $\mathbf{W}(t)\boldsymbol{\tau} + \mathbf{w}_e(t) = \mathbf{0}$.

and $\mathbf{w}_e(t)$ *are* $k_1 \geq 0$ *times differentiable, and that* $\phi(\boldsymbol{\tau})$ *and* $g_i(\boldsymbol{\tau})$ *are* $k_2 \geq 2$ *times differentiable, then the unique solution* $\boldsymbol{\tau}(t)$ *of the time dependent optimization problem in Eq.*(I.2.7) *is* $\min\{k_1, k_2 - 1\}$ *times differentiable.*

Proof. Let us consider an arbitrary time instant t_0 and define $\boldsymbol{\tau}_0 = \boldsymbol{\tau}(t_0)$ the unique solution of the optimization problem Eq.(I.2.7) for $\mathbf{W}_0 = \mathbf{W}(t_0)$, $\mathbf{w}_{e0} = \mathbf{w}_e(t_0)$. Since the implicit inequality constraints $\underline{\boldsymbol{\tau}} < \boldsymbol{\tau} < \overline{\boldsymbol{\tau}}$ and $g_i(\boldsymbol{\tau}) < 0$ are strict and have, by assumption, some common solutions with the linear constraints $\mathbf{W}(t)\boldsymbol{\tau} + \mathbf{w}_e(t) = \mathbf{0}$, they cannot be active and Lagrange theorem can be applied to show that the solution $\boldsymbol{\tau}_0$ of the optimization problem (I.2.7) satisfies the system of equations

$$\begin{cases} \nabla\phi(\boldsymbol{\tau}) + \mathbf{W}^T\boldsymbol{\lambda} = \mathbf{0}, \\ \mathbf{W}\boldsymbol{\tau} + \mathbf{w}_e = \mathbf{0}, \end{cases} \tag{I.2.8}$$

for $\mathbf{W} = \mathbf{W}_0$ and $\mathbf{w}_e = \mathbf{w}_{e0}$, where $\boldsymbol{\lambda}$ is the vector of Lagrange multipliers. This is a square system of equations with variables $\boldsymbol{\tau} \in \mathbb{R}^m$, $\boldsymbol{\lambda} \in \mathbb{R}^n$ and where $\mathbf{W}$ and $\mathbf{w}_e$ are regarded as parameters. Every variables and parameters appear linearly in the system of Eq.(I.2.8). Note that $\nabla\phi(\boldsymbol{\tau})$ is $k_2 - 1 \geq 1$ times differentiable with respect to $\boldsymbol{\tau}$ (because $\phi(\boldsymbol{\tau})$ is supposed $k_2 \geq 2$ times differentiable). Therefore, the whole system in Eq.(I.2.8) is $k_2 - 1$ times differentiable with respect to all variables and parameters. Its Jacobian matrix, with respect to the variables $\boldsymbol{\tau}$ and $\boldsymbol{\lambda}$, is

$$\begin{pmatrix} \nabla^2\phi(\boldsymbol{\tau}) & \mathbf{W}^T \\ \mathbf{W} & \mathbf{0}_{n\times n} \end{pmatrix}, \tag{I.2.9}$$

which is well known to be regular, provided that $\nabla^2\phi(\boldsymbol{\tau})$ is regular and that $\mathbf{W}$ is full rank. Those conditions are satisfied for $\boldsymbol{\tau}_0$ (because $\nabla^2\phi(\boldsymbol{\tau}_0)$ is symmetric definite positive due to the strict convexity of $\phi(\boldsymbol{\tau})$) and $\mathbf{W}_0$. Therefore, one can apply the implicit function theorem to characterize the variation of the solution $\boldsymbol{\tau}_0$ when parameters $\mathbf{W}_0$ and $\mathbf{w}_{e0}$ change: there exist neighborhoods $\mathcal{N}_{\mathbf{W}}$ of $\mathbf{W}_0$ and $\mathcal{N}_{\mathbf{w}_e}$ of $\mathbf{w}_{e0}$ and solutions $\boldsymbol{\tau}^*(\mathbf{W}, \mathbf{w}_e)$ and $\boldsymbol{\lambda}^*(\mathbf{W}, \mathbf{w}_e)$ defined inside those neighborhoods and $k_2 - 1$ times differentiable, which satisfy the system in Eq.(I.2.8). Thus, since $\mathbf{W}(t)$ and $\mathbf{w}_e(t)$ are continuous, by definition of the continuity there exists a neighborhood $\mathcal{N}_t$ of t_0 such that, for all $t \in \mathcal{N}_t$, $\mathbf{W}(t) \in \mathcal{N}_{\mathbf{W}}$ and $\mathbf{w}_e(t) \in \mathcal{N}_{\mathbf{w}_e}$. In these neighborhoods, the function $\boldsymbol{\tau}^*(\mathbf{W}, \mathbf{w}_e)$ is $k_2 - 1$ times differentiable, while the functions $\mathbf{W}(t)$ and $\mathbf{w}_e(t)$ are k_1 times differentiable by assumption. Therefore, their composition $\boldsymbol{\tau}^*\big(\mathbf{W}(t), \mathbf{w}_e(t)\big)$ is $\min\{k_1, k_2 - 1\}$ times differentiable. Finally, since the solution to the system of equations at each time instant is unique, $\boldsymbol{\tau}(t) = \boldsymbol{\tau}^*\big(\mathbf{W}(t), \mathbf{w}_e(t)\big)$ inside $\mathcal{N}_t$ and it is $\min\{k_1, k_2 - 1\}$ times differentiable at t_0. □

The main peculiarities of the existing TDAs and AC have been given so far. However, the limitations of the AC should still be pointed out to complete the global picture. Therefore, the following Remark aims at highlighting them.

Remark 8. *The first drawbacks is related to its iterative nature which, indeed, is typical among all the TDAs based on solving an optimisation problem. The second one is,*

instead, implicit in the generalised cost function in Eq.(I.2.6). *The possibility to include non-linear constraints can result in upper bound to differentiability given by* $\min\{k_1, k_2 - 1\}$.

I.2.2.2 Practical Computation of the Analytic Centre

This section aims to show how the use of a suitable solver, to solve the Analytic Centre optimisation problem in Eq.(I.2.7), can reduce the computation time of the solution w.r.t. build-in solvers demonstrating real-time capabilities. In particular, the benchmark is made by considering the Sequential Quadratic Program (SQP) algorithm [53] as a representative among the existing ones in the MATLAB library. The choice lies on SQP since it results to be the fastest among the available ones in solving Eq.(I.2.7). On the other hand, the Newton's Algorithm 1 is used [51]. It is well-known for its quick convergence and sensibility to the choice of the initial iteration. This latter can cause several problems in terms of convergence. Anyway, some stratagems that make the algorithm more robust exist. Indeed, it is possible to adapt the Newton's algorithm to manage infeasible starting points[7] and update the iterant at each solution. Moreover, since the objective function of Analytic Centre is strictly convex, it facilitates the convergence to the solution. All the simulations are performed in MATLAB using a MacBook Pro Retina 2015 with an Intel Core i5 2.7 GHz processor and 8 GB RAM 1867 MHz DDR3. With this aim in mind, let us compare the computational cost of the Newton and MATLAB fmincon-SQP methods to solve the minimization problem in the form of Eq.(I.2.7). The scope are to extract and compare the iteration number and computational time of mentioned methods while verifying that the obtained tension profiles coincide. Hereby, the study case considered resolves in a CDPR with 4 cables as depicted in Figure I.2.5-(a): the point-mass is supposed to follow a circular trajectory Eq.(I.2.10) (without losing generality), of radius $r_c = 0.5\,m$, in 10 seconds where velocity and acceleration are null at the start and end of the path. The mass of the load is set to $20\,kg$ and it is guided by four cables whose tension limits are fixed to $\underline{\tau} = 50\,N$ and $\overline{\tau} = 400\,N$, respectively.

$$\begin{cases} x(t) = r_c(\cos(2\pi s(t)) + 1.75) \quad s(t) \in [0,1], \quad t \in [0,10]s, \\ y(t) = r_c(\sin(2\pi s(t)) + 1.75), \end{cases} \tag{I.2.10}$$

with $s(t)$ being a 7-degree polynomial with the above-mentioned boundary condition acting up to the 3^{rd} derivative, while the objective function is

$$\phi(\boldsymbol{\tau}) = -\sum_{i=1}^{4} \log(\overline{\boldsymbol{\tau}} - \boldsymbol{\tau}_i) + \log(\boldsymbol{\tau}_i - \underline{\boldsymbol{\tau}}). \tag{I.2.11}$$

As far as the computational performance is concerned, the data acquired during the simulation, useful for the comparison, are collected in Table I.2.1. Moreover, in Fig. I.2.4,

[7] This means that the initial iterant satisfies the tension limits but does not necessarily satisfy the equilibrium Eq.(I.1.1).

Table I.2.1: Summary of the simulation data

Results	Newton	fmincon-SQP
Time Step	$0.001s$	$0.001s$
n_{iter} First Solution	5	10
Mean Computational Time	$6.7e^{-5}\frac{s}{sol.}$	$6.7e^{-3}\frac{s}{sol.}$
Max. Iteration Number	5	42
Stopping Criterion[8]	$\|\|Eq.(\text{I.2.8})\|\| < 10^{-10}$	fmincon default options

the computational time necessary to find a solution for each time step simulation is reported. Note that, at each call of the solver, the initial iterant is updated with the previous solution found. Furthermore, observe that the gradient of the cost function $\phi(\boldsymbol{\tau})$ was also provided. Both these expedients are employed to speed up the computation.

Therefore, analysing the data, it seems clear that implementing an ad-hoc algorithm to solve this optimization problem in Eq.(I.2.7) helps reducing the computational cost w.r.t. build-in functions. Indeed, Newton is generally 2-order faster than SQP.

Note coherency between the maximum number of iteration and the first call of the Newton method. With SQP, the maximum iteration number does not coincide with the first call. This discrepancies is due to the different architecture of the two algorithms which tackle the problem differently. Briefly, the SQP tries to approximate the objective with a quadratic model and solve the sequence of subproblems. Hence, it generally requires more iterations (and time) to converge. Though the maximum and the initial number of iteration do not coincide for the SQP, the computational time required for the first iteration results coherent, for both algorithms, as the most expensive, due to the distance between the initial (i.e. tentative) and the first solution.

To conclude, it is worth noticing the Newton trend in Fig. I.2.4: it is evident the presence of two steps at the start and end of the simulation. These are due to non-homogeneous distribution of the points along the trajectory which, because of $s(t)$, are more dense about the start and end of the path. The quick convergence of the method makes it sensible to the discretization of the trajectory.

Moreover, looking at both trends, it seems that Newton oscillates more than SQP. This is due to passive processes ongoing on the laptop. Indeed, their influence affect more the Newton trend since it works 2-order faster than SQP: a disturbance has minor effect over a big quantity.

I.2.3 Simulations and Case Studies

The implementation of the Analytic Centre, defined in Sec. I.2.2, to different case studies is conveyed in this section. In accordance with the previous tension distribution methods, mostly developed for CDPRs, this section will follow the same explanatory line to emphasize the peculiarities of the Analytic Centre, even though it applies for a wide

[8]Since (10^{-10}) is typically regarded as zero (numerically), requiring $||Eq.(\text{I.2.8})|| < 10^{-10}$ means that the residual value is zero and then one can consider the optimization solved.

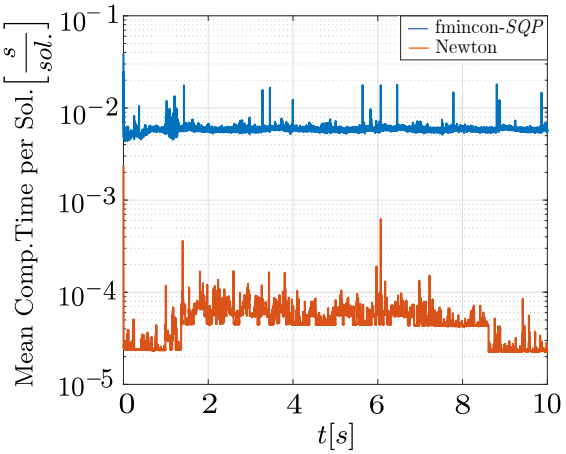

Figure I.2.4: Step time comparisons between Newton and fmincon-SQP algorithms. This graph represents the mean value of computational times. It is averaged over three simulations in order to reduce the passive effects of other processes running in parallel on the processor.

Algorithm 1 Newton Algorithm

Input: $\boldsymbol{\tau}_0$ % generally $\hat{\boldsymbol{\tau}}$
While: $||Eq.(\text{I.2.8})|| > \text{Tol}$ & iter $< \text{Max}_{\text{iter}}$
Compute: $\boldsymbol{\tau}_{k+1}$
Update: $\boldsymbol{\tau}_0 \rightarrow \boldsymbol{\tau}_{k+1}$
End
Output: $\boldsymbol{\tau}$ % last $\boldsymbol{\tau}_0$

range of CDPs [26], [28]. In particular, planar CDPRs with four and six cables and a planar MCDPR with four cables will be considered. In addition, also a spatial CDPR with eight cables is studied. Their dynamics will be simulated while cable tension profiles are computed using the Analytic Centre and various state-of-the-art methods. Indeed, the purpose of this section is to show and compare the capabilities of the Analytic Centre with respect to previous works in order to get its pros and cons. With this in mind, a total of four examples will be considered to reveal its main peculiarities.

In the first case study, Sec.I.2.3.1, the comparison with existing methods will focus on robustness, continuity and differentiability of the solutions.

The second example, Sec.I.2.3.2, aims to highlight the *generality* of the proposed method, illustrating the possibility to apply it with any *DoR* while providing feasible, robust and smooth tension profile solutions. Furthermore, the computational time of the methods that are capable of providing a feasible and continuous solution with general *DoR* is compared to confirm that the proposed method can operate in real-time.

The third case study described in Sec.I.2.3.3 lends itself well to emphasize the *ver-*

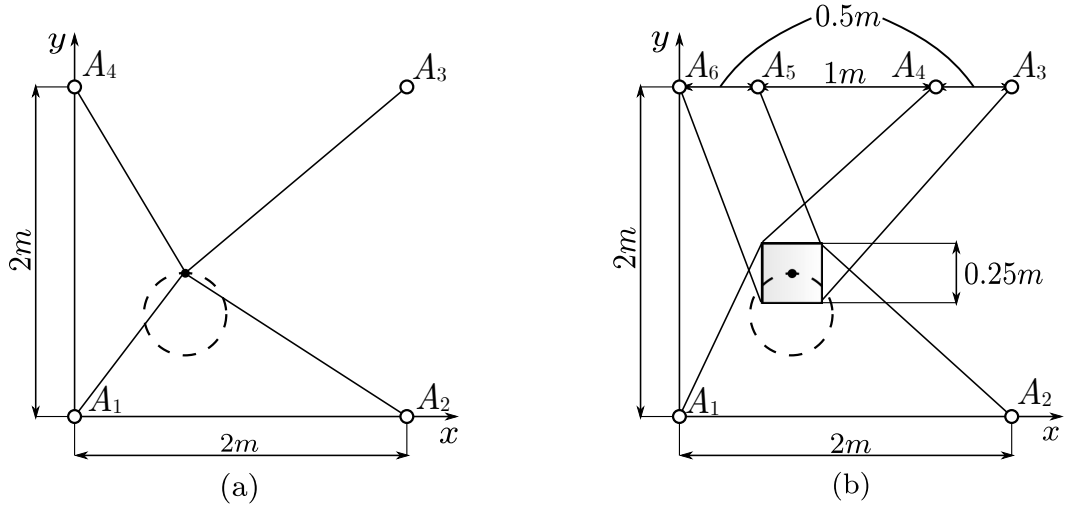

Figure I.2.5: Two planar CDPRs: (a) composed of four cables and a point-mass end-effector, (b) composed of six cables and a rigid-body platform end-effector

satility of the Analytic Centre. Indeed, it shows that it is possible to take into account non-linear time-varying constraints in a natural way, returning, again, a set of tensions with the aforementioned characteristics.

To conclude, the last simulation, Sec.I.2.3.4, summarizes all the previous results, demonstrating the Analytic Centre capabilities even when a spatial case is considered.

I.2.3.1 Planar CDPR composed of four cables and a point-mass end-effector

The architecture of the robot considered in this study, as well as the trajectory, is the same used in Section I.2.2.2.

During the tracking task, the robust index defined in Eq.(I.2.3) is computed. Moreover, several state-of-the-art methods are reproduced to determine the tension profiles according to different criteria. The obtained results are collected and depicted in Figure I.2.6. At a first sight, all implemented methods provide feasible solutions: the tension profiles found satisfy the maximum and minimum tension constraints of Eq.(I.1.4) (represented in each figure by the dashed red line) and the load equilibrium in Eq.(I.1.1). Moreover, the profiles look not symmetric since the trajectory has been shifted in the left-bottom corner of the robot workspace. The considered methods are now investigated one-by-one in order to remark on the relevant aspects necessary for the comparison.

Let's consider the QP method first, whose tension profiles are depicted in Figure I.2.6-(d) [36]. This approach tends to save energy required from the actuators by minimizing the tension components as much as possible. Indeed, the results show that two tension components τ_1 and τ_2 (cables below the load) are found to assume the minimum value. As a result, the robustness index is the lowest among the other methods, as shown in Fig.I.2.6-(f). In practice, tension profiles are continuous and differentiable but the robot

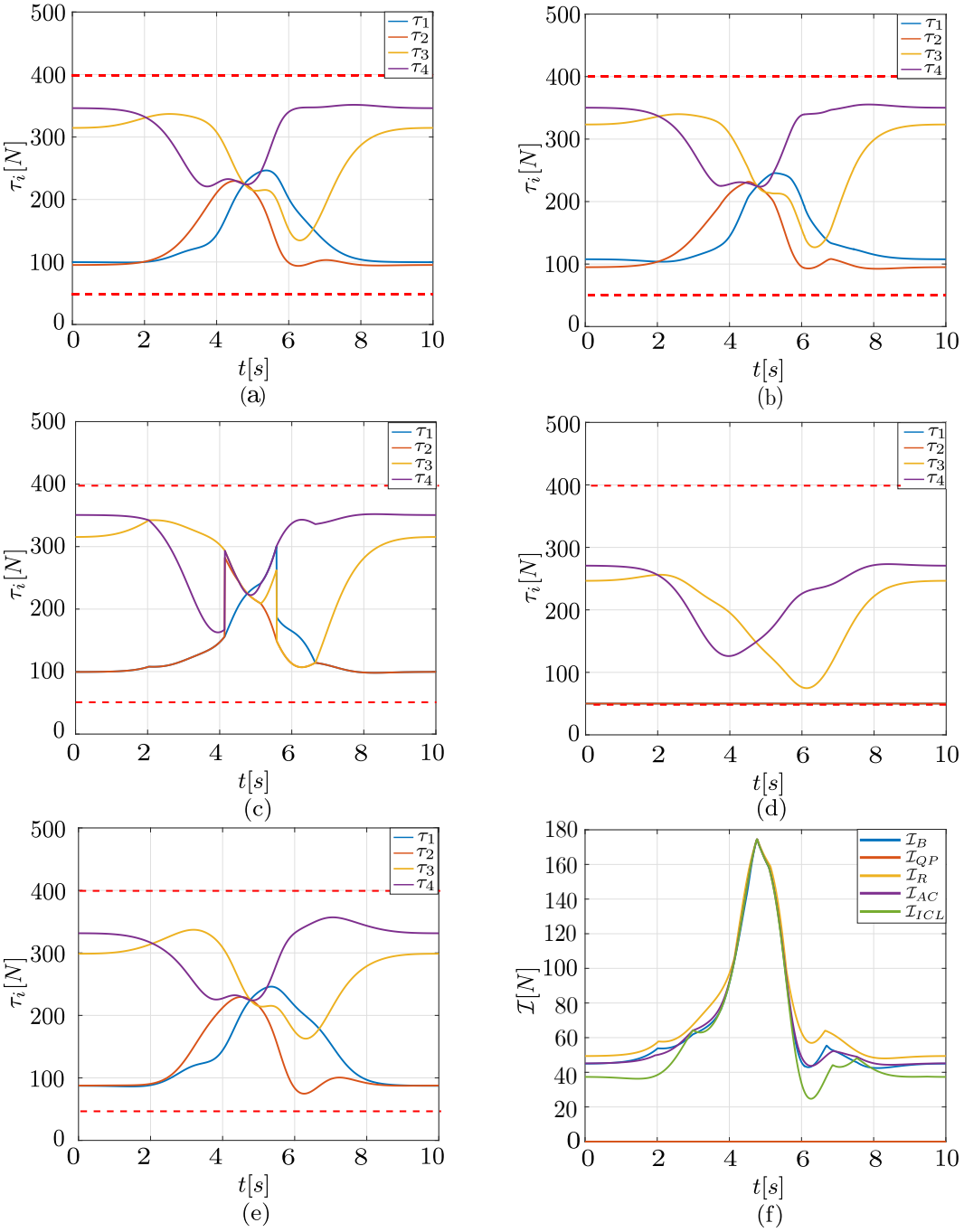

Figure I.2.6: Tension profiles for: (a) Analytic Centre approach, (b) Barycentric method, (c) Robust (LP) technique, (d) Quadratic Programming (QP) and (e) Improved-Closed Form. The trends of the robust index for the mentioned methods are reported in Figure (f).

suffers from low stiffness which can lead to undesired vibrations and oscillations of the platform.

On the other hand, the Robust solution reported in Fig.I.2.6-(c) is the one that has the highest robustness index value. Anyway, since this approach belongs to the family of LP optimization methods [31], the solution can result in discontinuities. This example reveals discontinuities of the solution while tracking a smooth circular trajectory. In some sense, achieving the maximum stiffness is akin admitting discontinuities in the tension profiles. Therefore, the presence of discontinuities, even when continuous trajectory and wrench are considered, can cause unwanted phenomena (e.g. vibrations) on the end-effector.

In Figure I.2.6-(b), the solution found using the Barycentric approach [40], [46] is similar in both tension profiles and the robustness is similar to the Analytic Centre solution reported in Fig. I.2.6-(a). Despite their affinity, there are crucial differences among them. Indeed, although the Barycentric provides robust and continuous profiles, there is no formal evidence of their differentiability. Moreover, even though this technique is general and then valid for any DoR, the sudden increase of computational cost makes it unfeasible already for $DoR = 3$. This latter will be better clarified in the next section.

The Improved-Closed Form [41] approach, whose solution is displayed in Fig.I.2.6-(e), gives continuous tension profiles with a close, but generally lower, robustness index value than the Analytic Centre method. It constitutes an improvement to the previous work [42]. Anyway, the absence of a formal proof, guaranteeing the convergence to a feasible solution, represents the main shortcoming of this approach.

So far, for the considered methods in the literature, the robustness, continuity and differentiability of the tensions were discussed. To sum up, these examples showed that, among these TDAs, the Analytic Centre is the only one able to preserve the mentioned properties simultaneously.

I.2.3.2 Planar CDPR composed of six cables and a rigid-body platform end-effector

The use of several cables serves as an example to demonstrate the generality w.r.t. DoR of the proposed method in finding a robust solution which is also continuous and differentiable. The scheme of the robot is depicted in figure I.2.5-(b). The centre of mass of the square platform is supposed to follow the same trajectory[9] as in the previous case of Sec.I.2.3.1. The axes of the mobile reference frame will remain parallel to those of the fixed one throughout the simulation. The mass of the load is $65\,kg$ and it is guided by six cables whose tension limits are the same as in the previous example. The choice of a large mass forces the system to the boundary of the WFW.

Simulation results are given in Figure I.2.7. Observe that, because of the several cables, $DoR = 3$ and therefore the Barycentric approach can not be applied. Indeed, the existing method [40], [46] relies on finding the barycenter of a 2D polytope Λ, defined

[9]Notice that the moment of inertia has not been considered here, as the motion is purely translational with no angular velocity or acceleration involved. This assumption does not have any repercussions on the results, as they focus on the applicability of the various methods themselves.

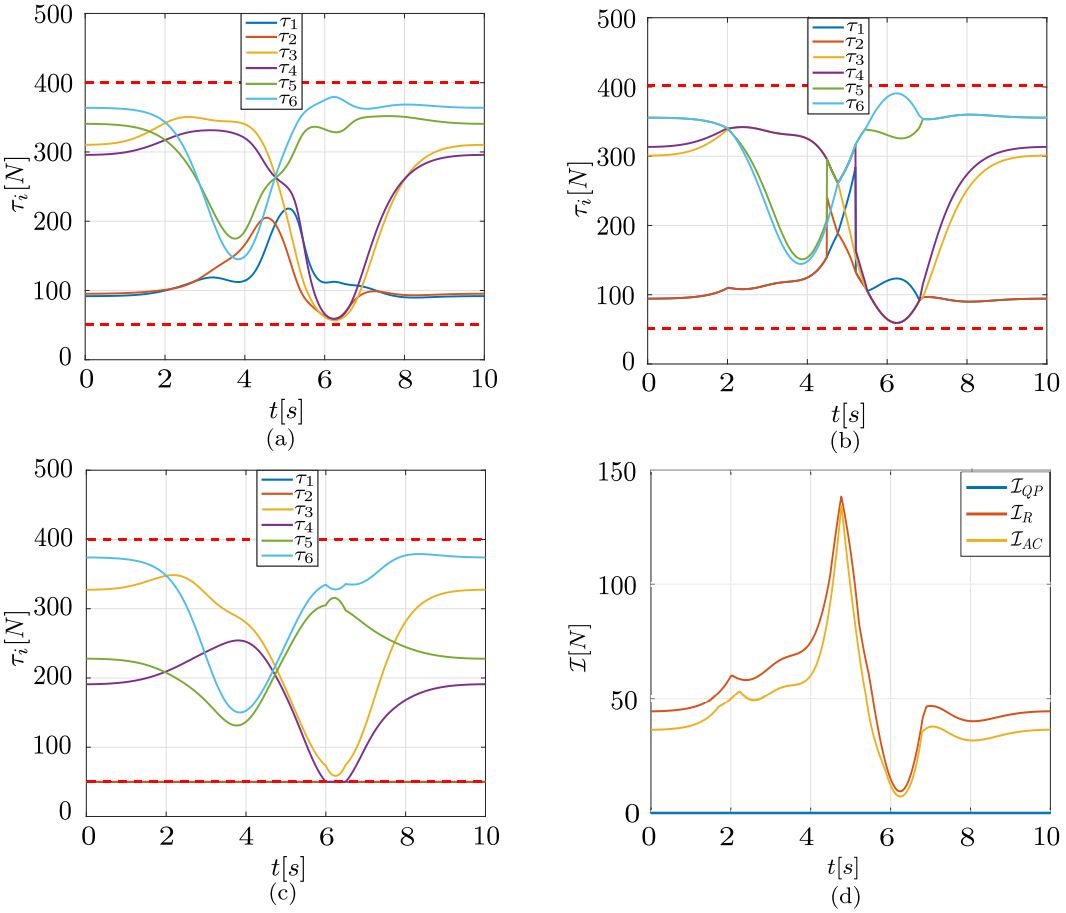

Figure I.2.7: Tension profiles for: (a) Analytic Centre, (b) Robust (LP) method and (c) Quadratic Programming (QP). The trends of the robustness index for the mentioned methods are reported in Figure (d).

in Eq.(I.1.7), by means of triangulation techniques. The latter can be efficiently applied in a low-dimensional space. Already from a dimension higher than two, this technique results impractical due to the increase in its computational cost. This issue, combined with the common structure of CDPRs, which often foresees a maximum of $DoR = 2$, prevented from a generalization. Anyway, the advent of CDP where a large redundancy can occur is, among the others, another motivation for the introduction of the Analytic Centre.

The Improved Closed-Form method, instead, fails in furnishing a feasible solution. This happens because the high mass pushes the cable tensions outside the limits. Hence, although it is an improved version of the Closed-Form method [42], it is not always able to converge in DoR steps. The same authors express this possibility in their work [41]. Thus, this case study identifies a reduced WFW coverage of the Improved Closed-Form w.r.t. the Analytic Centre, QP and Robust methods which find a feasible solution.

Table I.2.2: Summary of the simulation data

Results	Newton (AC)	fmincon-SQP (QP)
Time Step	$0.001s$	$0.001s$
n_{iter} first Solution	7	2
Mean Computational Time	$7.3e^{-5}\frac{s}{sol.}$	$6.8e^{-3}\frac{s}{sol.}$
Max. Iteration Number	7	3
Stopping Criterion	$\|\|Eq.(\text{I.2.8})\|\|_2 < 10^{-10}$	fmincon default options

Among the remaining methods, whose solutions are reported in Fig.I.2.7, the Analytic Centre approach appears to be the best compromise between robustness and continuity of the solution. Indeed, looking at Figure I.2.7-(d), the QP maintains the lowest robustness index, reducing the energy consumption at the price of a reduced stiffness of the robot, whereas the Robust method registers the highest index value but introduces discontinuities of tensions in time which can cause unwanted phenomena as well.

However, at this point, someone might wonder what is the performance of this method in terms of computational time. Hence, to make a fair comparison, the computational time required to determine the solution for each optimization problem is considered. In this regard, a comparison of the approaches that return *regular* continuous and feasible tension profiles for any DoR is given.

The graph in Fig.I.2.8 shows the time required by the solver to find a solution during the simulation for both the Analytic Centre and QP methods. In particular, these data are generated by averaging the solution times over 3 simulations to remove disturbances that can occur due to passive processes ongoing on the computer. For the Analytic Centre approach, the Newton algorithm discussed in I.2.2.2 is used to solve the optimization problem whereas, for the QP method, the Sequential Quadratic Programming (SQP) algorithm [53] is a natural choice, given the nature of the problem. The gradient of the objective function are provided in advance as well as the iterant are updated at each call, in order to speed up the solvers.

Looking at the graph in Fig.I.2.8, the computational times of the Newton method applied to the Analytic Centre is 2-order smaller than the QP. The differences in the iteration time are to be attributed to the diversity between the solvers, the objective functions and the absence of active constraints (i.e. inequalities) in the case of the Analytic Centre approach. The inequalities which define the QP optimization problem increase its complexity, forcing the solver consuming time for the few iterations required to converge. In both cases, the first iteration is the one which costs more. The maximum number of iterations recorded amounts to $n_{iter,AC} = 7$ and $n_{iter,QP} = 3$. Because the QP method is generally applied in real-time applications, it is reasonable to argue that also the Analytic Centre can be applied in real-time to control the cable tensions of a CDP. Table I.2.2 summarizes the discussed data used for time comparisons.

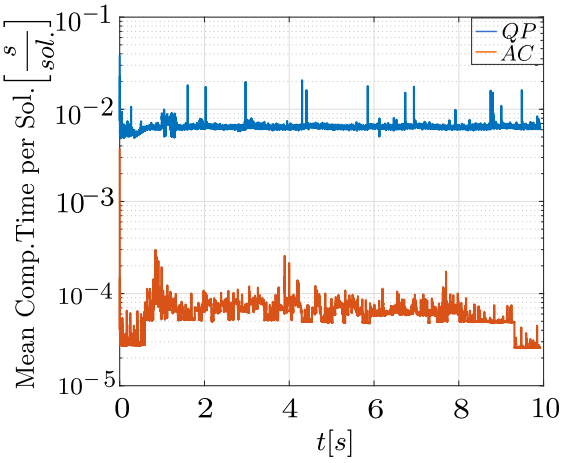

Figure I.2.8: Computational time per solution during the simulation. This graph represents the mean value of the computational times. It is averaged over three simulations in order to reduce the passive effects of other processes running in parallel on the processor.

I.2.3.3 Planar MCDPR composed of four cables and a point-mass end-effector

This example takes its cue from mobile cable systems [27], [48]. Indeed, in these systems, the choice of the cable tensions has to take into account the static friction between the ground and the Mobile Base (MB) to avoid sliding effects during the execution of a task. This motivates the need to introduce non-linear constraints in the cable tensions computation. The scheme of the MCDPR considered in this example is given in Fig. I.2.9. It constitutes a simplified version of the original MCDPRs. Indeed, in practice, friction is considered to act on the four wheels that move each MB instead of assuming its influence as concentrated on its centre of mass. However, this architecture is enough for the scope of this section and, although it constitutes a simplified model, it does not represent a limitation for the presented method. Later on, the MBs will be considered as fixed at the ground and therefore the robot will coincide with the study case discussed in Sec. I.2.3.1. This latter will allow to make comparisons and see the consequences on the MCDPR due to the differences in the tensions distribution when friction is not considered.

For the current case, the mass of the moving base is considered to be equal to $m_{\mathrm{MB}_1} = m_{\mathrm{MB}_2} = 65kg$ while the load mass is $5kg$. The static friction coefficient is $\mu = 0.5$. The load trajectory is the same as in the previous cases, and the same are the tension limits.
The equations which constitute the non-linear constraints $\mathcal{C}$ for the cable tensions are the followings

$$||\tau_1 \mathbf{q}_1 + \tau_4 \mathbf{q}_4||_2^2 \leq m_{\mathrm{MB}_1}^2 \, g^2 \, \mu^2, \quad ||\tau_2 \mathbf{q}_2 + \tau_3 \mathbf{q}_3||_2^2 \leq m_{\mathrm{MB}_2}^2 \, g^2 \, \mu^2. \tag{I.2.12a}$$

These can be derived by using the free-body diagram for both MB_1 and MB_2. Indeed,

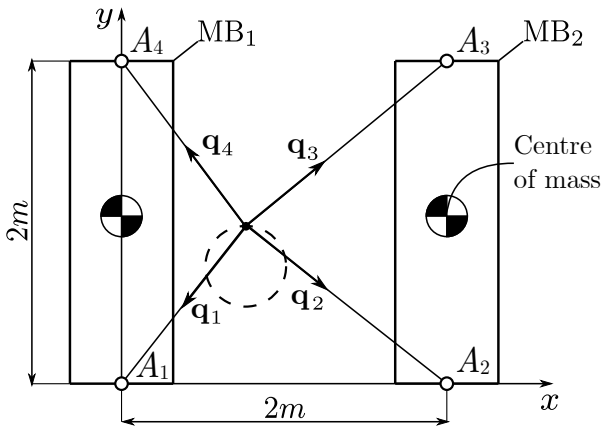

Figure I.2.9: Architecture of a planar MCDPR with 4 cables

the MB can be considered as decoupled systems.
The computed tension profiles are depicted in Fig.I.2.10a. The objective function used for this simulation is reported in Eq. (I.2.13) for sake of clarity.

$$\begin{aligned}\boldsymbol{\phi}(\boldsymbol{\tau}) = -\Big(\sum_{i=1}^{4}\log(\tau_i - \tau_{min,i}) + \sum_{i=1}^{4}\log(\tau_{max,i} - \tau_i) \\ + \log\big(-\big(\tau_1+\tau_4\big)^2 + m_{\mathrm{MB}_1}^2\, g^2\, \mu^2\big) + \log\big(-\big(\tau_2+\tau_3\big)^2 + m_{\mathrm{MB}_2}^2\, g^2\, \mu^2\big)\Big).\end{aligned} \tag{I.2.13}$$

The tension profiles show how the introduction of friction narrows the set of tensions that can be used to perform a task. In particular, the tensions, Fig.I.2.10a continuous line, assume reduced values compared to the case of fixed moving bases. In other words, avoiding sliding conditions for the MBs means reducing the tension values while performing a task. The consequences of neglecting friction while computing tension profiles can be visualized in Fig.I.2.10b. The trend of the constraints demonstrates that neglecting friction can cause the MBs to slide since the dotted curves exceed the static friction limit. An alternative way to display the same phenomena consists in investigating if the $\boldsymbol{\lambda}$ vectors of the two solutions, for $t = 3s$ and $t = 5s$, belong to the intersection between the feasible polygon and the non-linear constraints $\hat{\Xi} = \Lambda \cap \mathcal{C}$; the dual of Ξ. The equations necessary to map the constraints into Λ, as done in Figs.I.2.11a and I.2.11b, are the followings

$$\begin{aligned}&\boldsymbol{\tau}_{p,1}^2 + (\mathbf{N}\boldsymbol{\lambda})_1^2 + 2\boldsymbol{\tau}_{p,1}(\mathbf{N}\boldsymbol{\lambda})_1 + \boldsymbol{\tau}_{p,4}^2 + (\mathbf{N}\boldsymbol{\lambda})_4^2 + 2\boldsymbol{\tau}_{p,4}(\mathbf{N}\boldsymbol{\lambda})_4 + \\ &2\big(\boldsymbol{\tau}_{p,1}\boldsymbol{\tau}p,4 + \boldsymbol{\tau}_{1,p}(\mathbf{N}\boldsymbol{\lambda})_4 + \boldsymbol{\tau}_{4,p}(\mathbf{N}\boldsymbol{\lambda})_1 + (\mathbf{N}\boldsymbol{\lambda})_1(\mathbf{N}\boldsymbol{\lambda})_4\big) \leq m_{\mathrm{MB}_1}^2\, g^2\, \mu^2,\end{aligned} \tag{I.2.14}$$

$$\begin{aligned}&\boldsymbol{\tau}_{p,2}^2 + (\mathbf{N}\boldsymbol{\lambda})_2^2 + 2\boldsymbol{\tau}_{p,2}(\mathbf{N}\boldsymbol{\lambda})_2 + \boldsymbol{\tau}_{p,3}^2 + (\mathbf{N}\boldsymbol{\lambda})_3^2 + 2\boldsymbol{\tau}_{p,3}(\mathbf{N}\boldsymbol{\lambda})_3 + \\ &2\big(\boldsymbol{\tau}_{p,2}\boldsymbol{\tau}p,3 + \boldsymbol{\tau}_{2,p}(\mathbf{N}\boldsymbol{\lambda})_3 + \boldsymbol{\tau}_{3,p}(\mathbf{N}\boldsymbol{\lambda})_2 + (\mathbf{N}\boldsymbol{\lambda})_2(\mathbf{N}\boldsymbol{\lambda})_3\big) \leq m_{\mathrm{MB}_1}^2\, g^2\, \mu^2,\end{aligned} \tag{I.2.15}$$

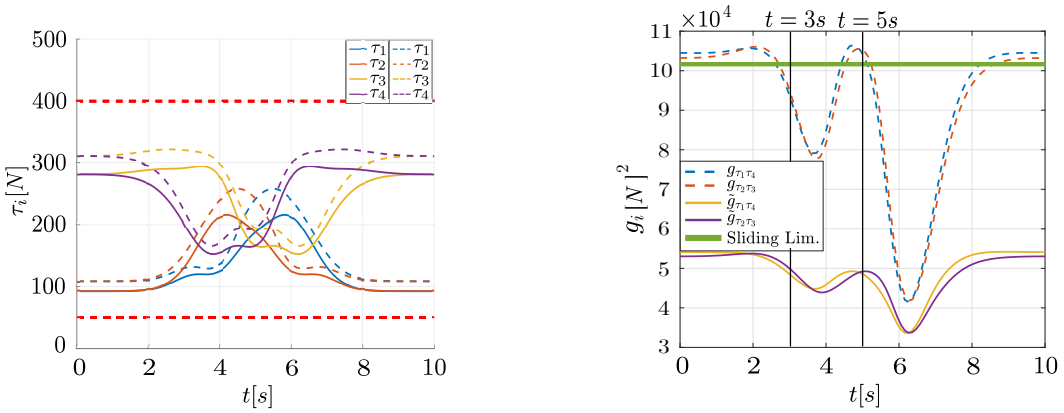

(a) (b)

Figure I.2.10: Comparisons of the results: Fig.(a) reports the cable tension for the MCDPR. The solid-line profiles refer to the case with non-linear constraints, whereas the dotted ones do not consider any additional constraints (i.e. the MBs are considered as fixed). Fig.(b) shows the trend of the non-linear constraint values of Eq.(I.2.12) for the two MBs. The constraints $\tilde{g}_{\tau_1\tau_4}$ and $\tilde{g}_{\tau_2\tau_3}$ take friction into account, while $g_{\tau_1\tau_4}$ and $g_{\tau_2\tau_3}$ do not. It can be seen that, for the present case, the $g_{\tau_i\tau_j}$ (dotted profiles) constraints exceed the sliding limit several times.

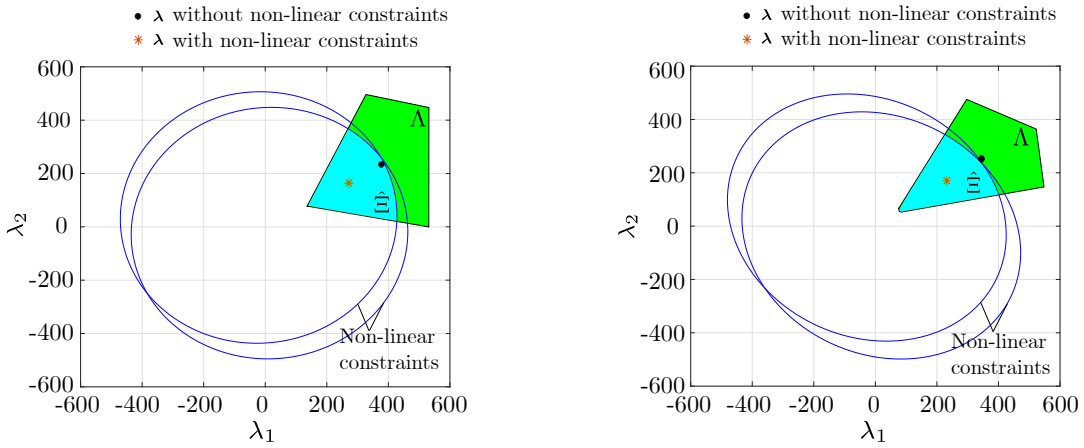

(a) (b)

Figure I.2.11: Intersection between the feasible polygon Λ and the non-linear constraints in Eq.I.2.12. These plots depict the case at (a) $t = 3s$ and (b) $t = 5s$. Notice that only the $\boldsymbol{\lambda}$ vector computed by considering the non-linear constraints is feasible in both cases.

where $\boldsymbol{\tau}_{p,i}$ and $(\mathbf{N}\boldsymbol{\lambda})_i$ represent the components of the particular and general solution presented in Eq.(I.1.6), respectively. Thus, the constraint Equations (I.2.14) and (I.2.15) in Λ can be retrieved by substituting Eq.(I.1.6) into Eqs.(I.2.12). In other words, it suffices to employ the composition rule for functions. Furthermore, observe that the

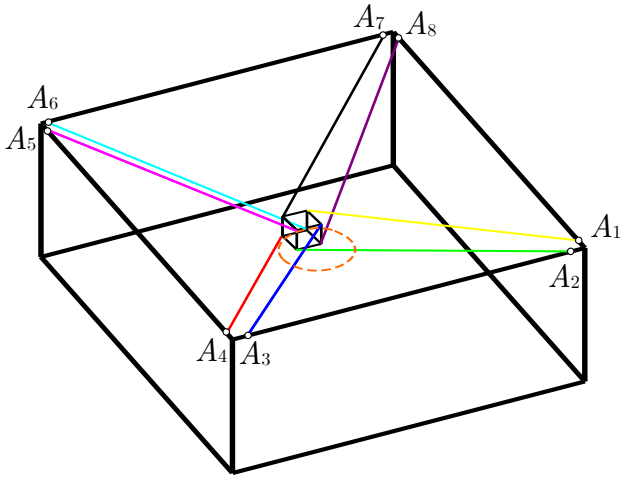

Figure I.2.12: Spatial architecture considered, see [29] for details.

elements $(\mathbf{N}\boldsymbol{\lambda})_i$ could be thought as $\boldsymbol{\tau}_{g,i}$ but, here, the explicit version with $\boldsymbol{\lambda}_i$ is clearer since the aim is to investigate the conic constraint intersection with the feasible polygon Λ. Indeed, as a confirmation of what displayed in Fig.I.2.10b, Figs.I.2.11a and I.2.11b demonstrate that the sliding condition occurs when $\boldsymbol{\lambda} \notin \hat{\Xi}$.

This example showed the ability of the Analytic Centre to deal with non-linear constraints, so far approximated as linear, as in [27], [48], for example. In addition, as done in Eq.(I.2.13), the possibility to *superimpose* general (linear and non-linear) time-varying constraints on specific cable tensions makes this approach compatible with Human Physical-Interaction (HP-I) or collaborative applications. Indeed, the mentioned applications ask to cope with humans, thus demanding to take precautions in terms of tension limit along specific cables which, usually, are close to a human [29].

I.2.3.4 Spatial CDPR composed of eight cables and a rigid-body end-effector

This example is intended to summarise the distinctive features of the TDAs analysed and the one proposed here. In particular, a spatial CDPR designed for collaborative tasks will be considered [29]. This robot considers eight cables and has 2 *DoRs*. The cables are fixed at the upper part of the frame, near the vertices of the cubic cell, as shown in the Figure I.2.12[10]. This choice avoids possible dangerous contact with the operator intent on collaborating with the platform.

For the purposes of this section, it is sufficient to consider a tracking task: the trajectory under consideration is always circular and arranged in the horizontal plane of Eq.(I.2.16), similar to the previous cases. The full dimension of the robot and its precise description can be found in [29]. The mass of the platform is $m = 7kg$ and it is guided by eight cables whose tension limits are fixed to $\underline{\tau} = \ 1\,N$ and $\overline{\tau} = 100\,N$, respectively.

[10]The real prototype is located in Nantes, France at LS2N.

$$\begin{cases} x(t) = r_c \cos(2\pi s(t)) \quad s(t) \in [0,1], \quad t \in [0,10]s, \\ y(t) = r_c \sin(2\pi s(t)), \\ z(t) = 2. \end{cases} \tag{I.2.16}$$

As done for the other case study, several TDAs are compared. Their tension profiles and robustness indices are reported in Fig.I.2.13. Alike the case study in Section I.2.3-A, all the methods provide feasible tension profiles and pertain to the main characteristics discussed above. However, as seen before, the existing methods result in optimal performances only for particular, predefined, operating conditions. In fact, in many cases (for certain tasks), some of their relevant properties are lost, such as continuity of tension profile, quick convergence, generality for any DoR, and so on.

A further aspect to be examined and added to the previous considerations is highlighted by the architecture considered. Indeed, this CDPR is redundant but not fully-constrained as the load is suspended. In the several case studies analysed in the state of the art, this type of architecture is not very common but nevertheless it is important for some recent applications.

In particular, the major difference that is evident, compared to the previous examples, concerns the values taken by the robustness indices.

In fact, this time, the QP method, see Fig.I.2.13-(f), does not have the lowest index. Moreover, the other methods show relatively little difference in terms of robustness. In some ways, they can be considered equivalent.

When it is the case of suspended loads, it has been seen [54] that the capability to optimise the cable tension is reduced. In other words, the absence of cables under the platform leads to a reduction of the area (hyper volume, in general) of the polygon Λ and thus in a reduced ability to generate a wrench on the load. This, also, explains why the range of variation of the various robustness indices is small compared to the previous cases (all fully-constrained). All indices are very similar to each other with the robust method, as always, that holds the maximum value.

To conclude, this example confirms that, in general, the existing methods result in optimal performances only for particular predefined operating conditions (i.e. task at hand and architecture). Instead, the Analytical Centre method always guarantee the best compromise in terms of robustness, smoothness of tension profiles, generality, and reliability.

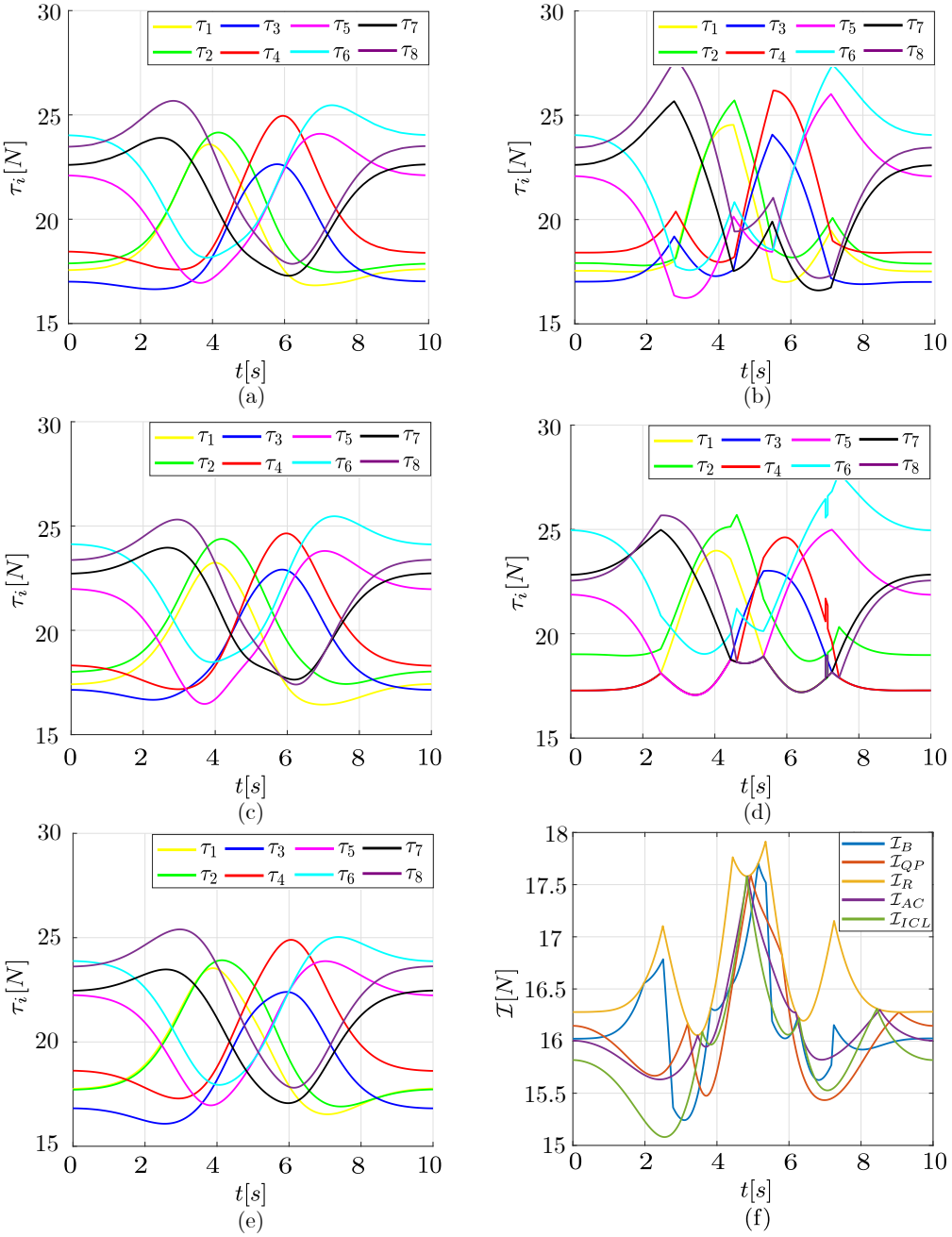

Figure I.2.13: Tension profiles for: (a) Analytic Centre approach, (b) Barycentric method, (c) Quadratic Programming (QP), (d) Robust (LP) technique and (e) Improved-Closed Form. The trends of the robustness index for the mentioned methods are reported in (f). Observe that the colors used for the tension profiles coincide with the colors of the cables in Fig. I.2.12.

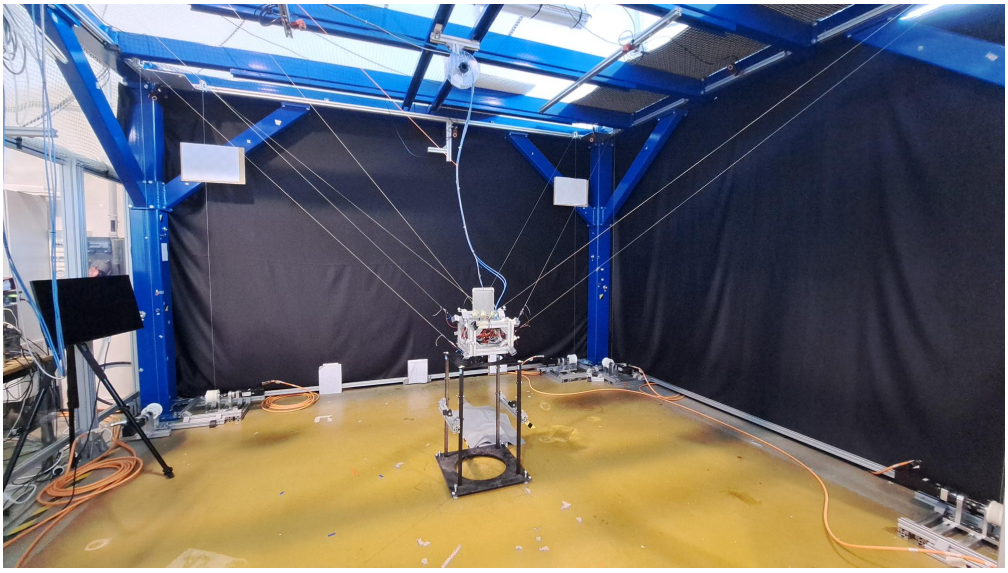

Figure I.2.14: CRAFT Prototype.

I.2.4 Analytic Centre Implementation and Experimental Tests

This section is dedicated to the investigation of the TDAs' behaviour when implemented in a real hardware. In particular, the experimental tests were realised on the CDPR prototype, CRAFT, situated in Nantes at the Laboratoire des Sciences du Numérique de Nantes (LS2N). The main idea consists in showing that the tension profiles measured follow the ideal, i.e. simulated, ones. Indeed, this would automatically validate the results discussed in the previous chapter.

I.2.4.1 CRAFT Prototype

CRAFT is a redundant CDPR with 8-cables where the platform is suspended as shown in Fig.I.2.14. The frame measures $4.35 \times 3.77 \times 2.75$m, the electric motors (PARKER SME60) and cable drums are located at the base of the robot.

Cables are made of VECTRAN and are attached to the platform by means of knots, see Figs. I.2.15 and I.2.17. Observe that between the platform and the cables, tension sensors (FUTEK FSH0497) are installed as depicted in Fig.I.2.16.

The platform dimensions are $0.28 \times 0.28 \times 0.20$m and it weighs $9kg$, it is made of aluminium bars and contains other useful sensors necessary for the state estimation such as gyro etc.

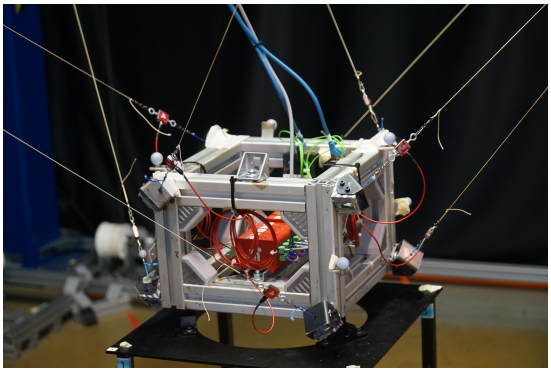

Figure I.2.15: CRAFT moving platform.

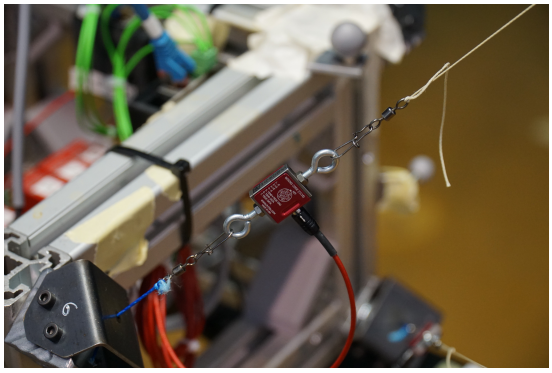

Figure I.2.16: Tension sensor.

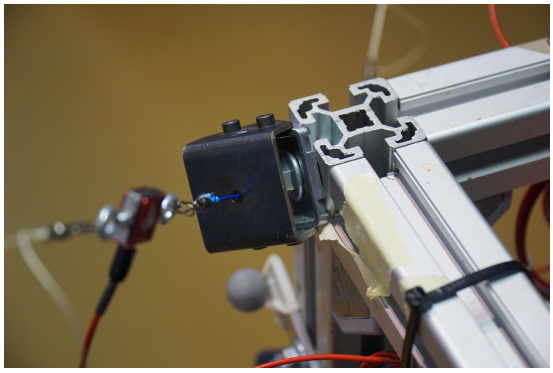

Figure I.2.17: Moving platform anchor point.

I.2.4.2 CRAFT Control Scheme

As mentioned, the future idea will be to control the robot using tensions instead of solving kinematic problems to identify the pose. However, here, the control is still kinematical and therefore in its preliminary phase. Typically called *Joint Space Control* [16]. Indeed, the TDA' solution is used in the loop and converted in joint values which, in turn, are used to control the robot. In particular, Scheme I.2.18 shows the contributes that intervene in controlling the robot[11]. Mathematically, the contributions intervening into determine the control tension $\boldsymbol{\tau}^c$ are

$$\boldsymbol{\tau}^c = \boldsymbol{\tau}_{TDA} + \boldsymbol{\tau}_{PID} + \boldsymbol{\tau}_f, \tag{I.2.17}$$

where $\boldsymbol{\tau}_{TDA}$ is the solution of the optimization problem based on the feedforward term, $\boldsymbol{\tau}_{PID}$ is the contribution of the control and $\boldsymbol{\tau}_f$ is the friction model of the cable wound on the pulley.

[11]Inverse Geometric Model (IGM) and Inverse Kinematic Model (IKM) are typically used to convert Cartesian coordinate into joint space ones.

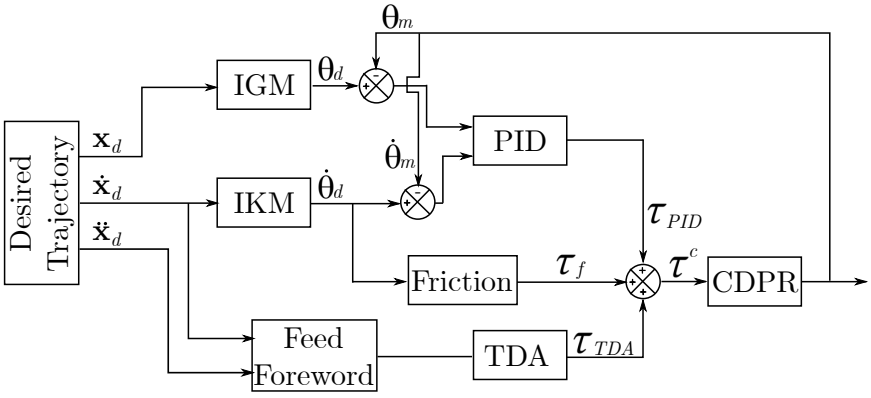

Figure I.2.18: CRAFT Control scheme.

I.2.4.3 CRAFT Ground Station

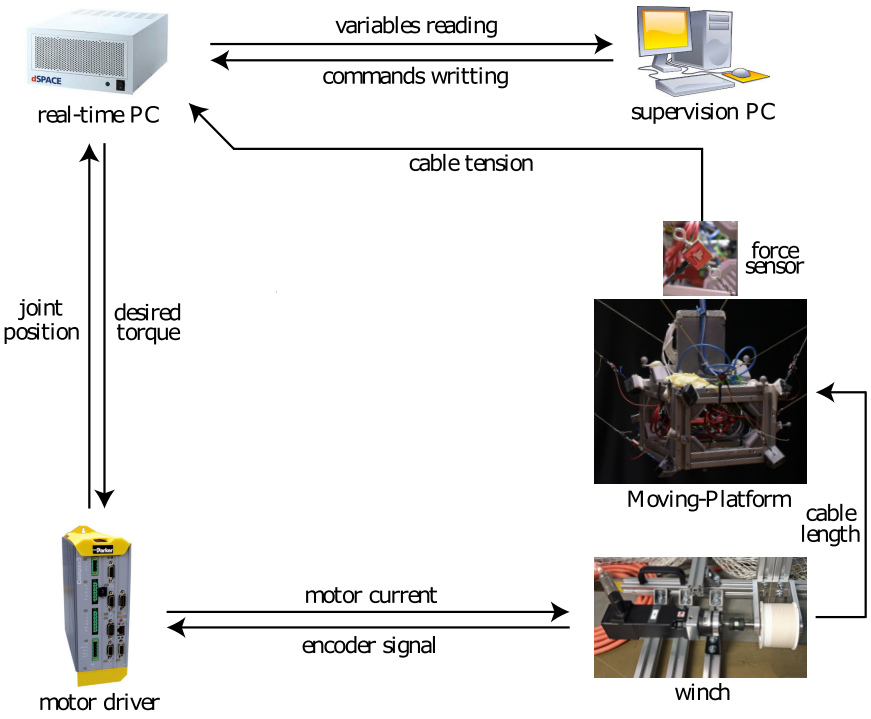

Figure I.2.19: CRAFT Ground Station.

The control scheme is implemented in MATLAB (Simulink) which generates the C-code using RTlib library [55]. The C-code is then uploaded on the so-called real-time PC or dSPACE. This latter, is responsible for reading sensor measures, writing and communicating with the electric motors.

The entire scheme is supervised by a supervisory PC commanded, in turn, by a

human; see Fig I.2.19.

I.2.4.4 Campaign of Tension Measures

Several campaigns of tests have been conducted and many practical problems have been faced to reach the following results. However, all the technical issues encountered and strategies employed are not reported hereby as they are out of the scope of this work. Indeed, here, the intention is barely to show promising results in terms of coherency between theory and practice.

Hence, the experiment reported here, a title of example, consists in performing a circular trajectory 5 times in $40s$.

In what follows, the tension profiles and the results of the TDAs discussed before and implemented are reported in Figures I.2.20 to I.2.24. Observe that measured data are averaged using Simulink tools[12].

[12] `https://www.mathworks.com/help/matlab/ref/movmean.html`

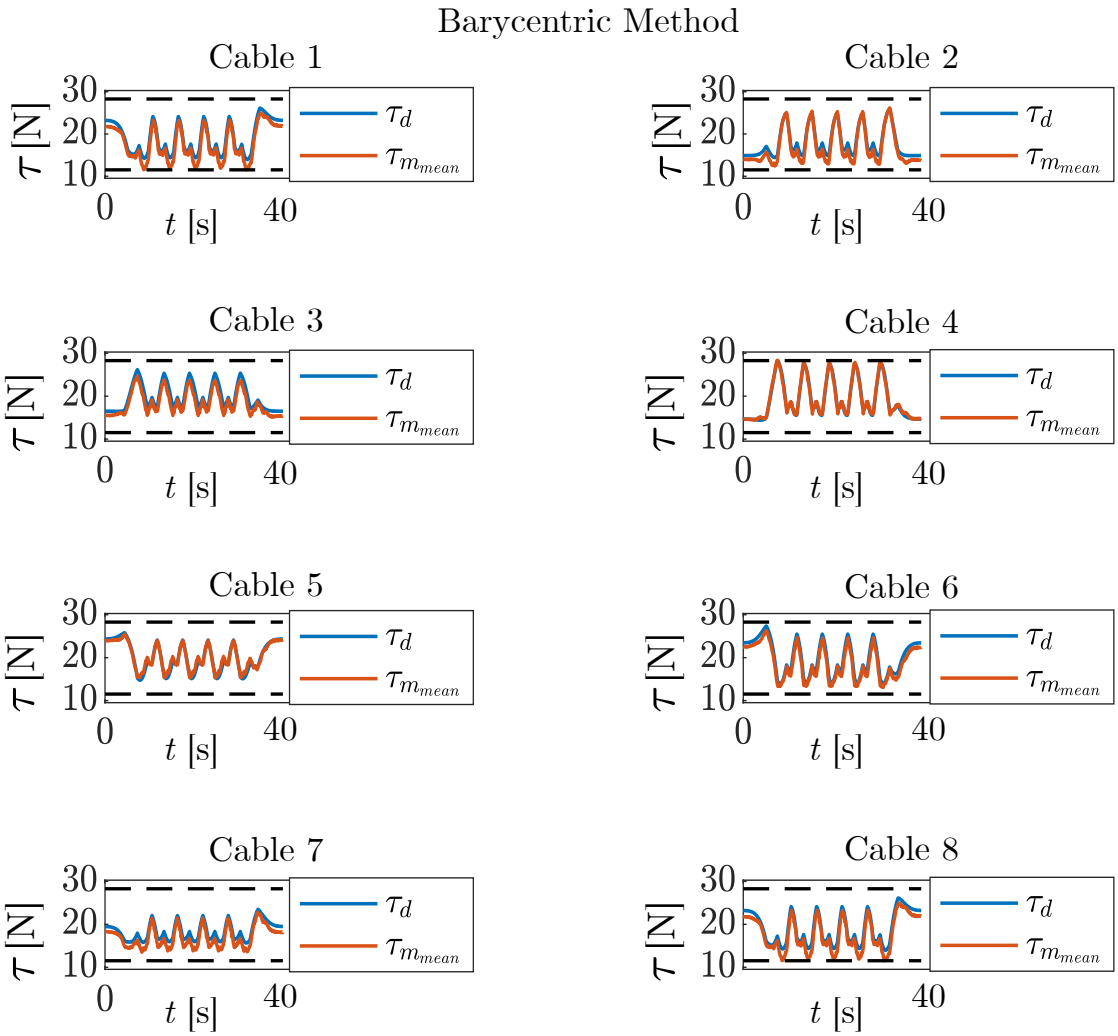

Figure I.2.20: Barycentric: desired and measured tension for each cable.

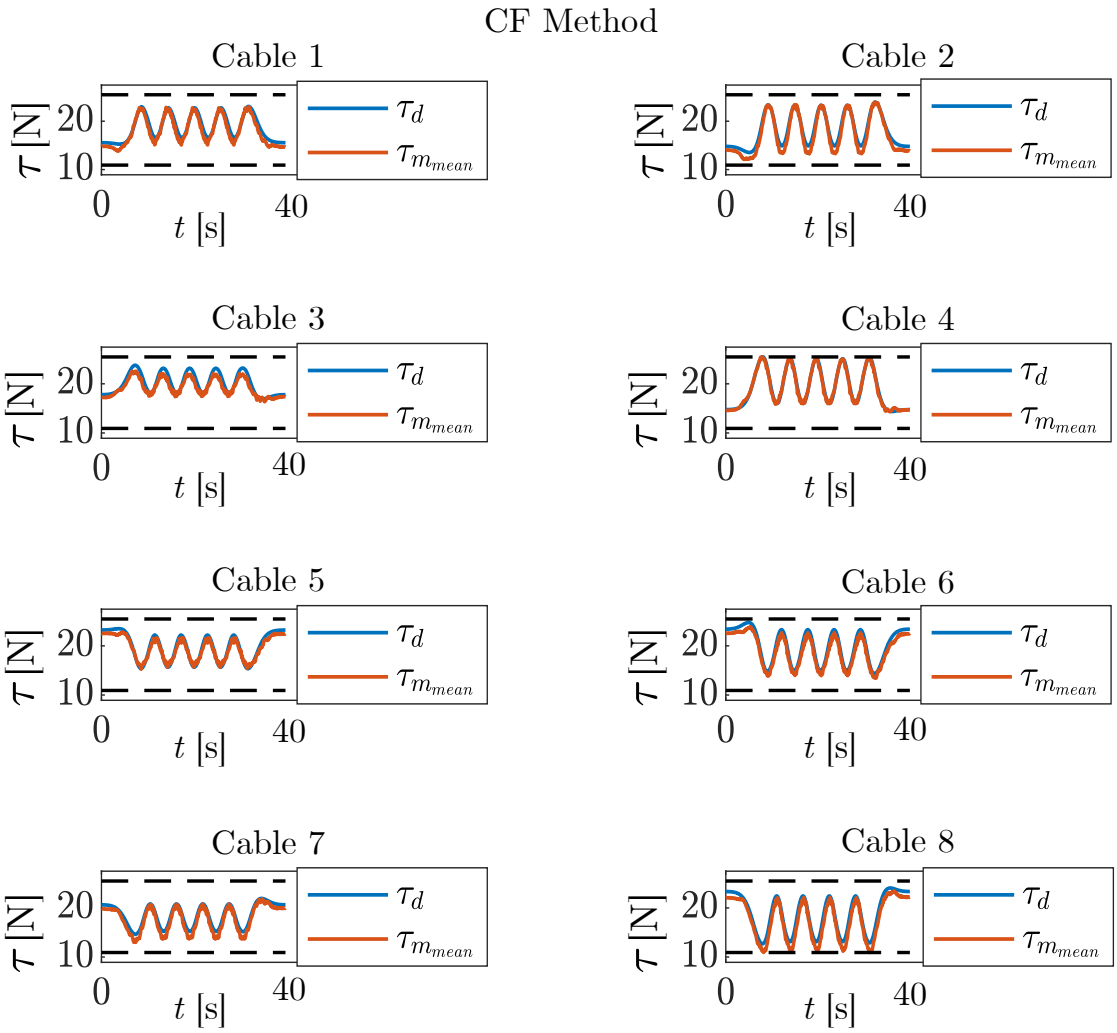

Figure I.2.21: ICF: desired and measured tension for each cable.

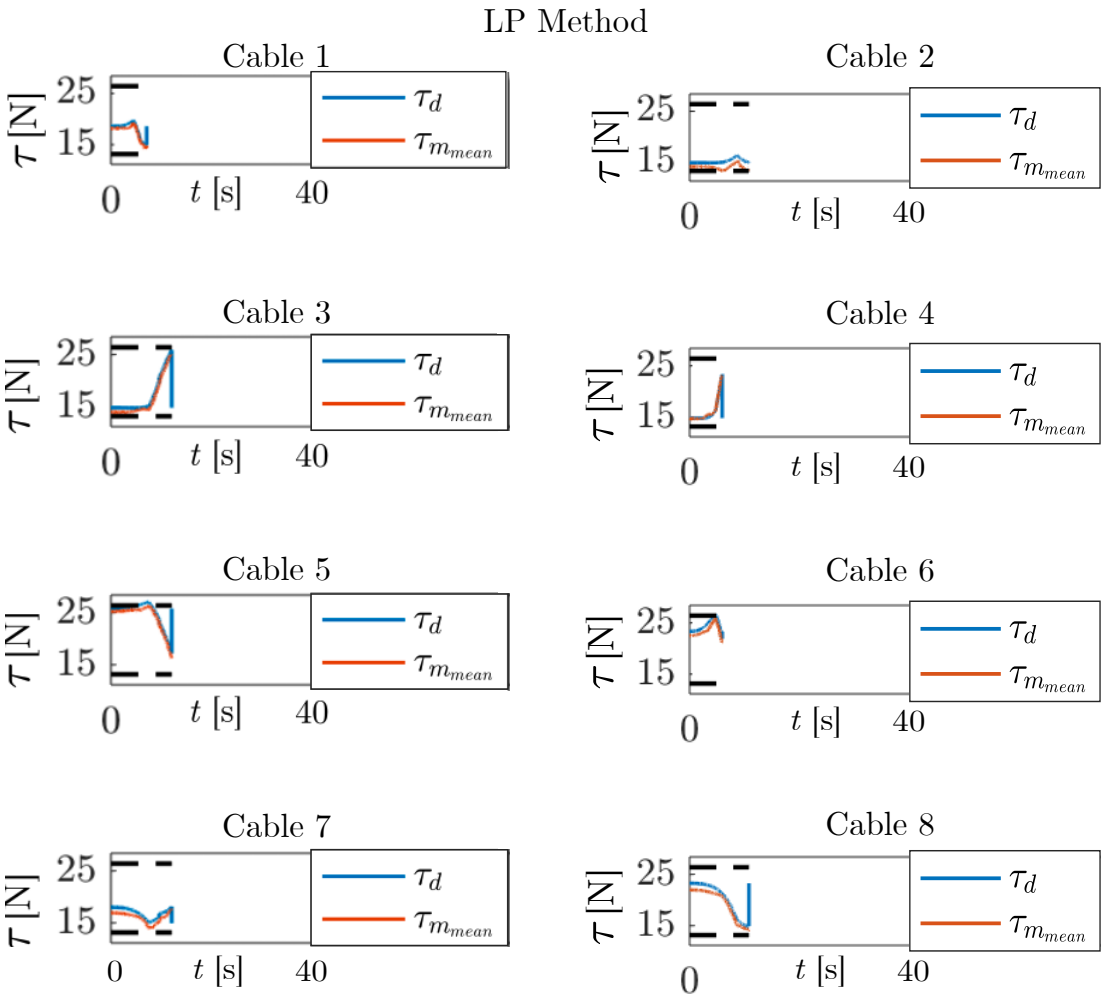

Figure I.2.22: LP: desired and measured tension for each cable.

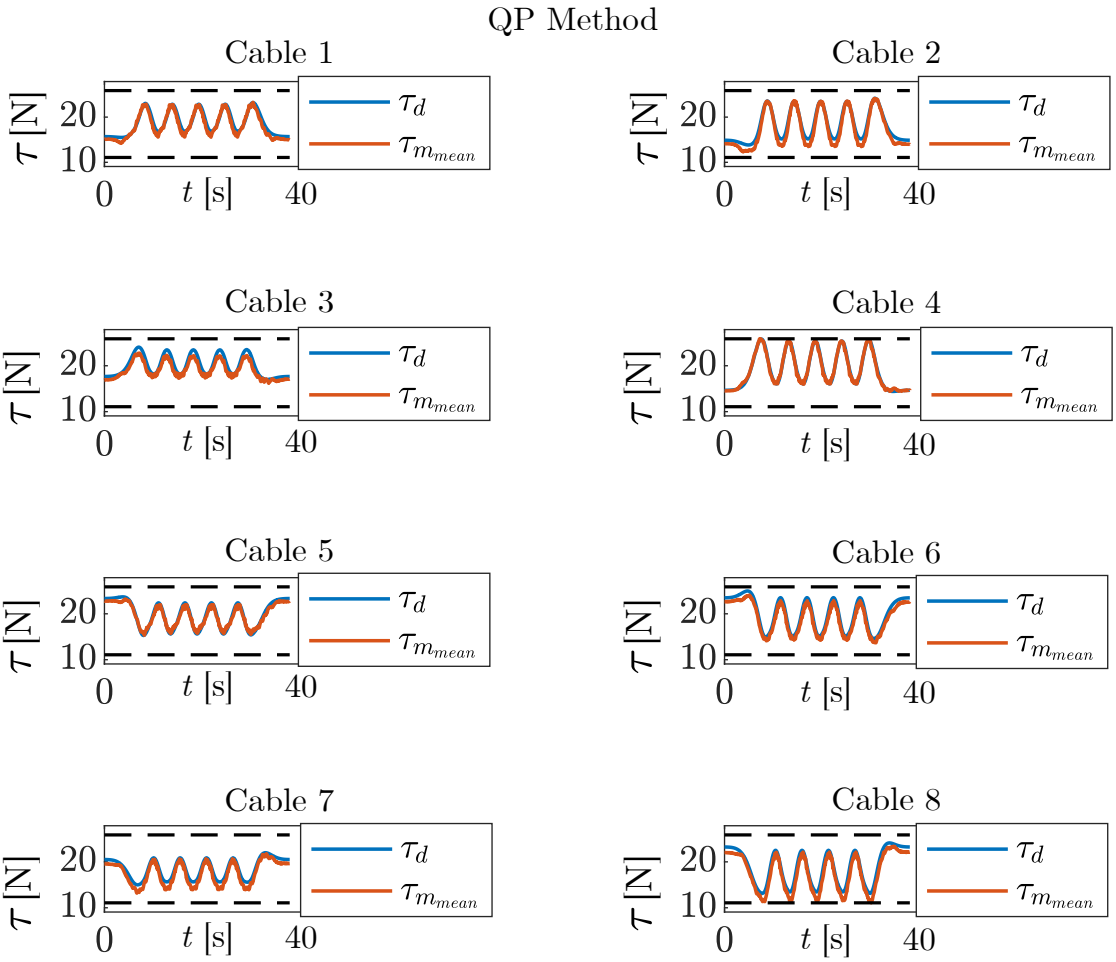

Figure I.2.23: QP: desired and measured tension for each cable.

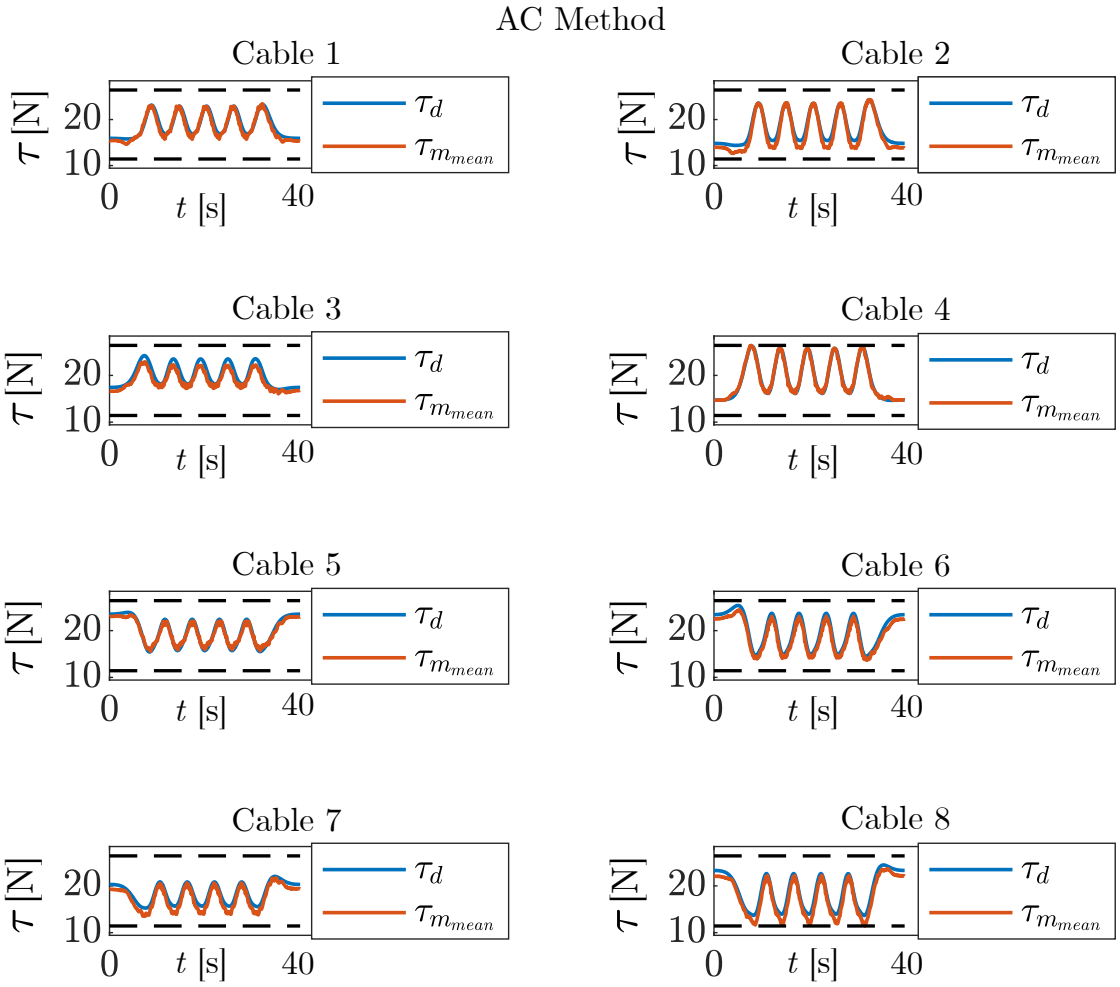

Figure I.2.24: AC: desired and measured tension for each cable.

First, the trend of the tension profiles seem to be almost coincident. One can explain the presence of discrepancies, between measured and desired values, by looking at the model used behind the optimization problem solved to find the desired tensions. In other words, while solving these optimization problem, one neglect several phenomena intervening in practice. Indeed, elasticity and flexibility of the cables, pulley model and friction are just some of them, not taken into account, while solving the tension problem.

All in all, these results seem to be supportive in view of the theoretical reported in Chapter I.2. Another aspect that seems to be relevant and merits a comment regards the recorded behaviour of LP method. Indeed, Fig.I.2.22 shows that the robot stops after a few seconds. This occurrence is mainly due to a safety procedure activated by the control scheme. As a matter of fact, the TDA requires an abrupt tension variation, higher than the one supported by the robot, leading it to an emergency stop. Therefore, it is important to explicitly recognize that, this scenario, is not linked to any discontinuity of the method rather to a quick tension change. Therefore, the presence of discontinuity is still to be investigated and demonstrated from a practical point of view.

Chapter I.3

Sensitivity Analysis and Criteria for Tension Distribution Comparisons

Abstract: *Several tension distribution algorithms have been developed so far. However, only a qualitative comparisons of them was done in the literature. Therefore, the aim of this chapter is twofold. First, the introduction of a performance index measuring the sensitivity, to quantitatively compare the TDAs is made. Secondly, the sensitivity analysis of the TDAs is discussed as a method for enchanting tension-based control. A study case where the sensitivity index is computed is reported. This show the possible use and its meaning.*

I.3.1 Introduction and Motivation

The importance of solving the tension distribution problem has been sufficiently stressed at this point. Indeed, in the previous Chapter, many algorithms were recalled and compared by means of the robust index. More extensively, in the literature, a qualitative comparison was done in [42]. In the same fashion of [42], Table I.3.1, is reported for the methods hereby considered to give an idea of what does it means a qualitative comparison.

Though the robust index has a physical meaning and can be used to compare the TDAs, it does not give any information about *how* to control the robot. Controlling the robot in tension rather than kinematically, as many of the actual controls are made, is one of the main research directions for CDP, see [16], for example. This is *where*, the intention of using sensitivity for both defining a performance index and gaining information for tension control, pops out. In particular, the idea consists of exploiting the sensitivity defined for general optimization problem [56].

Tension Distribution Method	Coverage of WFW	Continuity of the solution	Robust Index	Non-linear constraints	Computational time
Improved Closed Form	low	yes	high	no	fast
Quadratic Programming	high	yes	low	no	medium
Linear Programming	high	no	high	no	fast
Barycentric	high	yes	high	no	fast
Analytic Center	high	yes	medium/high	yes	fast

Table I.3.1: In this table [42], tension distribution algorithms are compared qualitatively.

I.3.2 Sensitivity Analysis of Tension Distribution Algorithms

The basic idea behind the study of sensitivity is, indeed, assessing *how much* the changes in the parameters of an optimization problem affect the optimal solution [56].

To reach this aim, it becomes of primary importance to estimate the variation of the tension vector $\delta\boldsymbol{\tau}$ w.r.t. a variation of the external wrench $\delta\mathbf{w}_e$. Therefore, taking advantage of the Karush–Kuhn–Tucker (KKT) theorem [51], it becomes possible to transform a generic optimization problem into a system of equations of the form

$$f(\boldsymbol{\tau}, \mathbf{W}, \mathbf{w}_e) = \begin{cases} \frac{\partial \mathscr{L}}{\partial \boldsymbol{\tau}} & = 0 \\ \mathbf{h}(\boldsymbol{\tau}) & = \mathbf{0} \\ \mathbf{g}(\boldsymbol{\tau}) & \leq \mathbf{0}, \end{cases} \tag{I.3.1}$$

where $h(\boldsymbol{\tau})$ and $g(\boldsymbol{\tau})$ represent the equality and inequality constraints, respectively while $\mathscr{L}$ is the Lagrangian function, namely

$$\mathscr{L} = \phi(\boldsymbol{\tau}) + \boldsymbol{\mu}^T \mathbf{g}(\boldsymbol{\tau}) + \boldsymbol{\lambda}^T \mathbf{h}(\boldsymbol{\tau}), \tag{I.3.2}$$

with $\phi(\boldsymbol{\tau}) : \mathbb{R}^m \to \mathbb{R}$ objective function or cost function to be minimized (or maximized). It is generally related to the optimization problem considered and can assume different forms, one example is the Eq. (I.2.5). Remaining symbols $\boldsymbol{\mu}$ and $\boldsymbol{\lambda}$ are known as the KKT multipliers.

Now, linearizing Eq.(I.3.1) gives

$$\frac{\partial f}{\partial \boldsymbol{\tau}} \delta\boldsymbol{\tau} + \frac{\partial f}{\partial \mathbf{w}_e} \delta\mathbf{w}_e = \mathbf{0}. \tag{I.3.3}$$

Rearranging this equation, the link between $\delta\boldsymbol{\tau}$ and $\delta\mathbf{w}_e$ is found, in compact form

$$\delta\boldsymbol{\tau} = -\left(\frac{\partial f}{\partial \boldsymbol{\tau}}\right)^{\dagger} \frac{\partial f}{\partial \mathbf{w}_e} \, \delta\mathbf{w}_e, \tag{I.3.4}$$

then, calling

$$\mathbf{S} = \left(\frac{\partial f}{\partial \boldsymbol{\tau}}\right)^{\dagger} \frac{\partial f}{\partial \mathbf{w}_e}, \tag{I.3.5}$$

one has

$$\delta\boldsymbol{\tau} = -\mathbf{S}\,\delta\mathbf{w}_e, \tag{I.3.6}$$

where $\mathbf{S}$ is the sensitivity matrix, formally

$$\mathbf{S} = \begin{pmatrix} \frac{\partial\tau_1}{\partial w_{e,1}} & \cdots & \frac{\partial\tau_1}{\partial w_{e,n}} \\ \vdots & \ddots & \vdots \\ \frac{\partial\tau_m}{\partial w_{e,1}} & \cdots & \frac{\partial\tau_m}{\partial w_{e,n}} \end{pmatrix} \quad i = 1,\ldots,m \quad j = 1,\ldots,n \tag{I.3.7}$$

where the indices i, j identify the components of $\mathbf{S}$ as well as those of the vectors $\boldsymbol{\tau}$ and $\mathbf{w}_e$.

At this point, all the elements necessary for the definition of the performance index have been collected. Consequently, borrowing the idea from [57] and considering $\delta\boldsymbol{\tau}$ as if it were the variable of the joint space while $\delta\mathbf{w}_e$ represents the term in the Cartesian space, respectively, the sensitivity index can be introduced as

$$\sigma = \max_{||\delta\mathbf{w}_e||_2=1} ||\delta\boldsymbol{\tau}||_\infty. \tag{I.3.8}$$

This, in complete analogy with the kinematic indices [57]–[59]. It was proven that optimization problem Eq.(I.3.8) can be directly solved by substituting Eq.(I.3.6) into Eq.(I.3.8)

$$\sigma = \max_{||\delta\mathbf{w}_e||_2=1} ||\mathbf{S}\,\delta\mathbf{w}_e||_\infty = ||\mathbf{S}||_{2,\infty}. \tag{I.3.9}$$

where the matrix norm at RHS is known as *mixed Hölder norm* [60].

Practically, since the columns of the matrix $\mathbf{S}$ identify the variation in the tension of each cable w.r.t. a variation of the wrench in a specific direction, this index estimates the maximum (upper bound) tension variation induced by a change in the external wrench. This can help quantify *how much* can be the variation in the tension along the cables. Observe that measuring cable tension experimentally is a hard task. Therefore, the possibility to gain some information (upper bound on $\delta\boldsymbol{\tau}$) based on knowledge of some disturbances can be useful when measuring cable tension with sensors.

Remark 9. *Taking a point-mass as end-effector only requires taking into account the resultant force acting on the load. Hence no dimensional unit issue arises. In case the load is a rigid body, then two separate indices can be used [58].*

Remark 10. *The linearized Equation* (I.3.6) *pops out to be similar to the closed-form solution* $\delta\boldsymbol{\tau} = -\mathbf{W}^\dagger\,\delta\mathbf{w}_e$. *However, the procedure here developed can be considered a generalization of it in the context of sensitivity. Indeed, taking the derivatives of Eq.*(I.3.1) *appearing in the definition of matrix* $\mathbf{S}$ *Eq.*(I.3.5)*, one can find the explicit form*

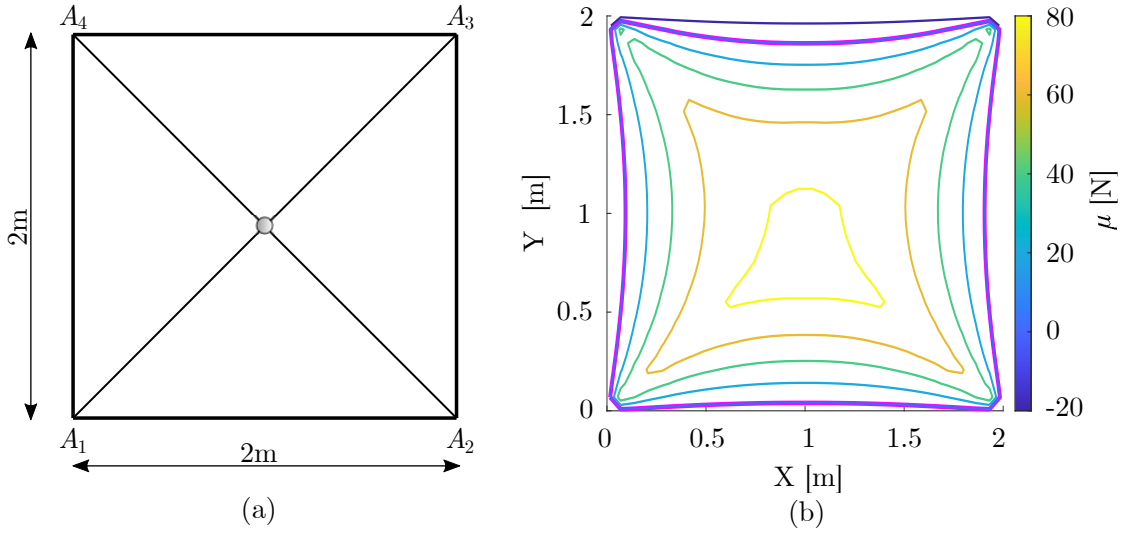

Figure I.3.1: Case study: (a) Planar CDPR with four cables and a point-mass load while (b) shows the WFW of the CDPR. Observe that the WFW is found by using the capacity margin μ [61], the purple curve $\mu = 0$ delimits its boundary.

$$\mathbf{S} = \begin{pmatrix} \nabla^2_{\boldsymbol{\tau}}\phi \\ \mathbf{W} \\ \mathbf{I} \\ -\mathbf{I} \end{pmatrix}^{\dagger} \begin{pmatrix} \mathbf{0} \\ \mathbf{I} \\ \mathbf{0} \\ \mathbf{0} \end{pmatrix}, \tag{I.3.10}$$

where $\nabla^2_{\boldsymbol{\tau}}\phi$ is the second-order gradient[1] of the objective function $\phi(\boldsymbol{\tau})$ w.r.t. the tension vector $\boldsymbol{\tau}$. Hence, from Eq.(I.3.10)*, one can observe that* $\mathbf{S}$ *reduces to* $\mathbf{W}^{\dagger}$ *when no optimization problem is considered, i.e. when $\phi(\boldsymbol{\tau})$ and $g(\boldsymbol{\tau})$ are not considered. Observing this analogy stresses the familiar relationship between the solution provided by the closed-form (pseudo-inverse) and the QP approach. Indeed, the solution with pseudo-inverse leads to minimize the distance from the origin $\boldsymbol{\tau} = \mathbf{0}$. The main difference with QP, then is the absence of tension limits $\underline{\boldsymbol{\tau}}, \overline{\boldsymbol{\tau}}$.*

I.3.3 Numerical Example

In this section, some simulations are performed to compare some of the existing TDAs. First of all, to evaluate the index, the workspace of the robot is discretized and only the points inside the WFW are considered. Subsequently, for every feasible point, the index is computed. The value assumed by the index σ is assigned to the point considered and a map is generated within the workspace. This process is repeated for each TDA reported above.

[1]Observe that computing the derivative of the Lagrangian function w.r.t. $\boldsymbol{\tau}$ resembles in computing the second-order gradient of the objective directly.

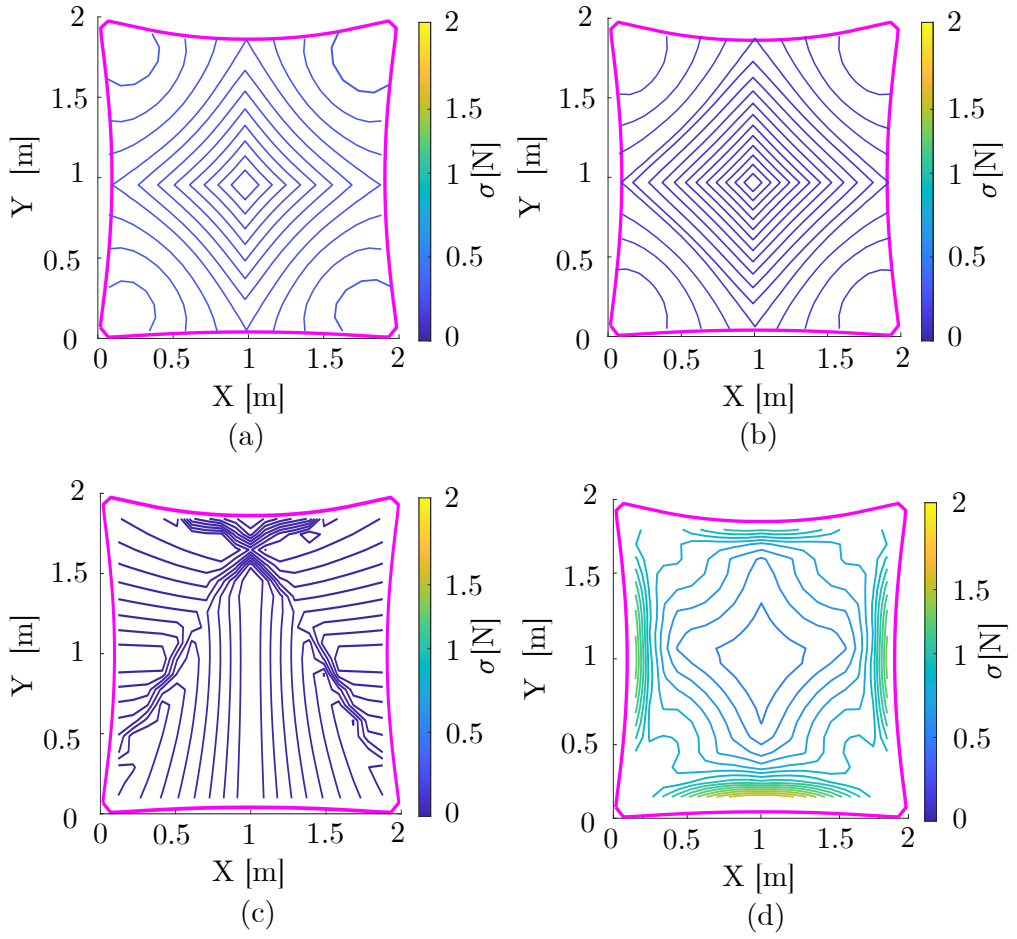

Figure I.3.2: Sensitivity: σ-map within the WFW for the LP method (a), the QP method (b), the 4-norm (c) and the Analytic Centre ones (d).

In the following discussion, a planar CDPR with four cables is considered. The load is a point mass ($DoR = 2$) of mass $m = 1kg$. Cable tension limits are set to be $\underline{\boldsymbol{\tau}} = \mathbf{10}N$ and $\overline{\boldsymbol{\tau}} = \mathbf{100}N$, respectively. The architecture of the robot and its WFW are depicted in Figure I.3.1 for sake of clarity. Results of the simulations and the characterization of the WFW by means of σ are depicted in Fig.I.3.2.

First, from Fig.I.3.2 one can understand that the AC method results to be more sensitive than all the other methods. This means that, around each point of the WFW, the LP, QP and 4-norm generate a $||\delta\boldsymbol{\tau}||$ that is lower than the one of the AC for a given $||\delta\mathbf{w}_e||_2 = 1$.

To fully grasp why this happens, one should focus on both *how the TDAs work* and *what happens inside the sensitivity matrix*, i.e., how the index works. With this in mind, let's pair the methods by affinity in order to shed light on the results and discuss the above-mentioned aspects. Hence, consider the QP and 4-norm together and LP and AC

consequently[2].

Now, starting from QP and 4-norm and analysing their results, one sees that some of the cable tensions assume the lowest values possible. In particular, for this case study, two tensions τ_1, τ_2 (attached at the bottom of the robot) take the lowest bound $\underline{\boldsymbol{\tau}}$ as they do not bear any wrench. Therefore, only the remaining components τ_3, τ_4 variate while the load moves inside the workspace. However, τ_3, τ_4 vary as less as possible (because of how the problem is defined), they just have to maintain the equilibrium of the load. This explains why the sensitivity σ assumes similar values ($\sigma < 0.38$) inside the WFW. However, looking at how QP and 4-norm approaches work, is not enough to understand why maps Figs.I.3.2 (b)-(c) are different. Indeed, this is due to the values assumed by $\nabla^2_{\boldsymbol{\tau}}\phi$ inside matrix $\mathbf{S}$. Computing the second-order gradient for both

$$\nabla^2_{\boldsymbol{\tau}}\phi_{QP} = 2\mathbb{I}_m \quad \nabla^2_{\boldsymbol{\tau}}\phi_{4-norm} = 12\,\mathrm{diag}(\tau_i)^2, \tag{I.3.11}$$

shows that $\nabla^2_{\boldsymbol{\tau}}\phi_{QP}$ is constant, i.e., it does not depend on the solution $\boldsymbol{\tau}$ while $\nabla^2_{\boldsymbol{\tau}}\phi_{4-norm}$ does. As a consequence, the σ-map is symmetric for the QP and it does not change if, for example, the external wrench changes.

Analogously, the same reasoning can be done for LP and AC. However, this time the values of σ are significantly different: the sensitivity of AC is far more higher than LP (QP and 4-norm as well). The reason why lies again in the second-order gradient (or matrix $\mathbf{S}$). Indeed, in both cases the solution $\boldsymbol{\tau}$ is robust but

$$\nabla^2_{\boldsymbol{\tau}}\phi_{LP} = 0, \tag{I.3.12}$$

results to be null while

$$\nabla^2_{\boldsymbol{\tau}}\phi_{AC} = \mathrm{diag}\left(\frac{1}{(\overline{\boldsymbol{\tau}} - \tau_i)^2} - \frac{1}{(\tau_i - \underline{\boldsymbol{\tau}})^2}\right), \tag{I.3.13}$$

depends on $\boldsymbol{\tau}$. Hence, because of the shape of $\nabla^2_{\boldsymbol{\tau}}\phi_{AC}$, its values take weight inside $\mathbf{S}$ generating the highest σ among LP, QP and 4-norm.

Other useful data can be acquired by computing the (numerical) gradient of σ namely, $\nabla\sigma$ reported in Fig.I.3.3. This information can be relevant when the task requires precision: no vibration or oscillation of the platform. In other words, it can be useful when a small variation of $\nabla\sigma$ is required. Indeed, in practice, $\nabla\sigma$ quantifies the possible tension variation between two points of the workspace. Not surprisingly, the AC method has smaller $\nabla\sigma$ than the others (smallest and homogeneous arrows inside the WFW). In fact, the AC homogeneity, in terms of $\nabla\sigma$, is probably linked to the property of smoothness of the tension profiles. Recall that smoothness of tension profiles means that there is a small variation in the cable tensions from one point of the workspace to another.

Collecting the information acquired from this case study, one can conclude σ allows for estimating an upper bound of $\delta\boldsymbol{\tau}$, assessing robustness as well as observing the

[2]The affinity can be understood by looking at the level-set reported in Figure I.2.1.

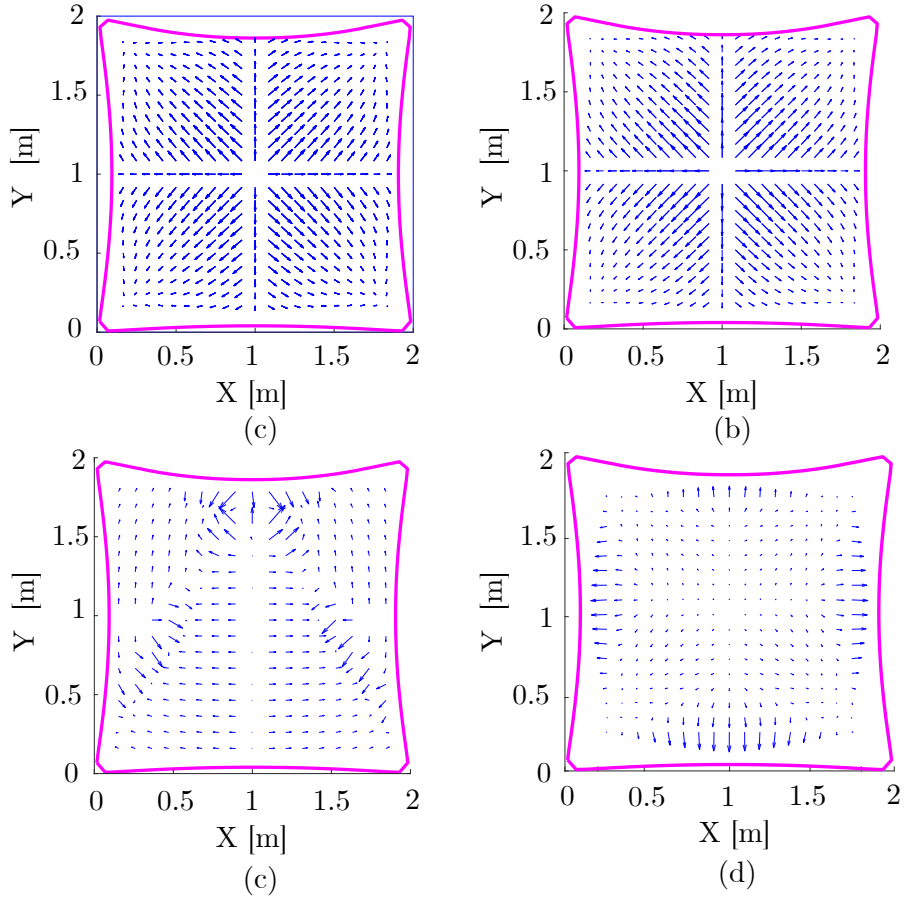

Figure I.3.3: Gradient: $\nabla\sigma$-map within the WFW for the LP method (a) the QP method (b) the 4-norm (c) and the Analytic Centre ones (d). Observe that the size of the arrows identifies the magnitude of the gradient.

continuity of the solution looking at $\nabla\sigma$. Hence, many of the peculiarities discussed in the previous Chapter, about the TDAs, can be somehow visualized with this index.

Although the definition of σ is analogous to the well-established performance index for kinematics, some information is lost due to the linearization process.

Remark 11. *The sensitivity defined through the linearization (local sensitivity) Eq.*(I.3.6) *returns different results from the one mentioned in Chapter I.2, Fig. I.2.1. Indeed, in this latter, both* $\mathbf{W}$ *and* $\mathbf{w}_e$ *were supposed to variate resembling, then, into a global sensitivity. Therefore, this should explicitly point out that the differences between global and local sensitivity are due to the linearization.*

Indeed, for example, it becomes impossible to assess the sensitivity of the single cables since it is absorbed by the use of the norm $||\delta\boldsymbol{\tau}||$. Moreover, because of the discontinuity of LP method, the tension variation σ is expected to be infinite however, due to the linearization this information is lost.

Hence, one can ask if these results and then even the local sensitivity can indeed be used in practise for tension control, for example. To answer this question, experimental validation have to be performed. In this context, the main assumption to be tested regards the variation of the platform pose when the external wrench acts on it. In other words, if the recorded pose variation is sufficiently small then one can consider the local linearization as valid. Probably, when tests will be undertaken, the stiffness model of the robot have to be included.

Chapter I.4

Sliding-Mode Adaptive PID Control

Abstract: *Facing external disturbances and system' uncertainties is challenging when a tracking task has to be satisfied. Therefore, a self-tuning gain techniques for a Proportional-Integral-Derivative (PID) control is introduced. To automatically tune the PID gains, a sliding mode condition is exploited. The stability of this approach, considering bounded disturbances/uncertainties, is guaranteed by introducing a supervisory control designed through the Lyapunov method. The proposed solution and its performances were tested through simulations and compared with typical techniques as PD and PID controls.*

I.4.1 Introduction and Motivation

Despite the existence of many control techniques, the motivation behind the introduction of adaptive control naturally stems from wanting CDPs safer and more reliable in several possible scenarios (e.g. wind or cable breakage) while performing a task. In other words, research is directed towards making these systems autonomous. In particular, the handling of highly non-linear phenomena is delegated to an adaptive control whose gains are adjusted through the use of a sliding-mode condition. The combination of a PID with a sliding mode control has previously been studied for handling chaotic phenomena [62].

In this regard, this chapter is firstly aimed at the introduction and design of this technique and, subsequently, its application to case studies such as aerial transportation or scenarios where a cable breaks are investigated. The literature of the respective cases will be briefly recalled in order to better contextualise the contribution.

I.4.2 Sliding-Mode Adaptive PID

The overall objective of the control is to ensure that the load follows the desired trajectory while, for a general CDP, pursuing the desired system configuration (cable direc-

tions) under the action of external disturbances.

I.4.2.1 Design of the Sliding Mode-Adaptive PID control

Let us consider the description of a dynamical system in general form [62]

$$\dot{\tilde{\mathbf{x}}} = f(\tilde{\mathbf{x}}) + \Delta f(\tilde{\mathbf{x}}) + g(\tilde{\mathbf{x}})\mathbf{u} + \boldsymbol{\delta}, \tag{I.4.1}$$

where $\tilde{\mathbf{x}}, \dot{\tilde{\mathbf{x}}} \in \mathbb{R}^n$ form the system' state $\mathbf{x} = (\tilde{\mathbf{x}}, \dot{\tilde{\mathbf{x}}})^T \in \mathbb{R}^{2n}$, $M_{\mathbf{x}}$, $f(\tilde{\mathbf{x}})$ and $\Delta f(\tilde{\mathbf{x}})$ represent the system model and the its uncertainties, $g(\tilde{\mathbf{x}})\mathbf{u}$ is the *affine* terms with $\mathbf{u}$ as control input and, the last terms $\boldsymbol{\delta}$ identifies the external disturbances. Observe that both disturbances and system uncertainties are assumed to be bounded above $\boldsymbol{\delta}(\cdot) \leq \boldsymbol{\delta}^u(\cdot)$, $f(\cdot) \leq f^u(\cdot)$ and $\Delta f(\cdot) \leq \Delta f^u(\cdot)$. A common and direct approach that can be used to define a control input consists in using the so-called *feedback linearization* techniques namely

$$\mathbf{u}^* = -g(\tilde{\mathbf{x}})^{-1}\big(f(\tilde{\mathbf{x}}) + \Delta f(\tilde{\mathbf{x}}) + \boldsymbol{\delta} + \ddot{\tilde{\mathbf{x}}}^{des} + \mathbf{k}_0\,\tilde{\mathbf{e}} + \mathbf{k}_1\dot{\tilde{\mathbf{e}}}\big), \tag{I.4.2}$$

where $\mathbf{e} = (\tilde{\mathbf{e}}, \dot{\tilde{\mathbf{e}}})^T \in \mathbb{R}^{2n}$ and $\dot{\mathbf{e}} = (\dot{\tilde{\mathbf{e}}}, \ddot{\tilde{\mathbf{e}}})^T \in \mathbb{R}^{2n}$ are the state error vectors which are the time derivatives of $\mathbf{e} = \mathbf{y} - \mathbf{x}$ with $\mathbf{y} = \left(\tilde{\mathbf{x}}^{des}, \dot{\tilde{\mathbf{x}}}^{des}\right)^T$ representing the desired state vector. Despite its simplicity, this control action is not robust technique because of the linerization. Hence, this aspect constitutes another way to stress the necessity of introducing a robust technique.

Remark 12. *Note that* $\mathbf{u}^*$ *depends on both* $f(\tilde{\mathbf{x}})$ *and* $\Delta f(\tilde{\mathbf{x}})$*. This will be useful in what follows to understand the condition of insensitivity of the proposed methodology to them.*

I.4.2.2 Control Architecture

Generally, when dealing with adaptive control, the control input is split in two terms [63], [64]

$$\mathbf{u} = \mathbf{u}_{PID} + \mathbf{u}_s, \tag{I.4.3}$$

where $\mathbf{u}_{PID}$ covers the role of the so-called equivalent control $\mathbf{u}_{eq}$ whereas $\mathbf{u}_s$ is the supervisory control. This latter is an additional control that keeps the system state within some defined boundaries and guarantees the stability of the dynamical system while the $\mathbf{u}_{PID}$ exploits a gradient-based adaptation law for updating its gains providing robustness of the control. The design of both $\mathbf{u}_s$ and $\mathbf{u}_{PID}$ that is intended to be used here has been defined in [62] and therefore only the key concepts are reported in the followings.

I.4.2.3 Design of the Supervisory Control

The primary role of the supervisory control $\mathbf{u}_s$ is to keep the system state inside a designed constraint set

$$\mathfrak{C} = \{\mathbf{x} \in \mathbb{R}^{2n} \,|\, ||\mathbf{x}|| \leq M_{\mathbf{x}}\}, \tag{I.4.4}$$

where $M_{\mathbf{x}}$ is a pre-specified parameter usually chosen such that $M_{\mathbf{x}} \geq ||\mathbf{y}||_\infty$. Its design relies on the errors dynamics and the Lyapunov criterion to guarantee the stability of the system. Hence, to asymptotically attain the zero-error condition, the following Lyapunov function candidate is considered

$$V_e = \frac{1}{2}\mathbf{e}^T\mathbf{\Phi}\mathbf{e}. \tag{I.4.5}$$

Observe that V_e represents an *output error energy* measuring the distance from a representative point in the state space to the desired output. Therefore, a plausible strategy to reach it is to exercise a control action that strictly decreases V_e. Before continuing this analysis, it is better to recall the role of the matrix $\mathbf{\Phi}$. Generally, it is defined as a positive definite and symmetric matrix that springs out as the solution of the Lyapunov equation [65]

$$\mathbf{A}^T\mathbf{\Phi} + \mathbf{\Phi}\mathbf{A} = -\mathbf{Q}, \tag{I.4.6}$$

where matrix $\mathbf{Q} \in \mathbb{R}^{2n\times 2n}$ is a given, positive definite symmetric matrix whereas matrix $\mathbf{A} \in \mathbb{R}^{2n\times 2n}$ pops out by rewriting the error dynamic as

$$\dot{\mathbf{e}} = \mathbf{A}\mathbf{e} + \mathbf{B}(\mathbf{u}^* - \mathbf{u}_{PID} - \mathbf{u}_s) \tag{I.4.7}$$

where the structure of both $\mathbf{A}$ and $\mathbf{B}$ is

$$\mathbf{A} = \begin{pmatrix} \mathbf{0} & \mathbf{I} \\ -\mathbf{k}_0 & -\mathbf{k}_1 \end{pmatrix} \quad \text{and} \quad \mathbf{B} = \begin{pmatrix} \mathbf{0} \\ g(\mathbf{x}, \dot{\mathbf{x}}) \end{pmatrix}, \tag{I.4.8}$$

note that $\mathbf{k}_0 \in \mathbb{R}^{n\times n}$ and $\mathbf{k}_1 \in \mathbb{R}^{n\times n}$ are diagonal matrices whose coefficients are chosen such that the roots of the characteristic polynomial, associated with the differential equation $\ddot{\tilde{\mathbf{e}}} + \mathbf{k}_1\dot{\tilde{\mathbf{e}}} + \mathbf{k}_0\tilde{\mathbf{e}} = \mathbf{0}$, belong to the left-half complex plane. This aspect is fundamental to guarantee the stability of the system and the convergence to zero of the error as time goes to infinity.

Hence, the design of $\mathbf{u}_s$ must comply with the decrease of V_e, which means that it must meet

$$\dot{V}_e < 0. \tag{I.4.9}$$

The derivative of the Lyapunov function can be computed as follows

$$\begin{aligned} \dot{V}_e &= \frac{1}{2}(\dot{\mathbf{e}}^T\mathbf{\Phi}\mathbf{e} + \mathbf{e}^T\mathbf{\Phi}\dot{\mathbf{e}}) \\ &= \frac{1}{2}(\mathbf{e}^T(\mathbf{A}^T\mathbf{\Phi} + \mathbf{\Phi}\mathbf{A})\mathbf{e} + 2\mathbf{e}^T\mathbf{\Phi}\mathbf{B}(\mathbf{u}^* - \mathbf{u}_{PID} - \mathbf{u}_s)) \\ &= -\frac{1}{2}\mathbf{e}^T\mathbf{Q}\mathbf{e} + \mathbf{e}^T\mathbf{\Phi}\mathbf{B}(\mathbf{u}^* - \mathbf{u}_{PID} - \mathbf{u}_s) \\ &\leq -\frac{1}{2}\mathbf{e}^T\mathbf{Q}\mathbf{e} + |\mathbf{e}^T\mathbf{\Phi}\mathbf{B}|(|\mathbf{u}^*| + |\mathbf{u}_{PID}|) - \mathbf{e}^T\mathbf{\Phi}\mathbf{B}\mathbf{u}_s. \end{aligned} \tag{I.4.10}$$

Therefore, to satisfy, the supervisory controller can be chosen as

$$\mathbf{u}_s = \text{sgn}(\mathbf{e}^T\mathbf{\Phi}\mathbf{B})(|\mathbf{u}^*| + |\mathbf{u}_{PID}|). \tag{I.4.11}$$

However, with this design of $\mathbf{u}_s$, it constantly intervenes in the control process. Further, the presence of *sgn* function leads to chattering. Therefore, to adhere with its supervisory definition and to reduce the chattering the set of constraints $\mathfrak{C}$ is used. In particular, the *Indicator function* I_f is introduced in the $\mathbf{u}_s$ design as follows

$$\tilde{\mathbf{u}}_s = I_f\,\mathbf{u}_s \quad \text{where} \quad I_f = \begin{cases} 1, & V_e > V_M, \\ 0, & V_e \leq V_M, \end{cases} \tag{I.4.12}$$

and

$$V_M = \frac{1}{2}\lambda_{min}(\mathbf{\Phi})(M_{\mathbf{x}} - ||\mathbf{y}||_\infty)^2, \tag{I.4.13}$$

where $\lambda_{min}(\mathbf{\Phi})$ is the minimum eigenvalue of the Lyapunov matrix $\mathbf{\Phi}$ [62], [65]. The introduction of the Indicator function completes its design. Indeed, thanks to this modification, $\tilde{\mathbf{u}}_s$ would intervene in the control process only when the system's state diverges from the desired state over the limits imposed by $M_{\mathbf{x}}$.

Remark 13. *Is worth observing that the value of* $\mathbf{u}^*$ *inside Eq.*(I.4.11) *is bounded above. Indeed, rearranging Equation* (I.4.2) *it becomes possible finding an estimate for* $\mathbf{u}^*$ *of the type* $\mathbf{u}^{*,u} = g^{-1}\big(\boldsymbol{\delta}^u + f^u + \Delta f^u + |\ddot{\tilde{\mathbf{x}}}^{des}| + |\mathbf{k}_0\tilde{\mathbf{e}}| + |\mathbf{k}_1\dot{\tilde{\mathbf{e}}}|\big)$.

I.4.2.4 Design of the Adaptive PID

The main control activity is then delegated to an Adaptive PID (APID) which adjusts its control action by automatically tuning its gains. The adaptation laws are derived with the aim to reach the so-called sliding mode $\mathcal{S} = 0$ (i.e. insensitivity to external disturbances) where $\mathcal{S}$ is the so-called sliding surface defined as [64]

$$\mathcal{S} = \dot{\tilde{\mathbf{x}}} - \mathbf{x}_r, \tag{I.4.14}$$

where the reference signal $\mathbf{x}_r$ is

$$\mathbf{x}_r = \dot{\tilde{\mathbf{x}}}^{des} + \mathbf{k}_1\tilde{\mathbf{e}} + \mathbf{k}_0\int \tilde{\mathbf{e}}\,dt. \tag{I.4.15}$$

Remark 14. *When the sliding mode occurs one has*

$$\mathcal{S} = 0 \quad \textit{and} \quad \dot{\tilde{\mathbf{x}}} = \mathbf{x}_r, \tag{I.4.16}$$

this, substituted in the derivative of $\mathbf{x}_r$, $\dot{\mathbf{x}}_r = \ddot{\tilde{\mathbf{x}}}^{des} + \mathbf{k}_1\dot{\tilde{\mathbf{e}}} + \mathbf{k}_0\tilde{\mathbf{e}}$, *returns* $\ddot{\tilde{\mathbf{e}}} + \mathbf{k}_1\dot{\tilde{\mathbf{e}}} + \mathbf{k}_0\tilde{\mathbf{e}} = \mathbf{0}$ *thus revealing that, when the system is in the sliding mode, it becomes insensitive to external disturbances. On the other hand, when* $\mathcal{S} \neq \mathbf{0}$, $\ddot{\tilde{\mathbf{e}}} + \mathbf{k}_1\dot{\tilde{\mathbf{e}}} + \mathbf{k}_0\tilde{\mathbf{e}} = g(\mathbf{x}, \dot{\mathbf{x}})(\mathbf{u}^* - \mathbf{u}_{PID} - \mathbf{u}_s)$ *and therefore the system is not fully insensitive to external disturbances since they appears inside* $\mathbf{u}^*$.

To guarantee approaching the sliding mode the Lyapunov function approach is exploited and the Lyapunov function candidate is then chosen as

$$V = \frac{1}{2}\mathcal{S}^2. \tag{I.4.17}$$

Hence requiring that $\mathcal{S}(t) \to \mathbf{0}$ for $t \to \infty$ coincide with reducing V. Consequently, the gradient method is applied to choose the gains which take directions of maximum slope over V. Now, a common expression for a PID controller that can compensate for the gravity acceleration is

$$\mathbf{u}_{PID} = \mathbf{K}_P\tilde{\mathbf{e}} + \mathbf{K}_I \int \tilde{\mathbf{e}}\, dt + \mathbf{K}_D\dot{\tilde{\mathbf{e}}} \; + g\mathbf{e}_3, \tag{I.4.18}$$

using the gradient method and the chain rule, it is possible to obtain the adaptation laws for the control gain matrices $\mathbf{K}_P$, $\mathbf{K}_I$ and $\mathbf{K}_D$

$$\dot{\mathbf{K}}_{P,ii} = -\gamma\frac{\partial\mathcal{S}\dot{\mathcal{S}}}{\partial\mathbf{K}_P} = -\gamma\frac{\partial\mathcal{S}\dot{\mathcal{S}}}{\partial\mathbf{u}_{PID}}\frac{\partial\mathbf{u}_{PID}}{\partial\mathbf{K}_P} = -\gamma\mathcal{S}\tilde{\mathbf{e}}\ , \tag{I.4.19a}$$

$$\dot{\mathbf{K}}_{I,ii} = -\gamma\frac{\partial\mathcal{S}\dot{\mathcal{S}}}{\partial\mathbf{K}_I} = -\gamma\frac{\partial\mathcal{S}\dot{\mathcal{S}}}{\partial\mathbf{u}_{PID}}\frac{\partial\mathbf{u}_{PID}}{\partial\mathbf{K}_I} = -\gamma\mathcal{S}\int \tilde{\mathbf{e}}\, dt, \tag{I.4.19b}$$

$$\dot{\mathbf{K}}_{D,ii} = -\gamma\frac{\partial\mathcal{S}\dot{\mathcal{S}}}{\partial\mathbf{K}_D} = -\gamma\frac{\partial\mathcal{S}\dot{\mathcal{S}}}{\partial\mathbf{u}_{PID}}\frac{\partial\mathbf{u}_{PID}}{\partial\mathbf{K}_D} = -\gamma\mathcal{S}\dot{\tilde{\mathbf{e}}}\ , \tag{I.4.19c}$$

where minus is placed opposite to the energy flow V and $\gamma \in \mathbb{R}^+$ is called learning rate[1].

To conclude, the behaviour of the controller can be resumed as follows: if $\mathbf{u}_s = \mathbf{0}$, the PID gains adapt themselves to decrease V to zero (i.e. reach the sliding mode) whereas if $\mathbf{u}_s \neq \mathbf{0}$, the PID gains are not able to decrease V and then also V_e under V_M.

I.4.3 Aerial Transportation in Presence of Wind

Nowadays quadrotors are increasingly attracting attention from researchers due to their agility and potential ability to accomplish tasks autonomously. These peculiarities make them suitable for a wide range of applications such as filming, grasping, and collaborative transportation [24]. The deployment of a team of quadcopters enables them to overcome the payload limits that affect them as individuals. However, the use of multiple quadrotors to steer a load leads to an increase in complexities in terms of control. Within this context, among the control techniques developed so far, both geometric control [10] and flatness [6] theories recorded quite large success in the research community. Indeed, in [14], a geometric control was designed to command a team of agents transporting a point-mass load with rigid links. Furthermore, in [9], the systems (i.e. cables-quadrotors-platform) were proven to be flat. Subsequently, these works gave rise to several contributions where flatness and/or geometric control were used to perform aerial transportation tasks with a rigid platform [15], [67] and also with flexible cables [68], [69]. Recently, in [70], the geometric control [15] was implemented in a real hardware that exploited the abilities of onboard cameras to estimate the system's state and accomplish tracking tasks. As a result, this work allowed disengaging flights

[1]To avoid cumbersome notation the subscripts ii (emphasizing the diagonal structure of the gain matrices) has been inserted only to the left hand side of the equation intending the derivative operation to be carried out component-wise. As typical in the literature [66].

from Motion Capture System (MOCAP). Indeed, one of the main objectives among researchers is to empower aerial systems to be as autonomous as possible in order to let them navigate in outdoor environments autonomously. Hence, a preliminary study investigating how to cope with external disturbances by means of varying the system stiffness was conduct in [54]. With this in mind, this section tackles the issues arising from the presence of wind during aerial transportation tasks. By nature, wind includes turbulence and gusting [71]. Consequently, the wind is a stochastic and chaotic phenomenon. Thus, by analogy, the control of chaotic systems [62], [72] was inspirational. In particular, a Sliding-Mode Adaptive PID (SM-APID) control that confers to a system with massless rigid links, quadrotors and a load (can be a point-mass or a rigid-body), the ability to track a given trajectory under the effect of wind is introduced. The Dryden wind model [73] was hereby considered to test the SM-APID ability.

Therefore, in what follows, the dynamical equations of the system see the introduction of aerodynamic forces in the dynamic model of aerial systems. Secondly, the above control, the SM-APID, is adapted to the considered case study. Moreover, numerical simulations demonstrate the validity and robustness of the proposed approach with respect to the existing control methods.

I.4.3.1 Point-Mass Load Case Study

In section, the tracking problem is addressed by considering the system as composed of a team of n quadrotors and n massless rigid links that collaborate to carry the point-mass load along the desired trajectory as illustrated in Figure I.4.1. The equations of motion were obtained by using the energetic method [8], [14], [15], [74]. Throughout all this and the following section the used symbols were summarized in the Nomenclature Section.

Since each quadrotors lies on the surface of a sphere of radius l_i i.e. length of the i^{th} link, the configuration manifold associated with the mentioned system is $\mathbb{R}^3 \times (\mathbb{S}^2 \times SO(3))^n$ where $\mathbb{S}^2 = \{\mathbf{q} \in \mathbb{R}^3 | \, ||\mathbf{q}|| = 1\}$ represents the 2-sphere set. Recalling that the action integral for the non conservative forces is

$$\mathfrak{a} = \int_{t_0}^{t_f} (\mathcal{T} - \mathcal{U} + \mathcal{W}_f + \mathcal{W}_m)\, dt, \tag{I.4.20}$$

where $\mathcal{T}$ is the kinetic energy, $\mathcal{U}$ is the potential energy and $\mathcal{W}_f$ and $\mathcal{W}_m$ represent the works of external forces and moment, respectively. Now, Hamilton's principle of least action states that the path a conservative system takes from configurations $\mathbf{\Psi}(t_0)$ to $\mathbf{\Psi}(t_f)$, where $\mathbf{\Psi}$ is the set of generalized coordinates belonging to the configuration manifold, is the one that makes the action stationary. In mathematical terms

$$\delta\mathfrak{a} = \int_{t_0}^{t_f} (\delta\mathcal{T} - \delta\mathcal{U} + \delta\mathcal{W}_f + \delta\mathcal{W}_m)\, dt = 0, \tag{I.4.21}$$

where δ expresses the variation in the integrated quantities. Hence, integrating all these

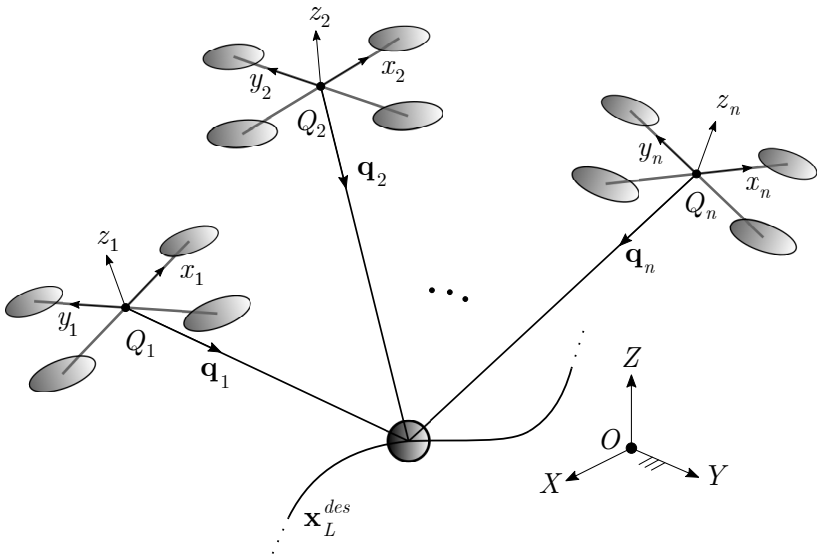

Figure I.4.1: Aerial System: general architecture of the aerial system considered.

terms by parts, see AppendixA, returns the equations of motion

$$\begin{cases} \dfrac{d}{dt}\mathbf{x}_L = \dot{\mathbf{x}}_L, & \text{(I.4.22)} \\ (\sum_{i=1}^{n} m_i \mathbf{q}_i \mathbf{q}_i^T + m_L \mathbf{I})(\ddot{\mathbf{x}}_L + g\mathbf{e}_3) = \sum_{i=1}^{n} \left(\mathbf{v}_i^{\parallel} - m_i l_i ||\boldsymbol{\omega}_i||^2 \mathbf{q}_i + (\mathbf{q}_i \cdot \mathbf{f}_{i,w})\mathbf{q}_i\right) + \mathbf{f}_{L,w}, & \text{(I.4.23)} \\ \dot{\mathbf{q}}_i = \boldsymbol{\omega}_i \times \mathbf{q}_i, & \text{(I.4.24)} \\ \dot{\boldsymbol{\omega}}_i = \dfrac{1}{l_i}\hat{\mathbf{q}}_i(\ddot{\mathbf{x}}_L + g\mathbf{e}_3) - \dfrac{1}{m_i l_i}\hat{\mathbf{q}}_i \mathbf{v}_i^{\perp} - \dfrac{1}{m_i l_i}\hat{\mathbf{q}}_i \mathbf{f}_{i,w}, & \text{(I.4.25)} \\ \dot{\mathbf{R}}_i = \mathbf{R}_i \hat{\boldsymbol{\Omega}}_i, & \text{(I.4.26)} \\ \mathbf{m}_i = \mathbf{J}_i \dot{\boldsymbol{\Omega}} + \boldsymbol{\Omega}_i \times \mathbf{J}_i \boldsymbol{\Omega}_i, & \text{(I.4.27)} \end{cases}$$

where $\mathbf{f}_{i,w}$ and $\mathbf{f}_{L,w}$ are the aerodynamic forces acting on the quadrotors and the load, respectively, the vector $\mathbf{v}_i$ represents the control force of the i^{th} drone such that $\mathbf{v}_i = f_i \mathbf{R}_i \mathbf{e}_3$ whereas the vectors $\mathbf{v}_i^{\parallel}$ and $\mathbf{v}_i^{\perp}$ denote the projection of $\mathbf{v}_i$ along and normal to $\mathbf{q}_i$, respectively

$$\mathbf{v}_i^{\parallel} = (\mathbf{I} + \hat{\mathbf{q}}_i^2)\mathbf{v}_i = (\mathbf{q}_i \cdot \mathbf{v}_i)\mathbf{q}_i = \mathbf{q}_i \mathbf{q}_i^T \mathbf{v}_i, \tag{I.4.28a}$$

$$\mathbf{v}_i^{\perp} = -\hat{\mathbf{q}}_i^2 \mathbf{v}_i = -\mathbf{q}_i \times (\mathbf{q}_i \times \mathbf{v}_i) = (\mathbf{I} - \mathbf{q}_i \hat{\mathbf{q}}_i^T)\mathbf{v}_i. \tag{I.4.28b}$$

The symbol $\hat{\cdot}$ denotes the *hat map*:$\hat{\cdot} : \mathbb{R}^3 \to \mathfrak{so}(3)$. The relationship between Eqs. (I.4.28a) and (I.4.28b) is depicted in Figure I.4.2 and it can be expressed as

$$\mathbf{v}_i = \mathbf{v}_i^{\perp} + \mathbf{v}_i^{\parallel}. \tag{I.4.29}$$

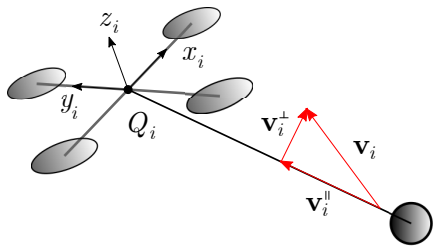

Figure I.4.2: Control force decomposition: representation of the i^{th} projection of the control force along a generic link.

Remark 15. *The need to distinguish between parallel and orthogonal components comes from the structure of the equations of motion. In fact, Equation* (I.4.23) *governs the translational dynamics of the load and then it contains the parallel component of the control force. On the other hand, Equation* (I.4.25) *governs the attitude of the load and therefore includes the orthogonal component of the control force. Those properties play a central role in designing the control.*

Remark 16. *Compared to previous works, Equations* (I.4.22)-(I.4.27) *present the introduction of the wind forces acting on the quadrotors and the payload.*

I.4.3.2 Aerial System Control

As already mentioned, in general the overall objective of the control is to ensure that the load follows the desired trajectory while pursuing the desired system configuration under the action of external disturbances. The *relative formation control* [14] is used. Thus, in particular, the objective is to find a set of control inputs such that $\mathbf{x}_L \longrightarrow \mathbf{x}_L^{des}$ and $\mathbf{q}_i \longrightarrow \mathbf{q}_i^{des}$ while $t \longrightarrow \infty$.

I.4.3.3 Design of the Parallel Components

The parallel component is chosen to track the desired trajectory of the load, in other words it is necessary to define $\mathbf{v}_i^{\parallel}$ s.t. $\mathbf{x}_L \longrightarrow \mathbf{x}_L^{des}$ while $t \longrightarrow \infty$.

Let's consider the load Equation (I.4.23). Since the translational dynamic is influenced only by the terms parallel to $\mathbf{q}_i$ then, it is possible to derive $\mathbf{v}_i^{\parallel}$ as

$$\mathbf{v}_i^{\parallel} = m_i l_i ||\boldsymbol{\omega}_i||^2 \mathbf{q}_i + \tau_i \mathbf{q}_i + \frac{m_i}{m_L} \mathbf{q}_i \mathbf{q}_i^T \sum_{j=1}^{n} \tau_j \mathbf{q}_j - (\mathbf{q}_i \cdot \mathbf{f}_{i,w}) \mathbf{q}_i, \tag{I.4.30}$$

To find the tensions to be applied along the links, it is enough to substitute (I.4.30) into (I.4.23) and make some arrangements to see that

$$(\ddot{\mathbf{x}}_L + g\mathbf{e}_3) = \frac{1}{m_L} \sum_{j=1}^{n} \tau_j \mathbf{q}_j + \Big(\sum_{i=1}^{n} m_i \mathbf{q}_i \mathbf{q}_i^T + m_L \mathbf{I} \Big)^{-1} \mathbf{f}_{L,w}, \tag{I.4.31}$$

and considering $\left(\sum_{i=1}^{n} \frac{m_i}{m_L}\mathbf{q}_i\mathbf{q}_i^T + \mathbf{I}\right)^{-1}$ as a dimensionless distribution mass-matrix $\mathbf{M}$, one has

$$(\ddot{\mathbf{x}}_L + g\mathbf{e}_3) = \frac{1}{m_L}\sum_{j=1}^{n}\tau_j\mathbf{q}_j + \frac{1}{m_L}\mathbf{M}\,\mathbf{f}_{L,w}, \tag{I.4.32}$$

which leads to

$$\ddot{\mathbf{x}}_L = -g\mathbf{e}_3 + \frac{1}{m_L}\mathbf{w} + \frac{1}{m_L}\boldsymbol{\delta}(t), \tag{I.4.33}$$

where $\boldsymbol{\delta}(t)$ represents the effect of the external disturbance whereas $\mathbf{w}$ is the wrench that act on the load. Rearranging this equation in the form of Newton' law, one has

$$\mathbf{w} = m_L\big((\ddot{\mathbf{x}}_L + g\mathbf{e}_3) - \frac{1}{m_L}\boldsymbol{\delta}(t)\big), \tag{I.4.34}$$

grouping the terms at RHS inside $\mathbf{u}$, returns

$$\mathbf{w}^{des} = m_L\mathbf{u}, \tag{I.4.35}$$

where the superscript *des* in $\mathbf{w}^{des}$ emphasizes that the control action coincides, up to the m_L constant, with the wrench that should be generated on the load to track the desired trajectory. In other words, it represents the action necessary to compensate for the external forces/disturbances and then correct the tracking error. As a consequence, the tensions necessary to steer the load, for $n \geq 3$, can be found using the closed-form solution Eq.I.1.6, reported here for sake of clarity

$$\boldsymbol{\tau} = \mathbf{W}^{\dagger}\mathbf{w}^{des} + \mathbf{N}\boldsymbol{\lambda}. \tag{I.4.36}$$

I.4.3.4 Design of the Orthogonal Components

The normal component is chosen to reach the desired *relative* configuration of the system, in other words it becomes necessary to define $\mathbf{v}_i^{\perp}$ s.t. $\mathbf{q}_i \longrightarrow \mathbf{q}_i^{des}$ while $t \longrightarrow \infty$. This correspond to the tracking problem on $\mathbb{S}^2$ which was studied in [10], [75]. In particular, the direction and angular velocity errors, are defined as follows

$$\mathbf{e}_{\mathbf{q}_i} = \mathbf{q}_i^{des} \times \mathbf{q}_i \quad \text{and} \quad \mathbf{e}_{\boldsymbol{\omega}_i} = \boldsymbol{\omega}_i + \hat{\mathbf{q}}_i^2\boldsymbol{\omega}_i^{des}, \tag{I.4.37}$$

whereas, the angular acceleration is

$$\dot{\boldsymbol{\omega}}_i = -K_{\mathbf{q}_i}\mathbf{e}_{\mathbf{q}_i} - K_{\boldsymbol{\omega}_i}\mathbf{e}_{\boldsymbol{\omega}_i} - (\mathbf{q}_i \cdot \boldsymbol{\omega}_i^{des})\dot{\mathbf{q}}_i - \hat{\mathbf{q}}_i^2\dot{\boldsymbol{\omega}}_i^{des}, \tag{I.4.38}$$

for positive gains $K_{\mathbf{q}_i}$ and $K_{\boldsymbol{\omega}_i}$. Now, substituting (A.55) into (I.4.25) yields to

$$\dot{\boldsymbol{\omega}}_i = \frac{1}{m_L l_i}\hat{\mathbf{q}}_i\sum_{j=1}^{n}\tau_j\mathbf{q}_j - \frac{1}{m_i l_i}\hat{\mathbf{q}}_i\mathbf{v}_i^{\perp} - \frac{1}{m_i l_i}\hat{\mathbf{q}}_i\mathbf{f}_{i,w}, \tag{I.4.39}$$

and $\mathbf{v}_i^{\perp} = -\hat{\mathbf{q}}_i^2\mathbf{v}_i$ leads us to the expression for the normal component $\mathbf{v}_i^{\perp}$ [14]

$$\mathbf{v}_i^{\perp} = m_L l_i\hat{\mathbf{q}}_i(-K_{\mathbf{q}_i}\mathbf{e}_{\mathbf{q}_i} - K_{\boldsymbol{\omega}_i}\mathbf{e}_{\boldsymbol{\omega}_i} - (\mathbf{q}_i \cdot \boldsymbol{\omega}_i^{des})\dot{\mathbf{q}}_i - \hat{\mathbf{q}}_i^2\dot{\boldsymbol{\omega}}_i^{des}) - \frac{m_i}{m_L}\hat{\mathbf{q}}_i^2\sum_{j=1,\,j\neq i}^{n}\tau_j\mathbf{q}_j + \hat{\mathbf{q}}_i^2\mathbf{f}_{i,w}. \tag{I.4.40}$$

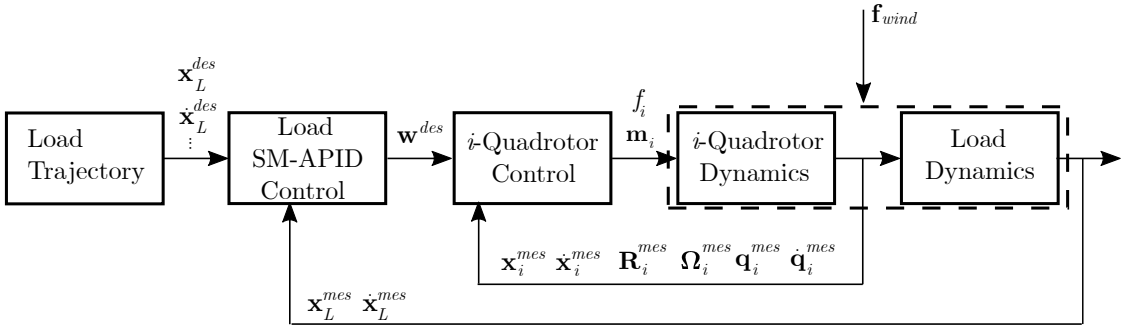

Figure I.4.3: Control scheme: it illustrates the various blocks that define the control logic and the quantities that are exchanged while the system is working.

I.4.3.5 Quadrotor's Attitude Control

To fully control the overall system, the attitude control of each quadrotor must be included; here it is reported once for sake of clarity. Hence, as done in [13], the control moment for each quadrotor is

$$\mathbf{m}_i = -K_{\mathbf{R}_i}\mathbf{e}_{\mathbf{R}_i} - K_{\mathbf{\Omega}_i}\mathbf{e}_{\mathbf{\Omega}_i} + \mathbf{\Omega}_i \times \mathbf{J}_i\mathbf{\Omega}_i - \mathbf{J}_i(\hat{\mathbf{\Omega}}_i\mathbf{R}_i^T\mathbf{R}_i^c\mathbf{\Omega}_i^c - \mathbf{R}_i^T\mathbf{R}_i^c\dot{\mathbf{\Omega}}_i^c), \tag{I.4.41}$$

where $\cdot^c$ stands for *controlled variables*, $\cdot^\vee$ denotes the *vee map*:$\cdot^\vee : \mathfrak{so}(3) \to \mathbb{R}^3$, $K_{\mathbf{R}_i}$, $K_{\mathbf{\Omega}_i}$ are diagonal positive-gain matrices and $\mathbf{e}_{\mathbf{R}_i}$, $\mathbf{e}_{\mathbf{\Omega}_i}$ are the errors for the attitude dynamics defined as

$$\mathbf{e}_{\mathbf{R}_i} = \frac{1}{2}(\mathbf{R}_i^{Tc}\mathbf{R}_i - \mathbf{R}_i^T\mathbf{R}_i^c)^\vee \quad \text{and} \quad \mathbf{e}_{\mathbf{\Omega}_i} = \mathbf{\Omega}_i - \mathbf{R}_i^T\mathbf{R}_i^c\mathbf{\Omega}_i^c, \tag{I.4.42}$$

Equation (I.4.41) together with

$$f_i = \mathbf{v}_i \cdot \mathbf{R}_i\mathbf{e}_3, \tag{I.4.43}$$

constitute the control actions for each agent of the system. The overall control scheme is depicted in Figure I.4.3.

I.4.3.6 Simulations

To shed some light on the peculiarities of the proposed approach numerical simulations are made. In particular, the tracking performances of different control are compared. An aerial system, with three rigid links and three quadrotors transporting a point-mass load, is considered. The task to be completed involves guiding the load along an elliptical trajectory. Both the load and the quadrotors were subjected to a wind that persisted for half of the simulation. To compute the aerodynamic forces $\mathbf{f}_{L,w}$ and $\mathbf{f}_{i,w}$ empirical equations are used for the former and some experimental measures for the latter, respectively. In particular, $\mathbf{f}_{L,w} = \frac{1}{2}C_dA_L\rho(v_w - ||\dot{\mathbf{x}}_L(t)||)^2\mathbf{e}_\infty$ where $\mathbf{e}_\infty$ represent the direction of the relative velocity (i.e. unit vector) and whose parameters were reported in the Table I.4.1 together with other useful parameters for the simulation. The value

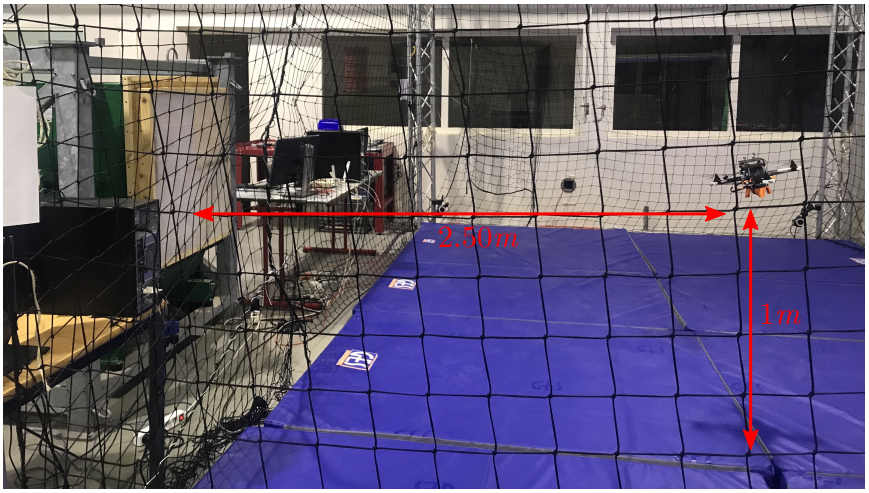

Figure I.4.4: Wind force estimation: quadrotor windswept during the experimental estimation of the aerodynamic force.

of $\mathbf{f}_{i,w}$ is difficult to derive empirically since the shape of quadrotors is complex and not unified. Consequently, its value was estimated through experimental tests carried out at the LS2N arena [76]. In particular, thanks to the use of a fan (shown in Figure I.4.4) and a first-order observer on a quadrotor, it was possible to determine a link between wind force and wind speed. This, together with the Dryden's model, allowed us to derive the wind forces acting on the drones as shown in Figure I.4.5b. All this continues to be an approximation of reality but their proper modelling is beyond the scope of this work. What is of interest instead, is to show that the presence of a persistent and time-varying force of aerodynamic nature, can be managed by the proposed control.

The initial configuration of the system and some phases of the task are shown in the following figure with the purpose of showing the overall behaviour of the system during the execution of the task Figure I.4.6. It is noteworthy that the system properly reconfigures itself to reach the desired output while counteracting the external disturbances. In addition, the sliding variables trends and the gains curves were reported in Figures I.4.5a and I.4.7, respectively. Figure I.4.7 shows that $k_{P_{(\cdot)}}$ and $k_{I_{(\cdot)}}$ gains stabilize after a transitory phase that last, approximately, 5 seconds whereas $k_{D_{(\cdot)}}$ gains continue to adjust in order to reach the sliding surface. Indeed, from Figure I.4.5a, one can see that the sliding variable values first decrease and then oscillate about zero for the entire duration of the simulation. The attainment of the sliding condition in finite time is not guaranteed with this design. Indeed, in Section I.4.2.4, the main requirement states as $\mathcal{S} \to 0$ for $t \to \infty$. It should also be noted that, since this condition is not reached in the first 10 seconds, when the wind changes intensity, Figure I.4.5b, the sliding variables locally increase their value and then decrease again. Thus, although the system may never achieve effective insensitivity from external disturbances, it does reduce their effect on the system by making the controller more robust. This can be observed with the following comparison.

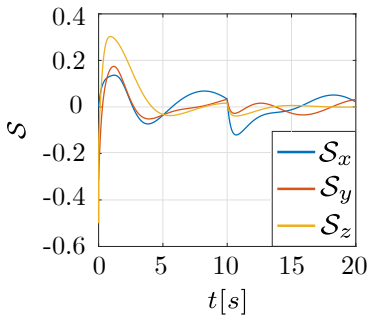

(a) Sliding variables: trends of the sliding variables in time.

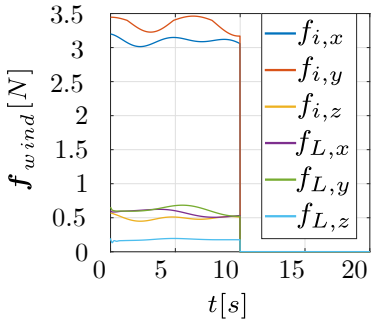

(b) Wind forces: wind force components acting on the aerial system.

Figure I.4.5: (a) represents the sliding variables along each direction while (b) depicts the wind forces acting on the load and drones.

Table I.4.1: Simulation parameters.

Parameter	Value	Parameter	Value
A_x	$0.8\,m$	$m_1 = m_2 = m_3$	$1.15\,kg$
A_y	$0.5\,m$	$l_1 = l_2 = l_3$	$1\,m$
m_L	$0.5\,kg$	$\mathbf{k}_0$	$\text{diag}\,(0.1 \quad 0.1 \quad 0.1)$
D	$0.2\,m$	$\mathbf{k}_1$	$\text{diag}\,(1 \quad 1 \quad 1)$
C_d	0.5	$\mathbf{J}_1 = \mathbf{J}_2 = \mathbf{J}_3$	$\text{diag}\,(0.01 \quad 0.1 \quad 0.14)\,kg \cdot m^2$
ρ	$1.2\ \frac{kg}{m^3}$	$\mathbf{K}_P(0) = \mathbf{K}_I(0) = \mathbf{K}_D(0)$	$\text{diag}\,(5 \quad 5 \quad 5)$
A_L	$\frac{\pi D^2}{4}$	$\mathbf{K}_P = \mathbf{K}_I = \mathbf{K}_D$	$\text{diag}\,(5 \quad 5 \quad 5)$
γ	10	$K_{\mathbf{q}_i} = K_{\boldsymbol{\omega}_i} = K_{\mathbf{R}_i} = K_{\boldsymbol{\Omega}_i}$	$\text{diag}\,(5 \quad 5 \quad 5)$
T	$20s$	$\boldsymbol{\Omega}_i(0) = \dot{\mathbf{x}}_L(0) = \boldsymbol{\omega}_i(0) = \boldsymbol{\omega}_i^{des}$	$(0 \quad 0 \quad 0)$
$\mathbf{R}_i(0)$	$\mathbf{I}$	$\mathbf{x}_L^{des}$	$(A_x \cos(\omega t) \quad A_y \sin(\omega t) \quad 0)\,m$
$\mathbf{i}_i^{des}$	$\mathbf{e}_1$	$\mathbf{x}_L(0)$	$(A_x \quad 0 \quad 0.5)\,m$
$\mathbf{q}_1(0)$	$(\sin 80° \quad 0 \quad -\cos 80°)$	$\mathbf{q}_1^{des}$	$(0 \quad -\sin 40° \quad -\cos 40°)$
$\mathbf{q}_2(0)$	$(0 \quad \sin 80° \quad -\cos 80°)$	$\mathbf{q}_2^{des}$	$(\sin 40° \quad 0 \quad -\cos 40°)$
$\mathbf{q}_3(0)$	$(-\sin 80° \quad 0 \quad -\cos 80°)$	$\mathbf{q}_3^{des}$	$(0 \quad \sin 40° \quad -\cos 40°)$

Comparisons are made by examining the controller developed in [14] (a PD control) and a revised version of it [70] (PID). To qualitatively compare their performance, reference can be made to Figures I.4.8 and I.4.9. The first two images show the trajectory followed by the load during the simulation with different control techniques. The third image shows the error trends along with the three directions (x, y and z). Therefore, from these pictures, it can be inferred that both PD and PID controllers fail to accomplish the task. In fact, the PD only manages to keep the error within a certain value. Instead the PID, thanks to the integral part, seems to recover the trajectory. However, during the recovery phase, the quadrotors perform a sudden manoeuvre which could not be achievable in reality since it could lead the system to crash. Indeed, the gains of these controllers (PD and PID) are chosen sufficiently high in order to guarantee the performance shown here and then to make comparisons. In general, with different gain values both the controllers are not able to conclude the task. On the other hand, this result confirms the robustness of the proposed controller.

Additional Figures I.4.10 and I.4.11 also show the error trend of the attitude of each quadrotor and the error of the configuration (link directions) as well. It should be noted

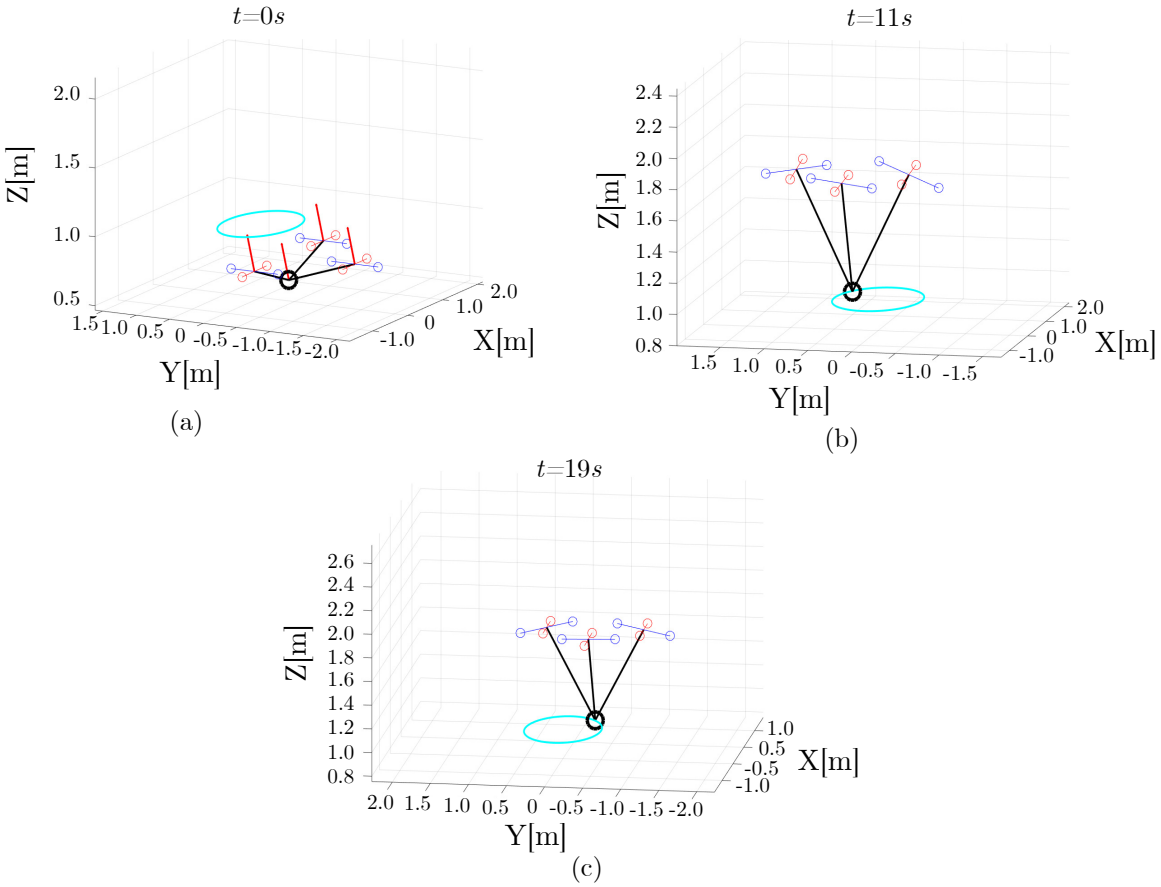

Figure I.4.6: Simulation phases: snapshots of the system during the simulation with SM-APID control. The snapshots show the system in (a) the initial condition $t = 0s$, (b) after one turn along the ellipses were the wind suddenly disappears $t = 11s$ and (c) in the final phase of the task $t = 19s$. The red arrows, where present, show the presence and direction of the aerodynamic force acting on the quadrotor and load.

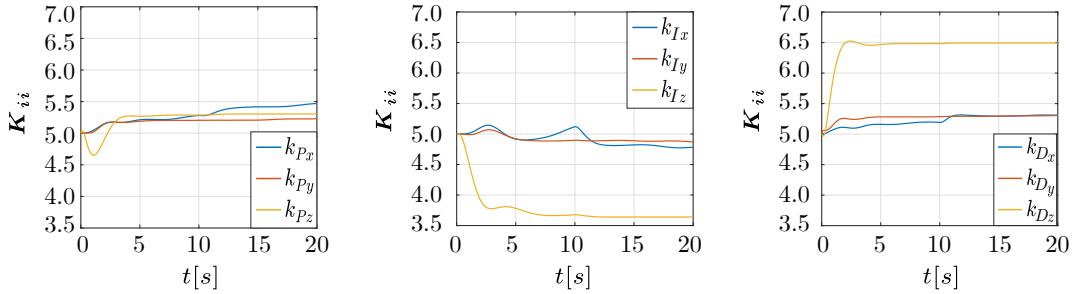

Figure I.4.7: Control gains: trends of the tuned gains in time.

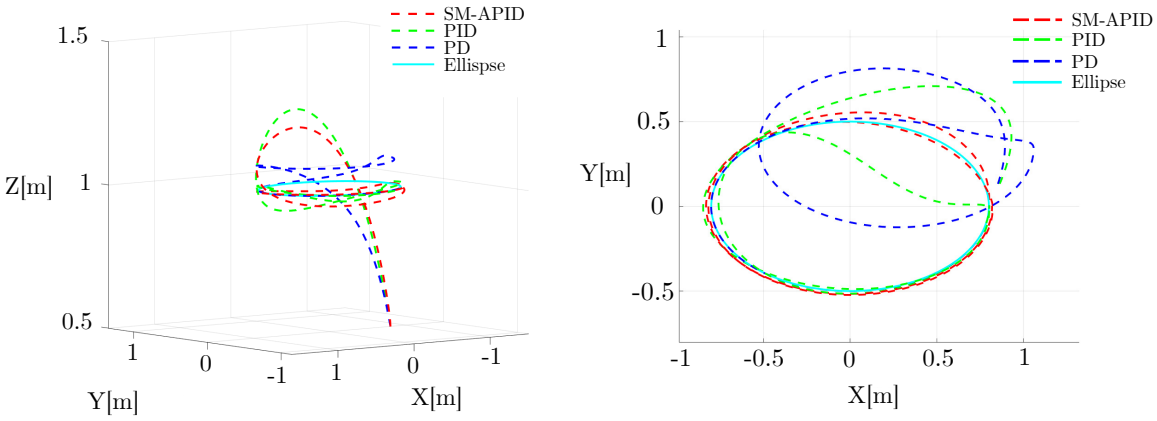

Figure I.4.8: Trajectories comparison: spatial and planar view of the undertaken load trajectory.

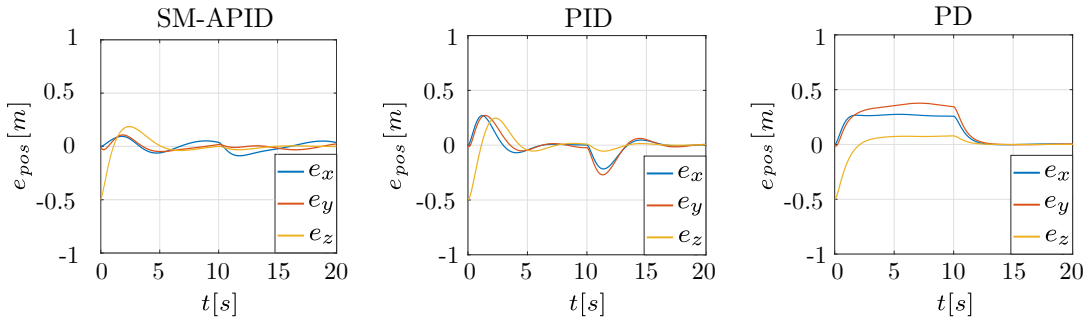

Figure I.4.9: Position errors: the components of the position errors for the three study cases are hereby depicted.

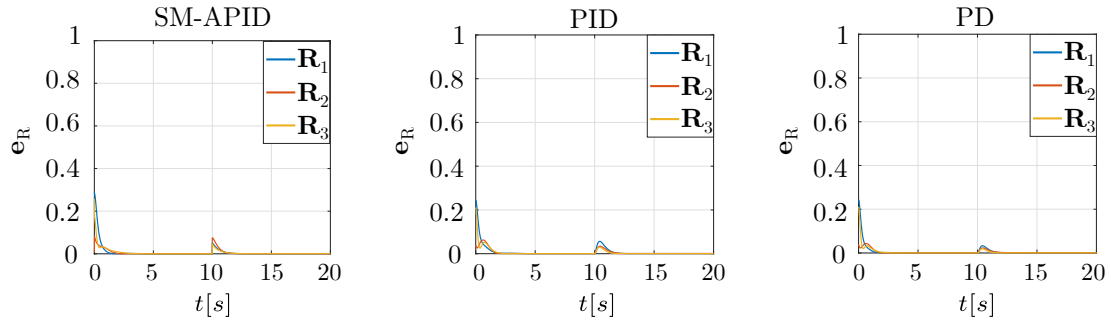

Figure I.4.10: Attitude errors: orientation error for each quadrotors in the three study cases is given. The error equation on $SO(3)$ is: $e_{\mathbf{R}} = \frac{1}{2}\,\mathrm{trace}(\mathbf{I} - \mathbf{R}_i^{Tc}\mathbf{R}_i)$.

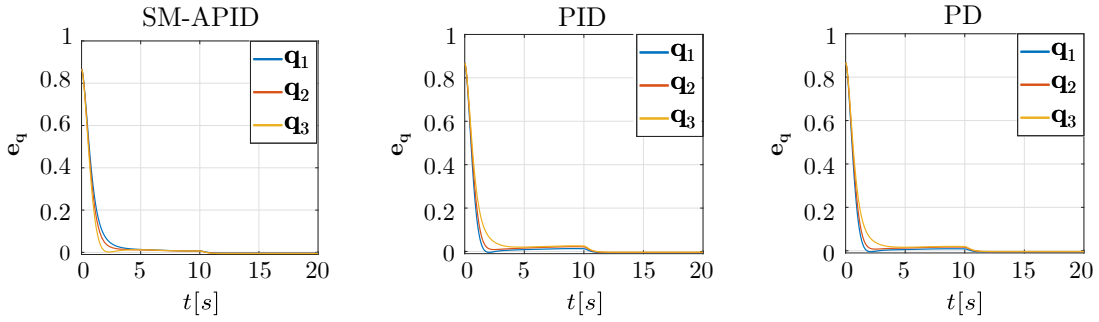

Figure I.4.11: Configuration errors: the link direction error for each bar in the three study cases is reported. The error equation on $\mathbb{S}^2$ is: $e_{\mathbf{q}} = 1 - \mathbf{q}_i \cdot \mathbf{q}_i^{des}$.

that the attitude and configuration errors are quite similar for both the PD and PID. In contrast, in the case of the SM-APID, it can be seen that the $\mathbf{e_R}$ converges slightly faster at zero while $\mathbf{e_q}$ error remains lower than PD and PID controllers. However, in all cases $\mathbf{e_q}$ is not zero because the controller does not compensate for the external disturbances. The reason why it is lower for the proposed controller is due to the presence of the term $\hat{\mathbf{q}}_i^2 \mathbf{f}_{i,w}$ in Equation (I.4.40). This is absent in the other two controllers.

On the other hand, a tangible way to compare the performances is provided by Table I.4.2. It makes a statistical analysis of the errors. In this case, Table I.4.2 refers to the position error only since, in this example, a tracking task is considered. To conclude, Table I.4.2 qualitatively confirms that, in general, the errors (MEAN, STD or RMSE) along each direction are smaller in the case of the SM-APID controller.

Table I.4.2: Error analysis: the Mean, STD and RMSE values for the trajectory tracking problems is computed for the three study cases.

Trajectory	Control Type	Statistics	Load position (m)		
			x	y	z
Ellipses	PD	MEAN	0.137	0.173	0.008
		STD	0.124	0.163	0.094
		RMSE	0.185	0.238	0.094
Ellipses	PID	MEAN	$1e^{-4}$	$2e^{-4}$	$1e^{-4}$
		STD	0.093	0.107	0.103
		RMSE	0.093	0.107	0.103
Ellipses	SM-APID	MEAN	0.002	0.001	$3e^{-4}$
		STD	0.049	0.034	0.090
		RMSE	0.049	0.034	0.090

I.4.3.7 Rigid-Body Load Case Study

In order to show the capabilities of the control introduced in this chapter, the extension of the previous results to the case of a rigid body transportation is considered in this

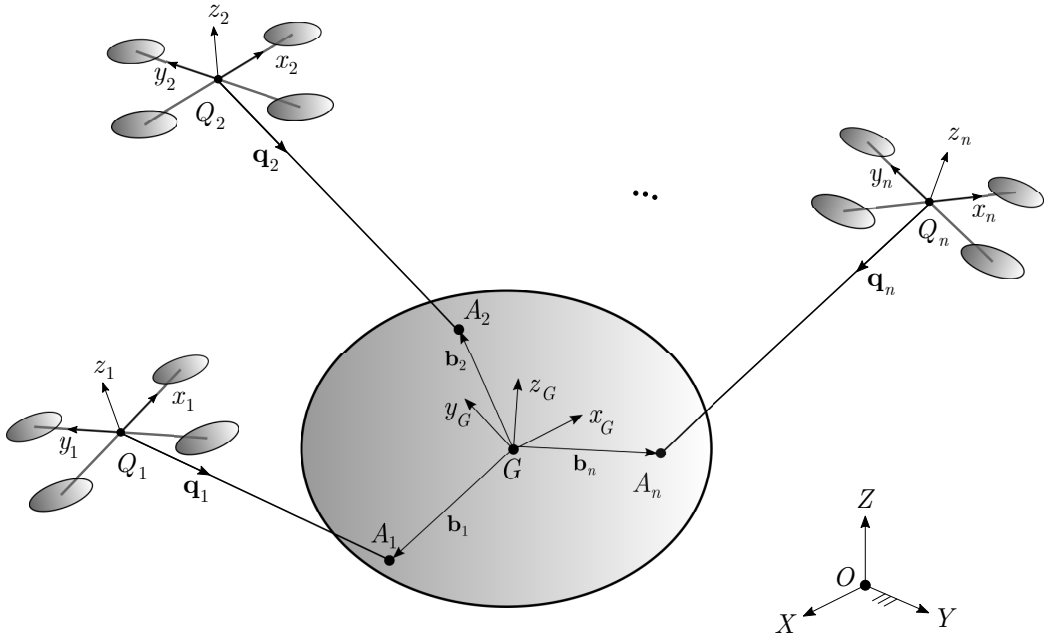

Figure I.4.12: Aerial System' Scheme: generic architecture of an aerial system with n quadrotors, rigid-bars and a rigid body platform.

section. Indeed, maintaining the same fashion as before, the equations of motion can be directly modified as follows

$$
\begin{cases}
\dfrac{d}{dt}\mathbf{x}_L = \dot{\mathbf{x}}_L, & \text{(I.4.44)}\\
\Big(\displaystyle\sum_{i=1}^{n} m_i\mathbf{q}_i\mathbf{q}_i^T + m_L\mathbf{I}\Big)(\ddot{\mathbf{x}}_L + g\mathbf{e}_3) - \displaystyle\sum_{i=1}^{n} m_i\mathbf{q}_i\mathbf{q}_i^T\mathbf{R}_o\tilde{\mathbf{r}}_i\dot{\boldsymbol{\Omega}}_o = & \\
\qquad \displaystyle\sum_{i=1}^{n}\big(\mathbf{v}_i^{\parallel} - m_i l_i||\boldsymbol{\omega}_i||^2\mathbf{q}_i + (\mathbf{q}_i\cdot\mathbf{f}_{i,w})\mathbf{q}_i - m_i\mathbf{q}_i\mathbf{q}_i^T\mathbf{R}_o\tilde{\boldsymbol{\Omega}}_o^2\mathbf{r}_i\big) + \mathbf{f}_{L,w}, & \text{(I.4.45)}\\
\dot{\mathbf{q}}_i = \boldsymbol{\omega}_i\times\mathbf{q}_i, & \text{(I.4.46)}\\
\dot{\boldsymbol{\omega}}_i = \dfrac{1}{l_i}\hat{\mathbf{q}}_i(\ddot{\mathbf{x}}_L + g\mathbf{e}_3 - \mathbf{R}_o\tilde{\mathbf{r}}_i\dot{\boldsymbol{\Omega}}_o - \mathbf{R}_o\tilde{\boldsymbol{\Omega}}_o^2\mathbf{r}_i) - \dfrac{1}{m_i l_i}\hat{\mathbf{q}}_i\mathbf{v}_i^{\perp} - \dfrac{1}{m_i l_i}\hat{\mathbf{q}}_i\mathbf{f}_{i,w}, & \text{(I.4.47)}\\
\dot{\mathbf{R}}_i = \mathbf{R}_i\hat{\boldsymbol{\Omega}}_i, & \text{(I.4.48)}\\
\mathbf{m}_i = \mathbf{J}_i\dot{\boldsymbol{\Omega}}_i + \boldsymbol{\Omega}_i\times\mathbf{J}_i\boldsymbol{\Omega}_i, \dot{\mathbf{R}}_o = \mathbf{R}_o\hat{\boldsymbol{\Omega}}_o, & \text{(I.4.49)}\\
\mathbf{m}_o = \mathbf{J}_o\dot{\boldsymbol{\Omega}}_o + \boldsymbol{\Omega}_o\times\mathbf{J}_o\boldsymbol{\Omega}_o - \mathbf{m}_{L,w}. & \text{(I.4.50)}
\end{cases}
$$

Basically, here, only the last Eq.(I.4.50) is added, w.r.t. the previous case, to describe the motion of the rigid platform hit by the wind $\mathbf{m}_{L,w}$.

I.4.3.8 Aerial System Control

As soon as the control part is considered, only the main changes are hereby highlighted, since the core idea is not changed. Therefore, the design of the parallel and orthogonal component are briefly reported. Observe that, the quadrotors'attitude and the architecture of the control scheme, presented before, are, again, identical and then not repeated here.

I.4.3.9 Design of the Parallel Components

The parallel component is chosen to track the desired pose $\mathbf{p}^{des} = (\mathbf{x}_L^{des}, \mathbf{R}_o^{des})$ of the load, in other words it is necessary to define $\mathbf{v}_i^{\parallel}$ s.t. $\mathbf{p} \longrightarrow \mathbf{p}^{des}$ while $t \longrightarrow \infty$.

Let's consider the load Equation (I.4.45). Then, it is possible to derive $\mathbf{v}_i^{\parallel}$ as

$$\mathbf{v}_i^{\parallel} = m_i l_i ||\boldsymbol{\omega}_i||^2 \mathbf{q}_i + \tau_i \mathbf{q}_i + m_i \mathbf{q}_i \mathbf{q}_i^T (\ddot{\mathbf{x}}_L + g\mathbf{e}_3 + \mathbf{R}_o \tilde{\boldsymbol{\Omega}}_o^2 \rho_i - \mathbf{R}_o \tilde{\boldsymbol{\rho}}_i \dot{\boldsymbol{\Omega}}_o) - (\mathbf{q}_i \cdot \mathbf{f}_{i,w}) \mathbf{q}_i, \quad \text{(I.4.51)}$$

where τ_i represent the tension along the i^{th} link. To find the tensions to be applied along the links, it is enough to refers to the platform dynamics described as in Eq.I.1.1 where, this time the wrench matrix assume its general form Eq.I.1.2.

Observe that $\mathbf{w}_e$ takes the role of the control actions $\mathbf{u}_f$ and $\mathbf{u}_m$ therefore, the closed-form solution takes the form

$$\boldsymbol{\tau} = -\operatorname{diag}(\mathbf{R}_o) \mathbf{W}^{\dagger} \begin{pmatrix} \mathbf{R}_o^T \mathbf{u}_f \\ \mathbf{u}_m \end{pmatrix}, \quad \text{(I.4.52)}$$

where $\mathbf{w}^{des} = (\mathbf{R}_o^T \mathbf{u}_f, \mathbf{u}_m)^T$ represents the action necessary to compensate for the external forces, disturbances and then correct the tracking error.

I.4.3.10 Design of the Orthogonal Components

The normal component is chosen to reach the desired configuration of the system, in other words it becomes necessary to define $\mathbf{v}_i^{\perp}$ s.t. $\mathbf{q}_i \longrightarrow \mathbf{q}_i^{des}$ while $t \longrightarrow \infty$ [10], [75]. In particular, the direction and angular velocity errors, are defined as follows

$$\mathbf{e}_{\mathbf{q}_i} = \mathbf{q}_i^{des} \times \mathbf{q}_i \quad \text{and} \quad \mathbf{e}_{\boldsymbol{\omega}_i} = \boldsymbol{\omega}_i + \hat{\mathbf{q}}_i^2 \boldsymbol{\omega}_i^{des}, \quad \text{(I.4.53)}$$

whereas, the desired angular acceleration is

$$\dot{\boldsymbol{\omega}}_i = -K_{\mathbf{q}_i} \mathbf{e}_{\mathbf{q}_i} - K_{\boldsymbol{\omega}_i} \mathbf{e}_{\boldsymbol{\omega}_i} - (\mathbf{q}_i \cdot \boldsymbol{\omega}_i^{des}) \dot{\mathbf{q}}_i - \hat{\mathbf{q}}_i^2 \dot{\boldsymbol{\omega}}_i^{des}, \quad \text{(I.4.54)}$$

for positive gains $K_{\mathbf{q}_i}$ and $K_{\boldsymbol{\omega}_i}$. Now, rearranging equations of motion and using Eq.(I.4.54) yields to the expression for the normal component $\mathbf{v}_i^{\perp}$ [14]

$$\mathbf{v}_i^{\perp} = m_L l_i \hat{\mathbf{q}}_i (-K_{\mathbf{q}_i} \mathbf{e}_{\mathbf{q}_i} - K_{\boldsymbol{\omega}_i} \mathbf{e}_{\boldsymbol{\omega}_i} - (\mathbf{q}_i \cdot \boldsymbol{\omega}_i^{des}) \dot{\mathbf{q}}_i - \hat{\mathbf{q}}_i^2 \dot{\boldsymbol{\omega}}_i^{des}) - \frac{m_i}{m_L} \hat{\mathbf{q}}_i^2 \sum_{j=1,\, j \neq i}^{n} \tau_j \mathbf{q}_j + \hat{\mathbf{q}}_i^2 \mathbf{f}_{i,w}. \quad \text{(I.4.55)}$$

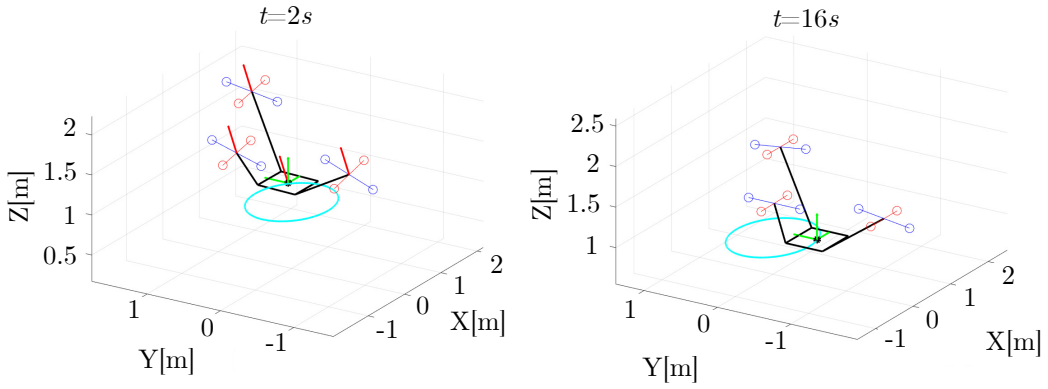

Figure I.4.13: Simulation: two phases of the simulation with the SM-APID control are depicted. One at the time $t = 2\,s$ where the wind (red arrows) acts on the entire systems whereas the second image depicts the reaction of the system when the wind is not present anymore namely at $t = 16\,s$.

I.4.3.11 Simulations

In this section, an aerial system with three quadrotors and rigid bars is considered. The aim consists in tracking an elliptical trajectory while orienting the platform in presence of wind.

Regarding the simulation data, the mass of the platform is $m_L = 0.5\,kg$, its length, width and height are $0.7\,m$, $0.5\,m$ and $0.2\,m$, respectively while its inertia matrix is $\mathbf{J}_o = \text{diag}(0.15, 0.15, 0.17)\,kg\,m^2$. Bar lengths are $l_i = 1m$ (massless). Quadrotors' masses are $m_i = 1.15kg$ while $\mathbf{J}_i = \text{diag}(0.1, 0.1, 0.14)kg\,m^2$. The attachment points on the platform are $\mathbf{b}_1 = (-0.35, -0.25, 0)\,m$, $\mathbf{b}_2 = (-0.35, 0.25, 0)\,m$ and $\mathbf{b}_3 = (0.35, 0.25, 0)\,m$. The initial conditions, necessary to replicate the results are $\mathbf{x}_L(0) = (0.75, 0, 0.5)$, $\boldsymbol{\Omega}_i(0) = \boldsymbol{\Omega}_o(0) = \dot{\mathbf{x}}_L(0) = \boldsymbol{\omega}_i(0) = (0, 0, 0)$ while the bar directions are

$\mathbf{q}_1(0) = (\sin 60, 0, -\cos 60)$, $\mathbf{q}_2(0) = (0, -\sin 60, -\cos 60)$ and $\mathbf{q}_3(0) = (-\sin 60, 0, -\cos 60)$ whereas $\mathbf{R}_o(0) = -\mathbf{I}$ and $\mathbf{R}_o^{des} = \mathbf{I}$. Wind actions on the system are generated by using the Dryden model, in analogy with the works [71], [77].

The entire simulation lasts $20s$ and in the middle of the simulation, the wind is suddenly removed to see the behaviour of the control and the reaction of the system. This should simulate the appearance and disappearance of the wind as experienced in practice.

Since the task resembles in tracking the desired pose, the interest in the simulation results, for the proposed SM-APID and PID controls, lies in the tracking pose errors reported in Fig.I.4.14. Although other data might be considered useful to grasp the whole behaviour of the system, they were reported and discussed extensively for the previous example and therefore, are not reported here.

Firstly, Figure I.4.13 is intended to give an idea of the task the system has to fulfill and how it behaves in the presence and absence of wind. As a general comment, it is

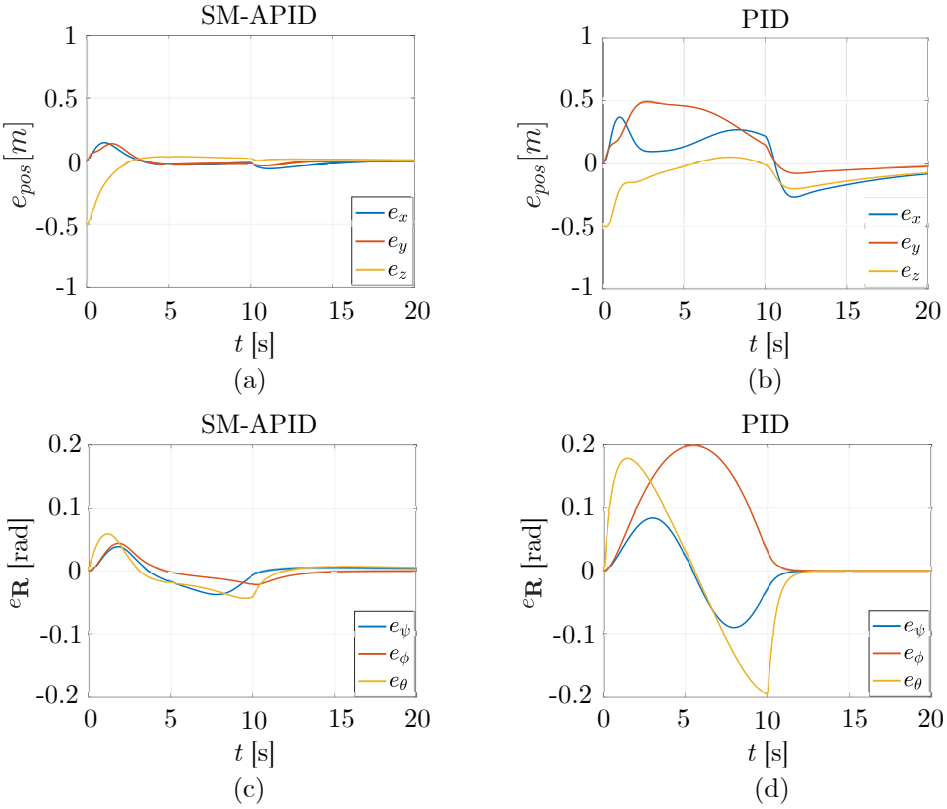

Figure I.4.14: Pose Errors: a comparisons between the position (a)-(b) and orientation (c)-(d) errors of the platform using the PID and SM-APID control. Observe that angles ψ, ϕ and θ represent the yaw, pitch and roll angles of the platform respectively.

evident how, in the presence of the wind, the drones' attitude is such that they attempt to resist it. In fact, their orientation is completely different when the wind disappears. Then, it can be seen from Fig. I.4.14 that the errors for both the position and orientation are always smaller in the case of the SM-APID control. This is then a clear evidence of the superior robustness of the proposed method w.r.t. the classical PID commonly used.

Second, from the PID graphs (a)-(c) one can see that, when the wind disappears at $t = 10s$ onward, the PID recovers as much as possible the accumulated error on both sides, i.e. position and orientation. However, even if the error is reduced, the system undertakes a sudden manoeuvre that can be considered unsafe or even unattainable. This behaviour is, however, not so pronounced in the case of SM-APID. Indeed, when the wind disappears, the gains stabilize and the errors tend to 0.

Finally, it is worth remembering that to achieve *acceptable* performances with a PID, the gains must be tuned iteratively thus spending a considerable amount of time when the simulation parameter changes. Thus, the ability to adjust gains automatically turns out to be an effective strategy that combines robustness and practicality. However, it should be pointed out that, as stated in Sec.I.4.2.4, if the external disturbance is not

sufficiently bounded, gain adaptation may not be prompt enough. In that case, the typical sliding mode would be activated guaranteeing the desired robustness at the price of introducing chattering.

I.4.4 Cable-Breakage Scenario for CDPR

Recently, the industry has been demanding for collaborative robots. In other words, a lot of effort is now spent in order to enable the robot working safely with the human to perform a task. In this regard, although cables fit perfectly for collaborative purposes, due to their inherent deformability, they are also the source of a major issue when a cable breaks.

The failure of a cable shrinks the Wrench Feasible Workspace (WFW), defined by [43], of the robot. As a consequence, the load suddenly lies outside the WFW and can not be controlled properly. The majority of the works in the literature focus on establishing a strategy for recovering the load to avoid dangerous collisions with the surrounding environment.

In [78], when the cable breaks, a recovery strategy, which consists in re-planning the load trajectory to bring it to a new equilibrium position within the new WFW, is employed. However, here, it is assumed the possibility to determine when the cable breaks, which, in general, is something unpredictable. Similarly, in [79] a straight-line path motion planning strategy is introduced to guide the load in a safe position inside the workspace. Furthermore, in [80], an after-failure oscillatory trajectory was proposed to steer the end-effector towards a safe landing location, guaranteeing positive and bounded tension limits.

The occurrence of a cable breakage can harm humans and the environment, hence in [81] the idea is to reduce the kinetic energy of the load while using potential fields to compute cable tensions outside the WFW. Another possibility explored by the same authors, [82], consists in reconfiguring the CDPR to restore and enlarge the WFW, thus recovering the control over the load.

Another branch of work regards the computation of the cable tensions distribution. In other words, researchers spent effort in developing the so-called Tension Distribution Algorithms (TDAs) both for normal operating conditions and when a cable fails. In particular, in [83] a methodology, based on the projection of the lost wire tension onto the null space of the Jacobian of the manipulator, is presented. In its subsequent work, [84], the correctional cable tension is based on Lagrange multiplier for minimizing the norms of the correctional and overall cable tension, respectively. Another recent contribution is given in [85], [86] where a method to calculate cable forces outside the WFW of a CDPR is presented. Force distributions are obtained based on the concept of distance with the aim of simplifying the implementation while reducing the numerical cost.

Looking at the global context, together the two classes of the above-mentioned works focus on finding the best recovery strategy and TDAs to govern the load when a cable fails. However, those contributions overlook the control part that could be used to make the system more robust and prepared in this scenario. The importance of a quick reaction

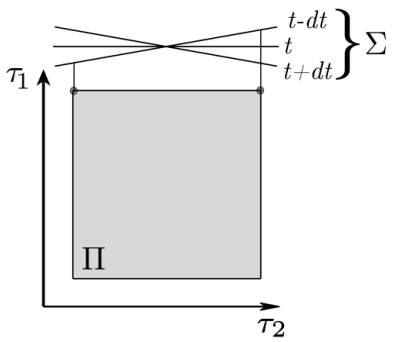

Figure I.4.15: Discontinuity: representation of both the ambiguity at time t and discontinuity of the solution when stepping from time $t - dt$ to $t + dt$ when $m = 2$.

by the control station has been pointed out in [87]. To this end, this section leverages on the introduced adaptive control to infer whether it has a positive impact on the guidance of the load [62], [77]. This solution should allow reaching an equilibrium position inside the resulting WFW (i.e. after cable failure), while limiting the load oscillation, without assuming any prior knowledge about when the cable breaks.

I.4.4.1 On the TDAs for Cable-Breakage Scenario

So far, several approaches were presented in the literature, [42], to solve the tension distribution problem. Here, the Analytic Centre (AC), presented in [47] and [88], is employed. To motivate the benefit of using this TDA, even in case of cable breakage, this section compares it with the Nearest Corner method, which is specifically developed for cable failure scenarios in a series of papers by [85], [86].

In other words, when the load is outside the WFW then $\Gamma = \emptyset$. Therefore, one can adopt a specific strategy to choose the cable tensions vector $\boldsymbol{\tau}$ in this case. However, one should notice that every technique would always be a fallback solution as it won't respect Π and Σ contemporary. Then, this latter will constitute an approximation that has to be compliant with the force boundaries Π so that it can be used for control purposes.

In this context, the most immediate idea, as explained in [85], [86], is basically to project the corners of the hypercube Π onto the affine space Σ and then using weights to select a tension $\boldsymbol{\tau}$ as the solution. Although this technique has the advantage of not being iterative and can be easily implemented, it still has issues that are not present with the AC.

One practically-relevant issue concerns the continuity of the solution. Similarly as in the Linear Programming (LP) method, [31], when the affine space undertakes a sequence of orientation, such that it becomes parallel to one face of Π, then the solution is not unique. Moreover, looking at the mentioned sequence of orientation in Fig.I.4.15, it is evident that one can step from one corner to another of Π hence generating a jump (discontinuity) in cable tension profiles.

The second aspect that should be considered, regards the weights used in this method.

Indeed, it seems that the weights determining the tension $\boldsymbol{\tau}$ are not bounded. This can cause problems as it can happen that the solution contains components requiring more than the highest (or lowest) tension value. In case the highest tension is selected, this will stress more the remaining cables and can generate a collapse of the overall structure if other cables fail.

As explained in [88], these phenomena does not occur when using the AC. Indeed, barrier functions guarantee the continuity of the solutions and automatically avoid selecting cable tensions outside Π. Notice that other TDAs can be suitable and then used while respecting continuity and returning a solution inside Π. However, the advantages of using the AC, as pointed out in [88], make it the preferred solution.

Remark 17. *Using an optimization problem somehow translates into reducing the distance between* Γ *and* Π*. Indeed, the solver aims at reducing the residual of Eq.*(I.1.1)*, while satisfying* Π*, as much as possible. Moreover, using AC, one could define a slack variable, [47], to mitigate the unfeasiblity* $\Gamma = \emptyset$*, similarly as done in [45].*

I.4.4.2 Study Cases

In this section, a CDPR with four cables suspending a point mass load is considered, see Fig.I.4.16 for sake of clarity. The tests consist in tracking a circular and helical trajectory till the cable breaks. When the cable failure occurs, the load is supposed to be positioned inside the new WFW at the pre-computed *safety* position $\tilde{\mathbf{x}}_s = (-1.2\sqrt{2}, -1.2\sqrt{2}, z(t_{cb}))$, while minimizing the kinetic energy by requiring $\dot{\tilde{\mathbf{x}}}_s = (0, 0, 0)$. Observe that one could also improve this procedure by introducing the strategy given in the literature; however, this is out of the scope of this section as the focus is on testing the control part. To simulate this scenario, the integration step is set to $dt = 10^{-3}s$ and it is supposed that the fourth cable is going to fail. This latter does not constitute a loss of generality as indeed, any other cable can be chosen to break by coherently changing the coordinate of $\tilde{\mathbf{x}}_s$ within the new WFW.

Regarding the simulation data, the entire simulations last $20s$, the mass of the load is $m_L = 2\,kg$ and it is supposed to follow a circular

$$\begin{cases} x(t) = \cos(2\pi s(t)) & s(t) \in [0,1], \\ y(t) = \sin(2\pi s(t)) & t \in [0,20]s, \\ z(t) = 1.5, \end{cases} \tag{I.4.56}$$

or a helical trajectory

$$\begin{cases} x(t) = \sin(\pi/8\, t), \\ y(t) = \cos(\pi/8\, t), \\ z(t) = 1 + 0.05\, t. \end{cases} \tag{I.4.57}$$

The gains for the PID are set to be equal to the initial ones of the APID, hence $\mathbf{K}_{P,ii} = \mathbf{K}_{I,ii} = \mathbf{K}_{D,ii} = 10$.

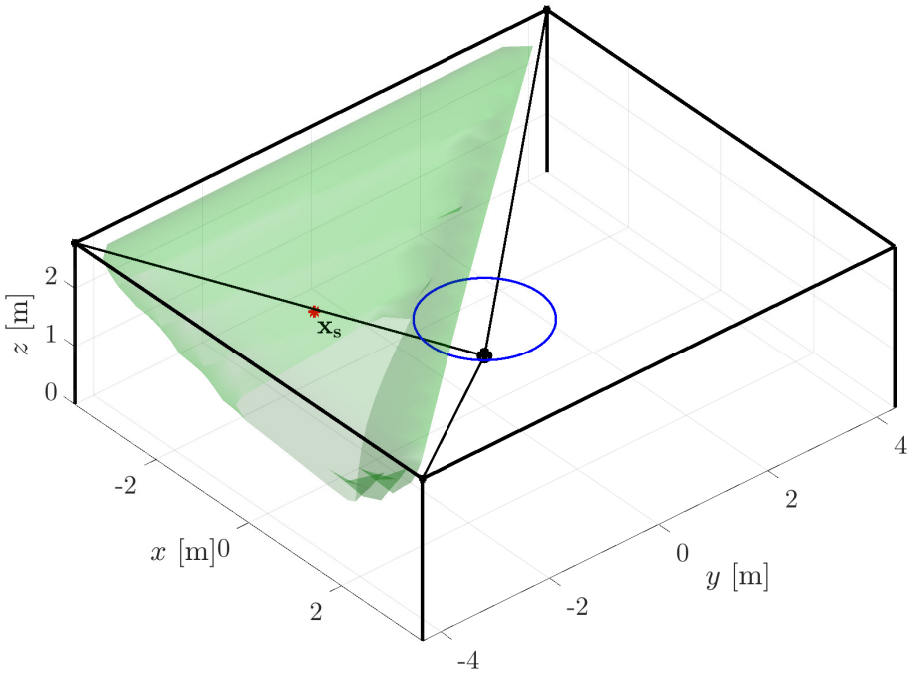

Figure I.4.16: WFW: the shape of the WFW is hereby depicted, using the capacity margin [61], when the fourth cable breaks. Clearly, when all the four cables are working, the volumes of the WFW here represented can be mirrored symmetrically and the trajectory result to be fully inside the green volume.

Remark 18. *Literature often reports simulations where, even if a cable breaks, the load remains over-constrained. However, a more significant scenario arises when the load becomes under-constrained after a cable breaks. This would place maximum demands on the controller and enable us to comprehend worst-case performance. Furthermore, notice that considering the suspended architecture makes the case even more challenging since the WFW is not approximated to a cube but to a flipped pyramid and, also, forces along the negative direction of the z-axis can not be generated.*

Study Case One

To start, let's consider the circular trajectory Eq.(I.4.56). Therefore, the tension profiles and the trends of the position and velocity errors for both the PID and APID control are depicted in Figs. I.4.17, I.4.18 and I.4.19, respectively. First, from the error trends, it is possible to see that, when the cable breaks at $t_{cb} = 5s$, the new $\tilde{\mathbf{x}}_s$ position is automatically defined by the control, and the load is guided toward it. Indeed, at t_{cb} the error suddenly increases since $\tilde{\mathbf{x}}_s$ is generally far from the actual load position. Moreover,

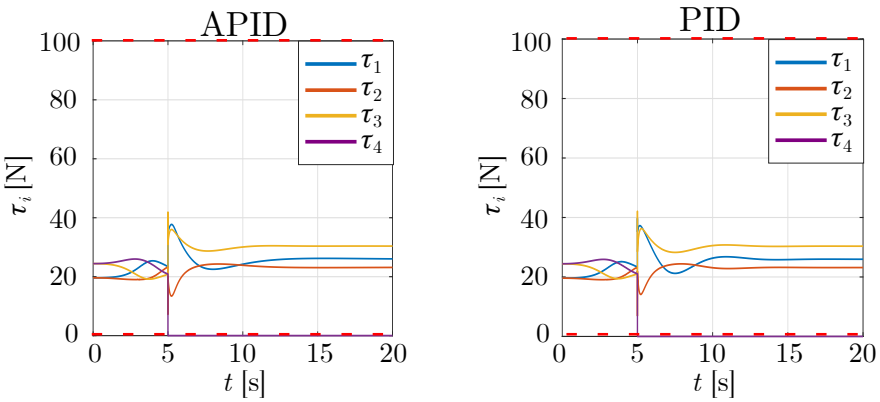

Figure I.4.17: Tension profiles: the trend of tension profiles when the fourth cable at $t_{cb} = 5s$ breaks are reported. The spike appearing in both the two graphs is due to the cable breakage. The tension distribution algorithm used is based on the Analytic centre defined in [88]; dotted red lines identify the cable tension limits.

it should be evident, comparing the trends, that the use of an adaptive technique makes the system more robust and safer than the PID, as the amplitude of the load oscillations is smaller, see Fig. I.4.18 about 6 to 13 seconds. Concerning the convergence to $\tilde{\mathbf{x}}_s$ and $\dot{\tilde{\mathbf{x}}}_s$, from Figs. I.4.18 and I.4.19, it should be clear that the APID performs better as it reaches 0 error before the PID.

A second noteworthy aspect regards the influence of t_{cb} on the control performances. In particular, changing the t_{cb} will help us demonstrate the independence of the APID when the cable fails as well as the robustness of the method. First, to do so, a criteria to compare the mentioned performances of the controls have to be defined. Hence, one can define a control *safer* if the radius of the ball, defined around $\tilde{\mathbf{x}}_s$, inside which the load stops, is smaller that the other.

Therefore, also the cases at $t_{cb} = 2.0s$ and $t_{cb} = 3.7s$ are considered. The results of the trajectories followed are depicted in Figs.I.4.20a, I.4.20b and I.4.20c. It seems clear that the PID leads to wider oscillations around $\tilde{\mathbf{x}}_s$ than the APID. The motivation is linked to its fixed gains. Indeed, once selected, they will not be optimal as, in general, the cable breaks unexpectedly.

Comparing the radius only shows the superiority of the APID in guaranteeing safety around a chosen $\tilde{\mathbf{x}}_s$. To show its independence from time and robustness, one should notice that the radius under which the load oscillates is always smaller than the one defined by the constraint $\mathfrak{C}$ in Eq.(9). In other words, $\mathfrak{C}$ traces a sphere, inside which the load should stay by adapting the gains. If this condition can not be satisfied, then the $\mathbf{u}_s$ intervenes as said at the end of Sec.I.4.2.4. Notice that the definition of $\mathfrak{C}$ depends on the scalar value $M_{\mathbf{x}}$ which, indeed, is independent from the time. Moreover, one should notice that the radius of the circle for the PID reduces while going from $t_{cb} = 2s$ to $t_{cb} = 5s$. In other words, the higher the time t_{cb}, the lower the radius. This can be explained by observing that, for this case study, the distance to $\tilde{\mathbf{x}}_s$ reduces when t_{cb}

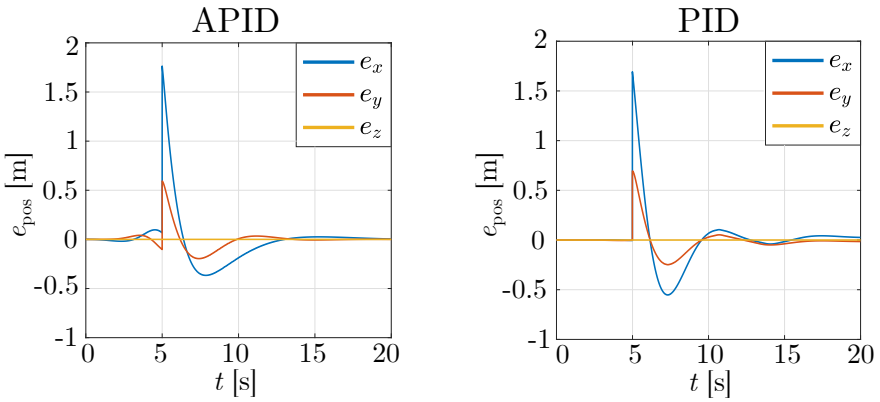

Figure I.4.18: Position errors: position errors recorded when the cable breaks at $t = 5s$, along the three Cartesian directions for both the controller PID and APID, respectively.

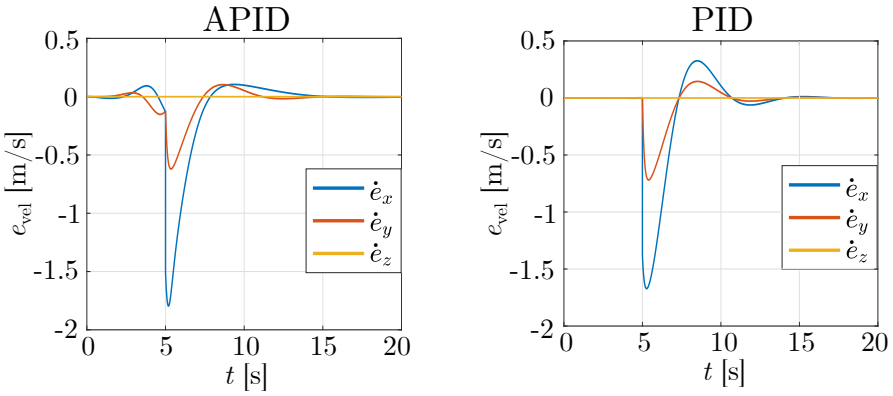

Figure I.4.19: Velocity errors: velocity errors recorded when the cable breaks at $t = 5s$, along the three Cartesian directions for both the controller PID and APID, respectively.

increases. Therefore, since the distance reduces, the amount of time where the motions of the load are uncontrolled reduces and then the PID should act less to reach 0 error.

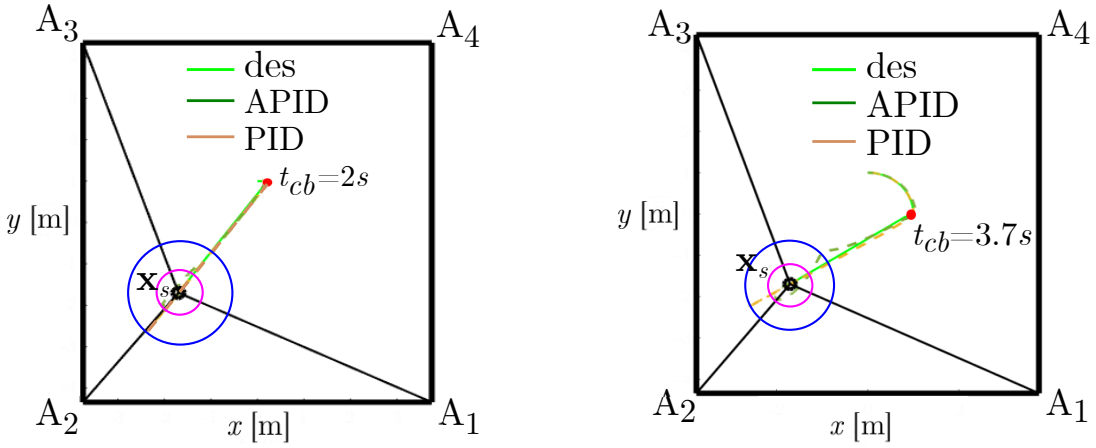

(a) $t_{cb} = 2s$. (b) $t_{cb} = 3.7s$.

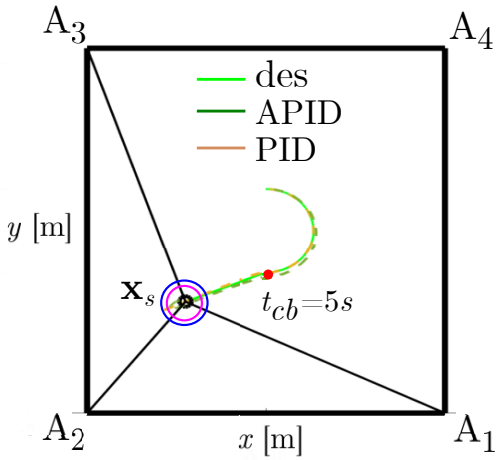

(c) $t_{cb} = 5s$.

Figure I.4.20: Multi-failure scenario: tracked trajectories for different cable-breakage times $t_{cb} = 2s, t_{cb} = 3.7s$ and $t_{cb} = 5s$ for both PID and APID controls. Note the large oscillations around the safe position $\tilde{\mathbf{x}}_s$ when using the PID.

Remark 19. *Setting parameter $M_{\mathbf{x}}$, defined in Sec.I.4.2.3, translates in requiring a certain level of safety. Clearly, $M_{\mathbf{x}} = 0$ means that the load must stop at $\tilde{\mathbf{x}}_s$ and no oscillations are permitted.*

For sake of completeness, the gains profiles, Fig. I.4.21, are also reported to show how they change over time. Observe that these graphs tell us when the load enters the new WFW. Indeed, this happens when the gains stabilize at a steady value.

The analysis can be concluded by considering the influence of γ on the APID performance. Here, γ has been considered fixed to $\gamma = 0.005$ in order to make fair comparisons with the PID. However, several possibilities are available. One can, for example, have different values along each Cartesian direction. Now, despite the broad range of pos-

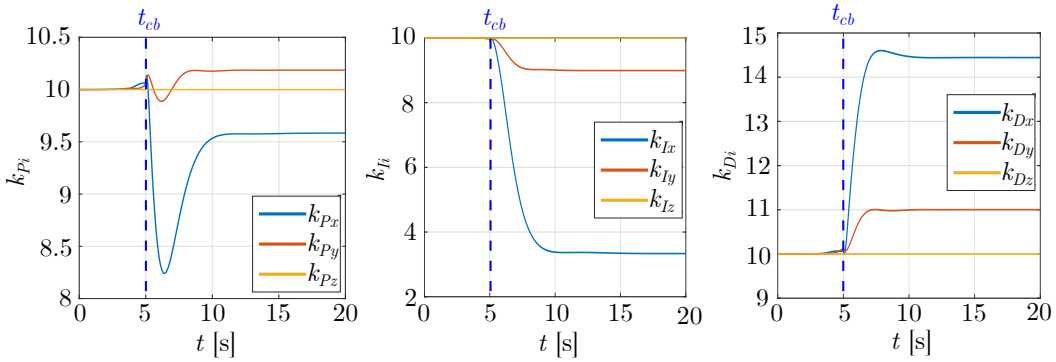

Figure I.4.21: Gain trends: gain profiles over time for the APID. Observe that, when the cable breaks at t_{cb}, there is a phase of transition before the gains stabilize again. The extremes of this transitional phase are t_{cb} and the instant of time when the load enters the new WFW.

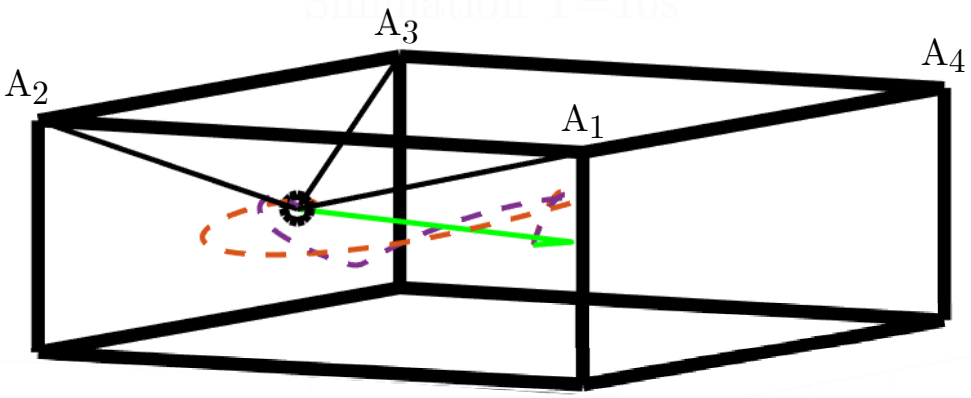

Figure I.4.22: APID control in a 3D perspective.

sibilities one has for choosing γ, practically, its influence on the global behaviour of the control is what interests us for designing the control. In this context, it appears clear that, when $\gamma \to 0$, then the APID behaves as the PID. Therefore, one can think that the higher is γ the better it is in terms of adaptation and then performance. This latter conclusion is, however, wrong. Indeed, increasing γ can lead to overreaction to errors change, see Eqs.(I.4.19a)-(I.4.19c). Practically speaking, this last phenomena is not a problem as far as the variation in the gains does not result in actuation saturation. Therefore, it is necessary to find a good compromise between the reaction to error change and the quickness of adaptation.

Study Case Two

In this section, the trajectory is considered as a helix in order to show the generality of the method and see if major changes in the result occur.

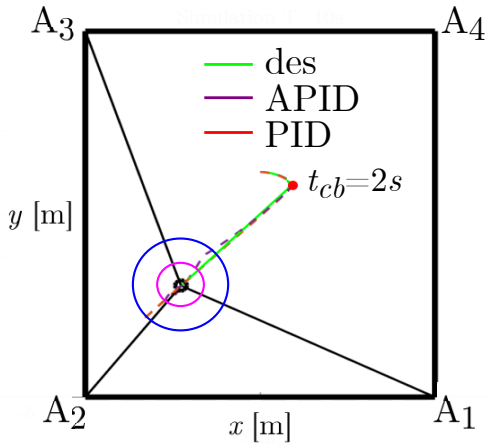

Figure I.4.23: APID control in a 2D perspective.

Similarly to what was done before, let us analyse the performance of both the PID and APID when the fourth cable breaks. For brevity, only the case $t_{cb} = 2s$ is reported as it is the worst case due to the large distance separating the point where the cable breaks and the $\tilde{\mathbf{x}}_s$.

Qualitatively comparing the trajectories undertaken by the load in Figs. I.4.23 and I.4.22 suffices to confirm what said before.

One additional information that can be added by looking at the spatial trajectory in Fig.I.4.22 regards the radius of the sphere around the safe position. In previous simulations, the error in the z direction was small (about 0) and then no doubts about taking the radius as the maximum distance along the x or y direction. This time, this consideration is not valid anymore. However, since typically the aim is to avoid lateral collisions first, it should be still valid taking the radius as the maximum along the x or y direction as safety criteria to compare the control performance.

Chapter I.5

Conclusions and Future Perspectives

I.5.1 Conclusions

The first part of this thesis contributed to generalising the concept of CDPRs. Leveraging on this, many useful ideas and contributions developed so far, believed for different types of robots, can indeed be shared.

In this flourishing context, the first chapter offers, first, a review of the existing TDAs and ties to spot their peculiarities by means of the robustness index. Consequently, the Analytic Centre was introduced. Its peculiarities were shown, discussed and then compared with the other TDAs. Simulations demonstrated its superiority under several perspectives such as continuity, differentiability, computational cost and capabilities in considering non-linear constraints. Eventually, also an experimental test is reported showing its applicability in a real hardware.

The second chapter, really builds up on the previous one. Here, the definition of local and global sensitivity and their differences were given. Moreover, preliminary results have to be validated as well to assess their utility.

Finally, the third chapter, proposes the design of an adaptive control to steer a load in the presence of external disturbances and/or model inaccuracies. This technique was applied to several scenarios such as aerial transportation in presence of wind and cable breakage in CDPRs. Simulations and results showed the flexibility and robust performances of it w.r.t. commonly used control.

I.5.2 Future Perspectives

As a starting point, all the proposed techniques and results require to be experimentally validated.

With this in mind, implementations and tests have been already started on CRAFT for assessing the reliability of the TDAs' results. However, further investigation has to be done: for instance, evidence of the discontinuities of the LP method, theoretically

established, should be practically found and a few other sensor issues, causing signal noise, should be tackled before considering the work as concluded.

The same can be inferred for the sensitivity analysis. For this latter, the sensors and the hardware to accomplish test are already set up. Anyway, before proceeding further, the definition of sensitivity needs to be generalised to account for general external wrenches and not only forces. Furthermore, as mentioned before, the stiffness model has to be included in the simulations. The final aim here, is to gain useful information to be used to tension control.

Regarding the control part, the subsequent idea is to implement the SM-APID on CRAFT. Test its performances w.r.t. the actual control and also stress it under cable breakage conditions.

The combinations of these three works should provide a robust, tension control scheme able to automatically manage external disturbances and model inaccuracies.

Part II

Persistent Manifolds

Chapter II.1

Introduction

II.1.1 Open Problems and Contributions

At the end of 20^{th} century, the development of screw theory, as a tool for designing robots, reached its maximum intensity and interest among researchers. However, lately, the discovery and advancement of electronics and computer science changed completely the panorama of robotics. Indeed, subsequently, several fundamental problems were left unsolved to face new other challenges. In this context, one of the major issues is studying 5-systems that guarantee *full-cycle mobility*. This question arises naturally by looking at Table II.1.3. Indeed, no 5-dimensional connected subgroups of $SE(3)$ exists. Thus, asking for the existence of 5-chains that still guarantee full-cycle mobility, even if not invariants, motivates the present study on persistent systems. Once their existence was proven, their synthesis and classification became the challenge to be solved. So far, as already discussed, only $2, 3$ and 4 persistent systems were classified: the screw systems generated by the chain moves in space like a rigid body while the chain moves.

Regarding their identification, given a screw system, not in canonical form, *how can be recognised in the sense of Hunt?*

Group theory can be used. Indeed, isotropy and completion groups discern among them. However, a more systematic and direct approach would be given by using polynomial invariants. This idea has been partially discussed and introduced in [89]. However, a lack of invariants prevents it from being complete and then to widespread properly.

To close, this II part deals with a first classification (not complete) of 5-persistent manifolds, investigates line motions as a spin-off of persistent manifolds studies and sets a couple of works regarding a general definition for persistent manifolds and their identifications by means of invariants. Theorem 7 stands as a novel addition within the context of existing literature, specifically presented in Sec. II.1.14. Its introduction alongside established results aims to enhance comprehension, serving as an extension of a prior literature finding.

II.1.2 Historical Notes

The word *cinématique* was coined by A.M. Ampère [90]. Typically, kinematics is defined as the branch of dynamics where actions (forces and moments) are not considered. In other words, it deals with the motions of rigid bodies without looking at what is acting on them. When adding *laws* to the terms motions, one asks how a rigid body moves when external actions are considered and then, *laws of motions* is seen as an extension of kinematics to dynamics.

To be precise, kinematics intends motion as the study of the displacements and all its derivatives such as velocity, acceleration, and so on. Hunt, in its book [91], narrows this definition by adding *geometry* to kinematics. Therefore, *kinematic geometry* refers to displacements only. Moreover, it includes small displacements and infinitesimal displacements as well. This latter allows leverage of all the concepts developed in modern mathematics that will be introduced in what follows.

Now, the importance of kinematics can be understood by posing a simple question which, in general, is also the motivation behind the necessity of using particular mathematical methods.

Is it possible to identify the architecture or topology of the mechanism that traces a given curve in space?

In other words, one asks how to build a mechanism based on the trajectory (set of successive predefined locations) it should follow. This well-known problem, in robotics, takes the name *synthesis of mechanisms*. The second part II, indeed, focuses on building up new concepts to synthesize particular types of mechanisms. There is also the reciprocal one, called *analysis of mechanisms*, where the robot architecture is known (already synthesized) and the investigation attempts to study its performances.

Driven by practical intuition and curiosity, Kempe proved that all algebraic curves can be traced by mechanisms. Later, Koenigs proved a similar theorem for spatial curves. Therefore, these works paved the way for establishing a robust bridges between curves (mathematics) and mechanisms [92], [93].

Historically, Descartes introduced coordinates and described curves by equations giving rise to the subject of Algebraic Geometry. This subject, indeed, consists in studying the properties of the set of solutions of an equation or a system of algebraic equations. This set is nowadays recognised under the name of *variety*.

Another field of mathematics, that will be used in what follows, is Differential Geometry. As the name suggests, it deals with differential calculus, developed by Newton and Leibniz, to extract the local properties (shape) of a surface. As time passed, the notion of surface was generalised to that of *manifold*: a space which, locally, looks like Euclidean space at every point.

Then, the link between these two subjects and robotics comes with the notion of Groups. This concept was introduced by Cayley generalising the notion of *substitutions* used for studying the symmetries of algebraic equations. Galois introduced this notion while he was studying the properties of the roots for polynomial equations. Subsequently, the notions of continuous group, introduced by Lie and Killing were used to describe the isometries of $\mathbb{R}^3$ which is the one mostly used in robotics.

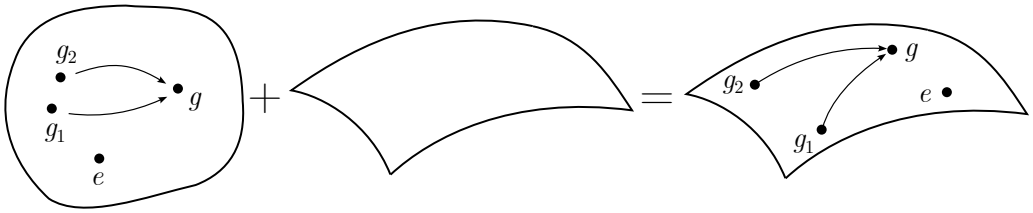

Figure II.1.1: Elementary structure of a Lie Group.

With this in mind, in the next sections, the basic mathematical tools will be recalled and then used to deal with chosen open problems.

II.1.3 Lie Groups and Group Actions

Let's start with the notion of groups and Lie groups that cover a main role in describing the kinematics of mechanisms in general [89].

A practical property of rigid bodies is that they displace noncommutatively. This naturally leads to continuous group structure to describe how their pose evolves in the Euclidean space. Observe that, saying *continuous group* is a synonym for the term Lie Group structure.

Definition 3. *A Lie Group G is a set of elements embodying simultaneously the properties of a group and smooth manifold.*

The group properties are well known and recalled hereby

Definition 4. *Let G be a set of elements $g_1, g_2, g_3 \in G$ hence the following properties holds*

1. *Associativity:* $(g_1 g_2)g_3 = g_1(g_2 g_3)$;
2. *Identity element:* $g_1 e = e g_1 = g_1$;
3. *Inverse element:* $g_1 g_1^{-1} = g_1^{-1} g_1 = e$.

The manifold property guarantees that any two points on G can be related by a smooth path (change of coordinates) and, moreover, at any point $g \in G$ one can define a differential dg tangent to G; so by Definition 3 one can visualize a Lie Group as in Fig.II.1.1. Observe that, perturbations from the identity element play a special role as infinitesimal displacement since they resemble into twists vectors[1].

A group action is essentially a function which transform an element of a given space into another of the same space as follows

[1]This is not true in general. Indeed, it is valid only if $G = SE(3)$.

Definition 5. *Let G be a Lie group. Hence, G acts on a set X if there exists a function $\rho : G \times X \to X$ such that*

1. $\rho(e, x) = x \quad \forall x \in X$;
2. $\rho(g_1 g_2, x) = \rho(g_1, \rho(g_2, x)) \quad \forall x \in X$.

Hence, ρ is the so-called action of G on X.

An important observation is related to those groups that can be matrix-represented. Indeed, in some cases, the action can be represented as $\rho(\mathbf{A}, \mathbf{x}) = \mathbf{A}\mathbf{x}$ with $\mathbf{A} \in G$ and $\mathbf{x} \in X$.

Before looking at the particular groups used in robotics, two important definitions are recalled: these will be necessary all the way down when discussing the classification of screw systems or the generalisation of persistent manifolds definition, for example.

Definition 6. *Let's G be a group. Then, if $x \in X$ is a point in a space X, all the elements g that leaves the point fixed constitute a subset*

$$\mathcal{I}_x =: \{g \in G \,|g(x) = x\},$$

called Isotropy subgroup of x.

Definition 7. *Let G be a group. Then, the set of all the elements of X reachable from some point by the action is called orbit of the group*

$$\mathcal{O}_x =: \{y \in X \,|g(x) = y\}.$$

A recurring group in robotics is the Special Orthogonal group

$$SO(3) = \{\mathbf{A} \in \mathbb{R}^{3\times 3} |\, \mathbf{A}^T\mathbf{A} = \mathbf{I},\, \det(\mathbf{A}) = 1\} \tag{II.1.1}$$

it represents the spatial rotations for rigid bodies. Now, since the motion of a rigid body in the Euclidean space is made by rotations and translations [94], [95] one could argue that, a general motion can be represented by a group given by the direct product between $SO(3)$ and $\mathbb{R}^3$. Mathematically

$$SE(3) = SO(3) \times \mathbb{R}^3, \tag{II.1.2}$$

however, this is not physical. Indeed, recalling the composition of rigid displacements from classical Newtonian mechanics book [96], one has

$$(\mathbf{A}_2, \mathbf{a}_2)(\mathbf{A}_1, \mathbf{a}_1) = (\mathbf{A}_2\mathbf{A}_1, \mathbf{A}_2\mathbf{a}_1 + \mathbf{a}_2), \tag{II.1.3}$$

suggesting that, instead of the direct product, the semi-direct is the appropriate ones to represents the Special Euclidean group

$$SE(3) = SO(3) \ltimes \mathbb{R}^3. \tag{II.1.4}$$

Note that, $SE(n)$ is not defined as a matrix group. However, a *representation*, can be used [89]. Formally a representation is a homomorphism from the group to the General Linear group $GL(n)$. For $SE(n)$ there exist an $n+1$ dimensional representation such that $SE(n) \to GL(n+1)$ is an injective homomorphism that leads to

$$(\mathbf{A}, \mathbf{a}) \mapsto \begin{pmatrix} \mathbf{A} & \mathbf{a} \\ \mathbf{0}^T & 1 \end{pmatrix}. \tag{II.1.5}$$

Hence, a rigid body displacement can be represented as

$$\begin{pmatrix} \mathbf{p}' \\ 1 \end{pmatrix} = \begin{pmatrix} \mathbf{A} & \mathbf{a} \\ \mathbf{0}^T & 1 \end{pmatrix} \begin{pmatrix} \mathbf{p} \\ 1 \end{pmatrix}, \tag{II.1.6}$$

where $(\mathbf{A}, \mathbf{a})$ is the action that makes the transformation (displacement) on points while $\mathbf{p}$ and $\mathbf{p}'$ are points in the body and reference frames, respectively.

A natural question arising when considering successive displacements concerns how to change reference frame. Typically, translating this into an equation is equivalent to apply the well-known *conjugation*

$$\rho(g_1, g_2) = g_2 g_1 g_2^{-1}, \tag{II.1.7}$$

evidently defined as the group action on itself.

II.1.4 Lie Algebra

In this section, a brief introduction to Lie Algebra and their representation is given. Lie Algebra's arise naturally from Lie groups (associated with a manifold). Indeed, often, the Lie Algebra is known as the infinitesimal generator of the group [97].

Let us try to build up the definition step by step. Firstly, it is required to settle the definition of tangent vectors to a manifold. Typically, one can take a path through the identity in a group G that is $\gamma : \mathbb{R} \to G$ such that $\gamma(0) = e$. Now, one can say that different paths are equivalent if their first derivatives, restricted at 0, coincide. A tangent vector is an equivalence class for this relation. The space of equivalence classes can be shown to be a vector space.

Another thing consists in asking what is the influence of the product on the group in their tangent spaces. Consider two paths in the group $p(t), q(s) : \mathbb{R} \to G$. Their first derivative at the identity is

$$\frac{d}{dt} p(t)\big|_{t=0} = \mathbf{Y}, \quad \frac{d}{ds} p(s)\big|_{s=0} = \mathbf{X}. \tag{II.1.8}$$

Now, to obtain the tangent vector in any local reference one needs to apply the conjugation $q(s)p(t)q(s)^{-1}$ and, subsequently, to restrict their derivatives to the identity

$$\frac{d}{ds}\Big(\frac{d}{dt}\big(q(s)p(t)q(s)^{-1}\big)\big|_{t=0}\Big)\big|_{s=0} = \frac{d}{ds}q(s)\big|_{s=0}\mathbf{Y}q(0)^{-1} + q(0)\mathbf{Y}\frac{d}{ds}q(s)^{-1}\big|_{s=0} = \\ = \mathbf{XY} - \mathbf{YX}, \tag{II.1.9}$$

which leads to the so-called *commutator* for the tangent space. When referring to a Lie Group, this is called *Lie Bracket*.

Hence, the definition of a Lie Algebra structure can derived as

Definition 8. *A Lie Algebra* $\mathfrak{g}$ *is a vector space over a field* k *with a bilinear bracket* $[\cdot,\cdot]:\mathfrak{g}\times\mathfrak{g}\to\mathfrak{g}$ *such that the following properties hold*

1. *skew-symmetry:* $[x,y] = -[y,x]$,
2. *Jacoby-Identity:* $[x,[y,z]] + [z,[x,y]] + [y,[z,x]] = 0$,

$\forall x, y \in \mathfrak{g}$.

II.1.5 Lie Algebra of $SO(3)$ and $SE(3)$

In this section, the Lie Algebra of the Lie Groups used in robotics and their main properties are explicitly reported. Let us start with the $SO(3)$ and take $\gamma(t) = \mathbf{R}(t) \in SO(3)$ recalling that $\mathbf{R}(0) = \mathbf{I}$ and $\mathbf{R}(t)^T\mathbf{R}(t) = \mathbf{I}$. Differentiating last property

$$\frac{d}{dt}\mathbf{R}(t)^T\mathbf{R}(t) + \mathbf{R}(t)^T\frac{d}{dt}\mathbf{R}(t) = 0, \tag{II.1.10}$$

when $t = 0$

$$\dot{\mathbf{R}}(0)^T + \dot{\mathbf{R}}(0) = 0, \tag{II.1.11}$$

hence, the Lie Algebra is given by the set of anti-symmetric matrices and will be named $\mathfrak{so}(3)$.

When $SE(3)$ is considered, one can take

$$\gamma : t \to \begin{pmatrix} \mathbf{R}(t) & \mathbf{x}(t) \\ \mathbf{0}^T & 1 \end{pmatrix}, \tag{II.1.12}$$

as a curve in the group. Then, taking the derivative, one obtain an element of the form

$$\mathbf{S} = \begin{pmatrix} \mathbf{\Omega} & \mathbf{v} \\ \mathbf{0}^T & 0 \end{pmatrix}, \tag{II.1.13}$$

where $\mathbf{\Omega} \in \mathbb{R}^{3\times3}$ is a skew matrix and $\mathbf{v} \in \mathbb{R}^3$ which represent an element of the algebra $\mathfrak{se}(3)$. Furthermore, $\mathbf{S}$ is also known as twist, in matrix form. The same, can also be represented in vector form as

$$\mathbf{s} = \begin{pmatrix} \boldsymbol{\omega} \\ \mathbf{v} \end{pmatrix}. \tag{II.1.14}$$

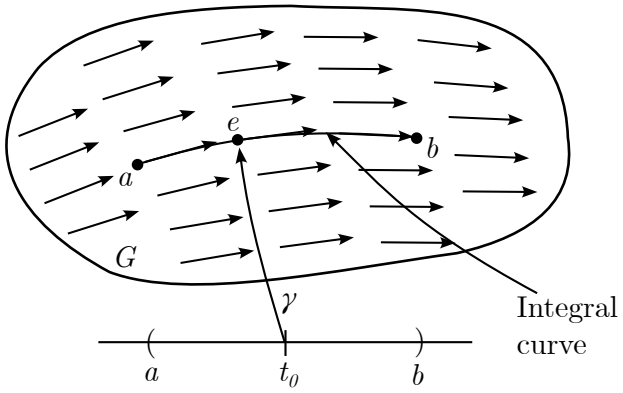

Figure II.1.2: A left-invariant vector field on G generated by left-shifting the tangent vector at the identity.

II.1.6 The Exponential map

Lie Algebra elements can be seen as *left-invariant vector fields* on the group. Given a tangent vector at the identity, one can left-act on it and obtain a tangent at every group element. In other words, one produces a vector field by translating the tangent vector at the identity, see Fig.II.1.2. Thus, if $\mathbf{X}$ is the tangent at the identity, $g\mathbf{X}$ will be the tangent at g. Hence, there is a one-to-one correspondence between tangent vectors at the identity and left-invariant vector fields.

Integral curves of a vector field are smooth curves of its points, such a curve would satisfy the differential equation

$$\frac{d\gamma}{dt} = \gamma\mathbf{X}, \tag{II.1.15}$$

whose analytical solution is

$$\gamma = e^{t\mathbf{X}}, \tag{II.1.16}$$

that passes through the identity when $t = 0$. Observe that, the exponential of a matrix $\mathbf{X}$ can be represented in power series as

$$e^{\mathbf{X}} = 1 + \mathbf{X} + \frac{\mathbf{X}}{2} + \cdots + \frac{\mathbf{X}^n}{n!} + \ldots. \tag{II.1.17}$$

The Exponential makes the link from the Lie Algebra to the group. In general, this map is not one-to-one and not onto. However, locally, the exponential maps a neighbourhood of $\mathbf{0}$, $\mathcal{N}_\mathbf{0}$, in the Lie algebra $\mathfrak{g}$ to a neighbourhood of the identity, $\mathcal{N}_\mathbf{I}$, in the group G.

II.1.7 The Adjoint representation

As for the group, which posses an action over the elements, one can ask how this action is represented on the algebra. Indeed, there is a natural representation of the group on

its Lie Algebra. This latter is known as *adjoint representation*. Therefore, assume a path in the group as

$$\gamma : t \to \mathbf{I} + t\mathbf{X} + t^2\mathbf{Q}(t), \tag{II.1.18}$$

where $\mathbf{X}$ is a Lie algebra element and $\mathbf{Q}(t)$ ensures that the image of the path stays in the group. Conjugating by g and differentiating setting $t = 0$, one gets

$$\mathrm{Ad}(g)\mathbf{X} = g\mathbf{X}g^{-1}, \tag{II.1.19}$$

which is the *adjoint action*. The shape of this action, when considering $SE(3)$ as a group is

$$\mathrm{Ad} : SE(3) \times \mathfrak{se}(3) \to \mathfrak{se}(3), \tag{II.1.20}$$

$$\mathrm{Ad} : (\mathbf{R}, \mathbf{t})(\boldsymbol{\omega}, \mathbf{v}) \mapsto (\mathbf{R}\boldsymbol{\omega}, \mathbf{TR}\boldsymbol{\omega} + \mathbf{Rv}), \tag{II.1.21}$$

explicitly

$$\mathrm{Ad}(g)\mathbf{s} = \begin{pmatrix} \mathbf{R} & \mathbf{0} \\ \mathbf{TR} & \mathbf{R} \end{pmatrix} \begin{pmatrix} \boldsymbol{\omega} \\ \mathbf{v} \end{pmatrix} = \begin{pmatrix} \mathbf{R}\boldsymbol{\omega} \\ \mathbf{TR}\boldsymbol{\omega} + \mathbf{Rv} \end{pmatrix}, \tag{II.1.22}$$

where $\mathbf{R} \in SO(3)$ and $\mathbf{T}$ is a skew-symmetric matrix representing a translations $\mathbf{t} \in \mathbb{R}^3$.

II.1.8 Screws, Twists and Plücker coordinates

Physically, the twists represent the first-order kinematic of a rigid body. Ball, in his treatise [98], introduced the concept of *screws*. In particular, this latter are elements of projective space that is, rays through the origin in the Lie Algebra $\mathfrak{se}(3)$. Formally

Definition 9. *A screw $\$(h)$ is a line in $\mathbb{R}^3$ together with a scalar quantity, h, called pitch. To uniquely specify the axis of the screw, four independent parameters are needed. The pitch gives a fifth. So, the set of all screws is a five-parameters family. Analytically, the pitch is*

$$h = \frac{\boldsymbol{\omega} \cdot \mathbf{v}}{\boldsymbol{\omega} \cdot \boldsymbol{\omega}}. \tag{II.1.23}$$

Definition 10. *A twist $\mathbf{s}$ is a screw $\$(h)$ together with a scalar quantity, $||\boldsymbol{\omega}|| \neq 0$ called amplitude. Six independent parameters are needed to define a twist.*

Graphically, a screw can be identified by taking a point $\mathbf{p}$

$$\mathbf{p} = \frac{\boldsymbol{\omega} \times \mathbf{v}}{\boldsymbol{\omega} \cdot \boldsymbol{\omega}}, \quad ||\boldsymbol{\omega}|| \neq 0, \tag{II.1.24}$$

on the screw itself, the meaning can be understood by looking Fig.II.1.3. It is worth observing that the infinitesimal displacement (screw motion) assumes a different physical meaning depending on the value of $\boldsymbol{\omega}$ and $\mathbf{v}$. Indeed, if $\boldsymbol{\omega} = 0$, $h = \infty$ and the screw

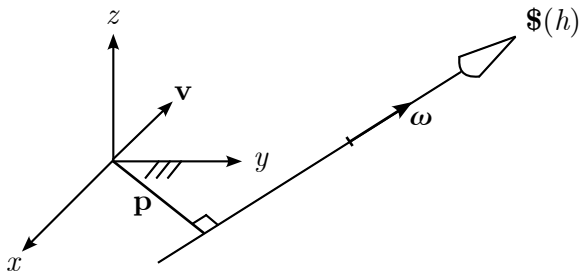

Figure II.1.3: Plücker coordinates: physical meaning.

motion will be a translation. Instead, when $\mathbf{v} = 0$, $h = 0$ and the screw motion will be a pure rotation about $\boldsymbol{\omega}$.

So far, the Lie Bracket has been defined but not physically interpreted. Therefore, with the above-mentioned physical insight, one can understand that, given $\mathbf{s}_1 = (\boldsymbol{\omega}_1, \mathbf{v}_1)$ and $\mathbf{s}_2 = (\boldsymbol{\omega}_2, \mathbf{v}_2)$, then

$$[\mathbf{s}_1, \mathbf{s}_2] = \begin{pmatrix} \boldsymbol{\omega}_1 \times \boldsymbol{\omega}_2 \\ \boldsymbol{\omega}_1 \times \mathbf{v}_2 + \mathbf{v}_1 \times \boldsymbol{\omega}_2 \end{pmatrix}, \tag{II.1.25}$$

that is a twist orthogonal to both $\mathbf{s}_1$ and $\mathbf{s}_2$.

II.1.9 The Klein Quadric

The pair $\boldsymbol{\omega}$ and $\mathbf{v}$, generally seen as six homogeneous coordinates defining a line in $\mathbb{R}^3$, finds a particular correspondence in the projective space $\mathbb{PR}^5$.

Now, the terms *particular*, used above, wanted to emphasize that not all the points in $\mathbb{PR}^5$ represent lines in $\mathbb{R}^3$. Indeed, for a line one has $\boldsymbol{\omega} = \mathbf{p}_1 - \mathbf{p}_2$ and $\mathbf{v} = \mathbf{p}_1 \times \mathbf{p}_2$, with $\mathbf{p}_1, \mathbf{p}_2$ points on the line itself, which set $\boldsymbol{\omega}^T \mathbf{v} = 0$. In terms of Plücker coordinates

$$\omega_x v_x + \omega_y v_y + \omega_z v_z = 0. \tag{II.1.26}$$

This is an homogeneous equation of degree 2 whose solutions lie on a four-dimensional quadric in $\mathbb{PR}^5$. This latter quadric is called as Klein quadric. Points of $\mathbb{PR}^5$ not on the Klein quadric are not lines in $\mathbb{R}^3$. Conversely, no line in $\mathbb{R}^3$ has $\boldsymbol{\omega} = 0$. Therefore, $\omega_x = \omega_y = \omega_z = 0$ defines a 2-dimensional plane in the quadric identifying lines which are not real. Points lying on this 2-plane are known as lines at infinity.

To conclude, there is a correspondence between lines in $\mathbb{R}^3$ and Klein quadric (excluding the 2-plane).

II.1.10 Dual Quaternion and Study quadric

This section seeks to revise some mathematical concepts necessary to describe and represent rigid motions.

The group of proper isometries of $\mathbb{R}^3$ can be represented in the tensor product of the quaternions $\mathbb{H}$ with the ring of dual numbers $\mathbb{D}$ as $\mathbb{H} \otimes \mathbb{D}$. A typical dual quaternion has the form $\mathbf{h} = \mathbf{h}_0 + \varepsilon \mathbf{h}_1$, where $\mathbf{h}_0$ and $\mathbf{h}_1$ are quaternions and ε is the dual unit which commutes with scalars and quaternions and squares to zero, $\varepsilon^2 = 0$. The quaternions have the form

$$\mathbf{h}_0 = a_0 + a_1\mathbf{i} + a_2\mathbf{j} + a_3\mathbf{k}, \quad \mathbf{h}_1 = c_0 + c_1\mathbf{i} + c_2\mathbf{j} + c_3\mathbf{k}, \tag{II.1.27}$$

Since dual quaternions represent rigid body motions, $\mathbf{h}_0$ counts for the rotational part while $\mathbf{h}_1$ contributes to the translation one, vectors $\mathbf{i}, \mathbf{j}$ and $\mathbf{k}$ are known as generators which satisfy the relations $\mathbf{i}^2 = \mathbf{j}^2 = \mathbf{k}^2 = -1$ as well as $\mathbf{ij} = \mathbf{k}$, $\mathbf{jk} = \mathbf{i}$, $\mathbf{ki} = \mathbf{j}$ and so on. For unitary quaternions, another property satisfied is $\mathbf{h}_0\mathbf{h}_0^- = 1$ where $\mathbf{h}_0^- = a_0 - a_1\mathbf{i} - a_2\mathbf{j} - a_3\mathbf{k}$ is the quaternion conjugate.

Therefore, to represent a rotation about the origin of a given point $\mathbf{p} = x\mathbf{i} + y\mathbf{j} + z\mathbf{k}$ one has

$$\mathbf{p}' = \mathbf{h}_0\mathbf{p}\mathbf{h}_0^-. \tag{II.1.28}$$

Whereas, for a general rigid motion, the dual numbers are employed and the action on points of $\mathbb{R}^3$ represented by quaternions of the form $\mathbf{1} + \varepsilon\mathbf{p}$ is then given as

$$\mathbf{1} + \varepsilon\mathbf{p}' = (\mathbf{h}_0 + \varepsilon\mathbf{h}_1)(\mathbf{1} + \varepsilon\mathbf{p})(\mathbf{h}_0^- - \varepsilon\mathbf{h}_1^-). \tag{II.1.29}$$

Observe that in both cases $\mathbf{h}_0$ and $-\mathbf{h}_0$ or $\mathbf{h}$ and $-\mathbf{h}$ represent the same rotation or displacements, respectively, because of the double covering nature of quaternion.

The elements of $SE(3)$ can be represented by points in the projective space $\mathbb{PR}^7$ by taking the quaternion coefficients $(a_0 : a_1 : a_2 : a_3 : c_0 : c_1 : c_2 : c_3)$ as homogeneous coordinates in $\mathbb{PR}^7$. Notice that, not every dual quaternion represents a rigid displacement, thus the conditions to be satisfied are

$$\mathbf{h}_0\mathbf{h}_0^- = 1 \quad \text{and} \quad \mathbf{h}_0\mathbf{h}_1^- + \mathbf{h}_1\mathbf{h}_0^- = 0, \tag{II.1.30}$$

which in coordinates become

$$a_0^2 + a_1^2 + a_2^2 + a_3^2 = 1 \quad \text{and} \quad a_0c_0 + a_1c_1 + a_2c_2 + a_3c_3 = 0, \tag{II.1.31}$$

respectively. As the constraint $a_0^2 + a_1^2 + a_2^2 + a_3^2 = 1$ is redundant, only the quadric equation $a_0c_0 + a_1c_1 + a_2c_2 + a_3c_3 = 0$ have to be effectively satisfied. This latter is known as Study quadric and discriminates, among all the possible combinations of coordinates of points, the ones that are indeed rigid motions. Thus, only points lying on the Study quadric are considered rigid displacements and then in one-to-one correspondence with $SE(3)$. Lastly, among these points, an exception have to be considered as the elements satisfying the 3-plane equation $a_0 = a_1 = a_2 = a_3 = 0$ correspond to elements at infinity and are then referred to as A_∞.

As a conclusion of this section, one can observe that rotational matrices can be written in terms of Study parameters as

$$\mathbf{R} = \frac{1}{\Delta}\begin{pmatrix} a_0^2+a_1^2-a_2^2-a_3^2 & 2(a_1a_2-a_0a_3) & 2(a_1a_3+a_0a_2) \\ 2(a_1a_2+a_0a_3) & a_0^2-a_1^2+a_2^2-a_3^2 & 2(a_2a_3-a_0a_1) \\ 2(a_1a_3-a_0a_2) & 2(a_2a_3+a_0a_1) & a_0^2-a_1^2-a_2^2+a_3^2 \end{pmatrix}, \tag{II.1.32}$$

where $\Delta = \mathbf{h}_0\mathbf{h}_0^-$ and, therefore also

$$\mathbf{TR} = \frac{2}{\Delta}\begin{pmatrix} 2(a_2c_2+a_3c_3) & -a_0c_3+a_1c_2+a_2c_1-a_3c_0 & a_0c_2+a_1c_3+a_2c_0+a_3c_1 \\ a_0c_3+a_1c_2+a_2c_1+a_3c_0 & -2(a_1c_1+a_3c_3) & -a_0c_1-a_1c_0+a_2c_3 \\ -a_0c_2+a_1c_3-a_2c_0+a_3c_1 & a_0c_1+a_1c_0+a_2c_3+a_3c_2 & -2(a_1c_1+a_2c_3) \end{pmatrix}, \tag{II.1.33}$$

additional information can be found in [89].

II.1.11 Screw Systems

A *screw system* is a vector subspace of $\mathfrak{se}(3)$. Hunt [91] was the first that proposed a coarse classification of them. Subsequently, Donelan and Gibson [99] gave a formal, rather mathematical, classification. In this context, Selig [89], retrieved Gibson-Hunt's classification by using group theory. This latter is the one considered and reported here.

Given an n-system or n-dimensional vector subspace, one can always find n linearly independent screws that generate it. Now, a formal classification requires the notion of equivalence[2].

Definition 11. *Two screw systems,* $S_1 = \text{span}(\mathbf{s}_1, \mathbf{s}_2, \ldots, \mathbf{s}_n)$ *and* $S_2 = \text{span}(\mathbf{s}_1^{'}, \mathbf{s}_2^{'}, \ldots, \mathbf{s}_n^{'})$ *are equivalent if there is a rigid transformation* $\mathbf{M} \in GL(n)$ *that can transform* S_1 *into* S_2*.*

Remark 20. *Classifying screw systems can be seen to be equivalent to describe the orbits of the group.*

While speaking about transformation on screws, one could ask whether invariant forms, with respect to an action of $SE(3)$, exist. In this regard, it is possible to show that only two invariant bilinear forms can be found. The first one is the so-called reciprocal product, given two twists $\mathbf{s}_1$, $\mathbf{s}_2$, one has

$$\mathbf{s}_1^T\mathbf{Q}_0\mathbf{s}_2 = (\boldsymbol{\omega}_1, \mathbf{v}_1)\begin{pmatrix} \mathbf{0} & \mathbf{I} \\ \mathbf{I} & \mathbf{0} \end{pmatrix}\begin{pmatrix} \boldsymbol{\omega}_2 \\ \mathbf{v}_2 \end{pmatrix}, \tag{II.1.34}$$

and the second is the Killing form

[2]In what follows, as in the literature, screw \$ and twist $\mathbf{s}$ will be confused. The distinction will be explicitly made when necessary.

$$\mathbf{s}_1^T \mathbf{Q}_\infty \mathbf{s}_2 = (\boldsymbol{\omega}_1, \mathbf{v}_1) \begin{pmatrix} 2\mathbf{I} & \mathbf{0} \\ \mathbf{0} & \mathbf{0} \end{pmatrix} \begin{pmatrix} \boldsymbol{\omega}_2 \\ \mathbf{v}_2 \end{pmatrix}. \tag{II.1.35}$$

Invariance here means that

$$\mathrm{Ad}(g)^T \mathbf{Q}_0 \,\mathrm{Ad}(g) = \mathbf{Q}_0 \quad \text{and} \quad \mathrm{Ad}(g)^T \mathbf{Q}_\infty \,\mathrm{Ad}(g) = \mathbf{Q}_\infty. \tag{II.1.36}$$

Each symmetric bilinear form determines a quadratic form. In particular, the general matrix representing both these forms is

$$\mathbf{Q}_p = \alpha \mathbf{Q}_\infty + \beta \mathbf{Q}_0, \tag{II.1.37}$$

where $\alpha, \beta \in \mathbb{R}$ and $\mathbf{Q}_p$ are denoted as pitch quadrics. Hence, the quadric equation in the Plücker coordinates is

$$2\alpha(\boldsymbol{\omega} \cdot \boldsymbol{\omega}) + \beta(\boldsymbol{\omega} \cdot \mathbf{v}) = 0. \tag{II.1.38}$$

The introduction of these quadrics is fundamental to classify screw systems. Indeed, the reciprocal product can be used to identify the so-called reciprocal screw systems S_r. This latter is an unique set of screws found as

$$\mathbf{s}_i^T \mathbf{Q}_0 \mathbf{s} = 0 \quad \forall\, \mathbf{s}_i \in S,\, \mathbf{s} \in S_r, \tag{II.1.39}$$

these constitute a set of equations with six unknown coordinates of $\mathbf{s}$. Evidently, the reciprocal systems have $6 - n$ linearly independent screws.

Remark 21. *Using this fact, only* $1, 2$ *and* 3*-systems have to be classified as the reciprocal, being complementary, are automatically classified as well.*

At this point, two concepts are left to fully grasp Hunt's classification. Let's start with the concept of *completion group*.

Suppose $\mathbf{s}_1, \mathbf{s}_2, \ldots, \mathbf{s}_n$ generates a vector subspace of $\mathfrak{se}(3)$ which, in general, it is not a subalgebra,

$$S_1 = \mathrm{span}(\mathbf{s}_1, \mathbf{s}_2, \ldots, \mathbf{s}_n). \tag{II.1.40}$$

Defining the commutators $[S_1, S_1]$ as

$$[S_1, S_1] = \mathrm{span}([\mathbf{s}_i, \mathbf{s}_j]) \quad \text{s.t.} \quad \mathbf{s}_i, \mathbf{s}_j \in S_1, \tag{II.1.41}$$

then, because it is not an algebra, as mentioned, one could get screws outside S_1, hence to include them

$$S_2 = S_1 + [S_1, S_1]. \tag{II.1.42}$$

Observe that, if $[S_1, S_1] = 0$ then S_1 is a commutative subalgebra[3]. If, $S_2 = S_1$ then S_2 is a subalgebra since the brackets lie inside S_2 itself. When these relations do not hold, $S_1 \subset S_2$ is the only information one gets.

[3]In general, commutative means $[S_i, S_j] = -[S_j, S_i]$.

Completion Group	Gibson-Hunt Type	Normal Form	Isotropy Group
$\mathbb{R}^2$	IIC	$\mathbf{s}_1 = (0,0,0,1,0,0)^T$ $\mathbf{s}_2 = (0,0,0,0,1,0)^T$	$E(2) \times \mathbb{R}$
$SO(2) \times \mathbb{R}$	IB^0	$\mathbf{s}_1 = (1,0,0,0,0,0)^T$ $\mathbf{s}_2 = (0,0,0,1,0,0)^T$	$O(2) \times \mathbb{R}$
$SO(3)$	IIA $(p = 0)$	$\mathbf{s}_1 = (1,0,0,0,0,0)^T$ $\mathbf{s}_2 = (0,1,0,0,0,0)^T$	$O(2)$
$H_p \ltimes \mathbb{R}^2$	IIB $(p \neq 0)$	$\mathbf{s}_1 = (1,0,0,p,0,0)^T$ $\mathbf{s}_2 = (0,0,0,0,1,0)^T$	$\mathbb{Z}_2 \times \mathbb{Z}_2 \times \mathbb{R}^2$
$SE(2)$	IIB $(p = 0)$	$\mathbf{s}_1 = (1,0,0,0,0,0)^T$ $\mathbf{s}_2 = (0,0,0,0,1,0)^T$	$\mathbb{Z}_2 \times \mathbb{Z}_2 \times \mathbb{R}^2$
$SE(2) \times \mathbb{R}$	IB $(p \neq 0)$	$\mathbf{s}_1 = (1,0,0,0,0,0)^T$ $\mathbf{s}_2 = (0,0,0,1,p,0)^T$	$\mathbb{Z}_2 \times \mathbb{Z}_2 \times \mathbb{R}$
$SE(3)$	IIA $(p \neq 0)$	$\mathbf{s}_1 = (1,0,0,p,0,0)^T$ $\mathbf{s}_2 = (0,1,0,0,p,0)^T$	$O(2)$
$SE(3)$	IA $(p_a \neq p_b)$	$\mathbf{s}_1 = (1,0,0,p_a,0,0)^T$ $\mathbf{s}_2 = (0,1,0,0,p_b,0)^T$	$\mathbb{Z}_2 \times \mathbb{Z}_2$

Table II.1.1: 2-systems Gibson-Hunt Classification: equivalence by means of isotropy and completion groups.

However, this process can be iterated knowing that it will stop [4] as $\mathfrak{se}(3)$ is six-dimenstional only. So, in general one has

$$S_{i+j} = S_i + [S_i, S_j]. \tag{II.1.43}$$

Finally, the subalgebra found at the end of the process is the completion group of S_1.

Remark 22. *Every screw system has an unique combination of completion and isotropy group.*

Lastly, the second concept one needs rely on computing the isotropy group. Based on Isotropy group Definition 6, elements of the isotropy group satisfy

$$(\text{Ad}(g)\mathbf{s}_1) \wedge \cdots \wedge (\text{Ad}(g)\mathbf{s}_n) = \mathbf{s}_1 \wedge \cdots \wedge \mathbf{s}_n, \tag{II.1.44}$$

where the symbol $\wedge$ represents the wedge product. Finally, computing them for the $2,3$-systems in canonical form one gets the following Tables II.1.1 and II.1.2; see [89] for more details.

[4] Proof can be found in [89].

Completion Group	Gibson-Hunt Type	Normal Form	Isotropy Group
$\mathbb{R}^3$	IID	$\mathbf{s}_1 = (0,0,0,1,0,0)^T$ $\mathbf{s}_2 = (0,0,0,0,1,0)^T$ $\mathbf{s}_3 = (0,0,0,0,0,1)^T$	$SE(3)$
$SO(3)$	IIA ($p=0$)	$\mathbf{s}_1 = (1,0,0,0,0,0)^T$ $\mathbf{s}_2 = (0,1,0,0,0,0)^T$ $\mathbf{s}_3 = (0,0,1,0,0,0)^T$	$SO(2)$
$SE(2)$	IIC ($p=0$)	$\mathbf{s}_1 = (1,0,0,0,0,0)^T$ $\mathbf{s}_2 = (0,0,0,0,1,0)^T$ $\mathbf{s}_3 = (0,0,0,0,0,1)^T$	$E(2)\times\mathbb{R}$
$H_p \ltimes \mathbb{R}^2$	IIC ($p\neq 0$)	$\mathbf{s}_1 = (1,0,0,p,0,0)^T$ $\mathbf{s}_2 = (0,0,0,0,1,0)^T$ $\mathbf{s}_3 = (0,0,0,0,0,1)^T$	$E(2)\times\mathbb{R}$
$SE(2)\times\mathbb{R}$	IC ($p\neq 0$)	$\mathbf{s}_1 = (1,0,0,0,0,0)^T$ $\mathbf{s}_2 = (0,0,0,0,1,0)^T$ $\mathbf{s}_2 = (0,0,0,1,0,p)^T$	$\mathbb{R}^2$
$SE(2)\times\mathbb{R}$	IC^0	$\mathbf{s}_1 = (1,0,0,0,0,0)^T$ $\mathbf{s}_2 = (0,0,0,0,1,0)^T$ $\mathbf{s}_3 = (0,0,0,1,0,0)^T$	$\mathbb{Z}_2\times\mathbb{R}^2$
$SE(3)$	IIB	$\mathbf{s}_1 = (1,0,0,p,0,0)^T$ $\mathbf{s}_2 = (0,1,0,0,p,0)^T$ $\mathbf{s}_3 = (0,0,0,0,0,1)^T$	$E(2)$
$SE(3)$	IB_0 ($p_a\neq p_b$)	$\mathbf{s}_1 = (1,0,0,p_a,0,0)^T$ $\mathbf{s}_2 = (0,1,0,0,p_a,0)^T$ $\mathbf{s}_3 = (0,0,0,1,0,p_b)^T$	$\mathbb{Z}_2$
$SE(3)$	IB_3 ($p_a\neq p_b$)	$\mathbf{s}_1 = (1,0,0,p_a,0,0)^T$ $\mathbf{s}_2 = (0,1,0,0,p_b,0)^T$ $\mathbf{s}_3 = (0,0,0,0,0,1)^T$	$\mathbb{Z}_2\times\mathbb{Z}_2\times\mathbb{R}^2$
$SE(3)$	IIA ($p\neq 0$)	$\mathbf{s}_1 = (1,0,0,p,0,0)^T$ $\mathbf{s}_2 = (0,0,0,0,p,0)^T$ $\mathbf{s}_3 = (0,0,0,0,0,p)^T$	$SO(3)$
$SE(3)$	IA_2 ($p_a\neq p_b$)	$\mathbf{s}_1 = (1,0,0,p_a,0,0)^T$ $\mathbf{s}_2 = (0,1,0,0,p_b,0)^T$ $\mathbf{s}_3 = (0,0,1,0,0,p_b)^T$	$O(2)$
$SE(3)$	IA_1 ($p_a\neq p_b\neq p_c\neq p_a$)	$\mathbf{s}_1 = (1,0,0,p_a,0,0)^T$ $\mathbf{s}_2 = (0,1,0,0,p_b,0)^T$ $\mathbf{s}_3 = (0,0,1,0,0,p_c)^T$	$\mathbb{Z}_2\times\mathbb{Z}_2$

Table II.1.2: 3-systems Gibson-Hunt Classification: equivalence by means of isotropy and completion groups.

Regarding the Hunt type classification, the meaning of the nomenclature can be summarised as follows

- A system: have no ∞ pitch screws;
- B system: have one ∞ pitch screw;
- C system: have a line of ∞ pitch screws;
- D system: have only ∞ pitch screws.

Then, if the pitches of all the screws in the screw system are equal then one calls it a II system otherwise I.

Remark 23. *One could ask why using elements of the algebra to find particular groups such as completion and the isotropy ones. The answer lies in the Lie's third theorem.*

Theorem 2. *[Lie's Third Theorem [97]]*
Suppose G and H are Lie groups with Lie algebra $\mathfrak{g}$ and $\mathfrak{h}$ and that $f : \mathfrak{g} \to \mathfrak{h}$ is a Lie algebra homomorphism. If G is simply connected then there is a unique Lie group homomorphism $\phi : G \to H$ such that $d\phi = f$ is the differential of ϕ at the identity.

Note that a group is "simply connected" if every loop can be shrunk continuously to a point.

Lie's theorem then tells us that a group can be constructed by exponentiating its Lie algebra. Attention must be paid to this concept. The correspondence between Lie algebra and Lie groups is not one-to-one. To show this, consider that $SO(3), SU(2)$ and $O(3)$[5]. They are different groups but share the same Lie algebra.

II.1.12 Invariant Screw Systems

Hérve [100] was probably the first to use group theory in kinematics. Indeed, he was the first to identify rigid-body displacement as connected subgroup of $SE(3)$. These latter, indeed, coincide with the *full-cycle mobility* chains introduced by Hunt; see Table II.1.3.

Subsequently, because the class of these systems is relatively small (there exists only a few of them), the question of whether other types of mechanisms, guaranteeing full-cycle mobility exist, spread among researchers. Indeed, only a few of the canonical screw systems are Invariants.

In particular, Carricato's work focused, initially, on mechanisms with special motion capabilities. In [101], the classification of Translational Parallel Manipulators (TPMs) was introduced. This work represents the seed from which, a few years later, Persistent Screw Systems (PSSs) were introduced. They constitute a generalisation of full-cycle mobility ones which, in turn, were renamed Invariant Screw Systems (ISSs).

[5] $SU(2)$ and $O(3)$ are the Special Unitary and Orthogonal group, respectively. For more details, the reader is referred to [97]

Dimension	Subgroups			
1	$SO(2)$	$\mathbb{R}$	H_p	
2	$SO(2) \times \mathbb{R}$	$\mathbb{R}^2$		
3	$SO(2) \ltimes \mathbb{R}^2 = SE(2)$	$SO(3)$	$\mathbb{R}^3$	$H_p \ltimes \mathbb{R}^2$
4	$SO(2) \ltimes \mathbb{R}^3 = SE(2) \times \mathbb{R}$			
5	-			
6	$SE(3)$			

Table II.1.3: Connected subgroups of $SE(3)$.

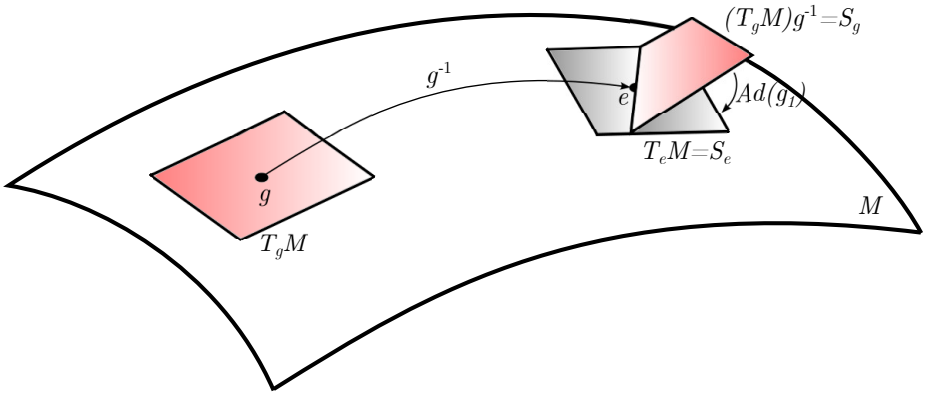

Figure II.1.4: Manifold setting: representation of the considered manifold M as a results of the intersection between the Study quadric and a generic constraints. Tangent spaces T_gM and T_eM are also represented both at g and identity e element of M.

Remark 24. *The adjective "invariant" or "persistent" refers to the properties of the screw systems. Indeed, while the associated kinematic chain moves, the vector space generated maintains some properties. In particular, if upon displacement it has the same dimension, shape and pose then the screw system is invariant. When the pose is not preserved, it becomes persistent.*

Remark 25. *Full-cycle mobility roughly means that, as the robot moves, it preserves the same instantaneous DoF. Observe that the "invariant" terms is still consistent if referred to DoF.*

II.1.13 Persistent Screw Systems

This section collects together the definition of persistence and reviews some literature results. This will give the motivation and constitute the fertile ground where to build up this work.

Let's begin with the definition of a persistent submanifold of $SE(3)$. In the following, T_gM denotes the tangent space to the submanifold M at the point $g \in M$. In particular, $T_eSE(3)$ denotes the tangent space to the identity element $e \in SE(3)$ which is isomorphic

to the Lie algebra $\mathfrak{se}(3)$.

Definition 12 (Persistent Submanifold)**.** *Let M be a submanifold of $SE(3)$. The submanifold M is persistent if and only if, for all $g \in M$ one has,*

$$T_e M = g_1 (T_g M) g^{-1} g_1^{-1}, \tag{II.1.45}$$

where g_1 is some element of $SE(3)$. Assuming that M contains the identity element e this can be expressed by writing $S_e \subset \mathfrak{se}(3)$ as the screw system at the identity and $S_g \subset \mathfrak{se}(3)$ as the screw system at g and asserting,

$$S_e = g_1 S_g g_1^{-1}, \qquad \text{for all } g \in M. \tag{II.1.46}$$

The definition requires that the conjugacy class of the screw systems determined by the tangent spaces at each point of the submanifold is the same, see Figure II.1.4. In what follows, the function Φ is defined as $\Phi : M \longrightarrow SE(3)$, given by $\Phi(g) = g_1$.

Remark 26. *Persistent 3 and 4 screw systems were systematically classified in [102], [103]. Numerical techniques have been applied to search for these systems and could be used again for 5-chains, see [104]. However, it was soon realised that the property of persistence properly belongs to submanifolds of the group of rigid-body displacements $SE(3)$. In [105], one dimensional submanifolds, that is curves, were investigated. From the start, it was appreciated that subgroups were persistent, called invariant screw systems and regarded as trivial examples. This explains why the general approach, relying on manifolds instead of looking at screw systems, is preferred and used all the way through this work.*

II.1.14 Some Properties of Persistent Submanifolds

Now, a sequence of results is hereby reported,

Theorem 3. *[Carricato and Rico Martínez [106]]*
Let $G \subset SE(3)$ be a subgroup of $SE(3)$. Then, G is a persistent submanifold of $SE(3)$, with $\Phi(g) = e$, that is the identity element in the group.

Proof. Let g be a point in the subgroup. Any path through g can be written, at least locally as,

$$\gamma(t) = e^{t\mathbf{s}} g, \tag{II.1.47}$$

where $\mathbf{s}$ is an element of the Lie algebra to the subgroup. Taking the derivative, setting $t = 0$ and translating back to the identity gives,

$$\left(\frac{d\gamma(t)}{dt} \right) \gamma(t)^{-1} \Big|_{t=0} = \mathbf{s} e^{t\mathbf{s}} g g^{-1} e^{-t\mathbf{s}} = \mathbf{s}. \tag{II.1.48}$$

That is $\Phi(g) = e$, the identity for all elements in the subgroup. □

Remark 27. *This result shows the connection between persistent and invariant manifolds. In particular, it demonstrates that the persistent ones constitute a generalisation of the invariant; as mentioned in the previous section.*

Theorem 4. *[Carricato and Zlatanov [107]]*
Let $G_1, G_2 \subset SE(3)$ be subgroups. Then, their product $M = G_1G_2$, is a persistent submanifold of $SE(3)$.

Proof. Consider a point $g_1g_2 \in M = G_1G_2$ where $g_1 \in G_1$ and $g_2 \in G_2$. Paths through this point can be written as $\gamma(t) = e^{t\mathbf{s}_1}g_1e^{t\mathbf{s}_2}g_2$, where $\mathbf{s}_1$ is an element of the Lie algebra of G_1 and $\mathbf{s}_2$ is in the Lie algebra of G_2. The Lie algebra elements corresponding to the point are given by,

$$\mathbf{s} = \left(\frac{d\gamma(t)}{dt}\right)\gamma(t)^{-1}\Big|_{t=0} = \mathbf{s}_1 + e^{t\mathbf{s}_1}g_1\mathbf{s}_2e^{t\mathbf{s}_2}g_1^{-1}e^{-t\mathbf{s}_1} \tag{II.1.49}$$

at $t = 0$ one gets $\mathbf{s} = \mathbf{s}_1 + g_1\mathbf{s}_2g_1^{-1}$. Now, since G_1 is a subgroup, it acts on its Lie algebra and there will be an element $\mathbf{s}_1' = g_1^{-1}\mathbf{s}_1g_1$. So, now,

$$\mathbf{s} = g_1(\mathbf{s}_1' + \mathbf{s}_2)g_1^{-1}. \tag{II.1.50}$$

Since $\mathbf{s}_1$ and $\mathbf{s}_2$ range over all the elements of their respective subalgebras, one can see that $(\mathbf{s}_1' + \mathbf{s}_2)$ ranges over all the elements of the sum of the subalgebras. This is not necessarily a subalgebra but it is a vector subspace of $\mathfrak{se}(3)$ and hence a screw system. Thus, in this case, the function $\Phi(g_1g_2) = g_1$ is the projection onto the first factor of the product. □

Notice that, the subgroups can overlap. Indeed, the intersection of any two subgroups must contain the identity element. In general, the intersection of two subgroups is itself a subgroup since the product of any pair of elements of G_1 will be in G_1 and, likewise, if the elements are in G_2, their product must lie in G_2. So, a pair of elements from the intersection of G_1 and G_2 will lie in both G_1 and G_2, that is, the intersection will be closed under the multiplication in the ambient group. Of course, the intersection might just be the trivial subgroup, $\{e\}$, in which case the sum of the sub algebras will be a direct sum.

Theorem 5. *[Carricato and Zlatanov [107]]*
If M is a persistent submanifold of $SE(3)$ then so is M^{-1}, that is, the manifold consisting of the inverses of all the elements in M.

Proof. If M is persistent then, for any point g in the manifold the paths through g can be written $\gamma(t) = e^{t\mathbf{s}}g$ where $\mathbf{s}$ is in the screw system determined by g. Corresponding to these paths are the paths in M^{-1} through g^{-1}, $\gamma(t)^{-1} = g^{-1}e^{-t\mathbf{s}}$. Differentiating, setting $t = 0$ and translating back to the identity one get,

$$\left(\frac{d\gamma(t)^{-1}}{dt}\right)\gamma(t)\Big|_{t=0} = -g^{-1}\mathbf{s}g. \tag{II.1.51}$$

Since M is persistent, there is a g_1 such that, for every $\mathbf{s}$ in the screw systems associated to g, $g_1 \mathbf{s} g_1^{-1}$ lies in the screw system associated with e the identity. So, for any $\mathbf{s}' = -g^{-1}\mathbf{s}g$ in the screw system associated to g^{-1} in M^{-1} one has that, $g_1 g \mathbf{s}' g^{-1} g_1^{-1}$ is in the screw system associated with the identity element. That is, $\Phi(g) = g_1 g$. □

Theorem 6. *[Wu et al. [108]]*
All symmetric subspaces of $SE(3)$ are persistent.

For the proof of this see [108]. In this case, $\Phi(g) = g^{1/2}$.

Theorem 7. *[Selig and Di Paola]*
Let G_1, G_2 and G_3 be subgroups of $SE(3)$, and let $\mathbf{s}_1$, $\mathbf{s}_2$ and $\mathbf{s}_3$ be typical element of the Lie algebras to G_1, G_2 and G_3 respectively. The product $M = G_1 G_2 G_3$ is a persistent submanifold of $SE(3)$ if the screws $[\mathbf{s}_2, \mathbf{s}_3]$, $[\mathbf{s}_2, [\mathbf{s}_2, \mathbf{s}_3]]$, $[\mathbf{s}_2, [\mathbf{s}_2, [\mathbf{s}_2, \mathbf{s}_3]]]$ and $[\mathbf{s}_2, [\mathbf{s}_2, [\mathbf{s}_2, [\mathbf{s}_2, \mathbf{s}_3]]]]$ lie in the screw system generated by $\mathbf{s}_1$, $\mathbf{s}_2$, $\mathbf{s}_3$ for all $\mathbf{s}_i$ in their respective Lie algebras.

Proof. Consider a point $g_1 g_2 g_3 \in M$, $M = G_1 G_2 G_3$ where $g_1 \in G_1$, $g_2 \in G_2$ and $g_3 \in G_3$. A path through this point can be written as $\gamma(t) = e^{t\mathbf{s}_1} g_1 e^{t\mathbf{s}_2} g_2 e^{t\mathbf{s}_3} g_3$ where $\mathbf{s}_1$ is an element of the Lie algebra of G_1, $\mathbf{s}_2$ is in the Lie algebra of G_2 and $\mathbf{s}_3$ is in the Lie algebra of G_3. Hence, a Lie algebra element corresponding to the path $\gamma(t)$ is

$$\mathbf{s} = \Big(\frac{d\gamma(t)}{dt}\Big)\gamma(t)^{-1}\Big|_{t=0} = \mathbf{s}_1 + g_1 \mathbf{s}_2 g_1^{-1} + g_1 g_2 \mathbf{s}_3 g_2^{-1} g_1^{-1}. \tag{II.1.52}$$

This, can be rewritten as

$$\mathbf{s} = g_1(\mathbf{s}_1^{'} + \mathbf{s}_2 + g_2 \mathbf{s}_3 g_2^{-1}) g_1^{-1}, \tag{II.1.53}$$

using that $g_1 \mathbf{s}_1^{'} g_1^{-1} = \mathbf{s}_1$, as in Theorem 4. The group element g_2 can be written as exponential of a generic screw $\mathbf{s}_2^{'}$ in the Lie algebra of G_2, $g_2 = e^{\mathbf{s}_2^{'}}$. Now, recall that the adjoint action of g_2 on $\mathbf{s}_3$ can be written as

$$g_2 \mathbf{s}_3 g_2^{-1} = e^{\mathrm{ad}(\mathbf{s}_2^{'})} \mathbf{s}_3. \tag{II.1.54}$$

Therefore, from [89, §4.4.3], the exponential can be written as

$$\begin{aligned} &e^{\mathrm{ad}(\mathbf{s}_2^{'})} = \\ &\mathbf{I}_6 + \frac{1}{2\theta}(3\sin\theta - \theta\cos\theta)\,\mathrm{ad}(\mathbf{s}_2^{'}) + \frac{1}{2\theta^2}(4 - 4\cos\theta - \theta\sin\theta)\,\mathrm{ad}(\mathbf{s}_2^{'})^2 + \\ &\frac{1}{2\theta^3}(\sin\theta - \theta\cos\theta)\,\mathrm{ad}(\mathbf{s}_2^{'})^3 + \frac{1}{2\theta^4}(2 - 2\cos\theta - \theta\sin\theta)\,\mathrm{ad}(\mathbf{s}_2^{'})^4, \end{aligned} \tag{II.1.55}$$

where θ is the magnitude of the rotational part of $\mathbf{s}_2^{'}$. As a matter of notation, the iterated Lie algebra commutator is written as power as follows

$$\mathrm{ad}(\mathbf{s}_2^{'})^2 \mathbf{s}_3 = [\mathbf{s}_2^{'}, [\mathbf{s}_2^{'}, \mathbf{s}_3]], \quad \mathrm{ad}(\mathbf{s}_2^{'})^3 \mathbf{s}_3 = [\mathbf{s}_2^{'}, [\mathbf{s}_2^{'}, [\mathbf{s}_2^{'}, \mathbf{s}_3]]], \ldots \tag{II.1.56}$$

this establishes the conditions for which $g_2\mathbf{s}_3 g_2^{-1}$ lies in the screw systems generated by $\mathbf{s}_1, \mathbf{s}_2$ and $\mathbf{s}_3$ for all g_2. Indeed, if commutators lie in the screw systems then the submanifold M will be persistent with $\Phi(g_1 g_2 g_3) = g_1$.

□

Remark 28. *The introduction of Theorem 7, was motivated by a combination of several factors. The first goes back to the numerical investigation of 3 persistent systems [104]. This led to the identification of a new persistent system "$S_{3,7}$" [108, §4.4] previously not found in [102]. Naturally, this raised the question of whether, indeed, the persistent systems had all been identified or not. Therefore a general result would have been perfect for verifying the existence of other persistent systems.*
The second key aspect occurs when looking at the tables identifying persistent 3-systems. Among them, one can see that these are given by the product of 3 subgroups, for example $\mathcal{HRH}$. So, the extension of the Theorem 4 to the use of three subgroups seemed a natural investigation to undertake.
The combination of both aspects motivated the construction of mentioned result and the unification, in one stroke, of 3-systems and the possible generation of persistent POEs of dimension 5; see the examples at the end of the next chapter.

Chapter II.2

Persistent Manifolds of Dimension Five

Abstract: *So far, not much has been reported regarding the identification and classification of persistent five systems. This section looks at 5-dimensional submanifolds of $SE(3)$. At each point of a submanifold the tangent space, when translated to the identity in the group becomes a screw system. For persistent submanifolds, these screws systems are all conjugate to each other by a rigid-body transformation. Therefore, the idea is to build up a library of examples and non-examples of 5-persistent submanifolds. Observe that, no claim of an exhaustive list is made moreover, many of the presented examples are already known. However, the link to geometric problems is novel. Furthermore, the introduction of a new theorems to decide whether or not a 5-dimensional submanifold is persistent are reported.*

II.2.1 Introduction and Motivation

As already mentioned, finding out full-cycle mobility 5D screw systems is one of the main motivations behind the investigation of persistence manifolds, in general.

Therefore, one should observe that many 5 manifolds can be described using linear or quadratic constraints. In other words, submanifolds can be seen as the intersection of the Study quadric and linear or quadratic hypersurface. Then, the purpose is to find which of these are persistent and which are not.

II.2.2 Five Persistent Manifolds

A five-dimensional submanifold has a five-dimensional tangent space at each of its points. Mapping these to the tangent space at the identity in $SE(3)$ will produce a 5-system of screws. For the submanifold to be persistent, these 5-systems must be *congruent* to each other for any pair of points in the submanifold, see Definition 12 in Sec. II.1.13. Five-systems of screws can be classified up to rigid-body congruences by a single invariant, the

pitch of the dual wrench. For any system of 5 linearly independent twists, $\mathbf{s}_1, \mathbf{s}_2, \ldots, \mathbf{s}_5$, there is a unique (up to multiplication by a non-zero scalar) wrench $\mathbf{w}_d$, which is dual to all the twists,

$$\mathbf{w}_d^T \mathbf{s}_i = 0, \qquad \text{for} \quad i = 1, 2, \ldots, 5. \tag{II.2.1}$$

So, if at every point of the 5-dimentional submanifold M, the pitch of the dual wrench is the same, the submanifold must be persistent. Conversely, if the submanifold is persistent the pitch of the dual wrench will be constant over the submanifold.
The dual wrench can be found by means of determinants, let,

$$\mathbf{w}_d = \begin{pmatrix} m_x \\ m_y \\ m_z \\ f_x \\ f_y \\ f_z \end{pmatrix} \qquad \text{and} \qquad \mathbf{s}_i = \begin{pmatrix} \omega_{ix} \\ \omega_{iy} \\ \omega_{iz} \\ v_{ix} \\ v_{iy} \\ v_{iz} \end{pmatrix} \qquad i = 1, 2, \ldots, 5, \tag{II.2.2}$$

be the dual wrench and twists. Now one has that,

$$m_x = \begin{vmatrix} \omega_{1y} & \omega_{2y} & \omega_{3y} & \omega_{4y} & \omega_{5y} \\ \omega_{1z} & \omega_{2z} & \omega_{3z} & \omega_{4z} & \omega_{4z} \\ v_{1x} & v_{2x} & v_{3x} & v_{4x} & v_{5x} \\ v_{1y} & v_{2y} & v_{3y} & v_{4y} & v_{5y} \\ v_{1z} & v_{2z} & v_{3z} & v_{4z} & v_{5z} \end{vmatrix}, \qquad f_x = -\begin{vmatrix} \omega_{1x} & \omega_{2x} & \omega_{3x} & \omega_{4x} & \omega_{5x} \\ \omega_{1y} & \omega_{2y} & \omega_{3y} & \omega_{4y} & \omega_{5y} \\ \omega_{1z} & \omega_{2z} & \omega_{3z} & \omega_{4z} & \omega_{4z} \\ v_{1y} & v_{2y} & v_{3y} & v_{4y} & v_{5y} \\ v_{1z} & v_{2z} & v_{3z} & v_{4z} & v_{5z} \end{vmatrix},$$

$$m_y = -\begin{vmatrix} \omega_{1x} & \omega_{2x} & \omega_{3x} & \omega_{4x} & \omega_{5x} \\ \omega_{1z} & \omega_{2z} & \omega_{3z} & \omega_{4z} & \omega_{4z} \\ v_{1x} & v_{2x} & v_{3x} & v_{4x} & v_{5x} \\ v_{1y} & v_{2y} & v_{3y} & v_{4y} & v_{5y} \\ v_{1z} & v_{2z} & v_{3z} & v_{4z} & v_{5z} \end{vmatrix}, \qquad \text{and} \qquad f_y = \begin{vmatrix} \omega_{1x} & \omega_{2x} & \omega_{3x} & \omega_{4x} & \omega_{5x} \\ \omega_{1y} & \omega_{2y} & \omega_{3y} & \omega_{4y} & \omega_{5y} \\ \omega_{1z} & \omega_{2z} & \omega_{3z} & \omega_{4z} & \omega_{4z} \\ v_{1x} & v_{2x} & v_{3x} & v_{4x} & v_{5x} \\ v_{1z} & v_{2z} & v_{3z} & v_{4z} & v_{5z} \end{vmatrix},$$

$$m_z = \begin{vmatrix} \omega_{1x} & \omega_{2x} & \omega_{3x} & \omega_{4x} & \omega_{5x} \\ \omega_{1y} & \omega_{2y} & \omega_{3y} & \omega_{4y} & \omega_{4y} \\ v_{1x} & v_{2x} & v_{3x} & v_{4x} & v_{5x} \\ v_{1y} & v_{2y} & v_{3y} & v_{4y} & v_{5y} \\ v_{1z} & v_{2z} & v_{3z} & v_{4z} & v_{5z} \end{vmatrix}, \qquad f_z = -\begin{vmatrix} \omega_{1x} & \omega_{2x} & \omega_{3x} & \omega_{4x} & \omega_{5x} \\ \omega_{1y} & \omega_{2y} & \omega_{3y} & \omega_{4y} & \omega_{5y} \\ \omega_{1z} & \omega_{2z} & \omega_{3z} & \omega_{4z} & \omega_{4z} \\ v_{1x} & v_{2x} & v_{3x} & v_{4x} & v_{5x} \\ v_{1y} & v_{2y} & v_{3y} & v_{4y} & v_{5y} \end{vmatrix}.$$

Notice that pairing $\mathbf{w}_d$ with any $\mathbf{s}_i$ will give the determinant of a 6×6 matrix with a repeated column which is, of course, zero.

The pitch p of the wrench is given by,

$$p = \frac{f_x m_x + f_y m_y + f_z m_z}{f_x^2 + f_y^2 + f_z^2}. \tag{II.2.3}$$

However, there is a quicker way to compute this from the twists in the 5-system, it is not necessary to compute these 5×5 determinants.

Let $\mathbf{J}$ be the 6×5 matrix whose columns are the five twists,

$$\mathbf{J} = \left(\mathbf{s}_1 \middle| \mathbf{s}_2 \middle| \mathbf{s}_3 \middle| \mathbf{s}_4 \middle| \mathbf{s}_5\right) \tag{II.2.4}$$

Now compute the 5×5 determinant [89],

$$\text{pitch}(\alpha,\, \beta) = \det\left(\mathbf{J}^T(\alpha\mathbf{Q}_0 + \beta\mathbf{Q}_\infty)\mathbf{J}\right) = -p_0\alpha^5 + p_\infty\alpha^4\beta. \tag{II.2.5}$$

The result is a polynomial in the variables α and β, but only two terms are non-zero. Setting $\beta = 0$, it is easy to see from the Cauchy–Binet formula that the coefficient of α^5 is $-p_0 = -2(f_x m_x + f_y m_y + f_z m_z)$. By differentiating the determinant with respect to β, again, using the Cauchy–Binet formula again it is possible to show that, $p_\infty = 2(f_x^2 + f_y^2 + f_z^2)$. Hence, the pitch of the 5-system is given by,

$$p = \frac{p_0}{p_\infty}. \tag{II.2.6}$$

II.2.3 Intersections with Hyperplanes

In [109] it was found that all algebraic subgroups and symmetric subspaces of $SE(3)$ are either linear subspaces of the Study quadric or the intersection of the Study quadric with a linear subspace.

Rotations about a fixed axis form a line in the Study quadric as do translations in a fixed direction. Finite, non-zero pitch screw displacements with a fixed axis are also one-parameter subgroups but in the Study quadric they are not algebraic. If a subspace contains only algebraic curves then it will be a linear space. Of course, not all intersections of the Study quadric with linear spaces are subgroups or symmetric spaces. This section looks at some general cases.

II.2.3.1 Tangent Spaces

To find the tangent space to an algebraic variety, one can simply take the partial derivatives of the equations defining the variety with respect to the coordinates. Evaluating the partial derivatives at a point in the variety then gives linear equations for the tangent space at that point. For example, consider the Study quadric, this is given by the single quadratic equation,

$$\Psi = a_0c_0 + a_1c_1 + a_2c_2 + a_3c_3 = 0. \tag{II.2.7}$$

The partial derivatives are,

$$\frac{\partial\Psi}{\partial a_0} = c_0, \qquad \frac{\partial\Psi}{\partial a_1} = c_1, \qquad \frac{\partial\Psi}{\partial a_2} = c_2, \qquad \frac{\partial\Psi}{\partial a_3} = c_3,$$
$$\frac{\partial\Psi}{\partial c_0} = a_0, \qquad \frac{\partial\Psi}{\partial c_1} = a_1, \qquad \frac{\partial\Psi}{\partial c_2} = a_2, \qquad \frac{\partial\Psi}{\partial c_3} = a_3.$$

The equation of the tangent plane at the identity $\mathbf{e} = (1, 0, 0, 0, 0, 0, 0, 0)$ is therefore,

$$\left(\frac{\partial\Psi}{\partial a_0}\right)_{\mathbf{e}} a_0 + \left(\frac{\partial\Psi}{\partial a_1}\right)_{\mathbf{e}} a_1 + \cdots + \left(\frac{\partial\Psi}{\partial c_3}\right)_{\mathbf{e}} c_3 = \left(\frac{\partial\Psi}{\partial c_0}\right)_{\mathbf{e}} c_0 = c_0 = 0. \tag{II.2.8}$$

That is, the tangent at the identity to the Study quadric is the hyperplane $c_0 = 0$. This projective 6-plane can be viewed as a vector space if one uses an affine patch containing the identity element. This could be the patch where $a_0 \neq 0$, then dividing by a_0 and using a_0, c_0 as coordinates for the tangent vectors,

$$\mathbf{s} = \left(\frac{a_1}{a_0}, \frac{a_2}{a_0}, \frac{a_3}{a_0}, \frac{c_1}{a_0}, \frac{c_2}{a_0}, \frac{c_3}{a_0} \right). \tag{II.2.9}$$

Now, suppose one takes the intersection of the Study quadric with a general hyperplane. A general hyperplane is given by a linear equation of the form,

$$\Pi = w_0 a_0 + w_1 a_1 + w_2 a_2 + w_3 a_3 + v_0 c_0 + v_1 c_1 + v_2 c_2 + v_3 c_3 = 0, \tag{II.2.10}$$

where the w_i and v_j are constants. It is easy to see that the tangent plane here is the same as the original hyperplane since,

$$\frac{\partial \Pi}{\partial a_i} = w_i, \quad \text{and} \quad \frac{\partial \Pi}{\partial c_i} = v_i, \qquad i = 0, 1, \ldots, 3. \tag{II.2.11}$$

For our purposes one needs to be able to right translate this hyperplane to the identity.

Recall that the multiplying a quaternion $\mathbf{b} = b_0 + b_1\mathbf{i} + b_2\mathbf{j} + b_3\mathbf{k}$ on the right by another quaternion $\mathbf{a} = a_0 + a_1\mathbf{i} + a_2\mathbf{j} + a_3\mathbf{k}$ can be represented as a matrix multiplication,

$$\mathbf{ba} = \begin{pmatrix} 1 & \mathbf{i} & \mathbf{j} & \mathbf{k} \end{pmatrix} \begin{pmatrix} a_0 & -a_1 & -a_2 & -a_3 \\ a_1 & a_0 & a_3 & -a_2 \\ a_2 & -a_3 & a_0 & a_1 \\ a_3 & a_2 & -a_1 & a_0 \end{pmatrix} \begin{pmatrix} b_0 \\ b_1 \\ b_2 \\ b_3 \end{pmatrix}. \tag{II.2.12}$$

Indeed, one can write,

$$R(\mathbf{a}) = \begin{pmatrix} a_0 & -a_1 & -a_2 & -a_3 \\ a_1 & a_0 & a_3 & -a_2 \\ a_2 & -a_3 & a_0 & a_1 \\ a_3 & a_2 & -a_1 & a_0 \end{pmatrix}, \tag{II.2.13}$$

and consider quaternions as 4-vectors in the following.

For a unit quaternion, the inverse is given by the quaternion conjugate. In terms of the $R(\mathbf{a})$, again for a unit quaternion $\mathbf{a}$ one has,

$$R(\mathbf{a}^{-1}) = R(\mathbf{a}^{-}) = R(\mathbf{a})^T = \begin{pmatrix} a_0 & a_1 & a_2 & a_3 \\ -a_1 & a_0 & -a_3 & a_2 \\ -a_2 & a_3 & a_0 & -a_1 \\ -a_3 & -a_2 & a_1 & a_0 \end{pmatrix}. \tag{II.2.14}$$

This extends simply to dual quaternions. Given a dual quaternion $\mathbf{h} = \mathbf{a} + \varepsilon\mathbf{c}$ the right action of $\mathbf{h}^{-1}$ on an 8-vector can be represented as 8×8 partitioned matrix,

$$\mathcal{R}(\mathbf{h}^{-1}) = \begin{pmatrix} R(\mathbf{a}^{-}) & \mathbf{0} \\ R(\mathbf{c}^{-}) & R(\mathbf{a}^{-}) \end{pmatrix}. \tag{II.2.15}$$

This gives the action of $SE(3)$ (or more accurately its double covering group) on the dual quaternions written as 8-vectors. The action on the dual space of hyperplanes is given by the inverse transpose of this representation,

$$\mathcal{R}(\mathbf{h}^{-1})^{-T} = \mathcal{R}(\mathbf{h})^T = \begin{pmatrix} R(\mathbf{a}^-) & R(\mathbf{c}^-) \\ \mathbf{0} & R(\mathbf{a}^-) \end{pmatrix}. \tag{II.2.16}$$

Note that, this assumes that $\mathbf{a}^-\mathbf{c} + \mathbf{c}^-\mathbf{a} = 0$, which is equivalent to the equation for the Study quadric.

So, if one has an hyperplane given by an 8-vector, partitioned into two 4-vector, $\mathbf{w} = (w_0, w_1, w_2, w_3)^T$ and $\mathbf{v} = (v_0, v_1, v_2, v_3)^T$ as above, taking the dual and translating this back to the identity will be given by,

$$\begin{pmatrix} \mathbf{w}' \\ \mathbf{v}' \end{pmatrix} = \begin{pmatrix} R(\mathbf{a}^-) & R(\mathbf{c}^-) \\ \mathbf{0} & R(\mathbf{a}^-) \end{pmatrix} \begin{pmatrix} \mathbf{w} \\ \mathbf{v} \end{pmatrix} \tag{II.2.17}$$

Assuming that $\mathbf{h}$ lies on the hyperplane Π means that the identity element will lie on the translated hyperplane Π', so $w_0' = 0$. Intersecting the hyperplane Π' with the hyperplane tangent to the Study quadric at the identity gives the wrench dual to the screw system as,

$$\mathbf{w}_d = \begin{pmatrix} w_1' \\ w_2' \\ w_3' \\ v_1' \\ v_2' \\ v_3' \end{pmatrix}. \tag{II.2.18}$$

II.2.3.2 Examples

Example 1
In [109], it was found that the canonical form for a particular symmetric space is given by the intersection of the Study quadric with the hyperplane $a_3 = 0$. From Theorem 6 one already knows this will be a persistent submanifold. To check this using the methods outlined above, one has $w_3 = 1$ and all w_is and v_js are zero. So, one has,

$$\begin{pmatrix} \mathbf{w}' \\ \mathbf{v}' \end{pmatrix} = \begin{pmatrix} R(\mathbf{a}^-) & R(\mathbf{c}^-) \\ \mathbf{0} & R(\mathbf{a}^-) \end{pmatrix} \begin{pmatrix} 0 \\ 0 \\ 0 \\ 1 \\ 0 \\ 0 \\ 0 \\ 0 \end{pmatrix} = \begin{pmatrix} 0 \\ a_2 \\ -a_1 \\ a_0 \\ 0 \\ 0 \\ 0 \\ 0 \end{pmatrix} \tag{II.2.19}$$

and thus the wrench dual to the 5D screw system determined by a point $\mathbf{h}$ in the

hyperplane will be given by,

$$\mathbf{w}_d = \begin{pmatrix} a_2 \\ -a_1 \\ a_0 \\ 0 \\ 0 \\ 0 \end{pmatrix}. \tag{II.2.20}$$

The wrench is a pure couple and so has infinite pitch independent of the point chosen on the submanifold. Since the pitch of this wrench is constant this confirms that the submaifold is persistent.

Example 2

Suppose one looks at the submanifold that is the intersection of the Study quadric with the hyperplane $c_3 = 0$. The corresponding wrench is now,

$$\mathbf{w}_d = \begin{pmatrix} c_2 \\ -c_1 \\ c_0 \\ a_2 \\ -a_1 \\ a_0 \end{pmatrix}. \tag{II.2.21}$$

The pitch of this wrench is,

$$p = \frac{a_0c_0 + a_1c_1 + a_2c_2}{a_0^2 + a_1^2 + a_2^2}. \tag{II.2.22}$$

If the point lies on both the Study quadric and the hyperplane, one has that $a_0c_0+a_1c_1+a_2c_2 + a_3c_3 = 0$ and $c_3 = 0$. Hence, the pitch is zero for all points in the submanifold and therefore this is also a persistent submanifold.

Finally here, consider the hyperplane given by $a_3 + \beta c_3 = 0$, the wrench is now,

$$\mathbf{w}_d = \begin{pmatrix} a_2 + \beta c_2 \\ -a_2 - \beta c_1 \\ a_0 + \beta c_0 \\ \beta a_2 \\ -\beta a_1 \\ \beta a_0 \end{pmatrix}, \text{ with } p = \frac{\beta a_0(a_0 + \beta c_0) + \beta a_1(a_1 + pc_1) + \beta a_2(a_2 + \beta c_2)}{\beta^2(a_0^2 + a_1^2 + a_2^2)}. \tag{II.2.23}$$

simplifying the expression for the pitch using the equations for the Study quadric and the hyperplane gives,

$$p = \frac{a_0^2 + a_1^2 + a_2^2 - \beta a_3^2}{\beta(a_0^2 + a_1^2 + a_2^2)}. \tag{II.2.24}$$

It is clear that this quantity varies as the point on the submanifold changes, hence this submanifold is not persistent.

If these hyperplanes are subject to a rigid-body displacement then it is clear that whether or not they are persistent will not change. If one could classify hyperplanes in $\mathbb{PR}^7$ up to rigid-body displacements, then it would be possible to give a more complete result as to which hyperplanes produce persistent submanifolds and which do not.

II.2.4 Intersection with Quadrics

In this section, a few examples of intersections of the Study quadric with other quadric hypersurfaces are given. Such submanifolds of the Study quadrics often arise in geometrical constraint problems and are sometimes referred to as constraint varieties. In many of these cases, the submanifold of group elements can be realised as the possible displacements of the end-effector of a simple serial kinematic chain.

A quadric hypersurface in $\mathbb{PR}^7$ is a degree 2 variety with 6-dimension. Any such variety can be written as,

$$\mathbf{h}^T \mathsf{Q} \mathbf{h} = 0, \tag{II.2.25}$$

where, as usual, $\mathbf{h} = (a_0, a_1, a_2, a_3, c_0, c_1, c_2, c_3)^T$ and Q is and 8×8 symmetric matrix.

II.2.4.1 Point-Plane Constraint

The set of rigid-body displacements that maintain the incidence of a given point with a fixed plane form a 5-dimensional submanifold of the Study quadric. This submanifold is the intersection of the Study quadric with another quadric hypersurface in $\mathbb{PR}^7$. In [110], this latter quadric was shown to be given by the 8×8 symmetric matrix $\mathsf{Q}_\pi(\mathbf{p}, \mathbf{n})$, which in partitioned form is,

$$\mathsf{Q}_\pi(\mathbf{p}, \mathbf{n}) = \begin{pmatrix} \mathsf{W} & \mathsf{N} \\ \mathsf{N}^T & 0 \end{pmatrix} \tag{II.2.26}$$

where $\mathbf{p}$ represents a point on plane Π while $\mathbf{n}$ is the normal vector to Π. Hence, matrices W, N are defined as

$$\mathsf{W} = \begin{pmatrix} \mathbf{0} & (\mathbf{n} \times \mathbf{p})^T \\ (\mathbf{n} \times \mathbf{p}) & \mathbf{N}\mathbf{P}^T + \mathbf{P}\mathbf{N}^T \end{pmatrix} \qquad \text{and} \qquad \mathsf{N} = \begin{pmatrix} \mathbf{0} & -\mathbf{n}^T \\ \mathbf{n} & \mathbf{N} \end{pmatrix} \tag{II.2.27}$$

with $\mathbf{P}, \mathbf{N}$ anti-symmetric matrices of vectors $\mathbf{p}, \mathbf{n}$. In this case, it is not necessary to find the tangents spaces to show that the submanifold is persistent.

The submanifold defined by a point-plane constraint can be realised as an open-loop kinematic chain consisting of a revolute joint in the direction $\mathbf{n}$, prismatic joint perpendicular to $\mathbf{n}$ and a spherical joint with its centre at $\mathbf{p}$. As the end-effector of this $\mathcal{RPS}$ linkage moves, the centre of the $\mathcal{S}$-joint will remain on the plane determined by $\mathbf{n}$ and $\mathbf{p}$. By inspection, it is clear that a pure force directed along a line through the centre of the $\mathcal{S}$-joint and parallel to $\mathbf{n}$ can do no work. So, as the linkage moves in the submanifold there is always a pitch zero wrench dual to the instantaneous screw system. This is enough to show that the submanifold is persistent.

Another way to see that this submanifold is persistent is to observe that it is the product of two subgroups. One subgroup is conjugate to $SE(2)$ and produces displacements

that preserve the plane. The other is conjugate to $SO(3)$ and preserves the position of the point. The two subgroups intersect in the subgroup of rotations about the line through $\mathbf{p}$ parallel to $\mathbf{n}$ and so, by Theorem 4, the submanifold must be persistent.

II.2.4.2 Point-Sphere Constraint

Here the submanifold defined by a point-sphere constraint is considered. This is the space of displacements that maintain a point $\mathbf{p}$ on the surface of a sphere centred at $\mathbf{c}$. In complete analogy with the previous section, this is given by the quadratic equation where the symmetric matrix is

$$\mathsf{Q}_S(\mathbf{p},\mathbf{c}) = \begin{pmatrix} \mathsf{U} & \mathsf{P}+\mathsf{C} \\ \mathsf{P}^T+\mathsf{C}^T & 2\mathbf{I} \end{pmatrix}, \tag{II.2.28}$$

with

$$\mathsf{U} = \begin{pmatrix} 0 & (\mathbf{c}\times\mathbf{p})^T \\ (\mathbf{c}\times\mathbf{p}) & \mathsf{P}\mathsf{C}^T+\mathsf{C}\mathsf{P}^T \end{pmatrix}, \quad \mathsf{P} = \begin{pmatrix} \mathbf{0} & \mathbf{p}^T \\ -\mathsf{p} & \mathsf{P} \end{pmatrix}, \quad \mathsf{C} = \begin{pmatrix} \mathbf{0} & \mathbf{c}^T \\ -\mathsf{c} & \mathsf{C} \end{pmatrix}, \tag{II.2.29}$$

where P,C are anti-symmetric matrices corresponding to $\mathbf{p}$ and $\mathbf{c}$, respectively; see [111] for further details.

This submanifold can be shown to be persistent without having to compute the tangent spaces explicitly. It is not difficult to see that the possible displacements that maintain the constraint consist of rotations about $\mathbf{p}$ followed by any rotation about the centre of the sphere $\mathbf{c}$. So, the submanifold is a product of two subgroups, both isomorphic to $SO(3)$. Hence, the submanifold is persistent by Theorem 4. Alternatively, one can argue that the submanifold is generated mechanically by the end effector of a linkage comprised of two $\mathcal{S}$-joints. A pure force directed along the line joining the centres of the two $\mathcal{S}$-joints will do no work on the linkage so the submanifold is persistent.

II.2.4.3 Plane Tangent to a Sphere

Let π' be a plane tangent to a sphere centred at $\mathbf{p}$ and consider the parallel plane π to π' which contains $\mathbf{p}$. As π' moves remaining tangent to the sphere, π will move always containing the centre of the sphere. Therefore, the possible displacements of π' that keep it tangent to the sphere are the same as the displacements of π that maintain its incidence with $\mathbf{p}$. Hence, the submanifold of displacements of a plane that preserve tangency with a sphere is the inverse of the submanifold of displacements that maintain a point in a fixed plane. Thus, this submanifold is necessarily persistent by Theorem 5 and because the point-plane constraint submanifold is persistent. The submanifold can also be viewed as a product of two subgroups $SE(2)$ and $SO(3)$. Hence, it is persistent by Theorem 4 as well. The submanifold can be realised as the motions of the end-effector of an $\mathcal{SPP}$ open-loop chain.

II.2.4.4 Lines in a Linear Line Complex

In general this is a non-example, the submanifold of displacements that keep a given line in a fixed linear line complex is not persistent in general[1]. However, there is a special case that is persistent.

A *general* linear line complex is a 3-dimensional set of lines satisfying a linear equation in the Plücker coordinates of the line, the linear equation can be summarised at,

$$\mathbf{m} \cdot \boldsymbol{\omega} + \mathbf{f} \cdot \mathbf{v} = 0. \tag{II.2.30}$$

where $\boldsymbol{\omega}$, $\mathbf{v}$ are the Plücker coordinates of the line and $\mathbf{m}$, $\mathbf{f}$ are constants determining the complex. In [111], it was shown that the equation of the submanifold that comprises the displacements of the line that keep it in the complex are quadratic in the Study parameters,

$$\mathbf{h}^T \mathsf{Q}_c \mathbf{h} = 0. \tag{II.2.31}$$

Where the 8×8 matrix Q_c has the partitioned form,

$$\Lambda = \mathsf{Q}_c = \begin{pmatrix} \Xi & \Upsilon \\ \Upsilon & 0 \end{pmatrix}, \tag{II.2.32}$$

with,

$$\Xi = \begin{pmatrix} 0 & (\boldsymbol{\omega} \times \mathbf{m} + \mathbf{v} \times \mathbf{f})^T \\ (\boldsymbol{\omega} \times \mathbf{m} + \mathbf{v} \times \mathbf{f}) & \mathbf{M\Omega} + \mathbf{\Omega M} + \mathbf{FV} + \mathbf{VF} \end{pmatrix}, \Upsilon = \begin{pmatrix} 0 & (\boldsymbol{\omega} \times \mathbf{f})^T \\ (\boldsymbol{\omega} \times \mathbf{f}) & \mathbf{\Omega F} + \mathbf{F\Omega} \end{pmatrix}. \tag{II.2.33}$$

To simplify these equations it has been assumed that the line initially lies in the complex, that is that $\mathbf{m} \cdot \boldsymbol{\omega} + \mathbf{f} \cdot \mathbf{v} = 0$. As usual, $\mathbf{M}$, $\mathbf{\Omega}$ and so forth, represent the 3×3 anti-symmetric matrices corresponding to $\mathbf{m}$, $\boldsymbol{\omega}$ and so forth.

To keep the computations as simple as possible one can choose coordinates so that the axis of the complex is aligned with the z-axis of the coordinate. This will make,

$$\mathbf{f} = \begin{pmatrix} 0 \\ 0 \\ 1 \end{pmatrix} \qquad \text{and} \qquad \mathbf{m} = \begin{pmatrix} 0 \\ 0 \\ p \end{pmatrix} \tag{II.2.34}$$

where p is the pitch of the complex. One can also choose the initial line in the complex to be as simple as possible, for example one can choose the x-axis so that,

$$\boldsymbol{\omega} = \begin{pmatrix} 1 \\ 0 \\ 0 \end{pmatrix} \qquad \text{and} \qquad \mathbf{v} = \begin{pmatrix} 0 \\ 0 \\ 0 \end{pmatrix}. \tag{II.2.35}$$

With these choices one gets,

$$\Xi = \begin{pmatrix} 0 & 0 & -p & 0 \\ 0 & 0 & 0 & p \\ -p & 0 & 0 & 0 \\ 0 & p & 0 & 0 \end{pmatrix} \qquad \text{and} \qquad \Upsilon = \begin{pmatrix} 0 & 0 & -1 & 0 \\ 0 & 0 & 0 & 1 \\ -1 & 0 & 0 & 0 \\ 0 & 1 & 0 & 0 \end{pmatrix}. \tag{II.2.36}$$

[1]The question whether a line motion give rises to a persistent motion generated other interesting results; see Chapter II.3.

The equation of the quadric is then,

$$\mathbf{h}^T \mathsf{Q}_c \mathbf{h} = -2p(a_0a_2 - a_1a_3) - 2(a_0c_2 - a_1c_3 + a_2c_0 - a_3c_1) = 0. \tag{II.2.37}$$

It will be convenient later to write,

$$pq_1 + q_2 = 0, \tag{II.2.38}$$

where

$$q_1 = p(a_0a_2 - a_1a_3), \quad q_2 = (a_0c_2 - a_1c_3 + a_2c_0 - a_3c_1), \tag{II.2.39}$$

The partial derivatives at $\mathbf{h}$, are then,

$$\begin{pmatrix} \partial\Lambda/\partial a_0 \\ \partial\Lambda/\partial a_1 \\ \partial\Lambda/\partial a_2 \\ \partial\Lambda/\partial a_3 \\ \partial\Lambda/\partial c_0 \\ \partial\Lambda/\partial c_1 \\ \partial\Lambda/\partial c_2 \\ \partial\Lambda/\partial c_3 \end{pmatrix}_{\mathbf{h}} = 2 \begin{pmatrix} -pa_2 - c_2 \\ pa_3 + c_3 \\ -pa_0 - c_0 \\ pa_1 + c_1 \\ -a_2 \\ a_3 \\ -a_0 \\ a_1 \end{pmatrix}. \tag{II.2.40}$$

Translating this back to the identity gives,

$$\mathcal{R}(\mathbf{h}^-) \begin{pmatrix} \partial\Lambda/\partial a_0 \\ \partial\Lambda/\partial a_1 \\ \partial\Lambda/\partial a_2 \\ \partial\Lambda/\partial a_3 \\ \partial\Lambda/\partial c_0 \\ \partial\Lambda/\partial c_1 \\ \partial\Lambda/\partial c_2 \\ \partial\Lambda/\partial c_3 \end{pmatrix}_{\mathbf{h}} = 2 \begin{pmatrix} 0 \\ 2p(a_1a_2 + a_0a_3) + 2(a_0c_3 + a_1c_2 + a_2c_1 + a_3c_0) \\ -p(a_0^2 + a_1^2 - a_2^2 - a_3^2) - 2(a_0c_0 + a_1c_1 - a_2c_2 - a_3c_3) \\ 0 \\ -2(a_0a_2 - a_1a_3) \\ 2(a_0a_3 + a_1a_2) \\ -(a_0^2 + a_1^2 - a_2^2 - a_3^2) \\ 0 \end{pmatrix}. \tag{II.2.41}$$

The pitch of the wrench is then,

$$p = \frac{2\Delta\Psi - 4q_1(pq_1 + q_2) + p\Delta^2}{(\Delta + 2q_1)(\Delta - 2q_1)} = \frac{p\Delta^2}{(\Delta^2 - 4q_1^2)}, \tag{II.2.42}$$

where the last equality results from setting the expression for the Study quadric $\Psi = (a_0c_0 + a_1c_1 + a_2c_2 + a_3c_3)$ and the expression for the constraint quadric $(pq_1 + q_2)$ to zero. Recall that $\Delta = a_0^2 + a_1^2 + a_2^2 + a_3^2$. In general, this pitch is not constant and so the submanifold is not persistent. However, if p, the pitch of the line complex, is zero then the pitch of the wrench also vanished and in this case the submanifold is persistent.

The space of lines reciprocal to a pitch zero screw is called a special linear line complex. The special linear line complex consists of all lines meeting or parallel to a

fixed-line. The submanifold of displacements that maintain the incidence of a given line with a fixed line can be realised with a $\mathcal{UPU}$ linkage. That is a universal joint a prismatic joint and another universal joint. The first revolute joint of the first $\mathcal{U}$-joint must coincide with the axis of the fixed line and the axis of the last revolute joint of the final $\mathcal{U}$-joint must coincide with the moving line. A pure force along the line perpendicular to both the fixed an moving lines through their meeting point will do no work on the end-effector of the linkage.

II.2.4.5 A Singular Quadric

A quadratic complex is nothing else than a set of lines that satisfy a quadratic constraint. Hereby, a singular quadratic complex is considered. Practically, one can consider lines perpendicular to a fixed direction or, more generally, lines at a fixed angle to a fixed direction and asses if this constraint generates a persistent five submanifold. Assume the screw is defined as $\mathbf{s} = (\mathbf{0}, \mathbf{v})$ while the generic line is $\ell = (\mathbf{w}, \mathbf{u})$. Therefore, the mentioned constraint reads as

$$(\mathbf{v}^T\mathbf{w})^2 = \mathbf{w}^T\mathbf{w}\cos\phi, \tag{II.2.43}$$

which, in matrix form becomes

$$\ell^T\mathsf{Q}_\ell\ell = 0, \tag{II.2.44}$$

where Q_ℓ is a symmetric matrix of the form

$$\mathsf{Q}_\ell = \begin{pmatrix} \mathbf{X} & \mathbf{0} \\ \mathbf{0} & \mathbf{0} \end{pmatrix}, \tag{II.2.45}$$

Again, one can understand if the submanifold of displacements is persistent by looking at which rigid motion change the incidence angle ϕ. Therefore, taking the Adjoint action of $SE(3)$, one should investigate for which g

$$\mathrm{Ad}(g)\ell^T\mathsf{Q}_\ell\ell = 0 \tag{II.2.46}$$

is satisfied. Hence, to simplify computation without losing generality, assume $\phi = pi/2$ therefore, the above constraints reads as

$$\begin{pmatrix} \mathbf{R} & \mathbf{0} \\ \mathbf{TR} & \mathbf{R} \end{pmatrix} (\mathbf{0}^T, \quad \mathbf{v}^T) \begin{pmatrix} \mathbf{0} & \mathbf{I} \\ \mathbf{I} & \mathbf{0} \end{pmatrix} \begin{pmatrix} \mathbf{w} \\ \mathbf{u} \end{pmatrix} = 0 \tag{II.2.47}$$

which is satisfied for every translation $\mathbf{T}$ and every rotation $\mathbf{R}$ about $\mathbf{v}$ and $\mathbf{w}$. Therefore, this means that exist a product of two subgroups generating this persistent manifold. In particular, this would be $SO(2) \ltimes \mathbb{R}^3$, isomorphic to the Schönfliess subgroup of $SE(3)$, and the subgroup of rotations $SO(2)$.

Mechanically, this set of lines can be generated by a $\mathcal{CPC}$ linkage. Here, the direction of the central prismatic joint must be parallel to the common perpendicular between the axes of the two cylindrical joints. Again it is straightforward to see that the submanifold

must be persistent since a pure torque about the common perpendicular to the cylindrical joints will do no work on the linkage.

Here persistent submanifolds defined by quadrics were investigated. To close this section, a couple of general results concerning these constraint submanifolds are given.

Theorem 8. *The space of group elements that keep a point on a smooth surface is persistent.*

Theorem 9. *The space of group elements that keep a plane tangent to a smooth surface is persistent.*

Proof. The proof are combined as these results are very similar. Consider the infinitesimal displacements that keep a point on a surface. These will be twists and the linear span of all such twists form a screw system. This screw system corresponds to the tangent space to the submanifold at the given configuration of the system.

For a point on a surface, the 5-dimensional screw system is generated by any three purely rotational twists about the point and pure rotations about the principle curvature axes of the surface. These axes are located a distance $1/k_1$ and $1/k_2$ from the surface, where k_1 and k_2 are the values of the principle curvature of the surface at the point. These axes are oriented perpendicularly to the planes of the circles of principle curvature, see [89, §6.5.3] and [112]. A pure force directed along the normal to the surface at the point will do no work on the screw system since it's axis meets all the axes of the screws in the screw system. If the point on the surface has zero as one or both of its principle curvatures then the corresponding twists in the screw system will be infinite pitch twists directed along a perpendicular to the normal vector of the surface. This will still be dual to any force along the normal line to the surface. Hence, by the results of Section II.2.2 the submanifold will be persistent.

The 5-dimensional screw system that infinitesimally keeps a plane tangent to a surface can be generated by the principle curvature axes of the surface, infinitesimal rotations about the normal line to the surface through the contact point between the plane and the surface and the infinitesimal translations parallel to the plane. A pure force along the normal line does not work on the screw system as it is perpendicular to the translations and meets the axes of the rotations. □

II.2.5 Some 5-Dimensional POE-Submanifolds

So far many, but not all, submanifolds have been described as the intersection of the Study quadric with a particular constraint. However, it should be clear that other 5 manifolds exist. Therefore, the Product of Exponential (POE) formula can be used. It is well known that it parameterises submanifolds associated to a kinematic chain. In this view, exploiting Theorem (7), one can show that, first, product of three subgroups, for example 3 systems, can be persistent. Secondly, looking at 5 manifolds, it is possible to extend these 3 chains to higher dimensional persistent systems.

II.2.5.1 Extensions of the $\mathcal{HRH}$ Chain

In [102] Carricato showed that, given a couple of conditions on the pitches and twist angles on a chain consisting of a helical $\mathcal{H}$, revolute $\mathcal{R}$ and final helical $\mathcal{H}$ joint, generate a persistent system. This can be extended in a simple way to a five joint persistent chain by considering the first joint to be an element of a 3-dimensional subgroup.

First, let's understand why the $\mathcal{HRH}$ chain is persistent. Suppose one has a 3-joint open loop chain with joints described by twists $\mathbf{s}_1$, $\mathbf{s}_2$ and $\mathbf{s}_3$. Where these twists are given in some home configuration. They determine a screw system that one can denote as

$$S_e = \operatorname{span}(\mathbf{s}_1,\, \mathbf{s}_2,\, \mathbf{s}_3) \tag{II.2.48}$$

As the chain moves, the twist will move and, in general, will be given by

$$\mathbf{s}_1 \longmapsto \mathbf{s}_1, \quad \mathbf{s}_2 \longmapsto e^{\theta_1 \mathbf{s}_1}\mathbf{s}_2 e^{-\theta_1 \mathbf{s}_1}, \quad \mathbf{s}_3 \longmapsto e^{\theta_1 \mathbf{s}_1} e^{\theta_2 \mathbf{s}_2}\mathbf{s}_3 e^{-\theta_2 \mathbf{s}_2} e^{-\theta_1 \mathbf{s}_1}. \tag{II.2.49}$$

The screw system generated by these twists is,

$$S_\theta = e^{\theta_1 \mathbf{s}_1}\operatorname{span}(\mathbf{s}_1,\, \mathbf{s}_2,\, e^{\theta_2 \mathbf{s}_2}\mathbf{s}_3 e^{-\theta_2 \mathbf{s}_2}) e^{-\theta_1 \mathbf{s}_1}. \tag{II.2.50}$$

For the submanifold generated by this chain to be persistent one must have that the screw system,

$$\operatorname{span}(\mathbf{s}_1,\, \mathbf{s}_2,\, e^{\theta_2 \mathbf{s}_2}\mathbf{s}_3 e^{-\theta_2 \mathbf{s}_2}) \tag{II.2.51}$$

is fixed.

To investigate the case where $\mathbf{s}_2$ is a pure rotation, let,

$$\mathbf{s}_2 = \begin{pmatrix} 0 \\ 0 \\ 1 \\ 0 \\ 0 \\ 0 \end{pmatrix} \quad \text{and} \quad \mathbf{s}_3 = \begin{pmatrix} 0 \\ \sin\alpha_2 \\ \cos\alpha_2 \\ 0 \\ -d_2\cos\alpha_2 + p\sin\alpha_2 \\ d_2\sin\alpha_2 + p\cos\alpha_2 \end{pmatrix}, \tag{II.2.52}$$

be the second and third joints of the chain with α_2 being the angle between the two twists. Note that, one can always choose the origin of coordinates to be located at point on the axis of $\mathbf{s}_2$ that meets the common perpendicular to the axis of $\mathbf{s}_3$. One can also always orient our coordinate axis so that the axis of $\mathbf{s}_2$ is along the z-direction and the common perpendicular between the axes of $\mathbf{s}_2$ and $\mathbf{s}_3$ lies along the x-direction.

As $\mathbf{s}_3$ turns about $\mathbf{s}_2$, the Rodrigues formula tells us that,

$$e^{\theta_2 \mathbf{s}_2}\mathbf{s}_3 e^{-\theta_2 \mathbf{s}_2} = e^{\theta_2 \operatorname{ad}(\mathbf{s}_2)}\mathbf{s}_3 = \mathbf{s}_3 + \sin\theta[\mathbf{s}_2,\, \mathbf{s}_3] + (1-\cos\theta)\big[\mathbf{s}_2,\, [\mathbf{s}_2,\, \mathbf{s}_3]\big]. \tag{II.2.53}$$

The commutators are,

$$[\mathbf{s}_2,\, \mathbf{s}_3] = \begin{pmatrix} -\sin\alpha_2 \\ 0 \\ 0 \\ d_2\cos\alpha_2 - p\sin\alpha_2 \\ 0 \\ 0 \end{pmatrix} \text{ and } [\mathbf{s}_2,\, [\mathbf{s}_2,\, \mathbf{s}_3]] = \begin{pmatrix} 0 \\ -\sin\alpha_2 \\ 0 \\ 0 \\ d_2\cos\alpha_2 - p\sin\alpha_2 \\ 0 \end{pmatrix}. \tag{II.2.54}$$

Notice, $[\mathbf{s}_2, \mathbf{s}_3]$ and $[\mathbf{s}_2, [\mathbf{s}_2, \mathbf{s}_3]]$ have the same pitch $(p - d_2 \cot \alpha_2)$ and the axes of these twists meet the axis of $\mathbf{s}_2$ and are mutually perpendicular. This means that the three twists $\mathbf{s}_2$, $[\mathbf{s}_2, \mathbf{s}_3]$ and $\big[\mathbf{s}_2, [\mathbf{s}_2, \mathbf{s}_3]\big]$ generate a IA_2 3-dimensional screw system. For $\mathbf{s}_3$, to lie in this system, it is clear that it must satisfy the condition $d_2 \sin \alpha_2 + p \cos \alpha_2 = 0$. If this condition is satisfied,

$$p = -d_2 \tan \alpha_2, \tag{II.2.55}$$

and thus

$$-d_2 \cos \alpha_2 + p \sin \alpha_2 = -d_2 / \cos \alpha_2 = p / \sin \alpha_2. \tag{II.2.56}$$

Consequently,

$$\mathbf{s}_3 = \begin{pmatrix} 0 \\ \sin \alpha_2 \\ \cos \alpha_2 \\ 0 \\ p / \sin \alpha_2 \\ 0 \end{pmatrix} \tag{II.2.57}$$

and

$$\mathbf{s}_3 = \cos \alpha_2 \mathbf{s}_2 - \big[\mathbf{s}_2, [\mathbf{s}_2, \mathbf{s}_3]\big]. \tag{II.2.58}$$

This ensures that the twist $\mathbf{s}_2 + e^{\theta_2 \mathbf{s}_2} \mathbf{s}_3 e^{-\theta_2 \mathbf{s}_2}$ lies in the same IA_2 3-system for all values of θ_2. For $\mathbf{s}_1$ one can take any twist in this IA_2 3-system. For example, one could choose,

$$\mathbf{s}_1 = \begin{pmatrix} 0 \\ \sin \alpha_1 \\ \cos \alpha_1 \\ 0 \\ -d_1 \cos \alpha_1 + p \sin \alpha_1 \\ 0 \end{pmatrix}, \tag{II.2.59}$$

where $p = -d_1 \tan \alpha_1$. One could also have chosen $\mathbf{s}_1$ to be any rotation of the above twist about $\mathbf{s}_2$ or even,

$$\mathbf{s}_1 = [\mathbf{s}_2, \mathbf{s}_3] = \begin{pmatrix} -\sin \alpha_2 \\ 0 \\ 0 \\ d_2 \cos \alpha_2 - p \sin \alpha_2 \\ 0 \\ 0 \end{pmatrix} \tag{II.2.60}$$

or any rotation of this about $\mathbf{s}_2$. This show that the product of 3 subgroups, $\mathcal{HRH}$ in this case, is persistent.

Now, to produce a 5-dimensional submanifold one can embed $\mathbf{s}_1$ in a 3-dimensional subgroup G_1, of $SE(3)$. The 5-system of screws given by such an arrangement will be the direct sum of the 3-system for the Lie algebra of G_1 with the IA_2 3-system described above. Since these systems share a twist, this is only a 5-dimensional screw system.

Moreover, arguing as in the proof of Theorem 4, at a point $g_1g_2g_3$ in the submanifold the tangent vectors translated back to the identity have the form,

$$\mathbf{s} = g_1(\dot{\theta}_1\mathbf{s}_1' + \dot{\theta}_2\mathbf{s}_2 + \dot{\theta}_1 e^{\theta_2\mathbf{s}_2}\mathbf{s}_3 e^{-\theta_2\mathbf{s}_2})g_1^{-1}. \tag{II.2.61}$$

$g_1^{-1}\mathbf{s}g_1$ is the sum of elements from the system IA_2 with elements from the Lie algebra of G_1 so stays in the required 5-system.

The only possible subgroup G_1 is the pseudo-planar subgroup $H_p \ltimes \mathbb{R}^2$, since this is the only 3-dimensional subgroup of $SE(3)$ that contains elements with finite, non-zero pitch.

II.2.5.2 Extensions of the $\mathcal{HPH}$ Chain

The same trick, used in the previous section, can be employed to extend the $\mathcal{HPH}$ persistent 3-chain to a persistent 5-chain. In this case, one has a little more freedom to choose the first twist in the 3-chain and hence also the 3-dimensional subgroup containing this twist. The second and third joints can be chosen to be

$$\mathbf{s}_2 = \begin{pmatrix} 0 \\ 0 \\ 0 \\ 0 \\ 0 \\ 1 \end{pmatrix} \quad \text{and} \quad \mathbf{s}_3 = \begin{pmatrix} 0 \\ \sin\alpha_2 \\ \cos\alpha_2 \\ 0 \\ h\sin\alpha_2 \\ h\cos\alpha_2 \end{pmatrix}. \tag{II.2.62}$$

That is, the $\mathcal{P}$-joint is directed in the z-direction, while the $z-y$ plane is chosen to contain the axis of the final $\mathcal{H}$-joint, which has pitch h. The origin of the coordinate system lies on this joint axis. Because $\mathbf{s}_2$ is a pure translation, the relevant commutator is only

$$[\mathbf{s}_2,\, \mathbf{s}_3] = \begin{pmatrix} 0 \\ 0 \\ 0 \\ -\sin\alpha_2 \\ 0 \\ 0 \end{pmatrix}. \tag{II.2.63}$$

Here no constraints on $\mathbf{s}_3$ are given, hence a general element of the 3 system generated by $\mathbf{s}_2, \mathbf{s}_3$ and $[\mathbf{s}_2,\, \mathbf{s}_3]$ can be written as

$$\mathbf{s} = a\mathbf{s}_2 + b\mathbf{s}_3 + c[\mathbf{s}_2,\, \mathbf{s}_3] = \begin{pmatrix} 0 \\ b\sin\alpha_2 \\ b\cos\alpha_2 \\ -c\sin\alpha_2 \\ bh\sin\alpha_2 \\ a + bh\cos\alpha_2 \end{pmatrix}, \tag{II.2.64}$$

where a, b and c are arbitrary parameters. The pitch of a general screw in the system is thus,

$$\text{pitch}(\mathbf{s}) = \frac{a\cos\alpha_2 + bh}{b}. \tag{II.2.65}$$

Clearly, when $b = 0$ this system contains a line of infinite pitch screws. Also, the system contains screws of different pitches, for example, there are zero pitch screws when $a = -bh\sec\alpha_2$. So this is a IC 3-system. There are two possible IC 3-systems distinguished by the pitch. If the pitch is zero, the system is class IC^0 otherwise it is IC ($p \neq 0$). By a sequence of rotations, translations and linear transformations of the generators, the screw system can be put into the normal form given in Table II.1.2. This reveals that the screw system has class IC ($p \neq 0$) with $p = \tan\alpha_2$. Note, that this does not depend on the original pitch h of the final $\mathcal{H}$-joint. The first joint can now be chosen to be given by any screw in the system. The pitch of this first screw is determined by the formula $\text{pitch}(\mathbf{s}_1) = (a/b)\cos\alpha_2 + h$ and so can be chosen to have any value. However, its direction and location will be limited to a line determined by the value of c chosen.

To extend this linkage to a 5-dimensional submanifold we can embed the first joint $\mathbf{s}_1$, in a 3-dimensional subgroup as before. If one chooses $\mathbf{s}_1$ to have finite, non-zero pitch then one can only embed this in a pseudo-planar subgroup $H_p \ltimes \mathbb{R}^2$ as in the previous section. One could also choose $\mathbf{s}_1$ to have zero pitch, in which case one can embed this in either a spherical subgroup $SO(3)$ or a planar subgroup $SE(2)$. The only restriction is that, if we choose $\mathbf{s}_1$ to have infinite pitch, one can not embed this in the $\mathbb{R}^3$ subgroup since $\mathbf{s}_2$ will also lie in this subgroup and so the submanifold produced will only be 4-dimensional.

Chapter II.3

Mechanisms Generating Line Trajectories

Abstract: *In this chapter the problem of designing mechanisms to guide a line along a ruled surface is considered. This is motivated by the idea of illustrating, by means of a physical model, the set of lines in a general linear line complex. Cylindrical symmetry implies that the problem reduces of designing a mechanism to move a line along the regulus of a rectangular hyperbolic paraboloid. This leads to the study of several simple ruled surfaces and congruences of lines. In particular this chapter studies the regulus of the elliptical hyperboloid, the cylindroid and linear line congruences. In each case relatively simple mechanisms are designed to constrain a line in the mechanism to a given space of lines.*

II.3.1 Introduction and Motivation

Over the years much attention has been paid to the design of mechanisms to produce a given point trajectory. Far less emphasis has been given to the design of mechanisms that move a line along a desired trajectory. Indeed the authors could find no mention of this problem in the literature of the past 120 years or so. In [113], "kinematically generated" ruled surfaces are considered. The application considered there was to 5-axis cylindrical milling and laser machining. However, no particular mechanisms were designed as the focus was on producing ruled surfaces that could be followed by general purpose machines. Of course, the subject of line geometry is central to kinematics, see for example the standard texts, [91], [114], [115] where various sets of lines are mentioned in connection with the kinematics of mechanisms and machines. The Mathematics of line geometry has also been used profitably in many other areas, in particular Mechanical Gearing, [116], [117], Computer Aided Design [118], Robotics and Geometric Optics.

In [119](p.37) Felix Klein refers to, and gives a sketch of, a mechanical model produced by Martin Schilling. This model was used to illustrate the linear line complex. The details of this mechanism seem to be lost. So, in part, this work is an attempt to

recreate this mechanism. Since the set of lines in the complex has a cylindrical symmetry, see Section II.3.2, one only needs to worry about the radial motion of the line. Subsequently, in Section II.3.2.1 it is shown that the radial lines, in the general linear line complex, form the regulus of a rectangular hyperbolic paraboloid. So the first problem addressed in this work is to design a mechanism to carry a line along this ruled surface.

A simple solution would be to represent the line by a rod that moves in a slotted cylinder, the shape of the slot determined by quartic curve shown in Fig.II.3.2. However, the intention here is to design a mechanism using standard elements, that is a mechanism consisting of only lower Reuleaux pair joints. This is facilitated by a knowledge of the set of rigid-body displacements that constrain a line to lie in a general linear complex. A constraint variety first studied by Blaschke, see [111].

This leads to the study of other simple ruled surfaces, in particular the regulus of a general elliptic hyperboloid and the cylindroid. Straightforward mechanism designs are given to guide a line in the mechanism through the lines of the given ruled surfaces. Finally, the problem of designing 2 degree-of-freedom mechanisms to move a line in linear congruences, elliptic, hyperbolic or parabolic is considered.

Let's setting-up some notation that will be used below. Lines in space can be written as dual quaternions using the Plücker coordinates of the line. In this formalism, a line takes the form,

$$\ell = (\omega_x \mathbf{i} + \omega_y \mathbf{j} + \omega_z \mathbf{k}) + \varepsilon(v_x \mathbf{i} + v_y \mathbf{j} + v_z \mathbf{k}). \tag{II.3.1}$$

A rotation with angle θ about the line ℓ is then given by the dual quaternion,

$$\mathbf{h}(\theta) = \cos(\theta/2) + \sin(\theta/2)\ell. \tag{II.3.2}$$

The Plücker coordinates of a line satisfies, as seen, the relation,

$$\boldsymbol{\omega} \cdot \mathbf{v} = 0. \tag{II.3.3}$$

This can be written as a matrix product,

$$(\omega_x,\, \omega_y,\, \omega_z,\, v_x,\, v_y,\, v_z) \begin{pmatrix} 0 & 0 & 0 & 1 & 0 & 0 \\ 0 & 0 & 0 & 0 & 1 & 0 \\ 0 & 0 & 0 & 0 & 0 & 1 \\ 1 & 0 & 0 & 0 & 0 & 0 \\ 0 & 1 & 0 & 0 & 0 & 0 \\ 0 & 0 & 1 & 0 & 0 & 0 \end{pmatrix} \begin{pmatrix} \omega_x \\ \omega_y \\ \omega_z \\ v_x \\ v_y \\ v_z \end{pmatrix}$$
$$= (\boldsymbol{\omega}^T,\, \mathbf{v}^T) \begin{pmatrix} \mathbf{0} & \mathbf{I} \\ \mathbf{I} & \mathbf{0} \end{pmatrix} \begin{pmatrix} \boldsymbol{\omega} \\ \mathbf{v} \end{pmatrix} = 0. \tag{II.3.4}$$

The reciprocal product of a pair of lines is then given by,

$$\ell_1^T \mathbf{Q}_0 \ell_2 = (\boldsymbol{\omega}_1^T,\, \mathbf{v}_1^T) \begin{pmatrix} \mathbf{0} & \mathbf{I} \\ \mathbf{I} & \mathbf{0} \end{pmatrix} \begin{pmatrix} \boldsymbol{\omega}_2 \\ \mathbf{v}_2 \end{pmatrix} = \boldsymbol{\omega}_1 \cdot \mathbf{v}_2 + \mathbf{v}_1 \cdot \boldsymbol{\omega}_2. \tag{II.3.5}$$

It can be shown that lines are coplanar if and only if their reciprocal product vanishes.

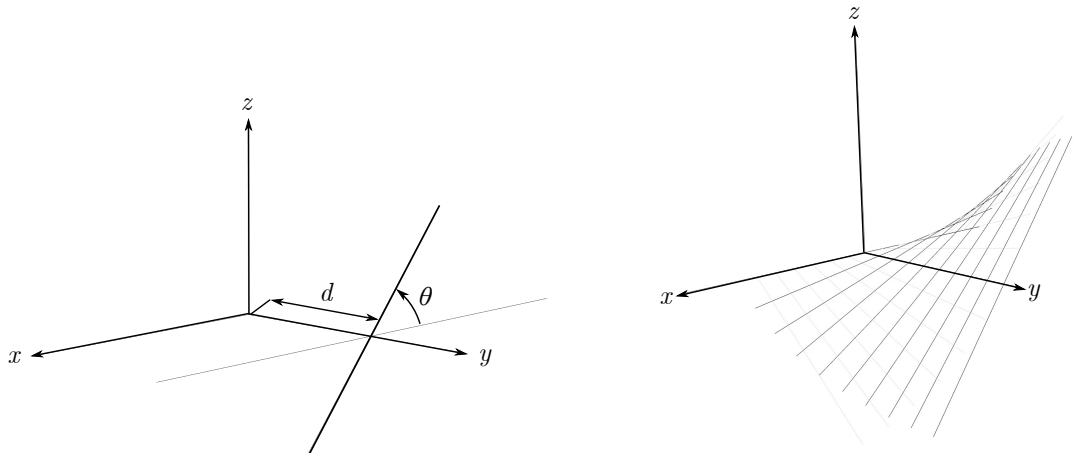

Figure II.3.1: Line Motions: (a) represents a line in the line complex perpendicular to the y-axis while (b) depicts the reguli of lines in a rectangular hyperbolic paraboloid. The heavy lines are the lines in the complex perpendicular to the y-axis.

II.3.2 The General Linear Line Complex

The set of lines that satisfy a linear equation in the Plücker coordinates form what is known as a linear complex of lines. In the past, these sets of lines were also known as screws.
The linear equation for the lines in the complex are [112],

$$m_x\omega_x + m_y\omega_y + m_z\omega_z + f_x v_x + f_y v_y + f_z v_z = 0. \tag{II.3.6}$$

Collecting the constant coefficients $m_x, \ldots, f_z$ into a column vector gives a wrench,

$$\mathbf{w}_d = \begin{pmatrix} m_x \\ m_y \\ m_z \\ f_x \\ f_y \\ f_z \end{pmatrix}. \tag{II.3.7}$$

However, this wrench can also be written as a twist $\mathbf{s}$, multiplied by the matrix, $\mathbf{Q}_0$. That is, $\mathbf{w}_d = \mathbf{Q}_0\mathbf{s}$, and the equation for the complex can be written,

$$\mathbf{s}^T\mathbf{Q}_0\ell = 0. \tag{II.3.8}$$

Multiplying the twist $\mathbf{s}$, by an arbitrary non-zero constant clearly does not affect the solution set to this homogeneous equation. Thus the twist is really a screw, hence justifying the identification of linear line complexes with screws.

Any property of a screw is therefore also a property of the corresponding linear line complex. In particular, line complexes have an axis and a pitch. By choosing suitable coordinates a general screw $\mathbf{s}$ can be put into the standard form,

$$\mathbf{s} = \begin{pmatrix} 0 \\ 0 \\ 1 \\ 0 \\ 0 \\ p \end{pmatrix}, \tag{II.3.9}$$

that is, with the axis of the screw aligned with the z-axis and where the pitch of the screw is p. The set of lines in the complex defined by $\mathbf{s}$ has a cylindrical symmetry about the screw axis. This can be seen by observing that the matrix $\mathbf{Q}_0$ is invariant under the action of the adjoint representation of $SE(3)$, for any group element g, one has, $\mathrm{Ad}(g)^T\mathbf{Q}_0\,\mathrm{Ad}(g) = Q_0$. Hence if c is in the cylindrical subgroup that preserves $\mathbf{s}$, that is $Ad(c)\mathbf{s} = \mathbf{s}$, then,

$$0 = \mathbf{s}^T\mathbf{Q}_0\ell = \mathbf{s}^T\,\mathrm{Ad}(c)^T\mathbf{Q}_0\,\mathrm{Ad}(c)\ell = \mathbf{s}^T\mathbf{Q}_0\,\mathrm{Ad}(c)\ell. \tag{II.3.10}$$

Hence, $\mathrm{Ad}(c)\ell$, the transform of the line ℓ by c, lies in the complex if ℓ is in the complex.

This means that, to understand the disposition of lines in the complex one only need to work out how the lines change as it moves away from the screw axis radially. So, consider a line whose closest point to the screw axis lies along the y-axis a distance d from the screw axis. Assume that the angle that the line makes with the x-axis is θ so that the Plücker coordinates of the line are,

$$\ell(\theta) = \begin{pmatrix} \cos\theta \\ 0 \\ \sin\theta \\ d\sin\theta \\ 0 \\ -d\cos\theta \end{pmatrix} \tag{II.3.11}$$

see Fig.II.3.1a. Substituting this into the linear equation for the complex gives,

$$\mathbf{s}^T\mathbf{Q}_0\ell = p\sin\theta - d\cos\theta = 0. \tag{II.3.12}$$

This means that as the line moves away from the screw axis the distance from the axis and angle to the axis are coupled according to the relation,

$$d = p\tan\theta. \tag{II.3.13}$$

When $\theta = 0$ and $d = 0$, the line coincides with the x-axis, but as the angle approaches $\pm\pi/2$ the distance increases without limit, that is, the further from the axis the line is the more nearly it is parallel to the axis of the complex. See Fig. II.3.1b.

Note that, all the lines in the complex are of this form or can be found from one of these lines by rotating about, and translating along the axis of the complex.

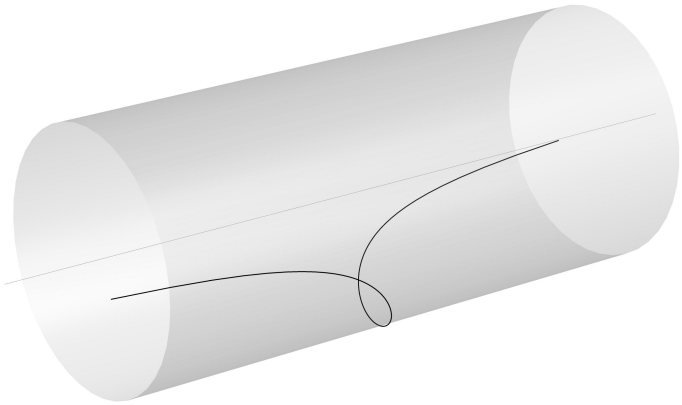

Figure II.3.2: The quartic curve on a cylinder.

II.3.2.1 The Ruled Surface of Lines along a Radius

The one-parameter family of lines defined by Equation (II.3.11) form a ruled surface. Points on this surface have the form,

$$\begin{pmatrix} x \\ y \\ z \end{pmatrix} = \begin{pmatrix} 0 \\ d \\ 0 \end{pmatrix} + \lambda \begin{pmatrix} \cos\theta \\ 0 \\ \sin\theta \end{pmatrix} = \begin{pmatrix} \lambda\cos\theta \\ p\tan\theta \\ \lambda\sin\theta \end{pmatrix}, \tag{II.3.14}$$

where λ is an arbitrary parameter. Eliminating the parameters, it can be see that,

$$pz/x = y, \tag{II.3.15}$$

or, if one introduces the homogenising variable w,

$$xy - pwz = 0. \tag{II.3.16}$$

That is, the ruled surface is a regulus of a rectangular hyperbolic paraboloid.

Such a surface has two rulings, the one given above and the other given by the lines,

$$\ell'(\phi) = \begin{pmatrix} 0 \\ \cos\phi \\ \sin\phi \\ 0 \\ -l\sin\phi \\ l\cos\phi \end{pmatrix}, \tag{II.3.17}$$

where $l = p\tan\phi$. Notice that, taking the reciprocal product of any pair of lines, one from each regulus gives,

$$\ell(\theta)^T \mathbf{Q}_0 \ell'(\phi) = p\sin\theta\sin\phi - p\sin\phi\sin\theta = 0, \tag{II.3.18}$$

that is, all the lines from one regulus are reciprocal to all the lines from the other regulus. This shows that all the lines from one regulus meet all the lines from the other regulus. In Fig. II.3.1b the grey lines belong to the second regulus on the surface.

II.3.2.2 The Motion Generating the Regulus

The regulus of lines described in the previous section can be produced by subjecting an initial line to a rigid-body motion. The regulus can be given by subjecting the x-axis to the motion,

$$\mathbf{M}(\theta) = \begin{pmatrix} \cos\theta & 0 & \sin\theta & 0 \\ 0 & 1 & 0 & p\,\tan\theta \\ -\sin\theta & 0 & \cos\theta & 0 \\ 0 & 0 & 0 & 1 \end{pmatrix}. \tag{II.3.19}$$

In general, the trajectories of points in space under this motion are given by,

$$\begin{aligned} X &= x\cos\theta + z\sin\theta, \\ Y &= y + p\tan\theta, \\ Z &= -x\sin\theta + z\cos\theta. \end{aligned} \tag{II.3.20}$$

Thinking of this as a curve in projective space $\mathbb{PR}^3$, by introducing the homogenising variable w, and writing $c = \cos(\theta/2)$ and $s = \sin(\theta/2)$, the equations for the trajectories become,

$$\begin{aligned} X &= x(c^2 - s^2)^2 + 2zcs(c^2 - s^2), \\ Y &= y(c^2 + s^2)(c^2 - s^2) + 2pcs(c^2 + s^2), \\ Z &= -2xcs(c^2 - s^2)^2 + z(c^2 - s^2)^2, \\ W &= w(c^2 + s^2)(c^2 - s^2). \end{aligned} \tag{II.3.21}$$

Here, $(c^2 + s^2) = 1$ has been used to render the equations homogeneous. Treating c and s as homogeneous parameters shows that the trajectories are generally degree 4 curves (quartic curves). Moreover, it can be seen that the curves satisfy $X^2 + Y^2 = x^2 + y^2$, so these trajectories lie on concentric cylinders about the y-axis; see Fig.II.3.2.

II.3.2.3 The Motion as a Curve in the Study Quadric

The corresponding curve in the Study quadric can be found by mapping the matrix in Equation (II.3.19) to the Study quadric using the mapping given in [111, §3.3] for example. After cancelling common factors the result is,

$$g(c,\, s) = \big(c(c^2 - s^2) + s(c^2 - s^2)\mathbf{j}\big) + \varepsilon p\big(cs^2 - c^2 s\mathbf{j}\big). \tag{II.3.22}$$

Notice, this is a twisted cubic curve, that is a rational cubic. The cubic intersects the 3-plane of unphysical elements A_∞ in a pair of points when the parameters satisfy $c = \pm s$.

In general, a degree n curve in the Study quadric will act on points in space to produce trajectories with degree $2n$. However, the degree can be reduced depending on how the curve in the Study quadric meets the 3-plane A_∞, see [120].

A twisted cubic curve lies on the intersection of three quadrics in a $\mathbb{PR}^3$. In this case these varieties are easy to find. One of the quadrics is the Study quadric of course. The 3-plane is given by the linear equations $a_1 = a_3 = c_1 = c_3 = 0$. The intersection of the 3-plane with the Study quadric gives the set of group elements producing rotations and translations about the y-axis, that is a subgroup of $SE(3)$ comprising of cylindrical displacements about the y-axis. Intersecting this 3-plane with the Study quadric gives a 2-dimensional quadric with equation,

$$a_0c_0 + a_2c_2 = 0. \tag{II.3.23}$$

The second quadric can be taken as the subvariety of rigid-body displacements that maintain a line in a fixed line complex. In [111, §5.4] it was shown that the rigid-body displacements that maintain a line $\ell^T = (\boldsymbol{\omega}^T, \mathbf{v}^T)$, in a complex determined by the screw $\mathbf{s}^T = (\mathbf{w}^T, \mathbf{u}^T)$, is a quadric in $\mathbb{PR}^7$. The equation for the quadric is most easily stated using an 8×8 partitioned matrix,

$$\mathbf{h}^T\mathbf{Q}\mathbf{h} = \begin{pmatrix}\mathbf{a}^T & \mathbf{c}^T\end{pmatrix}\begin{pmatrix}\Xi & \Upsilon \\ \Upsilon & 0\end{pmatrix}\begin{pmatrix}\mathbf{a} \\ \mathbf{c}\end{pmatrix} = 0. \tag{II.3.24}$$

Where $\mathbf{h}^T = (\mathbf{a}^T, \mathbf{c}^T) = (a_0, a_1, a_2, a_3, c_0, c_1, c_2, c_3)^T$ represents the homogeneous coordinates of a group element in $\mathbb{PR}^7$. The two 4×4 symmetric matrices Ξ and Υ are given in turn by,

$$\Xi = \begin{pmatrix}0 & (\boldsymbol{\omega} \times \mathbf{u} + \mathbf{v} \times \mathbf{w})^T \\ (\boldsymbol{\omega} \times \mathbf{u} + \mathbf{v} \times \mathbf{w}) & \mathbf{U}\boldsymbol{\Omega} + \boldsymbol{\Omega}\mathbf{U} + \mathbf{W}\mathbf{V} + \mathbf{V}\mathbf{W}\end{pmatrix} \tag{II.3.25}$$

and

$$\Upsilon = \begin{pmatrix}\mathbf{0} & (\boldsymbol{\omega} \times \mathbf{w})^T \\ (\boldsymbol{\omega} \times \mathbf{w}) & \boldsymbol{\Omega}\mathbf{W} + \mathbf{W}\boldsymbol{\Omega}\end{pmatrix}. \tag{II.3.26}$$

The matrices, $\mathbf{U}$, $\boldsymbol{\Omega}$ and so forth, represent the 3×3 anti-symmetric matrices corresponding to $\mathbf{u}$, $\boldsymbol{\omega}$ *etc.* With $\ell(0)$ and $\mathbf{s}$ as given above, the matrix representing the quadric is,

$$\mathbf{Q}_1 = \begin{pmatrix}
0 & 0 & -p & 0 & 0 & 0 & -1 & 0 \\
0 & 0 & 0 & p & 0 & 0 & 0 & 1 \\
-p & 0 & 0 & 0 & -1 & 0 & 0 & 0 \\
0 & p & 0 & 0 & 0 & 1 & 0 & 0 \\
0 & 0 & -1 & 0 & 0 & 0 & 0 & 0 \\
0 & 0 & 0 & 1 & 0 & 0 & 0 & 0 \\
-1 & 0 & 0 & 0 & 0 & 0 & 0 & 0 \\
0 & 1 & 0 & 0 & 0 & 0 & 0 & 0
\end{pmatrix}. \tag{II.3.27}$$

That is, the quadric is given by the equation,

$$p(a_1a_3 - a_0a_2) - (a_0c_2 - a_1c_3 + a_2c_0 - a_3c_1) = 0. \tag{II.3.28}$$

Intersecting this with the 3-plane of cylindrical displacements gives the 2-dimensional quadric with the equation,

$$pa_0a_2 + a_0c_2 + a_2c_0 = 0. \tag{II.3.29}$$

To find the third quadric one can inspect the parameterisation of the curve given in Equation (II.3.22) and see that the third quadric is,

$$p(a_0c_0 - a_2c_2) + 2(c_0^2 - c_2^2) = 0. \tag{II.3.30}$$

Of course, linear combinations of the 3 quadrics can also be used.

II.3.2.4 The Twist Velocity

The twist velocity of the motion can be found using (II.3.19),

$$\mathbf{S} = \dot{\mathbf{M}}\mathbf{M}^{-1} = \begin{pmatrix} 0 & 0 & 1 & 0 \\ 0 & 0 & 0 & p\sec^2\theta \\ -1 & 0 & 0 & 0 \\ 0 & 0 & 0 & 0 \end{pmatrix}. \tag{II.3.31}$$

As a 6-component vector the twist velocity S can thus be written,

$$\mathbf{s} = \begin{pmatrix} 0 \\ 1 \\ 0 \\ 0 \\ p\sec^2\theta \\ 0 \end{pmatrix}. \tag{II.3.32}$$

This shows that the axis of the twist is always aligned with the y-axis. The pitch of the twist is not constant, it changes as the line moves away from the axis of the complex. Writing h for the pitch of the motion one has that,

$$h = p\sec^2\theta = \frac{1}{p}(p^2 + d^2), \tag{II.3.33}$$

since the distance d of translation along the y-axis satisfies $d = p\tan\theta$.

The fixed axode of the motion is just the axis of the twist velocity. Clearly in this case the fixed axode degenerates to a single line, the y-axis.

The moving axode can be found from the axis of the twist velocity in the moving frame. That is the axis of $\mathbf{M}^{-1}\dot{\mathbf{M}}$. This gives the same result as the in the globally fixed frame and hence the moving axode also degenerates to a single line.

II.3.2.5 Line-Symmetry

Since the motion is about a fixed axis, the motion is line-symmetric. This results from an elementary theorem due to Krames [121, p. 395] (see also [122]).

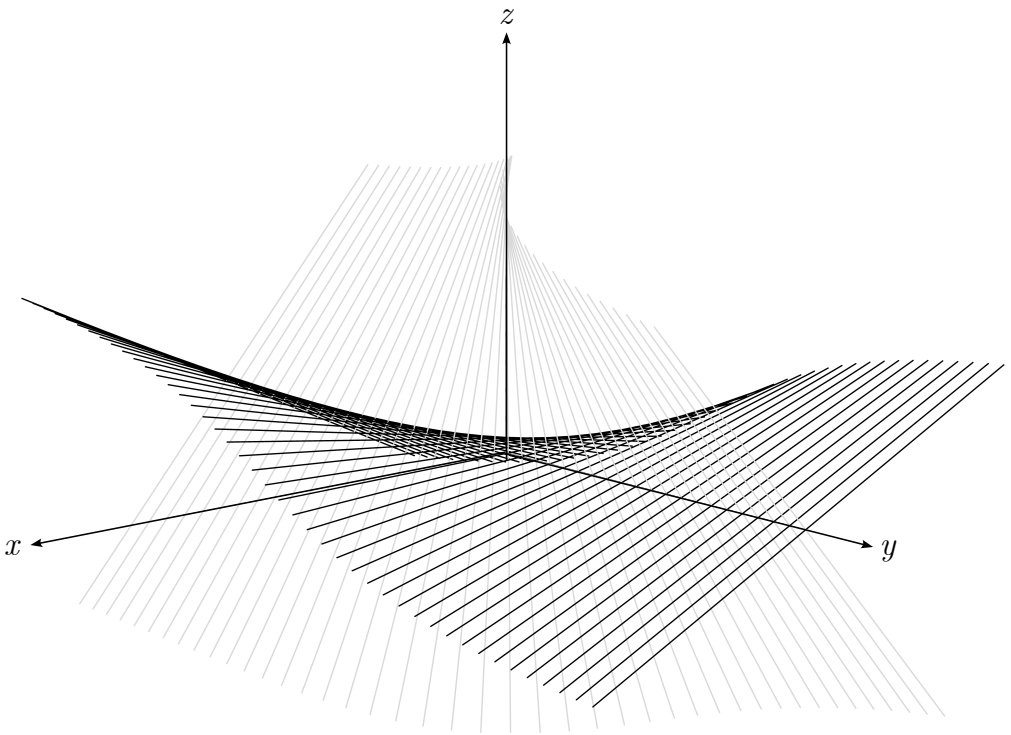

Figure II.3.3: Zindler's conoid.

The ruled surface that acts as the base for this motion can be found in several ways, we could employ the methods outlined in [122] for example. But in this case it is perhaps easiest to use simple geometry. So consider a half-turn that moves the x axis to the line $\ell(\theta)$ given in (II.3.11). The axis of this π rotation must cross the y-axis at right angles half way between the x-axis and the line $\ell(\theta)$. That is, it must pass through the point $(0,\, d/2,\, 0)$ and lie parallel to the xz-plane. Next, it must bisect the angle between the the x-axis and $\ell(\theta)$. However, there are two solutions for this, either the angle from the x-axis to the axis of the half-turn could be $\theta/2$ or $\theta/2+\pi/2$. That is the axis could have Plücker coordinates,

$$\begin{pmatrix} \cos(\theta/2) \\ 0 \\ \sin(\theta/2) \\ \frac{d}{2}\sin(\theta/2) \\ 0 \\ -\frac{d}{2}\cos(\theta/2) \end{pmatrix} \quad \text{or} \quad \begin{pmatrix} -\sin(\theta/2) \\ 0 \\ \cos(\theta/2) \\ \frac{d}{2}\cos(\theta/2) \\ 0 \\ \frac{d}{2}\sin(\theta/2) \end{pmatrix}. \tag{II.3.34}$$

This gives parameterisations of the surfaces, so that one can write the coordinates of

points on these surfaces as,

$$\begin{aligned} x &= \lambda\cos(\theta/2), & x &= -\mu\sin(\theta/2), \\ y &= d/2 = \frac{p}{2}\tan\theta, \quad \text{or} & y &= d/2 = \frac{p}{2}\tan\theta, \\ z &= \lambda\sin(\theta/2), & z &= \cos(\theta/2), \end{aligned} \tag{II.3.35}$$

where λ and μ are arbitrary parameters. In both cases, if one eliminates the parameters, θ and λ or μ, one gets the same equation for the ruled surface,

$$y = p\frac{xz}{x^2 - z^2}, \tag{II.3.36}$$

which can also be written as,

$$y(x^2 - z^2) - pxz = 0. \tag{II.3.37}$$

The ruled surface determined by the axes of the half-turns generating the motion is an example of Zindler's conoid, see [123] for example. The surface is illustrated in Fig. II.3.3.

In [124], Röschel finds all rational rigid-body motions that produce generic trajectories that are rational quartic curves. The motion here is an example of a type outlined in Chapter 3 of [124] with normal form given by Equation (3.7). All the motions considered in this chapter are line symmetric but the particular case where the base surface of the motion is Zindler's conoid was not considered in detail.

II.3.2.6 A Mechanism to Generate the Motion

Finally here, let's return to the problem of designing a mechanism that will allow a line to move but only take positions in the general line complex. A straightforward solution to this is the Schilling model referred to by Klein [119]. Presumably, the final cylindrical joint had a groove on the cylindrical part shaped as the quartic curve found above, and a corresponding notch on the mating part so that the end-effector followed the motion given in Eq.II.3.19, see Fig. II.3.2.

Here, the aim is to design a simple mechanism consisting of rigid links and lower Reuleaux pairs as joints only. Since the lines in the complex can be arbitrarily far from the axis of the complex, one can not expect to be able to use only revolute joints and will have to be content with only reproducing part of the complex of lines due to the finite extension of any real joint.

To begin with, restricting a line to be in the orbit of a cylindrical subgroup of $SE(3)$ is straightforward. All that is required is a cylindrical joint which could also be implemented using a revolute joint and a prismatic joint. Where the axis of the revolute joint and the direction of the prismatic joint are parallel. In our case, the axis of the cylindrical joint must meet and be perpendicular to the axis of the line complex. There is no simple, open chain of joints, that will produce the motion given by Equation II.3.19 — finding a more sophisticated, but still relatively simple linkage is the aim here. There are simple open chain linkages that can move a line so that it remains in a special linear

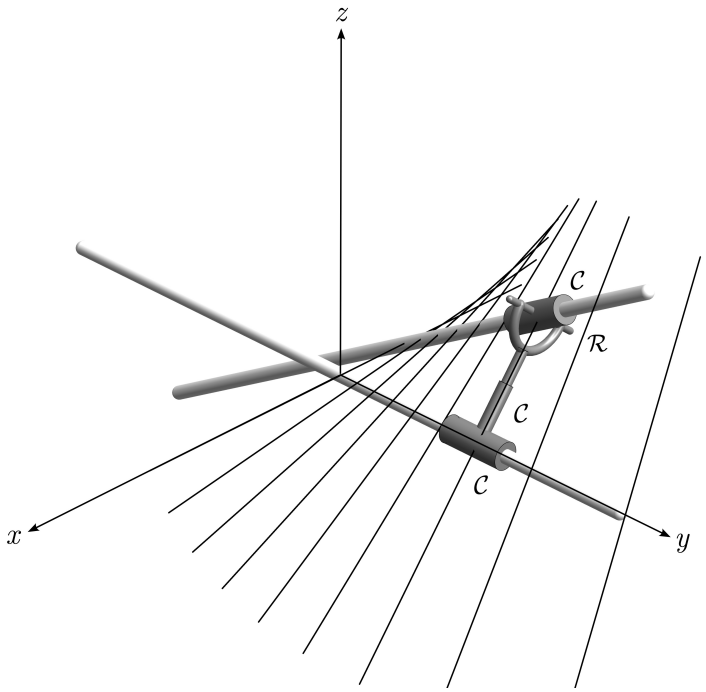

Figure II.3.4: Closed loop $\mathcal{CCRC}$ Mechanism to move a line in a rectangular hyperbolic paraboloid. The white links are the fixed links..

line complex. That is, the set of lines reciprocal to a fixed line. For example, the $\mathcal{UPU}$ linkages studied in [125] could be used, as could a $\mathcal{PSP}$ chain or the $\mathcal{CRC}$ chain. In $\mathbb{PR}^7$ the constraint variety for such a geometry has the same form as given above for lines in a general linear complex. Consider the set of displacements that maintain the same initial line $\ell(0)$, but now in the special linear complex of all lines meeting one of the lines in the second regulus $\ell'(\phi)$ for some ϕ. This is a quadric with the equation,

$$\big(p(a_1a_3 - a_0a_2) - (a_0c_2 - a_1c_3 + a_2c_0 - a_3c_1)\big)\sin\phi - \\ (p(a_0a_3 + a_1a_2)\sin\phi\tan\phi + (a_0c_3 + c_0a_3 + a_1c_2 + a_2c_1)\cos\phi = 0. \quad \text{(II.3.38)}$$

Now, intersecting this with the 3-plane of cylindrical displacements, $a_1 = a_3 = c_1 = c_3 = 0$ produces, $pa_0a_2 + a_0c_2 + a_2c_0 = 0$. This is the same quadric that has been found for the lines in the general linear complex. Moreover, this does not depend on ϕ, so any line in the second regulus could be used as the axis of the special linear complex. The proposed mechanism is illustrated in Fig. II.3.4. In this case a $\mathcal{CRC}$ chain has been chosen to provide the quadratic constraint.

There is one final point to check. The intersection of two quadrics in $\mathbb{PR}^3$ will give a quartic curve. The discussion above shows that in our case, the intersection of the Study quadric the quadratic constraint variety and the $\mathbb{PR}^3$ containing the cylindrical subgroup, will contain a component that is a twisted cubic curve. Hence, there must

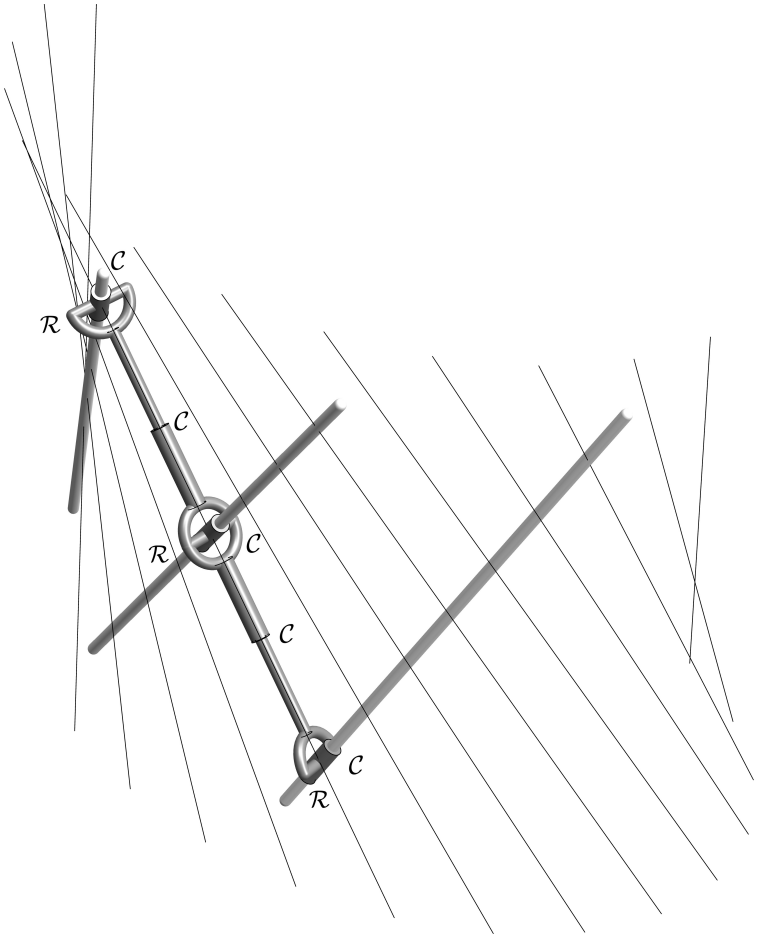

Figure II.3.5: Mechanism to Guide a Line along a Regulus of an Elliptical Hyperboloid. The white links are the fixed links.

be another component, necessarily a line. Depending on its location, this line could interfere with the functioning of the mechanism. However, the line is clearly given by $a_0 = a_2 = 0$ and hence lies on A_∞, the 3-plane of ideal or unphysical displacements, so this component will have no influence on any practical realisation of the mechanism.

The $\mathcal{CCRC}$ mechanism shown in Fig. II.3.4, only produces a motion that moves a line in a regulus of a rectangular hyperbolic paraboloid. To get the full range of motion such that the line can be placed anywhere in the linear complex all that is needed is to mount the mechanism above on another cylindrical joint, so that the axis of the joint is the same as the axis of the complex. Notice that, the resulting mechanism is not a serial chain or a single loop mechanism. It would consist of a cylindrical joint in series with a $\mathcal{CCRC}$ loop.

II.3.3 More Simple Examples of Ruled Surfaces and Mechanisms

The above considerations prompt questions about other ruled surfaces. In particular, can one design a mechanism to move a line along some other ruled surfaces? The simplest ruled surface that can be considered would be the regulus of a hyperboloid of one sheet. If one requires the ruled surface to be a regulus of a circularly symmetric hyperboloid, then the answer is trivial. It is well known that rotating a line about an axis skew to the line will produce such a ruled surface. In other words, the required mechanism is a single revolute joint.

II.3.3.1 The Regulus of an Elliptic Hyperboloid

If the required ruled surface to be traced is a regulus in an elliptic hyperboloid then the problem is a little harder. Suppose the surface is given by the equation,

$$\frac{x^2}{\alpha^2} + \frac{y^2}{\beta^2} - \frac{z^2}{\gamma^2} = 1. \tag{II.3.39}$$

The lines in the surface can be parameterised as,

$$\begin{pmatrix} x \\ y \\ z \end{pmatrix} = \begin{pmatrix} \alpha\cos\theta - \alpha\lambda\sin\theta \\ \beta\sin\theta + \beta\lambda\cos\theta \\ \pm\gamma\lambda \end{pmatrix}, \tag{II.3.40}$$

where different values of θ give different lines and λ is the parameter along the line. The two reguli are distinguished by the different signs for the last component.

The Plücker coordinates of these two familys of lines are given by,

$$\ell^+(\theta) = \begin{pmatrix} -\alpha\sin\theta \\ \beta\cos\theta \\ \gamma \\ \beta\gamma\sin\theta \\ -\alpha\gamma\cos\theta \\ \alpha\beta \end{pmatrix} \quad \text{and} \quad \ell^-(\phi) = \begin{pmatrix} -\alpha\sin\phi \\ \beta\cos\phi \\ -\gamma \\ -\beta\gamma\sin\phi \\ \alpha\gamma\cos\phi \\ \alpha\beta \end{pmatrix}. \tag{II.3.41}$$

It is easy to see that $\big(\ell^+(\theta)\big)^T \mathbf{Q}_0 \big(\ell^-(\phi)\big) = 0$ and hence every line in one regulus meets every line in the other family. This can be used to design the mechanism. This time one needs three fixed lines from the other regulus, say from ℓ^-. Then, $\mathcal{RC}$ joints allow the line to meet each fixed line but with all possible motion of the line within the special linear line complex defined by the fixed lines. A pair of $\mathcal{C}$ joints coaxial with the moving line then allow rotation about and translation along the line, see Figure II.3.5. Notice, this is not a single loop mechanism.

The fact that the hyperboloid was elliptical in section rather than circular was not important here. So, it should be possible to construct such a mechanism to move a line along the regulus of a circular hyperboloid.

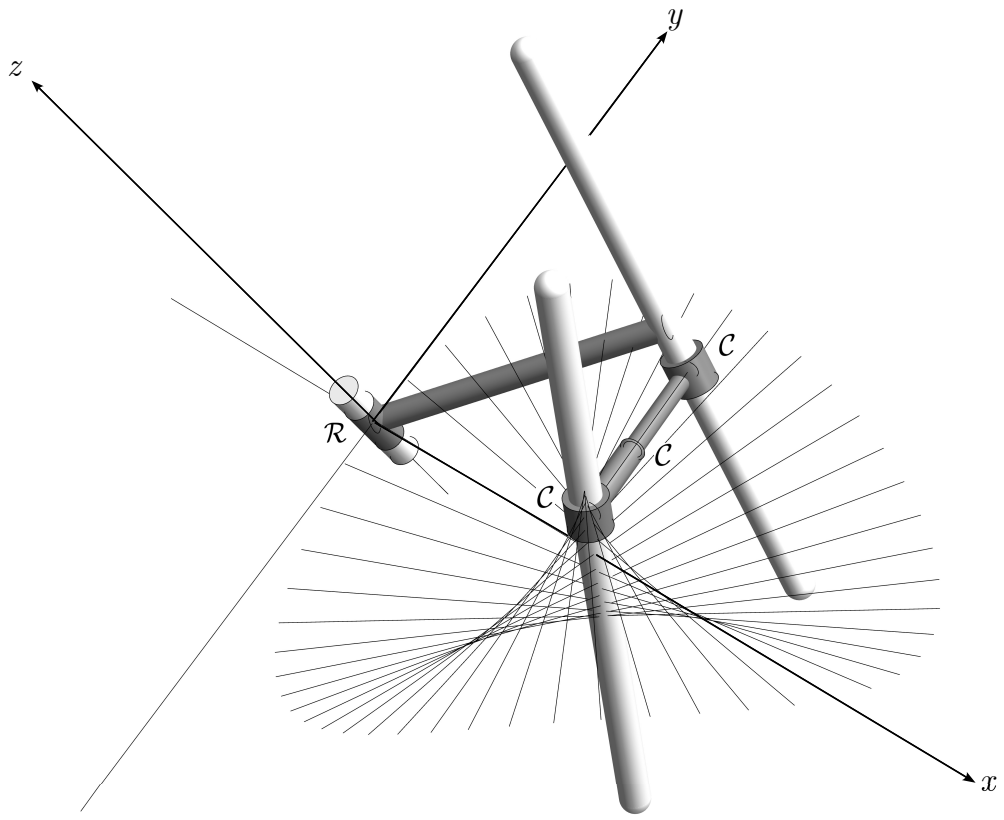

Figure II.3.6: Mechanism to Guide a Line along a Cylindroid. The white links are the fixed links.

Also note that there is at least one other mechanism that will produce a motion that guides a line along such a regulus. An elliptic trammel is a planar mechanism that can draw an ellipse. That is, a point on the coupler bar of such a mechanism will describe an ellipse. Intersecting the regulus of an elliptic hyperboloid with a plane perpendicular to its axis gives an ellipse. Each point of the ellipse lies on a single generator line of the regulus. However, if one rigidly attach a line to the point on the coupler of an elliptic trammel, the angle between the line and the line through the centre of the ellipse perpendicular to the plane of the mechanism will not be constant. So, a slightly more complex mechanism is required to solve this problem.

II.3.3.2 The Cylindroid

The cylindroid or Plücker's conoid is a ubiquitous figure in kinematics and the theory of mechanisms. It is a cubic surface with the canonical equation,

$$(x^2 + y^2)z = 2xy. \tag{II.3.42}$$

As a ruled surface, the generator lines can be parameterised as,

$$\ell = \begin{pmatrix} \cos\theta \\ \sin\theta \\ 0 \\ \sin\theta\sin 2\theta \\ \cos\theta\sin 2\theta \\ 0 \end{pmatrix} = \begin{pmatrix} c(c^2+s^2) \\ s(c^2+s^2) \\ 0 \\ 2cs^2 \\ 2c^2 s \\ 0 \end{pmatrix}, \tag{II.3.43}$$

where $c = \cos\theta$ and $s = \sin\theta$ are homogeneous parameters. This shows that the ruled surface is represented as a twisted cubic curve in the Klein quadric of lines in $\mathbb{PR}^3$.

The fact that the surface is a conoid, that is, all the lines meet a single fixed line at right-angles, means that one can find a simple parameterised motion that will move one line in the surface to each of the other lines comprising the surface. The desired motion is given by translating along the axis of the conoid and rotating around this axis,

$$\begin{aligned} \mathbf{G}(\theta) &= \begin{pmatrix} \cos\theta & -\sin\theta & 0 & 0 \\ \sin\theta & \cos\theta & 0 & 0 \\ 0 & 0 & 1 & 0 \\ 0 & 0 & 0 & 1 \end{pmatrix} \begin{pmatrix} 1 & 0 & 0 & 0 \\ 0 & 1 & 0 & 0 \\ 0 & 0 & 1 & \sin 2\theta \\ 0 & 0 & 0 & 1 \end{pmatrix} \\ &= \begin{pmatrix} \cos\theta & -\sin\theta & 0 & 0 \\ \sin\theta & \cos\theta & 0 & 0 \\ 0 & 0 & 1 & \sin 2\theta \\ 0 & 0 & 0 & 1 \end{pmatrix} \end{aligned} \tag{II.3.44}$$

In the Study quadric this motion is represented by a rational curve of degree 5,

$$\mathbf{h}(\theta) = \big(c(c^2+s^2)^2 + s(c^2+s^2)^2\mathbf{k}\big) + \varepsilon\big(-2cs^2(c^2-s^2) + 2c^2 s(c^2-s^2)\mathbf{k}\big), \tag{II.3.45}$$

where here $c = \cos(\theta/2)$ and $s = \sin(\theta/2)$. The intersection with A_∞ is given by the complex points $c = \pm is$ repeated twice. Applying this motion to a point in space produces a rational quartic curve lying on a cylinder with the same axis as the conoid,

$$\begin{aligned} X &= x(c^2-s^2)(c^2+s^2) - 2ycs(c^2+s^2), \\ Y &= 2xcs(c^2+s^2) + y(c^2-s^2)(c^2+s^2), \\ Z &= z(c^2+s^2)^2 + 4cs(c^2-s^2), \\ W &= w(c^2+s^2)^2. \end{aligned} \tag{II.3.46}$$

Again the parameters represent the sine and cosine of the half-angles here.

Consider a regulus of a hyperboloid. For the moment, assume that the hyperboloid is given by (II.3.39) as in the previous section. Further, assume that the regulus is given by $\ell^+(\theta)$ as in the previous section again. Now consider the ruled surface formed from the common perpendicular lines between one line in the regulus, $\ell^+(0)$ say, and all the other lines in the regulus, $\ell^+(\theta)$ for all θ. Since $\ell^+(0)$ is constant all the lines in the

ruled surface will meet $\ell^+(0)$ perpendicularly, so the surface is a conoid. The common perpendicular to the lines is given by the axis of the screw product,

$$\ell^+(0) \times \ell^-(\theta) = \begin{pmatrix} \beta\gamma(1-\cos\theta) \\ -\alpha\gamma\sin\theta \\ \alpha\beta\sin\theta \\ \alpha(\beta^2-\gamma^2)(1-\cos\theta) \\ \beta(\gamma^2-\alpha^2)\sin\theta \\ -\gamma(\alpha^2+\beta^2)\sin\theta \end{pmatrix}. \tag{II.3.47}$$

If one use half-angles to parameterise this twist one gets a common factor of $2\sin(\theta/2)$ which can be cancelled since these are homogeneous Plücker coordinates. The result can be written as,

$$\ell^+(0) \times \ell^-(\theta) = s \begin{pmatrix} \beta\gamma \\ 0 \\ 0 \\ \alpha(\beta^2-\gamma^2) \\ 0 \\ 0 \end{pmatrix} + c \begin{pmatrix} 0 \\ -\alpha\gamma \\ \alpha\beta \\ 0 \\ \beta(\gamma^2-\alpha^2) \\ -\gamma(\alpha^2+\beta^2) \end{pmatrix}, \tag{II.3.48}$$

where $s = \sin(\theta/2)$ and $c = \cos(\theta/2)$. This is a linear 2-system of screws with homogeneous parameters s and c, it is well known that the axes of the screws in such a system form a cylindroid, see [89] for example.

Notice that this is a known theorem in classical geometry: The common perpendiculars from one line in a regulus to every other line in a regulus form a cylindroid. However, the authors were not able to find this in the classical literature. The principal pitches of the 2-system can be found to be p_a, $p_b = -\beta\gamma/\alpha$, $\alpha(\beta^2-\gamma^2)/(\beta\gamma)$.

From the above result it is straightforward to design a mechanism to guide a line along a cylindroid. The simplest case is when the regulus belongs to a circularly symmetric hyperboloid, that is when $\alpha = \beta$. One can place a revolute joint along the axis of the hyperboloid and fix a cylindrical joint along one of the lines in the regulus. The revolute joint swings the axis of another cylindrical joint through the other lines of the regulus. Finally, a third cylindrical joint connects the other two cylindrical joints. The axis of this third cylindrical joint is perpendicular to the axes of the other two cylindrical joints and hence describes a cylindroid as the mechanism moves, see Figure II.3.6. The single loop mechanism shown in Figure II.3.6 does not take account of mechanical interference. It is intended to illustrate the concept only.

Finally here, an alternative mechanism could be found for this task by factorising the degree 5 motion polynomial, found in Equation (II.3.45), using the methods given in [126]. Alternatively, there might be a mechanism based on the Bennett mechanism using the associated cylindroid found by Huang [127].

II.3.4 Two and Three Parameter Examples

II.3.4.1 Special Linear Line Complexes

The, so called, special linear line complex corresponds to a pitch zero screw. Hence it consists of all lines reciprocal to a fixed line. That is, all lines coplanar to a fixed line. In the Study quadric the group elements that keep a line in a special linear congruence satisfy a quadratic equation. The equation is the same as the the equation for the general linear complex given in Eq.(II.3.24), only the blocks Ξ and Υ reflect the fact that the fixed screw, $\mathbf{s}^T = (\mathbf{w}^T, \mathbf{u}^T)$ is, in fact, a line.

There are several open loop mechanisms that can move a line in such a way that it remains in a special linear line complex, for example the $\mathcal{PSP}$ or $\mathcal{UPU}$ linkages, see [125].

Line complexes which correspond to infinite pitch screws do not seem to have a particular name. It is straightforward to see that the set of lines reciprocal to an infinite screw comprise the set of lines in space perpendicular to a fixed direction. That is, the lines lying in a set of parallel planes. The equation for the group elements in the Study quadric which maintain a line in such a complex is again given by a quadratic. This time, however, the diagonal block Υ, of the symmetric matrix in Eq.(II.3.24), is the 3×3 zero matrix, since $\mathbf{w} = \mathbf{0}$. This represents a singular quadric in $\mathbb{PR}^7$, where the singular set of the quadric is clearly the 3-plane A_∞.

It is not difficult to find a linkage that will move a line so that it remains in such a complex. For example, a $\mathcal{CPC}$ mechanism where the two $\mathcal{C}$-joints are perpendicular and the middle $\mathcal{P}$-joint is directed perpendicular to both cylindrical joints will do the job.

This prompts consideration of a closely related set of lines. Consider the set of lines in space that make a constant angle with a fixed line. The Plücker coordinates of such lines $\ell^T = (\boldsymbol{\omega}^T, \mathbf{v}^T)$, might be considered as satisfying an affine equation,

$$\mathbf{u} \cdot \boldsymbol{\omega} = \cos\alpha, \tag{II.3.49}$$

for a fixed angle α. In $\mathbb{PR}^5$ affine equations are not valid, but one can find a homogeneous equation for these lines by assuming that $\boldsymbol{\omega} \cdot \boldsymbol{\omega} \neq 0$. Then one can write a quadratic equation for the Plücker coordinates of the lines,

$$(\mathbf{u} \cdot \boldsymbol{\omega})^2 = \cos^2\alpha(\boldsymbol{\omega} \cdot \boldsymbol{\omega}). \tag{II.3.50}$$

A set of lines determined by a quadratic equation in the Plücker coordinates is called a quadratic line complex. These were objects of much classical study, see for example, [128]. The quadratic equation above corresponds to a singular quadric in $\mathbb{PR}^5$, where the singular set of the variety is the set of lines at infinity $\boldsymbol{\omega} = \mathbf{0}$.

It is not difficult to see that a $\mathcal{CPC}$ linkage will keep the axis of the final $\mathcal{C}$-joint in the finite part of this quadratic line complex if the first and final $\mathcal{C}$-joint are set at an angle of α and the $\mathcal{P}$-joint is directed parallel to the common perpendicular between the axes of the two $\mathcal{C}$-joints.

II.3.4.2 Linear Line Congruences

A line congruence is a two-parameter family of lines. A linear line congruence is the intersection of the Klein quadric of lines with a 3-dimensional plane in $\mathbb{PR}^5$. Put another way, a linear line congruence is the intersection of a pair of line complexes. Suppose that the two line complexes are determined by a pair of screws $\mathbf{s}_1$ and $\mathbf{s}_2$, then the congruence will also be contained in complexes determined by any linear combination of the screws, $\lambda\mathbf{s}_1 + \mu\mathbf{s}_2$. That is, for any constants λ and μ the congruence will satisfy,

$$(\lambda\mathbf{s}_1 + \mu\mathbf{s}_2)^T\mathbf{Q}_0\ell = 0. \tag{II.3.51}$$

This means that a congruence is determined by a 2-system of screws. Traditionally, the classification of these congruences has considered different congruences to be equivalent if they are related by a real projective transformation (projectivity), see [123]. Three types of linear line congruences are considered, these are distinguished by the number of real or imaginary lines in the 2-system of screws, that is the character of the solutions to the quadratic,

$$\begin{aligned} 0 = (\lambda\mathbf{s}_1 + \mu\mathbf{s}_2)^T\mathbf{Q}_0(\lambda\mathbf{s}_1 + \mu\mathbf{s}_2) \\ = \lambda^2\big(\mathbf{s}_1^T Q_0\mathbf{s}_1\big) + 2\lambda\mu\big(\mathbf{s}_1^T\mathbf{Q}_0\mathbf{s}_2\big) + \mu\big(\mathbf{s}_2^T\mathbf{Q}_0\mathbf{s}_2\big). \end{aligned} \tag{II.3.52}$$

If both solutions to this quadratic are complex then the congruence is said to be an elliptic congruence, when the quadratic has two real roots the congruence is called hyperbolic and the congruence is referred to a being parabolic if the root is repeated.

As mentioned, linear line congruences are determined by 2-systems of screws. So, a finer classification of these objects exists up to equivalence by rigid-body transformations, see [89]. The elliptic, hyperbolic and parabolic congruences are all examples of lines reciprocal to a IA 2-system (the general 2-system in Hunt's classification). The canonical form for the IA 2-system is given by basis elements,

$$\mathbf{s}_1 = \begin{pmatrix} 1 \\ 0 \\ 0 \\ p_a \\ 0 \\ 0 \end{pmatrix}, \quad \mathbf{s}_2 = \begin{pmatrix} 0 \\ 1 \\ 0 \\ 0 \\ p_b \\ 0 \end{pmatrix}. \tag{II.3.53}$$

Here, p_a and p_b are know as the principal screws of the system. The quadratic which determines the pitch zero screws in the system and hence the character of the congruence is,

$$\lambda^2 p_a + \mu^2 p_b = 0. \tag{II.3.54}$$

Hence, the congruence will be elliptic if the principal pitches have the same sign, $p_a p_b > 0$. It will be hyperbolic if they have opposite signs $p_a p_b < 0$. The congruence will be parabolic if $p_b = -p_a$.

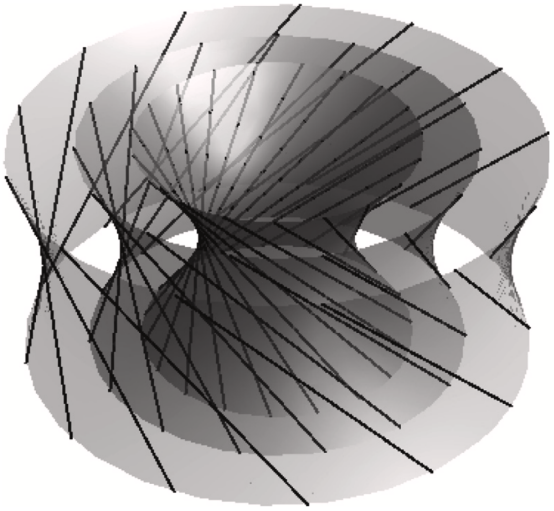

Figure II.3.7: The Elliptic Linear Line congruence.

An elliptic congruence consists of the lines from one regulus of a system of nested cylindrical hyperboloids, see [123]. This is illustrated in Fig. II.3.7. From the above, it is simple to give a 2 degree-of-freedom mechanism that can move a line so that it remains in such a congruence. Clearly, the lines in this congruence are the restriction of the lines in a single linear complex. So, if one mounts the mechanism shown in Fig. II.3.4 on an $\mathcal{R}$-joint whose axis is aligned with axis of the set of hyperboloids, then line determined by the middle $\mathcal{C}$-joint of the mechanism will trace out the lines in the elliptic congruence.

When the quadratic in Eq.(II.3.52) has two real roots the 2-system of screws contains two real lines and all the lines of the congruence will be reciprocal to these two lines. That is, the hyperbolic linear line congruence consists of all lines that meet a pair of lines. A mechanism can be readily designed that will move a line in such a congruence. All that is needed is to join a pair of linkages that maintain the incidence between a moving line and a fixed one. In Section II.3.2.6, a $\mathcal{CRC}$ linkage was used for this. To make the point that different choices are possible, the mechanism shown in Fig. II.3.8 uses a pair of $\mathcal{PSP}$ linkages. The two $\mathcal{P}$-joints where the linkages are joined can be replaced by a single $\mathcal{P}$-joint to create a 2 degree-of-freedom mechanism that moves a line in space so that it remains in a hyperbolic linear line congruence.

Turning to the parabolic linear line congruence, one can use the canonical basis given above but with $p_a = p$ and hence $p_b = -p$. The single line in the screw system is given

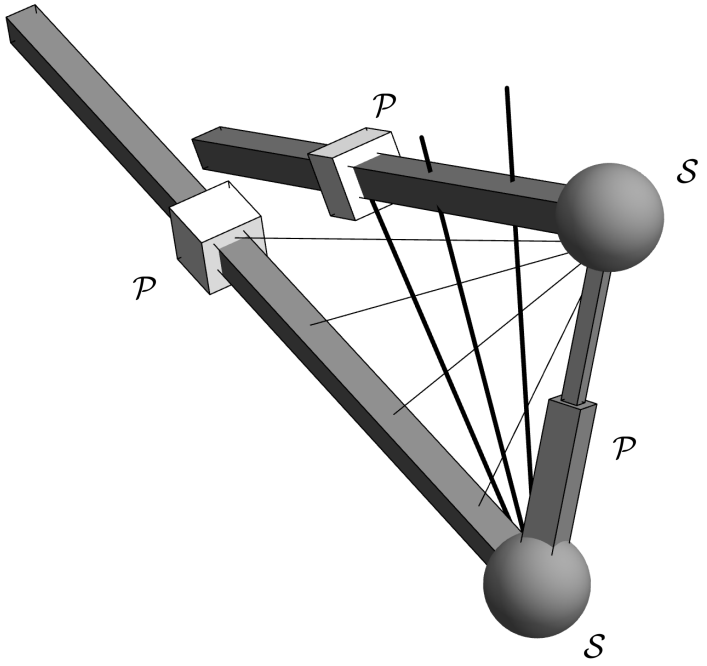

Figure II.3.8: Closed loop $\mathcal{PSPSP}$ mechanism to move a line in a hyperbolic linear line congruence. The white links are the fixed links.

by,

$$\mathbf{s}_0 = \begin{pmatrix} 1 \\ 1 \\ 0 \\ p \\ -p \\ 0 \end{pmatrix}, \tag{II.3.55}$$

points on this line are given by,

$$\mathbf{r} = \begin{pmatrix} \nu \\ \nu \\ -p \end{pmatrix}, \tag{II.3.56}$$

where ν is an arbitrary parameter. So lines in the singular complex determined by this line can be written as,

$$\ell = \begin{pmatrix} \boldsymbol{\omega} \\ \mathbf{r} \times \boldsymbol{\omega} \end{pmatrix} = \begin{pmatrix} \omega_x \\ \omega_y \\ \omega_z \\ \omega_y p + \omega_z \nu \\ -\omega_x p - \omega_z \nu \\ -\omega_x \nu + \omega_y \nu \end{pmatrix}. \tag{II.3.57}$$

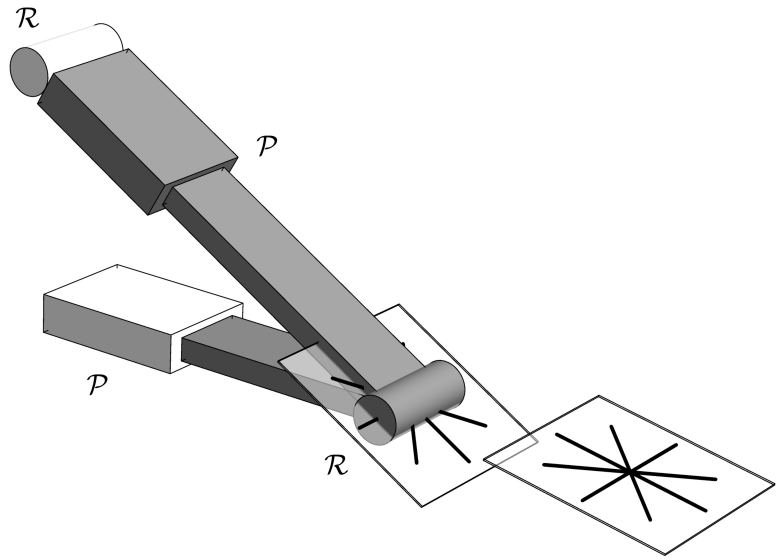

Figure II.3.9: An $\mathcal{RPRP}$ mechanism to move a line in a parabolic linear line congruence. The lines in the congruence will lie in the plane attached to the upper limb of the triangle and pass through the centre of the lower $\mathcal{R}$-joint. The white links are the fixed links.

Setting the reciprocal product of these lines with $\mathbf{s}_1$ to zero gives the lines in the congruence,

$$\mathbf{s}_2^T \mathbf{Q}_0 \ell = \omega_x p + \omega_y p + \omega_z \nu = \begin{pmatrix} p, & p, & \nu \end{pmatrix} \cdot \begin{pmatrix} \omega_x \\ \omega_y \\ \omega_z \end{pmatrix} = 0. \tag{II.3.58}$$

The lines in this parabolic congruence consist of lines meeting ℓ but through each point on ℓ one gets a plane star of lines. If the point is determined by the parameter ν then the normal vector to the plane is $\begin{pmatrix} p, & p, & \nu \end{pmatrix}^T$. When $\nu = 0$, that is the point on the line closest to the origin, the plane of lines is normal to the line ℓ. To produce a mechanism to move a line such that it is constrained to a parabolic congruence consider the planar triangular $\mathcal{RPRP}$ mechanism shown in Fig. II.3.9. As the lower limb of the triangle extends, simple trigonometry shows that a plane attached to the upper limb will follow the motion of the plane of lines in the congruence. This plane has to be centred at the lower $\mathcal{R}$-joint so that it follows the straight line determined by the lower limb. This design would make it difficult to include an $\mathcal{R}$-joint to rotate the line in the plane due to mechanical interference.

All in all, the mechanisms proposed above may not have many immediately obvious uses. The purpose of this chapter has been to give some examples of simple mechanisms that address the problem of guiding a line through a predetermined set of lines. However, the shape of the quartic curve traced by points on the line in the regulus suggests that there might be applications as a bistable or switching mechanism.

This design method illustrated in this work relies on an extensive knowledge of the

geometry of the problem. The idea is to have a sufficient knowledge of the geometry of the curve describing the motion, in particular the subvarieties that it can lie in. One also require a knowledge of the constraint varieties, or displacement varieties, that are generated by a range of different open loop chains.

Finally, as mentioned above, there is a classification of 2-systems of screws due to Gibson and Hunt, [129], [130]. A closer study of the congruences of lines reciprocal to these system can easily be envisaged.

Chapter II.4

Conclusions and Ongoing Work

II.4.1 Conclusions

In the second part of this manuscript, persistent submanifolds of dimension 5 were investigated. A first library of 5-persistent submanifolds was identified. Although this result is incomplete since many other 5-submanifolds exist, the most commonly used robotic-constraints were investigated and classified. The novelty, hereby, is the geometrical point of view introduced as well as the use of Cauchy-Binet formula to compute the pitch of a wrench.

While investigating submanifolds given by using constraints, another general result was given. Indeed, in the literature, the product of two subgroups is known to return a persistent manifold. However, looking at 3-persistent systems, there are several cases given by a product of three subgroups as $\mathcal{HPH}$ or $\mathcal{HRH}$, for example. Therefore, an extension of Theorem 5 was given in Theorem 7 to both complete previous results about system classification and find other 5 persistent POE manifolds.

II.4.2 Ongoing Work

Despite the possibility to pursue several new paths, the ongoing works focus on (i) the generalisation of the definition of persistence and (ii) the recognition of the invariants necessary to identify screw systems.

II.4.2.1 General Definition of Persistent Manifolds

As mentioned, persistency had been identified as a property of the manifold rather than of a particular chain. Therefore, the question of whether the manifold owns some particular structure that confers the persistent property is under study.

In this context, the following conjecture is formulated and the proof is still under study.

Conjecture 10. *Let M be a submanifold and $x \in M$. If M is persistent then it has an $H = SE(3)/\mathcal{I}_x$ structure. Viceversa, if M has an H-structure then M is persistent.*

Proof. Sketch
M PERSISTENT $\implies$ H-STRUCTURE
Let $S_e = T_eM$ be the screw systems at e, $v_g \in T_gM$ an element of the tangent space at g and $z = v_g g^{-1}$ the pull-back of v_g at the identity. Using that M is persistent then, by definition one has

$$\exists\, g_1 \text{ such that } g_1 z g_1^{-1} \in T_eM.$$

Now, every Lie group G has a principal *G-bundle* and is a *Fiber bundle* such that TM has as structure group made by $H = Aut(S_e)$ (Isotropy group). Therefore, taking

$$h \in H, \quad hg_1 z g_1^{-1} = S_h \in S_e.$$

H-STRUCTURE $\implies$ M PERSISTENT
If M has the H-structure then exist an action of H on TM such that

$$h(v_g) \in T_gM \text{ and } h(v_g) = u_g.$$

Take $z = v_g g^{-1}$ and $z' = u_g g^{-1}$. Now, to check if persistency holds, let g_1 be such that $g_1 z' g_1^{-1} \in T_eM$ therefore, if h commute with g_1 then

$$g_1 h v_g g^{-1} g_1^{-1} = g_1 u_g g^{-1} g_1^{-1}.$$

□

II.4.2.2 Screw Systems Identification through Invariants and Sub-invariants

The past decades saw the classification of screw systems as a core topic. There are several contributions in this field. In this context, the idea is to provide a systematic and straightforward technique for identifying a screw system using invariants and sub-invariants.

Now, let's summarize the preliminary results making use of tables which, also, give the entire view all in once. First, recall the equations for the invariants

$$\det(\mathbf{J}^T(\alpha\mathbf{Q}_0 + \beta\mathbf{Q}_\infty)J) = \alpha^2 i_1 + \alpha\beta i_2 + \beta^2 i_3,$$

$$\det(\mathbf{A} - \lambda\mathbf{Q}_0 - \mu\mathbf{Q}_\infty) = -\lambda^6 - \lambda^4 i_1 - \lambda^3\mu i_4 - \lambda^2\mu^2 i_5,$$

where $\mathbf{A} = \mathbf{s}_1^T\mathbf{s}_2 - \mathbf{s}_2^T\mathbf{s}_1$ and $\mathbf{J}$ is the Jacobian matrix $\mathbf{J} = (\mathbf{s}_1|\mathbf{s}_2)$ sometimes one also make use of $\tilde{\mathbf{J}} = \left([\mathbf{s}_1,[\mathbf{s}_1,\mathbf{s}_2]]\middle|[\mathbf{s}_2,[\mathbf{s}_1,\mathbf{s}_2]]\right)$ where the Lie brackets substitute the original vectors.

To be clear about the mentioned issue to be solved, hereby Table II.4.1 for 2 systems, given in [89] is reported.

The only 2 systems one cannot identify with these invariants are IB^0 and IB; see Table II.4.1. Therefore, let's compute the Lie brackets for all the 2 Systems. The scope consists in identifying other invariants or subinvariants to properly distinguish and identify them.

	$\det(\mathbf{J}^T(\alpha\mathbf{Q}_0 - \beta\mathbf{Q}_\infty)\mathbf{J})$			$\det(\mathbf{A} - \lambda\mathbf{Q}_0 - \mu\mathbf{Q}_\infty)$		
Hunt Type	i_1	i_2	i_3	i_1	i_4	i_5
IIC	0	0	0	0	0	4
IB^0	-1	0	0	-1	0	0
IIA ($p = 0$)	0	0	4	0	0	0
IIB ($p \neq 0$)	0	0	0	0	$4p$	$4p^2$
IIB ($p = 0$)	0	0	0	0	0	0
IB ($p \neq 0$)	-1	0	0	-1	0	0
IIA ($p \neq 0$)	$4p^2$	$-8p$	4	$4p^2$	$8p^3$	$4p^4$
IA ($p_a \neq p_b$)	$4p_ap_b$	$-4(p_a + p_b)$	4	$4p_ap_b$	$4(p_a^2p_b + p_ap_b^2)$	$4p_a^2p_b^2$

Table II.4.1: Invariants of 2 Systems

Notice that the outcome of the brackets can lead to degenerate cases. To be precise, let's distinguish the case in which only one bracket is the zero vector $\mathcal{D}_1$ and when both brackets are null $\mathcal{D}_2$. With the letter $\mathcal{I}$ instead, the new 2 system remains identical, up to conjugacy, to its initial Hunt Type. Consequently, computing the invariants depends on the system one gets. In other words, if the system is $\mathcal{D}_2$ evidently does not make much sense computing invariants whereas, when the $\mathcal{D}_1$ case occurs the 1 system contains its invariant, the pitch, which is the so-called subinvariant.

Hunt Type	$[[\mathbf{s}_1,[\mathbf{s}_1,\mathbf{s}_2]]$ $[\mathbf{s}_2,[\mathbf{s}_1,\mathbf{s}_2]]$	$\det(\tilde{\mathbf{J}}^T(\alpha\mathbf{Q}_0-\beta\mathbf{Q}_\infty)\tilde{\mathbf{J}})$			$\det(\tilde{\mathbf{A}}-\lambda\mathbf{Q}_0-\mu\mathbf{Q}_\infty)$			$\det(\mathbf{J}^T(\alpha\mathbf{Q}_0-\beta\mathbf{Q}_\infty)\mathbf{J})$			$\det(\mathbf{A}-\lambda\mathbf{Q}_0-\mu\mathbf{Q}_\infty)$			$\det(\mathbf{J}^T(\alpha\mathbf{Q}_0-\beta\mathbf{Q}_\infty)\tilde{\mathbf{J}})$		
		i_1	i_2	i_3	i_1	i_4	i_5	i_1	i_2	i_3	i_1	i_4	i_5	i_1	i_2	i_3
IIC	$\mathcal{D}_2$							0	0	0	0	0	4			
IB^0	$\mathcal{D}_2$							-1	0	0	-1	0	0			
IIA ($p=0$)	$\mathcal{I}$							0	0	0	4	0	0	0	0	4
IIB ($p\neq 0$)	$\mathcal{D}_1$, $p=\infty$							0	0	0	0	$-4p$	$4p^2$	0	0	0
IIB ($p=0$)	$\mathcal{D}_1$, $p=\infty$							0	0	0	0	0	0	0	0	0
IB ($p\neq 0$)	$\mathcal{D}_1$, $p=\infty$							-1	0	0	-1	0	0	0	0	0
IIA ($p\neq 0$)	$\mathcal{I}$	$36p^2$	$24p$	4	$4p^2$	$-8p^3$	$4p^4$	$4p^2$	$8p$	4	$4p^2$	$-8p^3$	$4p^4$	$16p^2$	$16p$	4
IA ($p_a\neq p_b$)	$\mathcal{I}$	$8p_a^2+20p_ap_b+8p_b^2$	$12(p_a+p_b)$	4	$4p_ap_b$	$-4(p_a^2p_b+p_ap_b^2)$	$4p_a^2p_b^2$	$4p_ap_b$	$4(p_a+p_b)$	4	$4p_ap_b$	$-4(p_a^2p_b+p_ap_b^2)$	$4p_a^2p_b^2$	$4p_a^2+8p_ap_b+4p_b^2$	$8(p_a+p_b)$	4

Hunt Type	$[\mathbf{s}_1, \mathbf{s}_2]$	$[\mathbf{s}_1, [\mathbf{s}_1, \mathbf{s}_2]]$	$[\mathbf{s}_2, [\mathbf{s}_1, \mathbf{s}_2]]$	$[\mathbf{s}_1[\mathbf{s}_2, [\mathbf{s}_1, \mathbf{s}_2]]]$
IIC	$(\mathbf{0}, \mathbf{0})^T$	$(\mathbf{0}, \mathbf{0})^T$	$(\mathbf{0}, \mathbf{0})^T$	$(\mathbf{0}, \mathbf{0})^T$
IB^0	$(\mathbf{0}, \mathbf{0})^T$	$(\mathbf{0}, \mathbf{0})^T$	$(\mathbf{0}, \mathbf{0})^T$	$(\mathbf{0}, \mathbf{0})^T$
IIA ($p = 0$)	$(\mathbf{k}, \mathbf{0})^T$	$(-\mathbf{j}, \mathbf{0})^T$	$(\mathbf{i}, \mathbf{0})^T$	$(\mathbf{0}, \mathbf{0})^T$
IIB ($p \neq 0$)	$(\mathbf{0}, \mathbf{k})^T$	$(\mathbf{0}, -\mathbf{j})^T$	$(\mathbf{0}, \mathbf{0})^T$	$(\mathbf{0}, \mathbf{0})^T$
IIB ($p = 0$)	$(\mathbf{0}, \mathbf{k})^T$	$(\mathbf{0}, -\mathbf{j})^T$	$(\mathbf{0}, \mathbf{0})^T$	$(\mathbf{0}, \mathbf{0})^T$
IB ($p \neq 0$)	$(\mathbf{0}, p\mathbf{k})^T$	$(\mathbf{0}, -p\mathbf{j})^T$	$(\mathbf{0}, \mathbf{0})^T$	$(\mathbf{0}, \mathbf{0})^T$
IIA ($p \neq 0$)	$(\mathbf{k}, 2p\mathbf{k})^T$	$-(\mathbf{j}, 3p\mathbf{j})^T$	$(\mathbf{i}, 3p\mathbf{i})^T$	$(\mathbf{0}, \mathbf{0})^T$
IA ($p_a \neq p_b$)	$(\mathbf{k}, (p_a + p_b)\mathbf{k})^T$	$-(\mathbf{j}, (2p_a + p_b)\mathbf{j})^T$	$(\mathbf{i}, (p_a + 2p_b)\mathbf{i})^T$	$(\mathbf{0}, \mathbf{0})^T$

Table II.4.2: Lie Brackets of the 2 Systems

This Table shows that for IA and IIA the invariant i_1 changes when computed with different Jacobians: this should be a matter of multiplying by a constant factor. However, at the same time, it gives us a way to distinguish between IB and IB^0 since their brackets end up in a $\mathcal{D}_1$ and $\mathcal{D}_2$ cases, respectively. The brackets then represent what can be called as subinvariants.

To close, this preliminary analysis showed the potentiality of using invariants and subinvariants to distinguish between screw systems. However, this procedure is still under investigation and subsequently have to be generalised to consider 3 systems as well.

Appendix A

Equations of Motion for Aerial Systems with Point Mass Load

An intrinsic form of the equations of motion is derived from the nonlinear configuration manifold [131]. These are developed in a coordinate-free fashion to avoid singularities and complexities that are associated with local parameterizations. The equations of motion can be obtained as follows:

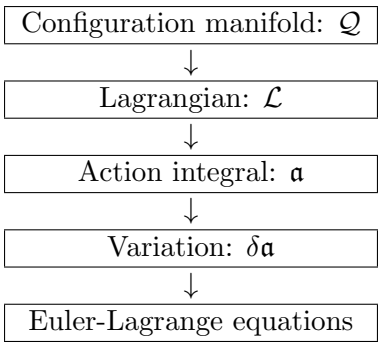

Therefore, in this case, the configuration manifold is given by $\mathcal{Q} = \mathbb{R}^3 \times (\mathbb{S}^2 \times SO(3))^n$.

Recalling that the Lagrangian is $\mathcal{L} = \mathcal{T} - \mathcal{U}$ with $\mathcal{T}$ and $\mathcal{U}$ denoting the kinetic and potential energy, respectively, then the action integral is

$$\mathfrak{a} = \int_{t_0}^{t_f} \mathcal{L}\, dt, \tag{A.1}$$

in particular, the extension for the non conservative forces is

$$\mathfrak{a} = \int_{t_0}^{t_f} (\mathcal{T} - \mathcal{U} + \mathcal{W}_f + \mathcal{W}_m)\, dt, \tag{A.2}$$

where $\mathcal{W}_f$ and $\mathcal{W}_m$ represent the works of external forces and moment, respectively. Now, Hamilton's principle of least action states that the path a conservative system

takes from a configuration $\mathbf{\Psi}(t_i)$ to $\mathbf{\Psi}(t_f)$, where $\mathbf{\Psi}$ is the set of generalized coordinates belonging to the configuration manifold, is the one that minimizes the action integral. In mathematical terms

$$\delta\mathfrak{a} = \int_{t_0}^{t_f} (\delta\mathcal{T} - \delta\mathcal{U} + \delta\mathcal{W}_f + \delta\mathcal{W}_m)\, dt = 0, \tag{A.3}$$

where δ expresses the variation of integrated quantities. Therefore, going through all the terms, the kinetic energy of the system is

$$\mathcal{T} = \frac{1}{2} m_L \dot{\mathbf{x}}_L \cdot \dot{\mathbf{x}}_L + \sum_{i=1}^{n} \frac{1}{2} m_i \dot{\mathbf{x}}_i \cdot \dot{\mathbf{x}}_i + \sum_{i=1}^{n} \frac{1}{2} \mathbf{\Omega}_i \cdot \mathbf{J}_i \cdot \mathbf{\Omega}_i, \tag{A.4}$$

since the relations between the i^{th} quadrotor and the load states are

$$\mathbf{x}_i = \mathbf{x}_L - l_i \mathbf{q}_i, \quad \text{and} \quad \dot{\mathbf{x}}_i = \dot{\mathbf{x}}_L - l_i \dot{\mathbf{q}}_i, \tag{A.5}$$

where l_i is the i^{th} link length, it is possible to entirely express $\mathcal{T}$ in terms of the system states

$$\begin{aligned}
\mathcal{T} &= \frac{1}{2} m_L \dot{\mathbf{x}}_L \cdot \dot{\mathbf{x}}_L + \sum_{i=1}^{n} \frac{1}{2} m_i (\dot{\mathbf{x}}_L - l_i \dot{\mathbf{q}}_i) \cdot (\dot{\mathbf{x}}_L - l_i \dot{\mathbf{q}}_i) + \sum_{i=1}^{n} \frac{1}{2} \mathbf{\Omega}_i \cdot \mathbf{J}_i \cdot \mathbf{\Omega}_i \\
&= \frac{1}{2} \Big(\sum_{i=1}^{n} m_i + m_L \Big) \dot{\mathbf{x}}_L \cdot \dot{\mathbf{x}}_L - \sum_{i=1}^{n} m_i l_i \dot{\mathbf{x}}_L \cdot \dot{\mathbf{q}}_i + \sum_{i=1}^{n} \frac{1}{2} m_i l_i^2 \dot{\mathbf{q}}_i \cdot \dot{\mathbf{q}}_i + \sum_{i=1}^{n} \frac{1}{2} \mathbf{\Omega}_i \cdot \mathbf{J}_i \cdot \mathbf{\Omega}_i,
\end{aligned} \tag{A.6}$$

the same applies to $\mathcal{U}$ energy

$$\begin{aligned}
\mathcal{U} &= \sum_{i=1}^{n} m_i g \mathbf{e}_3 \cdot \mathbf{x}_i + m_L g \mathbf{e}_3 \cdot \mathbf{x}_L \\
&= \sum_{i=1}^{n} m_i g \mathbf{e}_3 \cdot (\mathbf{x}_L - l_i \mathbf{q}_i) + m_L g \mathbf{e}_3 \cdot \mathbf{x}_L \\
&= \Big(\sum_{i=1}^{n} m_i + m_L \Big) g \mathbf{e}_3 \cdot \mathbf{x}_L - \sum_{i=1}^{n} m_i g l_i \mathbf{e}_3 \cdot \mathbf{q}_i,
\end{aligned} \tag{A.7}$$

Taking the variation of $\mathcal{T}$ and $\mathcal{U}$ [132] yields to

$$\begin{aligned}
\delta\mathcal{T} &= \mathcal{T}(\dot{\mathbf{x}}_L + \delta\dot{\mathbf{x}}_L, \dot{\mathbf{q}}_i + \delta\dot{\mathbf{q}}_i, \mathbf{\Omega}_i + \delta\mathbf{\Omega}_i) - \mathcal{T}(\dot{\mathbf{x}}_L, \dot{\mathbf{q}}_i, \mathbf{\Omega}_i) \\
&\approx \frac{\partial\mathcal{T}}{\partial\dot{\mathbf{x}}_L} \delta\dot{\mathbf{x}}_L + \frac{\partial\mathcal{T}}{\partial\dot{\mathbf{q}}_i} \delta\dot{\mathbf{q}}_i + \frac{\partial\mathcal{T}}{\partial\mathbf{\Omega}_i} \delta\mathbf{\Omega}_i \\
&= \Big[\Big(\sum_{i=1}^{n} m_i + m_L \Big) \dot{\mathbf{x}}_L - \sum_{i=1}^{n} m_i l_i \dot{\mathbf{q}}_i \Big] \cdot \delta\dot{\mathbf{x}}_L + \big(m_i l_i \dot{\mathbf{x}}_L + m_i l_i^2 \dot{\mathbf{q}}_i \big) \cdot \delta\dot{\mathbf{q}}_i + \mathbf{J}_i \mathbf{\Omega}_i \cdot \delta\mathbf{\Omega}_i,
\end{aligned} \tag{A.8}$$

$$\begin{aligned}\delta\mathcal{U} &= \mathcal{U}(\mathbf{x}_L + \delta\mathbf{x}_L, \mathbf{q}_i + \delta\mathbf{q}_i) - \mathcal{U}(\mathbf{x}_L, \mathbf{q}_i) \\ &\approx \frac{\partial \mathcal{U}}{\partial \mathbf{x}_L}\delta\mathbf{x}_L + \frac{\partial \mathcal{U}}{\partial \mathbf{q}_i}\delta\mathbf{q}_i \\ &= \Big(\sum_{i=1}^{n} m_i + m_L\Big) g\mathbf{e}_3 \cdot \delta\mathbf{x}_L - m_i g l_i \mathbf{e}_3 \cdot \delta\mathbf{q}_i,\end{aligned} \tag{A.9}$$

generally, the contributions of the forces and moments concerning the i^{th} body can be stated as follows

$$\delta\mathcal{W}_i = \sum_{k=1}^{N} \mathbf{f}_k \cdot \sum_{j=1}^{g} \frac{\partial \mathbf{r}_k}{\partial \mathbf{p}_j}\delta\mathbf{p}_j + \sum_{k=1}^{M} \mathbf{m}_k \cdot \sum_{j=1}^{g} \frac{\partial \mathbf{\Omega}_k}{\partial \dot{\mathbf{p}}_j}\delta\mathbf{p}_j, \tag{A.10}$$

where $\mathbf{f}_k$ are the N forces applied to the i^{th} body at position $\mathbf{r}_k$ whereas $\mathbf{m}_k$ are the M moments applied to the same body as well. The $\mathbf{p}_j$ are the g generalized coordinates $\mathbf{p}_j = \mathbf{x}_L, \mathbf{q}_i, \mathbf{R}_i$ regarding the the load or the i^{th} body. Hence, the overall works of external actions is

$$\delta\mathcal{W}_f = \sum_{i=i}^{n} \Big(\sum_{k=1}^{1} f_k \mathbf{R}_k \mathbf{e}_3 \cdot \sum_{j=1}^{3} \frac{\partial \mathbf{x}_k}{\partial \mathbf{p}_j}\delta\mathbf{p}_j + \sum_{k=1}^{1} \mathbf{f}_{k,e} \cdot \sum_{j=1}^{3} \frac{\partial \mathbf{x}_k}{\partial \mathbf{p}_j}\delta\mathbf{p}_j \Big)_i + \mathbf{f}_e \cdot \sum_{j=1}^{3} \frac{\partial \mathbf{x}_k}{\partial \mathbf{p}_j}\delta\mathbf{p}_j, \tag{A.11}$$

since in this case $N = 1$ it becomes possible to simplify the expression as follows

$$\begin{aligned}\delta\mathcal{W}_f &= \sum_{i=i}^{n} f_i \mathbf{R}_i \mathbf{e}_3 \cdot \sum_{j=1}^{3} \frac{\partial \mathbf{x}_i}{\partial \mathbf{p}_j}\delta\mathbf{p}_j + \sum_{i=i}^{n} \mathbf{f}_{i,e} \cdot \sum_{j=1}^{3} \frac{\partial \mathbf{x}_i}{\partial \mathbf{p}_j}\delta\mathbf{p}_j + \mathbf{f}_e \cdot \sum_{j=1}^{3} \frac{\partial \mathbf{x}_i}{\partial \mathbf{p}_j}\delta\mathbf{p}_j \\ &= \sum_{i=i}^{n} f_i \mathbf{R}_i \mathbf{e}_3 \cdot (\delta\mathbf{x}_L - l_i\delta\mathbf{q}_i) + \sum_{i=i}^{n} \mathbf{f}_{i,e} \cdot (\delta\mathbf{x}_L - l_i\delta\mathbf{q}_i) + \mathbf{f}_e \cdot \delta\mathbf{x}_L,\end{aligned} \tag{A.12}$$

where $\mathbf{f}_{i,e}$ and $\mathbf{f}_e$ are external forces (e.g. aerodynamic forces) acting on the quadrotors and the load, respectively. The same applies to the moments

$$\begin{aligned}\delta\mathcal{W}_m &= \sum_{i=i}^{n} \mathbf{m}_i \cdot \sum_{j=1}^{3} \frac{\partial \mathbf{\Omega}_i}{\partial \dot{\mathbf{p}}_j}\delta\dot{\mathbf{p}}_j \\ &= \mathbf{m}_i \cdot \sum_{i=i}^{n} \frac{\partial (\mathbf{R}^T \delta\dot{\mathbf{R}}_i)^\vee}{\partial \dot{\mathbf{R}}}\delta\mathbf{R}_i \\ &= \mathbf{m}_i \cdot (\mathbf{R}^T \delta\mathbf{R}_i),\end{aligned} \tag{A.13}$$

where the symbol $\overset{\vee}{\cdot}$ denote the *vee map* that is defined as $\overset{\vee}{\cdot} : \mathfrak{so}(3) \to \mathbb{R}^3$

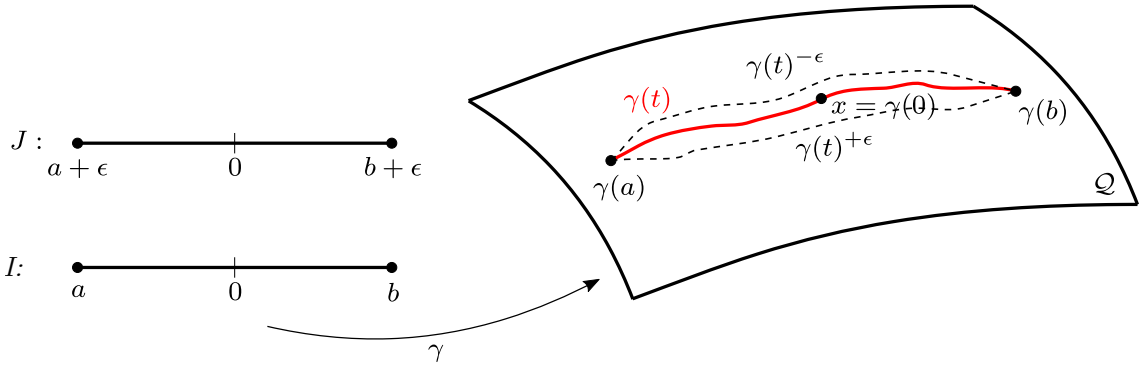

Figure A.1: Representation of the curve $\gamma(t)$ on the manifold $\mathcal{Q}$.

At this stage, the obtained variations can be used inside (A.3)

$$
\begin{aligned}
\delta\mathfrak{a} &= \int_{t_i}^{t_f} (\delta\mathcal{W}_m + \delta\mathcal{W}_f + \delta\mathcal{T} - \delta\mathcal{U})\, dt \\
&= \int_{t_i}^{t_f} \Big\{ \Big[f_i \mathbf{R}_i \mathbf{e}_3 - \Big(\sum_{i=1}^{n} m_i + m_L \Big) g \mathbf{e}_3 + \mathbf{f}_e + \sum_{i=1}^{n} \mathbf{f}_{i,e} \Big] \cdot \delta \mathbf{x}_L \\
&\qquad + \Big[\Big(\sum_{i=1}^{n} m_i + m_L \Big) \dot{\mathbf{x}}_L - \sum_{i=1}^{n} m_i l_i \dot{\mathbf{q}}_i \Big] \cdot \delta \dot{\mathbf{x}}_L \Big\}\, dt \qquad \text{(A.14)} \\
&+ \int_{t_i}^{t_f} \Big\{ \Big[m_i g l_i \mathbf{e}_3 - f_i l_i \mathbf{R}_i \mathbf{e}_3 - l_i \mathbf{f}_{i,e} \Big] \cdot \delta \mathbf{q}_i + \Big[- m_i l_i \dot{\mathbf{x}}_L + m_i l_i^2 \dot{\mathbf{q}}_i \Big] \cdot \delta \dot{\mathbf{q}}_i \Big\}\, dt \\
&+ \int_{t_i}^{t_f} \Big\{ \Big[\mathbf{m}_i \cdot (\mathbf{R}_i^T \delta \mathbf{R}_i) + \mathbf{J}_i \boldsymbol{\Omega}_i \cdot \delta \boldsymbol{\Omega}_i \Big] \Big\}\, dt,
\end{aligned}
$$

To solve the integration it is necessary to properly define the infinitesimal variations of a generic $\delta\mathbf{R}_i$ and $\delta\mathbf{q}_i$ since they vary on a specific configuration manifold.
Generally speaking, for a manifold $\mathcal{Q}$ and a point $x \in \mathcal{Q}$, a curve in time at x is defined as $\gamma(t) : I \to \mathcal{Q}$ [133], where:

- I is an interval containing 0;
- $\gamma(0) = x$.

A variation of $\gamma(t)$ is a map $\gamma^\epsilon(t) : J \times I \to \mathcal{Q}$ where:

- $I = [a, b]$ with $a, b \in \mathbb{R}$, J both contain 0;
- $\gamma^0(t) = \gamma(t)\ \forall t \in I$;
- $\gamma^\epsilon(a) = \gamma(a)\ \forall \epsilon \in J$;
- $\gamma^\epsilon(b) = \gamma(b)\ \forall \epsilon \in J$.

All these concepts can be collected and visualized in the following Figure A.1.
Hence, the infinitesimal variation of $\gamma(t)$ belonging to $\mathcal{Q}$ is found as

$$\delta\gamma(t) = \left.\frac{d}{d\epsilon}\right|_{\epsilon=0} \gamma^{\epsilon}(t) \in T_{\gamma(t)}\mathcal{Q}, \tag{A.15}$$

where $T_{\gamma(t)}\mathcal{Q}$ represents the tangent space of $\mathcal{Q}$ at $\gamma(t)$.
If a mechanical systems can be described in terms of Lie Groups and Lie Algebra then, the variations of a curves $g(t)$ in a Lie Group G can be expressed using the exponential map [132]

$$g^{\epsilon}(t) = g(t)e^{\epsilon\eta(t)}, \tag{A.16}$$

where $\eta(t) \in \mathfrak{g}$ and $\mathfrak{g}$ is the Lie Algebra of G.
In this case, the matrices $\mathbf{R}_i$ belong to $SO(3)$ defined above and its corresponding Lie Algebra is the set of skew-symmetric matrices $\mathfrak{so}(3)$, where

$$\mathfrak{so}(3) = \left\{\hat{\mathbf{\Omega}} \in \mathbb{R}^{3\times 3} \,|\, \hat{\mathbf{\Omega}}^T = -\hat{\mathbf{\Omega}}\right\}, \tag{A.17}$$

Thus, the exponential definition of the variation can be applied on a element $\mathbf{R}_i \in SO(3)$ as follows

$$\mathbf{R}_i^{\epsilon} = \mathbf{R}_i e^{\widehat{\epsilon\eta_i(t)}}, \tag{A.18}$$

where $\eta_i(t) \in \mathbb{R}^3$ identify the *generic* element of $\mathfrak{so}(3)$ and the *hat map* is defined as $\hat{\bullet} : \mathbb{R}^3 \to \mathfrak{so}(3)$. Thus, the infinitesimal variation of $\mathbf{R}_i$, according to (A.15), is

$$\delta\mathbf{R}_i = \left.\frac{d}{d\epsilon}\right|_{\epsilon=0} \mathbf{R}_i^{\epsilon}(t) = \mathbf{R}_i\hat{\eta}_i \in T_{\mathbf{R}_i}SO(3), \tag{A.19}$$

Accordingly the variations of $\dot{\mathbf{R}}_i$ and $\mathbf{\Omega}_i$ can be derived

$$\delta\dot{\mathbf{R}}_i = \dot{\mathbf{R}}_i\hat{\eta}_i + \mathbf{R}_i\dot{\hat{\eta}}_i, \tag{A.20}$$

$$\begin{aligned}
\delta\hat{\mathbf{\Omega}}_i &= \delta(\mathbf{R}^T\dot{\mathbf{R}}) \\
&= \delta\mathbf{R}^T\dot{\mathbf{R}} + \mathbf{R}^T\delta\dot{\mathbf{R}} \\
&= (\mathbf{R}\hat{\eta})^T\dot{\mathbf{R}} + \mathbf{R}^T(\dot{\mathbf{R}}\hat{\eta} + \mathbf{R}\dot{\hat{\eta}}) \\
&= \widehat{\mathbf{\Omega}_i\eta_i} + \dot{\hat{\eta}}_i,
\end{aligned} \tag{A.21}$$

or, equivalently

$$\delta\mathbf{\Omega}_i = \hat{\mathbf{\Omega}}_i\eta_i + \dot{\eta}_i, \tag{A.22}$$

Naturally, the variation on $\mathbb{S}^2$ must be defined. Although it is not a Lie group, $SO(3)$ acts transitively on $\mathbb{S}^2$, therefore it is possible to use the variation of $\mathbf{R}_i$ to define the one of $\mathbf{q}_i$

$$\mathbf{q}_i^{\epsilon} = e^{\epsilon\hat{\xi}_i}\mathbf{q}_i, \tag{A.23}$$

where $\xi_i \in \mathbb{R}^3$. The corresponding infinitesimal variation is

$$\delta\mathbf{q}_i = \frac{d}{d\epsilon}\bigg|_{\epsilon=0} e^{\epsilon\hat{\xi}_i}\mathbf{q}_i = \hat{\xi}_i\mathbf{q}_i \in T_{\mathbf{R}_i}\mathbb{S}^2, \tag{A.24}$$

similarly as before, it is possible to deduce

$$\delta\dot{\mathbf{q}}_i = \hat{\dot{\xi}}_i\mathbf{q}_i + \hat{\xi}_i\dot{\mathbf{q}}_i, \tag{A.25}$$

Coming back to $\delta\mathfrak{a}$, integrating all the terms by parts returns the equations of motion:

1. (I_1) Integrate the $\mathbf{x}_L$ term

$$\begin{aligned}\int_{t_i}^{t_f} \Big\{ \Big[\sum_{i=1}^{n} f_i\mathbf{R}_i\mathbf{e}_3 - \Big(\sum_{i=1}^{n} m_i + m_L\Big)g\mathbf{e}_3 + \mathbf{f}_e + \sum_{i=1}^{n}\mathbf{f}_{i,e}\Big] \cdot \delta\mathbf{x}_L \\ + \underbrace{\Big[\Big(\sum_{i=1}^{n} m_i + m_L\Big)\dot{\mathbf{x}}_L - \sum_{i=1}^{n} m_i l_i \dot{\mathbf{q}}_i\Big]}_{f} \cdot \underbrace{\delta\dot{\mathbf{x}}_L}_{\dot{g}} \Big\}\, dt,\end{aligned} \tag{A.26}$$

taking

$$\begin{cases} \dot{f} = \Big(\sum_{i=1}^{n} m_i + m_L\Big)\ddot{\mathbf{x}}_L - \sum_{i=1}^{n} m_i l_i \ddot{\mathbf{q}}_i, \\ g = \delta\mathbf{x}_L, \end{cases}$$

yields to

$$\begin{aligned}\int_{t_i}^{t_f} \Big\{ \Big[\sum_{i=1}^{n} f_i\mathbf{R}_i\mathbf{e}_3 - \Big(\sum_{i=1}^{n} m_i + m_L\Big)g\mathbf{e}_3 + \mathbf{f}_e + \sum_{i=1}^{n}\mathbf{f}_{i,e}\Big] \cdot \delta\mathbf{x}_L \Big\}\, dt \\ + \underbrace{\Big[\Big(\sum_{i=1}^{n} m_i + m_L\Big)\dot{\mathbf{x}}_L - \sum_{i=1}^{n} m_i l_i \dot{\mathbf{q}}_i\Big] \cdot \delta\mathbf{x}_L\Big|_{t_i}^{t_f}}_{=0} \\ - \int_{t_i}^{t_f} \Big\{ \Big[\Big(\sum_{i=1}^{n} m_i + m_L\Big)\ddot{\mathbf{x}}_L - \sum_{i=1}^{n} m_i l_i \ddot{\mathbf{q}}_i\Big] \cdot \delta\mathbf{x}_L \Big\}\, dt,\end{aligned} \tag{A.27}$$

rearranging and collecting the remaining terms leads to

$$\int_{t_i}^{t_f} \Big\{ \Big[\sum_{i=1}^{n} f_i \mathbf{R}_i \mathbf{e}_3 - \Big(\sum_{i=1}^{n} m_i + m_L \Big) g \mathbf{e}_3 - \Big(\sum_{i=1}^{n} m_i + m_L \Big) \ddot{\mathbf{x}}_L + \sum_{i=1}^{n} m_i l_i \ddot{\mathbf{q}}_i + \mathbf{f}_e + \sum_{i=1}^{n} \mathbf{f}_{i,e} \Big] \cdot \delta \mathbf{x}_L \Big\} dt, \tag{A.28}$$

2. (I_2) Integrate the $\mathbf{q}_i$ term

$$\int_{t_i}^{t_f} \Big\{ \Big[m_i \, g \, l_i \mathbf{e}_3 - f_i l_i \mathbf{R}_i \mathbf{e}_3 - l_i \mathbf{f}_{i,e} \Big] \cdot \delta \mathbf{q}_i + \Big[- m_i \, l_i \, \dot{\mathbf{x}}_L + m_i l_i^2 \dot{\mathbf{q}}_i \Big] \cdot \delta \dot{\mathbf{q}}_i \Big\} dt, \tag{A.29}$$

using the previously defined variations

$$\int_{t_i}^{t_f} \Big\{ \Big[m_i \, g \, l_i \mathbf{e}_3 - f_i l_i \mathbf{R}_i \mathbf{e}_3 - l_i \mathbf{f}_{i,e} \Big] \cdot (\xi_i \times \mathbf{q}_i) + \Big[- m_i \, l_i \, \dot{\mathbf{x}}_L + m_i l_i^2 \dot{\mathbf{q}}_i \Big] \cdot (\dot{\xi}_i \times \mathbf{q}_i + \xi_i \times \dot{\mathbf{q}}_i) \Big\} dt, \tag{A.30}$$

expanding all the terms

$$\int_{t_i}^{t_f} \Big\{ \mathbf{q}_i \times \Big(m_i \, g \, l_i \mathbf{e}_3 - f_i l_i \mathbf{R}_i \mathbf{e}_3 - l_i \mathbf{f}_{i,e} \Big) \cdot \xi_i + \underbrace{\mathbf{q}_i \times \Big(- m_i \, l_i \, \dot{\mathbf{x}}_L + m_i l_i^2 \dot{\mathbf{q}}_i \Big)}_{f} \cdot \underbrace{\dot{\xi}_i}_{\dot{g}} + \dot{\mathbf{q}}_i \times \Big(- m_i \, l_i \, \dot{\mathbf{x}}_L + m_i l_i^2 \dot{\mathbf{q}}_i \Big) \cdot \xi_i \Big\} dt, \tag{A.31}$$

taking

$$\begin{cases} \dot{f} = \mathbf{q}_i \times \Big(- m_i \, l_i \, \ddot{\mathbf{x}}_L + m_i l_i^2 \ddot{\mathbf{q}}_i \Big) + \dot{\mathbf{q}}_i \times \Big(- m_i \, l_i \, \dot{\mathbf{x}}_L + m_i l_i^2 \dot{\mathbf{q}}_i \Big), \\ g = \xi_i, \end{cases}$$

yields to

$$\int_{t_i}^{t_f} \Big\{ \mathbf{q}_i \times \Big(m_i\, g\, l_i \mathbf{e}_3 - f_i l_i \mathbf{R}_i \mathbf{e}_3 - l_i \mathbf{f}_{i,e} \Big) + \dot{\mathbf{q}}_i \times \Big(\cancel{- m_i\, l_i\, \dot{\mathbf{x}}_L + m_i l_i^2 \dot{\mathbf{q}}_i} \Big) \Big] \cdot \xi_i \Big\}\, dt$$
$$+ \underbrace{\mathbf{q}_i \times \Big[- m_i\, l_i\, \dot{\mathbf{x}}_L + m_i l_i^2 \dot{\mathbf{q}}_i \Big] \cdot \dot{\xi}_i \Big|_{t_i}^{t_f}}_{=0}$$
$$- \int_{t_i}^{t_f} \Big\{ \Big[\cancel{\dot{\mathbf{q}}_i \times \Big(m_i l_i^2 \mathbf{q}_i - m_i l_i \dot{\mathbf{x}}_L \Big)} + \mathbf{q}_i \times \Big(m_i l_i^2 \ddot{\mathbf{q}}_i - m_i l_i \ddot{\mathbf{x}}_L \Big) \Big] \cdot \xi_i \Big\}\, dt, \tag{A.32}$$

rearranging and collecting the remaining terms leads to

$$\int_{t_i}^{t_f} \Big\{ \mathbf{q}_i \times \Big(m_i\, g\, l_i \mathbf{e}_3 - f_i l_i \mathbf{R}_i \mathbf{e}_3 - l_i \mathbf{f}_{i,e} - m_i l_i^2 \ddot{\mathbf{q}}_i + m_i l_i \ddot{\mathbf{x}}_L \Big) \cdot \xi_i \Big\}\, dt, \tag{A.33}$$

3. (I_3) Integrate the $\mathbf{R}_i$ term

$$\int_{t_i}^{t_f} \Big\{ \mathbf{m}_i \cdot \Big(\mathbf{R}_i^T \delta \mathbf{R}_i \Big) + \mathbf{J}_i \boldsymbol{\Omega}_i \cdot \delta \boldsymbol{\Omega}_i \Big\}\, dt, \tag{A.34}$$

using the previously defined variations

$$\int_{t_i}^{t_f} \Big\{ \mathbf{m}_i \cdot \Big(\mathbf{R}_i^T \mathbf{R}_i \hat{\eta}_i \Big) + \mathbf{J}_i \boldsymbol{\Omega}_i \cdot \Big(\boldsymbol{\Omega}_i \times \eta_i + \dot{\eta}_i \Big) \Big\}\, dt, \tag{A.35}$$

expanding all the terms

$$\int_{t_i}^{t_f} \Big\{ \mathbf{m}_i \cdot \eta_i + \Big(\mathbf{J}_i \boldsymbol{\Omega}_i \times \boldsymbol{\Omega}_i \Big) \cdot \eta_i + \mathbf{J}_i \boldsymbol{\Omega}_i \cdot \dot{\eta}_i \Big\}\, dt, \tag{A.36}$$

exploiting the derivative rule

$$\int_{t_i}^{t_f} \Big\{ \mathbf{m}_i \cdot \eta_i + \Big(\mathbf{J}_i \boldsymbol{\Omega}_i \times \boldsymbol{\Omega}_i \Big) \cdot \eta_i + \frac{d}{dt} \Big(\mathbf{J}_i \boldsymbol{\Omega}_i \cdot \eta_i \Big) - \mathbf{J}_i \dot{\boldsymbol{\Omega}}_i \cdot \eta_i \Big\}\, dt, \tag{A.37}$$

rearranging and collecting the remaining terms leads to

$$\int_{t_i}^{t_f} \Big\{ \Big(\mathbf{m}_i - \boldsymbol{\Omega}_i \times \mathbf{J}_i \boldsymbol{\Omega}_i - \mathbf{J}_i \dot{\boldsymbol{\Omega}}_i \Big) \cdot \eta_i \Big\}\, dt, \tag{A.38}$$

then it is possible to rewrite the variation of the action as the sum of the single integrals

$$\delta\mathfrak{a} = I_1 + I_2 + I_3, \tag{A.39}$$

imposing null the variation, for each instant of time, yields

$$\begin{cases} \sum_{i=1}^{n} f_i \mathbf{R}_i \mathbf{e}_3 - \Big(\sum_{i=1}^{n} m_i + m_L\Big) g \mathbf{e}_3 - \Big(\sum_{i=1}^{n} m_i + m_L\Big) \ddot{\mathbf{x}}_L + \sum_{i=1}^{n} m_i l_i \ddot{\mathbf{q}}_i \\ \qquad\qquad + \mathbf{f}_e + \sum_{i=1}^{n} \mathbf{f}_{i,e} = 0, \\ \mathbf{q}_i \times \Big(m_i\, g\, l_i\, \mathbf{e}_3 - f_i l_i \mathbf{R}_i \mathbf{e}_3 - l_i \mathbf{f}_{i,e} - m_i l_i^2 \ddot{\mathbf{q}}_i + m_i l_i \ddot{\mathbf{x}}_L \Big), \\ \mathbf{m}_i - \boldsymbol{\Omega}_i \times \mathbf{J}_i \boldsymbol{\Omega}_i - \mathbf{J}_i \dot{\boldsymbol{\Omega}}_i = 0, \end{cases} \tag{A.40}$$

these, together with the kinematics equations

$$\begin{cases} \frac{d}{dt}\mathbf{x}_L = \dot{\mathbf{x}}_L, \\ \dot{\mathbf{q}}_i = \omega \times \mathbf{q}_i, \\ \dot{\mathbf{R}}_i = \mathbf{R}_i \hat{\boldsymbol{\Omega}}_i, \end{cases} \tag{A.41}$$

considering also

$$\begin{cases} \mathbf{q}_i \cdot \dot{\mathbf{q}}_i = 0, \\ \dfrac{d}{dt}(\mathbf{q}_i \cdot \dot{\mathbf{q}}_i) = \mathbf{q}_i \cdot \ddot{\mathbf{q}}_i + \dot{\mathbf{q}}_i \cdot \dot{\mathbf{q}}_i = 0, \\ \omega_i \cdot \mathbf{q}_i = 0, \\ \dot{\mathbf{q}}_i \times \mathbf{q}_i = (\omega_i \times \mathbf{q}_i) \times \mathbf{q}_i = -\mathbf{q}_i \times (\omega_i \times \mathbf{q}_i) = \mathbf{q}_i \underbrace{(\omega_i \cdot \mathbf{q}_i)}_{=0} - \omega_i \underbrace{(\mathbf{q}_i \cdot \mathbf{q}_i)}_{=1} = -\omega_i, \\ \ddot{\mathbf{q}}_i = \dot{\omega}_i \times \mathbf{q}_i + \omega_i \times \dot{\mathbf{q}}_i = (\omega_i \times \omega_i) \times \mathbf{q}_i + \omega_i \times (\omega_i \times \mathbf{q}_i) = 0, \\ \mathbf{q}_i \times \ddot{\mathbf{q}}_i = \mathbf{q}_i \times (\dot{\omega}_i \times \mathbf{q}_i + \omega_i \times \dot{\mathbf{q}}_i) = \dot{\omega}_i \underbrace{(\mathbf{q}_i \cdot \mathbf{q}_i)}_{=1} - \mathbf{q}_i \underbrace{(\mathbf{q}_i \cdot \omega_i)}_{=0} + \omega_i \underbrace{(\mathbf{q}_i \cdot \dot{\mathbf{q}}_i)}_{=0} \\ \qquad\qquad - \dot{\mathbf{q}}_i \underbrace{(\mathbf{q}_i \cdot \omega_i)}_{=0} = \dot{\omega}_i, \\ \mathbf{q}_i \times (\mathbf{q}_i \times \ddot{\mathbf{q}}_i) = \mathbf{q}_i (\mathbf{q}_i \cdot \ddot{\mathbf{q}}_i) - \ddot{\mathbf{q}}_i (\mathbf{q}_i \cdot \mathbf{q}_i) = -\mathbf{q}_i (\dot{\mathbf{q}}_i \cdot \dot{\mathbf{q}}_i) - \ddot{\mathbf{q}}_i, \\ \ddot{\mathbf{q}}_i = -\mathbf{q}_i \times (\mathbf{q}_i \times \ddot{\mathbf{q}}_i) - \mathbf{q}_i (\dot{\mathbf{q}}_i \cdot \dot{\mathbf{q}}_i) = 0, \end{cases} \tag{A.42}$$

allows to rewrite the equations (A.40) as

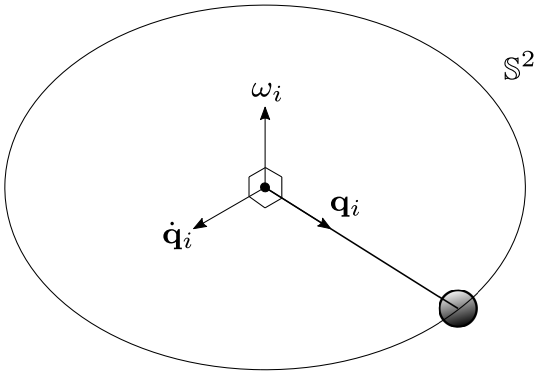

Figure A.2: Useful properties of directional vector $\mathbf{q}_i$ and its derivatives.

$$\begin{cases} \sum_{i=1}^{n} f_i \mathbf{R}_i \mathbf{e}_3 - \Big(\sum_{i=1}^{n} m_i + m_L\Big) g \mathbf{e}_3 - \Big(\sum_{i=1}^{n} m_i + m_L\Big) \ddot{\mathbf{x}}_L, \\ \qquad + \sum_{i=1}^{n} m_i l_i \big(- \mathbf{q}_i \times (\mathbf{q}_i \times \ddot{\mathbf{q}}_i) - \mathbf{q}_i (\dot{\mathbf{q}}_i \cdot \dot{\mathbf{q}}_i)\big) + \mathbf{f}_e + \sum_{i=1}^{n} \mathbf{f}_{i,e} = 0, \\ \mathbf{q}_i \times \ddot{\mathbf{q}}_i = \frac{1}{m_i l_i} \Big[\mathbf{q}_i \times \Big(m_i \, g \, l_i \, \mathbf{e}_3 - f_i l_i \mathbf{R}_i \mathbf{e}_3 - l_i \mathbf{f}_{i,w} + m_i l_i \ddot{\mathbf{x}}_L \Big) \Big], \\ \mathbf{m}_i - \boldsymbol{\Omega}_i \times \mathbf{J}_i \boldsymbol{\Omega}_i - \mathbf{J}_i \dot{\boldsymbol{\Omega}}_i = 0, \end{cases} \tag{A.43}$$

substituting the 2^{nd} equation into the 1^{st} leads to

$$\begin{aligned} \sum_{i=1}^{n} f_i \mathbf{R}_i \mathbf{e}_3 - \Big(\sum_{i=1}^{n} m_i + m_L\Big)(\ddot{\mathbf{x}}_L + g \mathbf{e}_3) - \sum_{i=1}^{n} m_i l_i \mathbf{q}_i (\dot{\mathbf{q}}_i \cdot \dot{\mathbf{q}}_i) + \mathbf{f}_e + \sum_{i=1}^{n} \mathbf{f}_{i,e} \\ - \sum_{i=1}^{n} \mathbf{q}_i \times \Big[\mathbf{q}_i \times \Big(m_i \, g \, \mathbf{e}_3 - f_i \mathbf{R}_i \mathbf{e}_3 - \mathbf{f}_{i,e} + m_i \ddot{\mathbf{x}}_L \Big) \Big] = 0, \end{aligned} \tag{A.44}$$

expanding all the terms and using the cross product rule allows to write

$$\begin{aligned} \sum_{i=1}^{n} f_i \mathbf{R}_i \mathbf{e}_3 - \Big(\sum_{i=1}^{n} m_i + m_L\Big)(\ddot{\mathbf{x}}_L + g \mathbf{e}_3) - \sum_{i=1}^{n} m_i l_i \mathbf{q}_i (\dot{\mathbf{q}}_i \cdot \dot{\mathbf{q}}_i) + \mathbf{f}_e + \sum_{i=1}^{n} \mathbf{f}_{i,e} \\ - \sum_{i=1}^{n} m_i \mathbf{q}_i \times \Big(\mathbf{q}_i \times (g \mathbf{e}_3 + \ddot{\mathbf{x}}_L) \Big) + \sum_{i=1}^{n} \mathbf{q}_i \Big(\mathbf{q}_i \cdot f_i \mathbf{R}_i \mathbf{e}_3 \Big) \\ - \sum_{i=1}^{n} f_i \mathbf{R}_i \mathbf{e}_3 (\mathbf{q}_i \cdot \mathbf{q}_i) - \sum_{i=1}^{n} \mathbf{f}_{i,e} (\mathbf{q}_i \cdot \mathbf{q}_i) + \sum_{i=1}^{n} \mathbf{q}_i (\mathbf{q}_i \cdot \mathbf{f}_{i,e}) = 0, \end{aligned} \tag{A.45}$$

using the outer product instead and rearranging, yields

$$-\Big(\sum_{i=1}^{n} m_i + m_L\Big)\big(\ddot{\mathbf{x}}_L + g\mathbf{e}_3\big) - \sum_{i=1}^{n} m_i l_i \mathbf{q}_i(\dot{\mathbf{q}}_i \cdot \dot{\mathbf{q}}_i) + \mathbf{f}_e - \sum_{i=1}^{n} m_i \hat{\mathbf{q}}_i{}^2(g\mathbf{e}_3 + \ddot{\mathbf{x}}_L) + \sum_{i=1}^{n} \mathbf{q}_i\Big(\mathbf{q}_i \cdot f_i \mathbf{R}_i \mathbf{e}_3\Big) + \sum_{i=1}^{n} \mathbf{q}_i(\mathbf{q}_i \cdot \mathbf{f}_{i,e}) = 0, \tag{A.46}$$

since

$$\sum_{i=1}^{n} m_i \mathbf{I}_3(g\mathbf{e}_3 + \ddot{\mathbf{x}}_L) = \sum_{i=1}^{n} m_i \hat{\mathbf{q}}_i{}^2(g\mathbf{e}_3 + \ddot{\mathbf{x}}_L) + \sum_{i=1}^{n} m_i \mathbf{q}_i \mathbf{q}_i^T(g\mathbf{e}_3 + \ddot{\mathbf{x}}_L), \tag{A.47}$$

then

$$\Big(\sum_{i=1}^{n} \mathbf{q}_i \cdot f_i \mathbf{R}_i \mathbf{e}_3 + \sum_{i=1}^{n} \mathbf{q}_i \cdot \mathbf{f}_{i,e} - \sum_{i=1}^{n} m_i l_i \dot{\mathbf{q}}_i \cdot \dot{\mathbf{q}}_i\Big)\mathbf{q}_i + \mathbf{f}_e = \Big(\sum_{i=1}^{n} m_i \mathbf{q}_i \mathbf{q}_i^T + m_L \mathbf{I}_3\Big)(g\mathbf{e}_3 + \ddot{\mathbf{x}}_L), \tag{A.48}$$

Hence, put all the equations together, return

$$\frac{d}{dt}\mathbf{x}_L = \dot{\mathbf{x}}_L, \tag{A.49}$$

$$(\sum_{i=1}^{n} m_i \mathbf{q}_i \mathbf{q}_i^T + m_L \mathbf{I})(\ddot{\mathbf{x}}_L + g\mathbf{e}_3) = \sum_{i=1}^{n} \big(\mathbf{v}_i^{\parallel} - m_i l_i ||\boldsymbol{\omega}_i||^2 \mathbf{q}_i + (\mathbf{q}_i \cdot \mathbf{f}_{i,e})\mathbf{q}_i\big) + \mathbf{f}_e, \tag{A.50}$$

$$\dot{\mathbf{q}}_i = \omega \times \mathbf{q}_i, \tag{A.51}$$

$$\dot{\boldsymbol{\omega}}_i = \frac{1}{l_i}\hat{\mathbf{q}}_i(\ddot{\mathbf{x}}_L + g\mathbf{e}_3) - \frac{1}{m_i l_i}\hat{\mathbf{q}}_i \mathbf{v}_i^{\perp} - \frac{1}{m_i l_i}\hat{\mathbf{q}}_i \mathbf{f}_{i,e}, \tag{A.52}$$

$$\dot{\mathbf{R}}_i = \mathbf{R}_i \hat{\boldsymbol{\Omega}}_i, \tag{A.53}$$

$$\mathbf{m}_i = \mathbf{J}_i \dot{\boldsymbol{\Omega}}_i + \boldsymbol{\Omega}_i \times \mathbf{J}_i \boldsymbol{\Omega}_i, \tag{A.54}$$

where the $\mathbf{I}_3$ is the identity matrix of dimension three, the vector $\mathbf{v}_i$ represents the control force of the i^{th} robot such that $\mathbf{v}_i = f_i \mathbf{R}_i \mathbf{e}_3$ whereas the vectors $\mathbf{v}_i^{\perp}$ and $\mathbf{v}_i^{\parallel}$ denote the projection of $\mathbf{v}_i$ along and to the plane normal to $\mathbf{q}_i$, respectively

$$\mathbf{v}_i^{\parallel} = (\mathbf{I} + \hat{\mathbf{q}}_i^2)\mathbf{v}_i = (\mathbf{q}_i \cdot \mathbf{v}_i)\mathbf{q}_i = \mathbf{q}_i \mathbf{q}_i^T \mathbf{v}_i, \tag{A.55}$$

$$\mathbf{v}_i^{\perp} = -\hat{\mathbf{q}}_i^2 \mathbf{v}_i = -\mathbf{q}_i \times (\mathbf{q}_i \times \mathbf{v}_i) = (\mathbf{I} - \mathbf{q}_i \hat{\mathbf{q}}_i^T)\mathbf{v}_i, \tag{A.56}$$

As a consequences of the equations (A.55) and (A.56), one has

$$\mathbf{v}_i = \mathbf{v}_i^{\perp} + \mathbf{v}_i^{\parallel}. \tag{A.57}$$

List of Figures

List of Tables

Bibliography

[1] I. H. B. Pizetta, A. S. Brandão, and M. Sarcinelli-Filho, "Load transportation by quadrotors in crowded workspaces," *IEEE Access*, 2020. DOI: 10.1109/ACCESS.2020.3043719.

[2] D. Sanalitro, H. Savino, M. Tognon, J. Cortés, and A. Franchi, "Full-pose manipulation control of a cable-suspended load with multiple uavs under uncertainties," *IEEE Robotics and Automation Letters*, 2020. DOI: 10.1109/LRA.2020.2969930.

[3] E. Rossi, M. Tognon, R. Carli, L. Schenato, J. Cortes, and A. Franchi, "Cooperative aerial load transportation via sampled communication," *IEEE Control Systems Letters*, 2020. DOI: 10.1109/LCSYS.2019.2924413.

[4] W. S. Richard M. Murray Muruhan Rathinam, "Differential flatness of mechanical control systems: A catalog of prototype systems," *Proceedings of the 1995 ASME International Congress and Exposition*, 1995. [Online]. Available: http://www.cds.caltech.edu/~murray/preprints/mrs95-imece.pdf.

[5] M. Fliess, J. Tevine, P. Martin, and P. Rouchon, "Nonlinear control and lie-backlund transformations: Towards a new differential geometric standpoint," *Proceedings of 1994 33rd IEEE Conference on Decision and Control*, 1994. DOI: 10.1109/CDC.1994.410906.

[6] L. Jean, *Analysis and control of nonlinear systems: A flatness-based approach*. Springer Science & Business Media, 2009.

[7] D. Mellinger and V. Kumar, "Minimum snap trajectory generation and control for quadrotors," *Proceedings - IEEE International Conference on Robotics and Automation*, 2011. DOI: 10.1109/ICRA.2011.5980409.

[8] S. Tang, K. Sreenath, and V. Kumar, "Aggressive maneuvering of a quadrotor with a cable-suspended payload," *Robotics: Science and Systems, Workshop on Women in Robotics*, 2014.

[9] S. Koushil, L. Taeyoung, and K. Vijay, "Geometric control and differential flatness of a quadrotor uav with a cable-suspended load," *52nd IEEE Conference on Decision and Control*, 2013. DOI: 10.1109/CDC.2013.6760219.

[10] F. Bullo and A. D. Lewis, *Geometric control of mechanical systems: modeling, analysis, and design for simple mechanical control systems*. Springer, Texts in Applied Mathematics, 2005. DOI: 10.1007/978-1-4899-7276-7.

[11] D. Mellinger, Q. Lindsey, M. Shomin, and V. Kumar, "Design, modeling, estimation and control for aerial grasping and manipulation," *IEEE International Conference on Intelligent Robots and Systems*, 2011. DOI: 10.1109/IROS.2011.6048556.

[12] N. Michael, D. Mellinger, Q. Lindsey, and V. Kumar, "The grasp multiple micro-uav testbed," *IEEE Robotics Automation Magazine*, 2010. DOI: 10.1109/MRA.2010.937855.

[13] T. Lee, M. Leok, and N. McClamroch, "Geometric tracking control of a quadrotor uav on se(3)," *Proceedings of the IEEE Conference on Decision and Control*, 2010. DOI: 10.1109/CDC.2010.5717652.

[14] T. Lee, K. Sreenath, and V. Kumar, "Geometric control of cooperating multiple quadrotor uavs with a suspended payload," *52nd IEEE Conference on Decision and Control*, 2013. DOI: 10.1109/CDC.2013.6760757.

[15] T. Lee, "Geometric control of quadrotor uavs transporting a cable-suspended rigid body," *IEEE Transactions on Control Systems Technology*, 2014. DOI: 10.1109/TCST.2017.2656060.

[16] J. C. Santos, "Model predictive tracking control of cable-driven parallel robots: From concept to real-time validation," Ph.D. dissertation, UNIVERSITÉ DE MONTPELLIER, 2020. DOI: https://theses.hal.science/tel-03154701.

[17] B. Alessandro, "Kinematics and statics of cable-driven parallel robots by interval-analysis-based methods," Ph.D. dissertation, Alma Mater Studiorum - Università di Bologna, 2015. DOI: 10.6092/unibo/amsdottorato/7151.

[18] J.-P. Merlet, *Parallel Robots*. Springer, 2006.

[19] A. Jorge, *Fundamentals of robotic mechanical systems*. Springer, 2002.

[20] M. Grebenstein, M. Chalon, and W. e. a. Friedl, "The hand of the dlr hand arm system: Designed for interaction," *The International Journal of Robotics Research*, 2012. DOI: 10.1177/0278364912459209.

[21] C. Paul, F. Valero-Cuevas, and H. Lipson, "Design and control of tensegrity robots for locomotion," *IEEE Transactions on Robotics*, 2006. DOI: 10.1109/TRO.2006.878980.

[22] C. F. Liew, D. DeLatte, N. Takeishi, and T. Yairi, "Recent developments in aerial robotics: A survey and prototypes overview," *arXiv preprint:1711.10085*, 2017.

[23] D. Villa, A. Brandão, and M. Sarcinelli-Filho, "A survey on load transportation using multirotor uavs," *Journal of Intelligent and Robotic Systems: Theory and Applications*, 2020. DOI: 10.1007/s10846-019-01088-w.

[24] M. Tognon and A. Franchi, *Theory and Applications for Control of Aerial Robots in Physical Interaction Through Tethers*. Springer Tracts in Advanced Robotics, 2020. DOI: https://doi.org/10.1007/978-3-030-48659-4.

[25] F. Ruggiero, V. Lippiello, and A. Ollero, "Aerial manipulation: A literature review," *IEEE Robotics and Automation Letters*, 2018. DOI: 10.1109/LRA.2018.2808541.

[26] C. Masone, H. Bülthoff, and P. Stegagno, "Cooperative transportation of a payload using quadrotors: A reconfigurable cable-driven parallel robot," *IEEE International Conference on Intelligent Robots and Systems*, 2016. DOI: 10.1109/IROS.2016.7759262.

[27] T. Rasheed, P. Long, and S. Caro, "Wrench-feasible workspace of mobile cable-driven parallel robots," *Journal of Mechanisms and Robotics*, 2020. DOI: 10.1115/1.4045423.

[28] H. Jamshidifar and A. Khajepour, "Static workspace optimization of aerial cable towed robots with land-fixed winches," *IEEE Transactions on Robotics*, 2020. DOI: 10.1109/TRO.2020.2998613.

[29] M. Métillon, C. Charron, K. Subrin, and S. Caro, "Performance and interaction quality variations of a collaborative cable-driven parallel robot," *Mechatronics*, 2022. DOI: https://doi.org/10.1016/j.mechatronics.2022.102839.

[30] A. Pott, "Cable-driven parallel robots," *Springer Tracts in Advanced Robotics*, 2018. DOI: 10.1007/978-3-319-76138-1.

[31] P. H. Borgstrom, B. L. Jordan, G. S. Sukhatme, M. A. Batalin, and W. J. Kaiser, "Rapid computation of optimally safe tension distributions for parallel cable-driven robots," *IEEE Transactions on Robotics*, 2009. DOI: 10.1109/TRO.2009.2032957.

[32] S.-R. Oh and S. K. Agrawal, "Cable-suspended planar parallel robots with redundant cables: Controllers with positive cable tensions," *IEEE International Conference on Robotics and Automation*, 2003. DOI: 10.1109/ROBOT.2003.1242055.

[33] D. C. Wei-Jung Shiang and J. Gorman, "Optimal force distribution applied to a robotic crane with flexible cables," *IEEE International Conference on Robotics and Automation*, 2000. DOI: 10.1109/ROBOT.2000.844880.

[34] C. Gosselin and M. Grenier, "On the determination of the force distribution in overconstrained cable-driven parallel mechanisms," *Meccanica*, 2011. DOI: https://doi.org/10.1007/s11012-010-9369-x.

[35] R. Verhoeven and M. Hiller, "Tension distribution in tendon-based stewart platforms," *Lenarčič, J., Thomas, F. (eds) Advances in Robot Kinematics*, 2002. DOI: https://doi.org/10.1007/978-94-017-0657-5_13.

[36] H. D. Taghirad and Y. B. Bedoustani, "An analytic-iterative redundancy resolution scheme for cable-driven redundant parallel manipulators," *IEEE Transactions on Robotics*, 2011. DOI: 10.1109/TRO.2011.2163433.

[37] M. Agahi and L. Notash, "Redundancy resolution of wire-actuated parallel manipulators," *Transactions of the Canadian Society for Mechanical Engineering*, 2009. DOI: https://doi.org/10.1139/tcsme-2009-0038.

[38] M. Hassan and A. Khajepour, "Optimization of actuator forces in cable-based parallel manipulators using convex analysis," *IEEE Transactions on Robotics*, 2008. DOI: 10.1109/TRO.2008.919289.

[39] M. Hassan and A. Khajepour, "Analysis of bounded cable tensions in cable-actuated parallel manipulators," *IEEE Transactions on Robotics*, 2011. DOI: 10.1109/TRO.2011.2158693.

[40] L. Mikelsons, T. Bruckmann, M. Hiller, and D. Schramm, "A real-time capable force calculation algorithm for redundant tendon-based parallel manipulators," *2008 IEEE International Conference on Robotics and Automation*, 2008. DOI: 10.1109/ROBOT.2008.4543805.

[41] A. Pott, "An improved force distribution algorithm for over-constrained cable-driven parallel robots," *6th International Workshop on Computational Kinematics (CK)*, 2013. DOI: 10.1007/978-94-007-7214-4_16.

[42] A. Pott, T. Bruckmann, and L. Mikelsons, "Closed-form force distribution for parallel wire robots," *Kecskeméthy, A., Müller, A. Computational Kinematics. Springer, Berlin, Heidelberg*, 2009. DOI: 10.1007/978-3-642-01947-0_4.

[43] S. Bouchard, C. Gosselin, and B. Moore, "On the ability of a cable-driven robot to generate a prescribed set of wrenches," *Journal of Mechanisms and Robotics*, 2010. DOI: 10.1115/1.4000558.

[44] C. R. Katharina Müller and T. Bruckmann, "Analysis of a real-time capable cable force computation method," *Cable-driven Parallel Robots: Proceedings of the Second International Conference on Cable-Driven Parallel Robots, Springer International Publishing*, 2014. DOI: 10.1007/978-3-319-09489-2_16.

[45] A. F. Côté, P. Cardou, and C. Gosselin, "A tension distribution algorithm for cable-driven parallel robots operating beyond their wrench-feasible workspace," *16th International Conference on Control, Automation and Systems (ICCAS)*, 2016. DOI: 10.1109/ICCAS.2016.7832301.

[46] M. Gouttefarde, J. Lamaury, C. Reichert, and T. Bruckmann, "A versatile tension distribution algorithm for n-dof parallel robots driven by $n + 2$ cables," *IEEE Transactions on Robotics*, 2015. DOI: 10.1109/TRO.2015.2495005.

[47] E. Ueland, T. Sauder, and R. Skjetne, "Optimal force allocation for overconstrained cable-driven parallel robots: Continuously differentiable solutions with assessment of computational efficiency," *IEEE Transactions on Robotics*, 2020. DOI: 10.1109/TRO.2020.3020747.

[48] D. M.-G. Tahir Rasheed Philip Long and S. Caro, "Tension distribution algorithm for planar mobile cable-driven parallel robots," *Cable-Driven Parallel Robots. Mechanisms and Machine Science. Springer,Cham*, 2018. DOI: 10.1007/978-3-319-61431-1_23.

[49] A. P. Tobias Bruckmann and M. Hiller, "Calculating force distributions for redundantlyactuated tendon-based stewart platforms," *Advances in Robot Kinematics (ARK), Ljubljana, Slovenia. Springer-Verlag*, 2006.

[50] Y. Nesterov and A. Nemirovskii, *Interior-Point Polynomial Algorithms in Convex Programming*. Society for Industrial and Applied Mathematics, 1994.

[51] S. Boyd and L. Vandenberghe, *Convex optimization*. Cambridge university press, 2004.

[52] R. Verhoeven, "Analysis of the workspace of tendon-based stewart platforms," Ph.D. dissertation, Universität Duisburg-Essen, 2004.

[53] S. J. W. Jorge Nocedal, *Numerical Optimization*. Springer New York, NY, 2006. DOI: https://doi.org/10.1007/978-0-387-40065-5.

[54] V. D. Paola, E. Ida, M. Zoppi, and S. Caro, "A preliminary study of factors influencing the stiffness of aerial cable towed systems," *ROMANSY, Springer International Publishing*, 2022. DOI: 10.1007/978-3-031-06409-8_29.

[55] dSPACE, *Real-time interface (rti)*, United Kingdom, 2023. [Online]. Available: https://www.dspace.com/en/ltd/home/products/sw/impsw/real-time-interface.cfm.

[56] E. Castillo, R. Mínguez, and C. Castillo, "Sensitivity analysis in optimization and reliability problems," *Reliability Engineering and System Safety*, 2008. DOI: https://doi.org/10.1016/j.ress.2008.03.010.

[57] K. C. Olds, "Global indices for kinematic and force transmission performance in parallel robots," *IEEE Transactions on Robotics*, 2015.

[58] G. Mottola, C. Gosselin, and M. Carricato, "Effect of actuation errors on a purely-translational spatial cable-driven parallel robot," *IEEE 9th Annual International Conference on CYBER Technology in Automation, Control, and Intelligent Systems (CYBER)*, 2019.

[59] P. Cardou, S. Bouchard, and C. Gosselin, "Kinematic-sensitivity indices for dimensionally nonhomogeneous jacobian matrices," *IEEE Transactions on Robotics*, 2010.

[60] D. S. Bernstein, "Matrix mathematics," *Princeton university press*, 2009.

[61] A. L. C. Ruiz, S. Caro, P. Cardou, and F. Guay, "Arachnis: Analysis of robots actuated by cables with handy and neat interface software," *2nd International Conference on Cable-Driven Parallel Robots*, 2015. DOI: 10.1007/978-3-319-09489-2_21.

[62] W.-D. Chang and J.-J. Yan, "Adaptive robust pid controller design based on a sliding mode for uncertain chaotic systems," *Chaos, Solitons & Fractals*, 2005. DOI: https://doi.org/10.1016/j.chaos.2004.12.013.

[63] Y.-C. Hsueh and S.-F. Su, "Supervisory controller design based on lyapunov stable theory," *2007 IEEE International Conference on Systems, Man and Cybernetics*, 2007. DOI: 10.1109/ICSMC.2007.4413948.

[64] S. Yuri, E. Christopher, F. Leonid, and L. Arie, *Sliding Mode Control and Observation*. Birkhäuser, New York, NY, 2014. DOI: https://doi.org/10.1007/978-0-8176-4893-0.

[65] J. Zabczyk, *Mathematical Control Theory, An Introduction*. Birkhäuser, Cham, 2020. DOI: https://doi.org/10.1007/978-3-030-44778-6.

[66] A. Noordin, M. A. Mohd Basri, Z. Mohamed, and I. Mat Lazim, "Adaptive pid controller using sliding mode control approaches for quadrotor uav attitude and position stabilization," *Arabian Journal for Science and Engineering*, 2021. DOI: 10.1007/s13369-020-04742-w.

[67] G. Wu and K. Sreenath, "Geometric control of multiple quadrotors transporting a rigid-body load," *53rd IEEE Conference on Decision and Control*, 2014. DOI: 10.1109/CDC.2014.7040351.

[68] G. F. A. and L. Taeyoung, "Stabilization of a rigid body payload with multiple cooperative quadrotors," *Journal of Dynamic Systems, Measurement, and Control*, 2016. DOI: 10.1115/1.4033945.

[69] P. Kotaru, G. Wu, and K. Sreenath, "Differential-flatness and control of quadrotor(s) with a payload suspended through flexible cable(s)," *2018 Indian Control Conference (ICC)*, 2018. DOI: 10.1109/INDIANCC.2018.8308004.

[70] G. Li, R. Ge, and G. Loianno, "Cooperative transportation of cable suspended payloads with mavs using monocular vision and inertial sensing," *IEEE Robotics and Automation Letters*, 2021. DOI: 10.1109/LRA.2021.3065286.

[71] K. Cole and A. Wickenheiser, "Spatio-temporal wind modeling for uav simulations," *arXiv*, 2019. DOI: arXiv:1905.09954.

[72] J.-J. Yan, "Design of robust controllers for uncertain chaotic systems with nonlinear inputs," *Chaos, Solitons & Fractals*, 2004. DOI: https://doi.org/10.1016/S0960-0779(03)00123-1.

[73] S. Waslander and C. Wang, "Wind disturbance estimation and rejection for quadrotor position control," *AIAA Infotech@Aerospace Conference*, 2009. DOI: 10.2514/6.2009-1983.

[74] K. Sreenath and V. Kumar, "Dynamics, control and planning for cooperative manipulation of payloads suspended by cables from multiple quadrotor robots," *Robotics: Science and Systems IX*, 2013. DOI: 10.15607/RSS.2013.IX.011.

[75] G. Wu and K. Sreenath, "Variation-based linearization of nonlinear systems evolving on $SO(3)$ and $\mathbb{S}^2$," *IEEE Access*, 2015. DOI: 10.1109/ACCESS.2015.2477880.

[76] J. Erskine, A. Chriette, and S. Caro, "Wrench analysis of cable-suspended parallel robots actuated by quadrotor unmanned aerial vehicles," *Journal of Mechanisms and Robotics*, 2019. DOI: 10.1115/1.4042513.

[77] V. Di Paola, A. Goldsztejn, M. Zoppi, and S. Caro, "Design of a sliding mode-adaptive pid control for aerial systems with a suspended load exposed to wind gusts," *Journal of Computational and Nonlinear Dynamics*, 2023. DOI: 10.1115/1.4062324.

[78] A. Berti, M. Gouttefarde, and M. Carricato, "Dynamic recovery of cable-suspended parallel robots after a cable failure," *Advances in Robot Kinematics 2016*, 2016. DOI: 10.1007/978-3-319-56802-7-35.

[79] G. Boschetti, C. Passarini, and A. Trevisani, "A strategy for moving cable driven robots safely in case of cable failure," *Advances in Italian Mechanism Science: Proceedings of the First International Conference of IFToMM Italy*, 2017. DOI: https://doi.org/10.1007/978-3-319-48375-7-22.

[80] C. Passarini, D. Zanotto, and G. Boschetti, "Dynamic trajectory planning for failure recovery in cable-suspended camera systems," *Journal of Mechanisms and Robotics*, 2019. DOI: 10.1115/1.4041942.

[81] R. Boumann and T. Bruckmann, "Development of emergency strategies for cable-driven parallel robots after a cable break," *Springer International Publishing, Cable-Driven Parallel Robots*, 2019. DOI: https://doi.org/10.1007/978-3-030-20751-9-23.

[82] R. Boumann and T. Bruckmann, "An emergency strategy for cable failure in reconfigurable cable robots," *Springer International Publishing, Cable-Driven Parallel Robots*, 2021. DOI: https://doi.org/10.1007/978-3-030-75789-2-18.

[83] L. Notash, "Failure recovery for wrench capability of wire-actuated parallel manipulators," *Robotica*, 2012. DOI: https://doi.org/10.1017/S0263574711001160.

[84] L. Notash, "Wrench recovery for wire-actuated parallel manipulators," *Robot Design, Dynamics and Control (ROMANSY), CISM*, 2013. DOI: 10.1007/978-3-7091-1379-0-25.

[85] R. Boumann and T. Bruckmann, "Computationally efficient cable force calculation outside the wrench-feasible workspace," *Robotics and Mechatronics, Springer International Publishing*, 2020. DOI: 10.1007/978-3-030-30036-4-15.

[86] R. Boumann and T. Bruckmann, "Real-time cable force calculation beyond the wrench-feasible workspace," *Robotics*, 2020. DOI: 10.3390/robotics9020041.

[87] G. Boschetti, R. Minto, and A. Trevisani, "Experimental investigation of a cable robot recovery strategy," *Robotics*, 2021. DOI: 10.3390/robotics10010035.

[88] V. Di Paola, A. Goldsztejn, M. Zoppi, and S. Caro, "Analytic center based tension distribution for cable-driven platforms (cdps)," *Working paper or preprint*, 2023. DOI: https://hal.science/hal-04023175. [Online]. Available: https://hal.science/hal-04023175.

[89] J. M. Selig, *Geometric Fundamentals of Robotics*. Springer New York, NY, 2007. DOI: https://doi.org/10.1007/b138859.

[90] A. André-Marie, *Essai sur la Philosophie des Sciences*. Chez Bachelier, 1834.

[91] K. Hunt, *Kinematic Geometry of Mechanisms*. Cambridge University Press, 1978. DOI: 10.1017/S026357470001571X.

[92] G. Hegedüs, Z. Li, J. Schicho, and H.-P. Schröcker, "From the fundamental theorem of algebra to kempe's universality theorem," *arXiv*, 2015. DOI: 10.48550/arXiv.1507.05317.

[93] Z. Li, J. Schicho, and H. Schröcker, "Kempe's universality theorem for rational space curves," *Foundations of Computational Mathematics*, 2017. DOI: 10.1007/s10208-017-9348-x.

[94] M. Chasles, *Note sur les propriétés générales du système de deux corps semblables entréux et placés d'une manière quelconque dans l'espace; et sur le déplacement fini ou infiniment petit d'un corps solide libre*. Bulletin des Sciences Mathématiques, Férussac, 1830.

[95] G. Mozzi, *Discorso matematico sopra il rotamento momentaneo dei corpi*. Donate Campo, 1763.

[96] H. Baruh, *Applied Dynamics*. CRC Press, 2014. DOI: https://doi.org/10.1201/b17897.

[97] S. Hassani, *Mathematical Physics: A Modern Introduction to Its Foundations*. Springer New York, NY, 2013. DOI: 10.1007/978-3-319-01195-0.

[98] R. S. Ball, *A Treatise on the Theory of Screws*. Hodges, Dublin, 1876.

[99] P. S. Donelan and C. G. Gibson, "On the hierarchy of screw systems," *Acta Applicandae Mathematicae*, 1993.

[100] J. Hervé, "The lie group of rigid body displacements, a fundamental tool for mechanism design," *Mechanism and Machine Theory*, 1999. DOI: https://doi.org/10.1016/S0094-114X(98)00051-2.

[101] C. Marco, "Singularity-free fully-isotropic translational parallel manipulators," Ph.D. dissertation, Alma Mater Studiorum - Università di Bologna, 2001.

[102] M. Carricato and R. Martínez, "Persistent screw systems of dimension three," *13th World Congress in Mechanism and Machine Science*, 2011.

[103] M. Carricato, "Persistent screw systems of dimension four," *Latest Advances in Robot Kinematics, Springer Netherlands*, 2012. DOI: 10.1007/978-94-007-4620-6_19.

[104] V. Di Paola, "Classification of 3-dimensional persistent screw systems: A numerical approach," M.S. thesis, University of Bologna, 2020.

[105] J. M. Selig and M. Carricato, "Persistent rigid-body motions and study's "ribaucour"problem," *Journal of Geometry*, 2017. DOI: 10.1007/s00022-016-0331-5.

[106] M. Carricato and R. Martínez, "Persistent screw systems," *Advances in Robot Kinematics: Motion in Man and Machine*, 2010.

[107] M. Carricato and D. Zlatanov, "Persistent screw systems," *Mechanism and Machine Theory*, 2014. DOI: https://doi.org/10.1016/j.mechmachtheory.2013.11.008.

[108] Y. Wu and M. Carricato, "Persistent manifolds of the special euclidean group se(3): A review," *Computer Aided Geometric Design*, 2020. DOI: https://doi.org/10.1016/j.cagd.2020.101872.

[109] J. M. Selig, Y. Wu, and M. Carricato, "Motion interpolation in lie subgroups and symmetric subspaces," *Computational Kinematics, Springer International Publishing*, 2018. DOI: 10.1007/978-3-319-60867-9_53.

[110] J. M. Selig, "On the geometry of point-plane constraints on rigid-body displacements," *Acta Applicandae Mathematicae*, 2011. DOI: https://doi.org/10.1007/s10440-011-9634-6.

[111] J. M. Selig, "On the geometry of the homogeneous representation for the group of proper rigid-body displacements," *Romanian Journal of Technical Sciences - Applied Mechanics.*, 2013.

[112] B. O'Neill, *Elementary Differential Geometry*. 1966.

[113] K. Sprott and Ravani, "Kinematic generation of ruled surfaces," *Advances in Computational Mathematics*, 2002.

[114] B. O. and R. B., *Theoretical Kinematics*. Dover Publications, New York, 1990.

[115] P. J., *Freedom in Machinery, Vol.1 and Vol.2*. Cambdridge University Press, Cambbridge, 2007.

[116] D. Dooner, *Kinematic Geometry of Gearing*. 2012.

[117] D. Dooner, "On the linear line complex and hyperboloidal gearing," *International Design Engineering Technical Conferences and Computers and Information in Engineering Conference*, 2000.

[118] R. B. Pottmann H. Peternell M., "An introduction to line geometry with applications," *Computer Aided Geometric Design*, 2000.

[119] F. Klein, *Elementary mathematics from an advanced standpoint*. Courier Corporation, 2004.

[120] J. Siegele, D. Scharler, and H. Schröcker, "Rational motions with generic trajectories of low degree," *Computer Aided Geometric Design*, 2020.

[121] J. Krames, "Über fußpunktkurven von regelflächen und eine besondere klasse von raumbewegungen (über symmetrische schrotungen i)," *Mh. f. Math. u. Phys.*, 1937.

[122] S. J.M. and M. Husty, "Half-turns and line symmetric motions," *Mechanism and Machine Theory*, 2011.

[123] H. Pottmann and J. Wallner, Computational line geometry *Mathematics and Visualization*. Springer-Verlag, Berlin, 2010.

[124] R. O., "Rationale räumliche zwangläufe vierter ordnung," *Akad. Wiss. Math.-Natur. Kl. Sitzungsber. II*, 1985.

[125] S. J.M., "Some mobile overconstrained parallel mechanisms," *Advances in Robot Kinematics : Proceedings of the 15th International Conference on Advances in Robot Kinematics*, 2016.

[126] G. Hegedüs, J. Schicho, and H. Schröcker, "Factorization of rational curves in the study quadric," *Mechanism and Machine Theory*, 2013.

[127] C. Huang, "The cylindroid associated with finite motions of the bennett mechanism," *Proceedings of the ASME Design Engineering Technical Conference, Irvine, CA*, 1996.

[128] J. C. Minshall, *A Treatise on the Line Geometry*. Cambridge University Press, 1903.

[129] C. Gibson and K. Hunt, "Geometry of screw systems—1: Screws: Genesis and geometry," *Mechanism and Machine Theory*, 1990. DOI: https://doi.org/10.1016/0094-114X(90)90103-Q.

[130] C. Gibson and K. Hunt, "Geometry of screw systems—2: Classification of screw systems," *Mechanism and Machine Theory*, 1990. DOI: https://doi.org/10.1016/0094-114X(90)90104-R.

[131] N. H. M. Taeyoung Lee Melvin Leok, "Global formulations of lagrangian and hamiltonian dynamics on manifolds: A geometric approach to modeling and analysis," *Springer Cham*, 2018. DOI: 10.1007/978-3-319-56953-6.

[132] L. Taeyoung, "Computational geometric mechanics and control of rigid bodies," Ph.D. dissertation, University of Michigan, Horace H. Rackham School of Graduate Studies, 2008. DOI: http://hdl.handle.net/2027.42/60804.

[133] F. Bullo and A. D. Lewis, *Geometric control of mechanical systems: modeling, analysis, and design for simple mechanical control systems*. Springer, 2019. DOI: 10.1007/978-1-4899-7276-7.

Titre : Un Traité sur les Problémes Ouverts en Robotique : Depuis les Plateformes Câblées aux Variétés Persitantes

Mots clés : Plateformes à câbles, contrôle adaptatif, cinématique théorique, systemes persistants

Résumé : Malgré les nombreux efforts en cours pour développer des questions dans le domaine de la robotique, il existe tout autant de problèmes ouverts et non résolus. Cette thèse se propose donc de s'attaquer à certains défis, dans le but d'effleurer la surface et de faire émerger de nouvelles idées ou de nouvelles voies. Les thèmes abordés seront divisés en deux parties. La première concerne le développement et l'amélioration des techniques de contrôle des systèmes robotiques à câbles. La seconde se concentre sur l'étude des variétés persistantes constituant des aspects de la cinématique théorique. En détail,

- la partie I concerne les robots parallèles à câbles. Elle développe à la fois une technique de calcul des tensions à appliquer aux câbles et la conception d'un contrôleur robuste. L'objectif est donc d'améliorer les deux éléments de base constituant le schéma de commande général d'un robot afin d'accroître les performances lors de l'exécution d'une task;
- La deuxième partie est dédiée à la cinématique théorique. La découverte et la classification des systèmes \textit{invariants} de torseurs ont permis d'éclairer de nombreux aspects de la mobilité et de la synthèse des chaînes cinématiques. De plus, cette dernière a généré l'émergence de nouvelles idées et de questions encore non résolues. Parmi celles-ci, l'une des plus connues concerne l'identification et la classification des variétés persistantes à 5 dimensions.

Title : A Treatise on Open Problems in Robotics: from Cable-Driven Platforms to Persistent Manifolds

Keywords : Cable-Driven Platforms, Adaptive Control, Theoretical Kinematics, Persistent Screw Systems

Abstract : Although many efforts are continuously devoted to the advancement of robotics, there are still many open and unresolved problems to be faced. This thesis, therefore, sets out to tackle some of them with the aim of scratching the surface and look a little further for new ideas or solutions. The topics covered are mainly two. The first part deals with the development and improvement of control techniques for cable-driven robot. The second focuses on the study of persistent manifolds seen as constituting aspects of theoretical kinematics. In detail,

- part I deals with cable-driven platforms. In it, both techniques for selecting cable tensions and the design of a robust controller are developed. The aim is, therefore, to enhance the two building blocks of the overall control scheme in order to improve the performance of these robots during the execution of tracking tasks.
- Part II delves into theoretical kinematics. The discovery and classification of invariant screw systems shed light on numerous aspects of robot mobility and synthesis. Nevertheless, this generated the emergence of new ideas and questions that are still unresolved. Among them, one of the more notable concerns the identification and classification of 5-dimensional.